PolyPublie
Polytechnique Montréal

POLYTECHNIQUE MONTRÉAL
UNIVERSITÉ D'INGÉNIERIE

Titre: Title:	Development of microporous membranes from PP/HDPE films through cast extrusion and stretching
Auteur: Author:	Seyed Hesamoddin Tabatabaei
Date:	2009
Type:	Mémoire ou thèse / Dissertation or Thesis
Référence: Citation:	Tabatabaei, S. H. (2009). Development of microporous membranes from PP/HDPE films through cast extrusion and stretching [Ph.D. thesis, École Polytechnique de Montréal]. PolyPublie. https://publications.polymtl.ca/8509/

Document en libre accès dans PolyPublie
Open Access document in PolyPublie

URL de PolyPublie: PolyPublie URL:	https://publications.polymtl.ca/8509/
Directeurs de recherche: Advisors:	Pierre Carreau, & Abdellah Ajji
Programme: Program:	Unspecified

Ce fichier a été téléchargé à partir de PolyPublie, le dépôt institutionnel de Polytechnique Montréal
This file has been downloaded from PolyPublie, the institutional repository of Polytechnique Montréal

https://publications.polymtl.ca

UNIVERSITÉ DE MONTRÉAL

DEVELOPMENT OF MICROPOROUS MEMBRANES FROM PP/HDPE FILMS THROUGH CAST EXTRUSION AND STRETCHING

SEYED HESAMODDIN TABATABAEI
DÉPARTEMENT DE GÉNIE CHIMIQUE
ÉCOLE POLYTECHNIQUE DE MONTRÉAL

THÈSE PRÉSENTÉE EN VUE DE L'OBTENTION
DE DIPLÔME DE PHILOSOPHIAE DOCTOR (Ph.D.)
(GÉNIE CHIMIQUE)
MAI 2009

© Seyed Hesamoddin Tabatabaei, 2009.

Library and Archives Canada

Published Heritage Branch

395 Wellington Street
Ottawa ON K1A 0N4
Canada

Bibliothèque et Archives Canada

Direction du Patrimoine de l'édition

395, rue Wellington
Ottawa ON K1A 0N4
Canada

Your file Votre référence
ISBN: 978-0-494-69193-9
Our file Notre référence
ISBN: 978-0-494-69193-9

NOTICE:

The author has granted a non-exclusive license allowing Library and Archives Canada to reproduce, publish, archive, preserve, conserve, communicate to the public by telecommunication or on the Internet, loan, distribute and sell theses worldwide, for commercial or non-commercial purposes, in microform, paper, electronic and/or any other formats.

The author retains copyright ownership and moral rights in this thesis. Neither the thesis nor substantial extracts from it may be printed or otherwise reproduced without the author's permission.

AVIS:

L'auteur a accordé une licence non exclusive permettant à la Bibliothèque et Archives Canada de reproduire, publier, archiver, sauvegarder, conserver, transmettre au public par télécommunication ou par l'Internet, prêter, distribuer et vendre des thèses partout dans le monde, à des fins commerciales ou autres, sur support microforme, papier, électronique et/ou autres formats.

L'auteur conserve la propriété du droit d'auteur et des droits moraux qui protège cette thèse. Ni la thèse ni des extraits substantiels de celle-ci ne doivent être imprimés ou autrement reproduits sans son autorisation.

In compliance with the Canadian Privacy Act some supporting forms may have been removed from this thesis.

While these forms may be included in the document page count, their removal does not represent any loss of content from the thesis.

Conformément à la loi canadienne sur la protection de la vie privée, quelques formulaires secondaires ont été enlevés de cette thèse.

Bien que ces formulaires aient inclus dans la pagination, il n'y aura aucun contenu manquant.

Canada

UNIVERSITÉ DE MONTRÉAL

ÉCOLE POLYTECHNIQUE DE MONTRÉAL

Cette thèse intitulée:

DEVELOPMENT OF MICROPOROUS MEMBRANES FROM PP/HDPE FILMS THROUGH CAST EXTRUSION AND STRETCHING

présentée par: TABATABAEI Seyed Hesamoddin

en vue de l'obtention de diplôme de: Philosophiae Doctor

a été dûment acceptée par le jury d'examen constitué de:

M. DUBOIS Charles, Ph.D., président

M. CARREAU Pierre, Ph.D., membre et directeur de recherche

M. AJJI Abdellah, Ph.D., membre et codirecteur de recherche

M. FAVIS Basil, Ph.D., membre

M. VLACHOPOULOS John, D.Sc., membre

DEDICATION

To my parents, sister and brothers,

and

in memory of my beloved niece,

Faezeh 1996-2005

ACKNOWLEDGEMENTS

First of all, I would like to express my deep and sincere gratitude to my supervisor, Prof. Pierre Carreau. His wide knowledge and his logical way of thinking as well as his patience, encouragements, advices, and guidance have been great value for me.

I am deeply grateful to my co-supervisor, Dr. Abdellah Ajji, for his detailed and constructive comments, and for his important support, encouragement, advices throughout this work.

Thanks also to the many other professors at Ecole polytechnique of Montreal: Prof. Basil Favis, Dr. Miroslav Grmela, Dr. Marie-Claude Heuzey, Dr. Gregory Patience, and Dr. Michel Huneault.

I wish also to thank my undergraduate professors at Isfahan University of Technology (IUT) particularly Dr. Mohsen Nasr Esfahani and Dr. Saeed Nouri for encouraging me to go to graduate school.

Special thanks to the technical staff of chemical engineering department, especially Melina Hamdine, Weawkamol Leelapornpisit, and Jacques Beausoleil. Thanks also to the technicians of industrial material institute (IMI), particularly Jacques Dufour, Francois Vachon, and Karine Théberge for helping me in the completion of this study. I am also thankful to Messrs. Patrick Cigana, Luc Parent, and Pierre-Marc Simard for their technical help at POLYNOV.

I warmly thank Mr. Amirhossein Maani, my undergraduate as well as graduate colleague, for his valuable advice, friendly help, and extensive discussions during this study. My sincere thanks are due to my friends in Ecole Polytechnique of Montreal, who their helps, discussions and encouragements were so valuable.

My special gratitude is due to my father, mother, sister, and brothers and their families for their lovely supports and encouragements.

Lastly but not least, I thank God my creator, savior and guide who has supported me all the time and carried me when I needed help. I can simply never do enough to thank him!

RÉSUMÉ

Les caractéristiques des résines telles que la masse moléculaire, la distribution des masses moléculaires et le nombre des longues branches dans les chaînes ainsi que les conditions de procédé sont des facteurs clés dans la production de films précurseurs pour la fabrication de membranes polymères. L'épaisseur, l'orientation et la connexion entre les cristaux contrôlent ultimement la structure de la membrane. Dans cette thèse, nous avons étudié le développement de membranes microporeuses ayant de hautes performances à partir le films monocouches et multicouches à base de polypropylène et de polyéthylène de haute densité (PP/HDPE). Ces membranes sont obtenues par extrusion suivi d'étirage uniaxial de la structure lamellaire en rangée à l'aide d'une installation de production industrielle (Polynov). Nous avons également étudié l'étirage de films de PP ayant une structure composée de lamelles et sphérulites ou sphérulites seulement à l'aide d'un équipement d'étirage dans la direction machine (MDO) pour observer les changements de la morphologie en relation avec les propriétés barrières, de déchirure et de perçage.

En plus de la fabrication des membranes par étirage, des études exhaustives des propriétés thermiques et rhéologiques de mélanges de différents polypropylènes linéaires (L-PP) avec des polypropylènes possédant de longues branches (LCB-PP) ont été effectuées. Elle ont fourni des informations très importantes concernant les caractéristiques des résines, particulièrement sur l'effet de la masse moléculaire M_w et

des longues branches sur les propriétés rhéologiques et thermiques, qui pourraient être très utiles pour des développements subséquents des membranes polymères.

ABSTRACT

One of the techniques to make porous membranes from polymers without using solvent and/or particles is based on the stretching a polymer film containing a row-nucleated lamellar structure. Resin characteristics such as molecular weight, molecular weight distribution, and amount of long chain branching as well as process conditions are the key factors for the production of the precursor films with appropriate crystalline morphology and orientation, which in turn control the final membrane properties. We have developed microporous membranes with high performances from monolayer as well as multilayer polypropylene/high density polyethylene (PP/HDPE) films through cast extrusion followed by uniaxial stretching of row-nucleated lamellar structure involving industrial scale capabilities. We also investigated the drawing of polypropylene films with coexisting rows of lamellae and spherulites and only spherulites using a machine direction orientation (MDO) unit. We have investigated changes in morphology in relation with the barrier properties as well as tear and puncture properties. A complete disruption of the initial structure was observed at high draw ratios and a correlation between orientation of both crystalline and amorphous phases and barrier properties was found.

In addition to the membrane fabrication by stretching, comprehensive investigations on the rheological and thermal properties of blends of different linear polypropylenes (L-PP) and a long chain branched polypropylene (LCB-PP) were performed. This provides valuable information concerning the resin characteristics particularly the effect

of molecular weight and long chain branching on the rheological and thermal properties, which was helpful in the membrane development.

CONDENSÉ EN FRANÇAIS

Les techniques de fabrication des membranes poreuses polymères sans utilisation de solvant ou ajout de particules ont été développées dans les années 70 du vingtième siècle pour diverses applications, en particulier pour les séparateurs dans les batteries lithium-ions et l'oxygénation du sang. Cependant, la majeure partie des informations relatives à ces techniques et procédés appartiennent aux compagnies qui les ont développées et ne sont pas disponibles pour la communauté scientifique. Une des techniques est basée sur l'étirage d'un film polymère ayant une structure lamellaire en rangée. Dans ce procédé, trois étapes consécutives sont effectuées pour obtenir les membranes poreuses: (1) préparation d'un film précurseur ayant une structure lamellaire en rangée par cristallisation induite sous cisaillement et élongation, (2) recuit du film précurseur à des températures proches du point de fusion de la résine pour éliminer les imperfections dans la phase cristalline et augmenter l'épaisseur des lamelles et, (3) étirage à basse et haute température pour créer et élargir les pores, respectivement. Pour produire les membranes microporeuse par la technique d'étirage, le film précurseur doit avoir une orientation moléculaire et un alignement des lamelles adéquats. Les caractéristiques des résines telles que la masse moléculaire, la distribution des masses moléculaires et le niveau des longues branches dans les chaînes ainsi que les conditions de procédé sont des facteurs clés dans la production de films précurseurs. Ainsi l'épaisseur, l'orientation et la connexion entre les cristaux contrôlent ultimement la structure de la membrane. Dans cette thèse, nous avons étudié le développement de membranes microporeuses

ayant de hautes performances à partir le films monocouches et multicouches à base de polypropylène et de polyéthylène de haute densité (PP/HDPE) obtenus par extrusion suivi d'étirage uniaxial de la structure lamellaire en rangée à l'aide d'une installation de production industrielle (Polynov). Nous avons également étudié l'étirage de films de PP ayant une structure composée de lamelles et sphérulites ou sphérulites seulement à l'aide d'un équipement d'étirage dans la direction machine (MDO) pour observer les changements de la morphologie en relation avec les propriétés barrières, de déchirure et de perçage.

Une revue de la littérature sur la classification des membranes, les facteurs importants affectant la structure cristalline, les travaux précédents sur la fabrication des membranes et les études d'orientation dans la direction machine des films semi-cristallins est présentée au chapitre 2. Les matériaux utilisés et la méthodologie pour la réalisation de nos objectifs sont présentés au chapitre 3. Le chapitre 4 explique brièvement l'organisation des articles. Au chapitre 5, l'influence des chaînes de haute masse moléculaire du PP sur sa cristallisation lamellaire en rangée a été étudiée à l'aide des techniques de diffraction des rayons X aux grands et petits angles (WAXD et SAXS), la spectroscopie infrarouge (FTIR) et les mesures mécaniques.

L'ajout de jusqu'à 10% en poids d'un PP de haute masse molaire (M_w) a un PP de basse masse M_w a amélioré l'orientation tant de la phase cristalline qu'amorphe. Les changements structuraux induit par le recuit ont également été explorés. Le recuit à 140 ^{o}C sans extension a contribué significativement à la perfection de la phase cristalline du

PP. On a montré qu'en utilisant des mélanges polymères, la densité des pores, leur taille et distribution, la porosité et la tortuosité des membranes poreuses pouvaient être mieux contrôlées.

Le chapitre 6 discute en détails les effets des paramètres de procédé tels que les conditions de refroidissement par l'air, la température du rouleau de refroidissement et le taux d'étirage sur l'orientation cristalline, la morphologie et les propriétés mécaniques des films produits à l'échelle industrielle à Polynov ainsi que sur la formation des membranes microporeuses. Le refroidissement à l'air et la température du rouleau de formage ont eu un rôle crucial sur l'orientation et le niveau de formation de lamelles dans les films. Les propriétés mécaniques en tension et la déchirure dans les directions machine (MD) et transverse (TD) des films ont été évaluées et reliées à la structure cristalline. Des augmentations significatives dans le module de Young, la contrainte au seuil, la résistance en tension et l'absorption d'énergie en tension dans la direction MD et une diminution drastique de l'élongation à la rupture dans la direction TD ont été observées pour les films ayant subi un refroidissement à l'air. Nous avons également reporté des résultats sur les membranes microporeuses qui élucident l'effet de la microstructure des films précurseurs en PP sur la morphologie et la perméabilité des membranes.

Le chapitre 7 présente les résultats sur la fabrication des membranes microporeuses tricouches PP/HDPE/PP par le procédé d'extrusion cast suivi d'étirage. Le rôle des paramètres de procédé et de recuit sur l'arrangement et l'orientation de la

phase cristalline développée dans les films monocouches ainsi que les composantes des films multicouches a été examiné et discuté. Un effet significatif du recuit sur la longue période des cristaux et l'épaisseur lamellaire a été observé. La cristallisation lamellaire en rangée et la trans-cristallisation observées sur la surface et à l'interface entre les couches, respectivement, ont été analysées. Des images par microscopie électronique à balayage (SEM) de la surface des membranes et de sections en épaisseur ont montré des pores plus grosses et une porosité plus élevée pour le HDPE comparé au PP. De plus, l'influence des variables d'étirages (i.e. temps et température) sur le taux de transmission de la vapeur d'eau (WVTR) a été considérée.

Tel que mentionné précédemment, l'étirage d'un film de morphologie lamellaire en "shish-kebab'' hautement orientée implique la séparation des lamelles superposées, conduisant à la formation de pores et la génération de membranes microporeuses. Par contre, l'étirage de films ayant une structure cristalline en sphérulites implique une transformation morphologique des sphérulites, ce qui affecte les propriétés finales des films. Au chapitre 8, les films précurseurs ayant une structure en sphérulites ou en sphérulites et lamelles combinées ont été étirés uniaxialement à 120 ^{o}C à l'aide d'un équipement d'étirage dans la direction machine (MDO). Les changements de la structure et la morphologie cristalline ont été examinés par DSC, FTIR, SAXS et WAXD et reliés aux propriétés barrières, de déchirure et de perçage. Des effets significatifs de la morphologie cristalline initiale ainsi que du rapport d'étirage (DR) sur l'alignement des phases amorphes et cristallines ont été observés. Nos résultats ont montré qu'en

augmentant le DR, les lamelles cristallines se brisent et réorientent le long de la direction d'étirage puis, à haut DR, ont été déformées et transformées en une structure fibrillaire. Le taux de transmission d'oxygène (OTR) des films orientés par MDO pouvait être corrélé avec les paramètres d'orientation ainsi que l'intensité du pic de transition β des segments de chaînes amorphes liant les blocs cristallins.

En plus de la fabrication des membranes par étirage, des études exhaustives sur les propriétés thermiques et rhéologiques de mélanges de différents polypropylènes linéaires (L-PP) avec ceux ayant de longues branches (LCB-PP) ont été effectuées. Même si cette dernière partie de la thèse s'écarte de l'étude des membranes microporeuses, elle fournit des informations très importantes concernant les caractéristiques des résines, particulièrement sur l'effet de la masse moléculaire M_w et des longues branches sur les propriétés rhéologiques et thermiques, qui pourraient être très utiles pour des développements subséquents des membranes. L'annexe A élucide l'impact de l'ajout des chaînes ayant de longues branches (LCB-PP) au L-PP sur ses propriétés rhéologiques, incluant le comportement extensionnel transitoire et en régime permanent sur une large gamme de vitesses de déformation. Les résultats en cisaillement obtenus sur des rhéomètres commerciaux ainsi que du rhéomètre à filière en fente ont été utilisés pour vérifier l'analogie de Cox-Merz pour les composants pur et les mélanges. Un rhéo-épaississement important a été observé pour le LCB-PP ainsi que pour tous les mélanges, mais diminuait avec l'augmentation de la vitesse de déformation et n'a pas été observé pour le L-PP. A l'annexe B, le rôle de la masse moléculaire du L-PP sur le

comportement rhéologique des mélanges LCB-PP/L-PP a été considéré. Se basant sur la relation d'additivité logarithme de la viscosité à faible cisaillement, les diagrammes Cole-Cole, les spectres de relaxation pondérés et le comportement élongationnel, les mélanges de L-PP de basse masse moléculaire avec le LCB-PP ont été évalués comme étant miscibles. Cependant, les mélanges de L-PP de haute masse moléculaire avec le LCB-PP étaient immiscibles. De plus, l'influence de l'ajout du LCB-PP au L-PP sur les propriétés thermiques, la vitesse de cristallisation et le comportement à l'état solide a été exploré.

TABLE OF CONTENT

DEDICATION iv

ACKNOWLEDGEMENTS v

RÉSUMÉ vii

ABSTRACT ix

CONDENSÉ EN FRANÇAIS xi

TABLE OF CONTENT xvii

LIST OF TABLES xxii

LIST OF FIGURES xxiii

LIST OF APPENDIXES xxxiii

LIST OF SYMBOLS xxxv

CHAPTER 1

INTRODUCTION 1

CHAPTER 2

LITERATURE REVIEW 6

2.1 Membrane classification 6

2.2 Techniques for membrane fabrication 8

2.3 Stretching 10

2.4 Polypropylene and polyethylene structure 15

2.5 Flow induced crystallization (FIC) 17

2.6 Microporous membranes by dry-stretching 32

2.6.1 HDPE microporous membranes by stretching 34

2.6.2 PP microporous membranes by stretching 36

2.6.3 PMP, POM and PVDF microporous membranes by stretching 39

2.7 Structure and properties of uniaxial and biaxial stretched films 43

2.8 Originality of the work 45

2.9 Objectives 46

CHAPTER 3

METHODOLOGY AND MATERIALS 47

3.1 Methodology 47

3.1.1 Material characterization 47

3.1.2 Extrusion parameters for the fabrication of precursor films 47

3.1.3 Annealing and stretching conditions 48

3.1.4 Film and membrane characterization 48

3.2 Materials 55

3.3 Processing 56

CHAPTER 4

ORGANIZATION OF ARTICLES 59

CHAPTER 5

Microporous Membranes Obtained from Polypropylene Blend Films by Stretching 61

5.1 Introduction 62

5.2 Experimental 66

5.2.1 Materials 66

5.2.2 Rheological characterization 67

5.2.3 Film and membrane preparation 68

5.2.4 Film and membrane characterization 68

5.3 Results and discussion 72

5.3.1 Rheological characterization 72

5.3.2 Film and membrane characterization 76

5.4 Conclusions 97

5.5 Acknowledgment 98

5.6 References 99

CHAPTER 6

Effect of Processing on the Crystalline Orientation, Morphology, and Mechanical Properties of Polypropylene Cast Films and Microporous Membrane Formation 103

6.1 Introduction 104

6.2 Experimental 107

6.2.1 Material 107

6.2.2 Film and membrane preparation 108

6.2.3 Film and membrane preparation 109

6.2.4 Rheological characterization 113

6.3 Results and discussion 113

6.4 Conclusions 141

6.5 Acknowledgement 143

6.6 References 143

CHAPTER 7

Microporous Membranes Obtained from PP/HDPE Multilayer Films by Stretching ... 146

7.1 Introduction 147

7.2 Experimental 151

7.2.1 Materials 151

7.2.2 Rheological characterization 152

7.2.3 Film and membrane preparation 153

7.2.4 Film and membrane characterization 153

7.3 Results and discussion 159

7.3.1 Rheological and film characterization 159

7.3.2 Membrane characterization 173

7.3.3 Effect of cold and hot stretching 176

7.4 Conclusions 182

7.5 Acknowledgement 184

7.6 References 184

CHAPTER 8

Structure and Properties of MDO Stretched Polypropylene 187

8.1 Introduction 188

8.2 Experimental 191

8.2.1 Material 191

8.2.2 Film preparation 191

8.2.3 Film characterization 193

8.3 Results and discussion 197

8.4 Conclusions 219

8.5 Acknowledgements 220

8.6 References 221

CHAPTER 9

GENERAL DISCUSSION 223

CHAPTER 10

CONCLUSIONS AND RECOMMENDATIONS 227

10.1 Conclusions 227

10.2 Recommendations 230

REFERENCES 233

APPENDIXES 240

LIST OF TABLES

Table 2.1 Different major techniques to prepare microporous polymeric membranes[11]..... 9

Table 2.2 Composition, thermal properties, and molecular weight of the LCB-PP polymers[48]..... 28

Table 3.1 Main characteristics of the neat polymers..... 56

Table 5.1. Main characteristics of neat polymers..... 67

Table 5.2. Properties of microporous membranes (28 μm thick). Annealing was performed at 140 °C for 30 min; DR=70, cold stretching of 35% followed by hot stretching of 55% (values are averaged over 5 tests for each sample)..... 92

Table 6.1 Crystal characteristics of the cast films obtained under different air cooling rates; DR=75..... 124

Table 6.2 Mechanical properties of the cast films along MD and TD (the numbers in parenthesis indicate the standard deviation of the measurements); DR=75..... 133

Table 7.1 Main characteristics of neat polymers..... 152

Table 7.2 Mechanical properties of the cast films along MD and TD (the numbers in parentheses indicate the standard deviation of the measurements); H-AFR..... 171

Table 7.3 Mechanical properties of microporous membranes (20 μm thick). Annealing was performed at 120 °C for 30 min; DR=70, cold stretching of 55% followed by hot stretching of 75% (the numbers in parentheses indicate the standard deviation of the measurements)..... 176

Table 1. Main characteristics of the neat polymers..... 243

Table 1. Main characteristics of the neat polymers..... 275

Table 2. Melting point (T_m), crystallization temperature (T_c), and degree of crystallinity (X_c) of the neat PPs as well as the blends (the numbers in parenthesis indicate the standard deviation of crystallinity)..... 294

LIST OF FIGURES

Fig. 2.1 Separation processes differing in the size of the particles to be separated[11] 7

Fig. 2.2 Schematic illustration of various polymeric membranes[11] 9

Fig. 2.3 Pore size distributions of the biaxially stretched samples[20] 11

Fig. 2.4 SEM images of biaxially stretched PP microporous sheets. The mean particle size of fillers is: No.1: 2μ, No.2: 1.3 μm, and No.3: 0.8 μm[21] 12

Fig. 2.5 SEM micrographs of surface of a PP film a) before and b) after stretching 14

Fig. 2.6 Stacked lamellar crystal structure observed on the surface of a) PVDF (AFM)[30], b) PVDF (SEM)[6], c) POM[7], d) PMP[7], e) PP, and f) PE 15

Fig. 2.7 The orthorhombic unit cell structure of polyethylene[5]. The right is also showing the monoclinic unit cell structure of polypropylene 17

Fig. 2.8 Crystallization of a PP under different flow conditions: a) quiescent crystallization, b) crystallization under low shear rate, and c) crystallization under high shear rate[43] 19

Fig. 2.9 Schematic of a) a spherulitic and b) a shish-kebab structure[50] 19

Fig. 2.10 Schematic of the types of row structure with the respective extrusion conditions and the main features of the PE WAXD patterns[5] 20

Fig. 2.11 Evolution of the storage modulus during crystallization of an iPP at T=135 °C, measured under quiescent conditions (o, 1) and after shearing at $\dot{\gamma}$=60 s^{-1} for t_s=1s (□, 2) and t_s=6 s (Δ, 3). Optical micrographs indicate the characteristic morphology for the three crystallization experiments[49] 22

Fig. 2.12 a) Schematic showing the effect of imposed shear conditions on the shift in the location of the critical molecular weight M^*. b) Critical orientation molecular weight M^* as a function of shear rate at 140 °C[49] 24

Fig. 2.13 Schematics of the formation of shear-induced primary nuclei and subsequent growth of oriented crystals at the surface undergoing maximum orientation in step-shear experiments[49] 25

Fig. 2.14 Half time of crystallization of the β-crystals at different shear rates[49]..... 25

Fig. 2.15 Pictograms of the nature of the shear induced nucleation and subsequent growth of oriented crystalline lamellae[47]..... 26

Fig. 2.16 2D SAXS images of PP-A and PP-B at selected times after shear (shear rate=60 s^{-1}, duration=5 s, and T=155 °C)[46]..... 27

Fig. 2.17 Comparison of 2D SAXS patterns of the four LCB-PP polymers 30 min after shear (shear rate=60 s^{-1}, t_s=0.25 s, T=140 °C)[48]..... 29

Fig. 2.18 Avrami plot of the crystallization data for LCB 01, 05, 07 polymers at 140 °C after shear (shear rate=60 s^{-1}, t_s=0.25 s)[48]..... 29

Fig. 2.19 Selected 2D WAXD patterns collected upon crystallization at 134 °C after shear (shear rate=70 s^{-1}, t_s=12 s)[60]..... 32

Fig. 2.20 Inner surface images of polyethylene hollow fiber a) precursor after annealing, b) membrane from unannealed precursor, and c) membrane from annealed precursor[79]..... 36

Fig. 2.21 SEM micrograph of the surface of PP (initial draw ratio of 56.5) samples cold stretched to 40% and heated set at 140 °C for 20 min[29]..... 38

Fig. 2.22 SEM micrographs of the surface of microporous membranes. Left PP28 (linear PP) and right Blend 2 wt% for initial DR=56[85]..... 39

Fig. 2.23 AFM phase images of POM a) annealed at 145 °C for 20 min and b) 50% cold stretched at 70 °C followed by 90% hot stretching at 160 °C[87]..... 41

Fig. 2.24 AFM phase images of PMP a) annealed at 205 °C for 20 min and b) 180% total (cold + hot) stretching[89]..... 41

Fig. 2.25 SEM micrograph of PVDF film showing lamellar opening[6]..... 43

Fig. 3.1 Illustration of the section just after die exit and chill rolls of the industrial scale cast unit for the fabrication of precursor films..... 58

Fig. 5.1 Complex viscosity as a function of angular frequency; T=190 °C..... 73

Fig. 5.2 Complex viscosity at different angular frequencies as a function of PP08 content; T=190 °C..... 74

Fig. 5.3 Weighted relaxation spectra for the neat PPs as well as for all the blends; T=190 °C (the vertical dash lines represent the range of frequencies covered during the experiments)... 75

Fig. 5.4 Cole-Cole plots for the neat PPs as well as for all the blends; T=190 °C..... 76

Fig. 5.5 Crystalline orientation function (obtained from FTIR) as a function of draw ratio for precursor films..... 77

Fig. 5.6 Crystallinity of films at various annealing conditions. (a) annealing at 140 °C, (b) annealing at 140 °C under 5% extension, and (c) annealing at 120 °C. Annealing was performed for 30 min; DR=70, cold stretching of 35% followed by hot stretching of 55%..... 78

Fig. 5.7 Crystalline and amorphous orientation parameters as a function of PP08 content. Annealing was performed at 140 °C for 30 min; DR=70..... 79

Fig. 5.8 Crystallinity of precursor films, annealed films, and membranes as a function of PP08 content. Annealing was carried out at 140 °C for 30 min; DR=70, cold stretching of 35% followed by hot stretching of 55%..... 82

Fig. 5.9 WAXD patterns of 10 wt% PP08 blend for (a) precursor film, (b) annealed sample, (c) membrane, (d) orientation features as $\cos^2(\phi)$ of the crystals along MD, TD, and ND, and (e) diffraction spectrum with integration through the circles. Annealing was performed at 140 °C for 30 min; DR=70, cold stretching of 35% followed by hot stretching of 55%..... 83

Fig. 5.10 SAXS intensity profiles for precursor, annealed, and stretched 10 wt% PP08 films. Annealing was performed at 140 °C for 30 min; DR=70, cold stretching of 35% followed by hot stretching of 55%..... 84

Fig. 5.11 SAXS patterns of precursor films. a) PP28 and b) 10 wt% PP08; DR=70..... 85

Fig. 5.12 Normalized maximum force for piercing as a function of PP08 content. Annealing was performed at 140 °C for 30 min; DR=70 and strain rate=25 mm/min..... 86

Fig. 5.13 Elongation at break for precursor films along the MD as a function of PP08 content; DR=70 and strain rate=25 mm/min..... 87

Fig. 5.14 Stress-strain curves along TD for precursor films of PP28 and blends; DR=70 and strain rate=25 mm/min..... 88

Fig. 5.15 WAXD patterns of the annealed films. a) PP28, b) 10 wt% PP08 blend, (c, d) film production axes and crystal block coordinates, respectively. Annealing was performed at 140

°C for 30 min; DR=70..... 89

Fig. 5.16 SEM micrographs of the surface (left images) and cross-section (right images) of the microporous membranes. a) PP28, b) 5 wt% PP08 blend, and c) 10 wt% PP08 blend; DR=70, cold stretching of 35%, followed by hot stretching of 55%..... 91

Fig. 5.17 Pore size distribution for microporous PP28, 5 wt% blend, and 10 wt % blend membranes; DR=70, cold stretching of 35% followed by hot stretching of 55%..... 94

Fig. 5.18 Normalized water vapor permeability for the 10 wt% PP08 blend membrane as a function of extension during cold stretching at temperatures of 25 °C and 45 °C; DR=70, hot stretching of 55%, and draw speed=50 mm/min..... 96

Fig. 5.19 Normalized water vapor permeability for the 10 wt% PP08 blend membrane as a function of extension during hot stretching at temperatures of 140 °C and 120 °C; DR=70, cold stretching of 35%, and draw speed=50 mm/min..... 97

Fig. 6.1 DSC scans of cast films for roll temperatures of 120, 110, and 100 °C. The top curves are the thermograms of cast films produced under N-AFR condition whereas the bottom curves are the thermograms of films fabricated under L-AFR; DR=75..... 116

Fig. 6.2 Crystalline orientation functions for different cast roll temperatures. The inset is a plot of the crystalline orientation function versus the air flow rate conditions for T_{cast}=120 °C; DR=75..... 117

Fig. 6.3 Amorphous orientation functions for different cast roll temperatures. The inset is a plot of the amorphous orientation function versus the air flow rate conditions for T_{cast}=120 °C; DR=75..... 117

Fig. 6.4 Crystal orientation functions for different air flow rate conditions at draw ratios of 60, 75, and 90; T_{cast}=120 °C..... 119

Fig. 6.5 2D WAXD patterns and azimuthal intensity profiles at 2θ of the 110 refection plane of PP at different air cooling conditions; T_{cast}=120 °C and DR=75..... 120

Fig. 6.6 Pole figures for the films obtained under different air cooling conditions. a) N-AFR, b) L-AFR, and c) M-AFR; T_{cast}=120 °C and DR=75. Schematics show the assumed crystal orientation..... 121

Fig. 6.7 Orientation characteristics as $\cos^2(\phi)$ of the crystal axes (*a*, *b* and *c*) along MD, TD, and ND; T_{cast}=120 °C and DR=75. The schematic represents the film production axes and crystal block coordinates..... 122

Fig. 6.8 2D SAXS patterns and azimuthal intensity profiles at the meridian of PP films for different air flow cooling conditions; T_{cast}=120 °C and DR=75..... 125

Fig. 6.9 Lorentz corrected SAXS intensity profiles for the films prepared under various air cooling conditions; T_{cast}=120 °C and DR=75..... 126

Fig. 6.10 SEM micrographs of the surface of films obtained under: a) N-AFR and T_{cast}=120 °C, b) N-AFR and T_{cast}=110 °C, and c) L-AFR and T_{cast}=120 °C. The right images are high magnification micrographs of the sections corresponding to the rectangles; DR=75. MD ↑ and TD →..... 129

Fig. 6.11 Typical stress-strain behavior for the films prepared under N-AFR and L-AFR conditions along MD (left figure) and TD (right figure); T_{cast}=120 °C and DR=75..... 131

Fig. 6.12 Mechanical properties of the films along MD for various air flow rate conditions; T_{cast}=120 °C and DR=75..... 131

Fig. 6.13 Elongation at break (left figure) and yield stress (right figure) of the films along TD for various air flow rate conditions; T_{cast}=120 °C and DR=75..... 132

Fig. 6.14 Proposed pictograms of the molecular structure for: a) no air cooled cast films and b) air cooled cast films (the solid lines represent the tear path along MD and the dash lines show the tear path along TD)..... 136

Fig. 6.15 Weighted relaxation spectra for different melt temperatures (the vertical dash lines represent the range of frequencies covered during the experiments)..... 138

Fig. 6.16 SEM micrographs of the surface of the films obtained at: a) N-AFR and b) L-AFR; T_{cast}=120 °C and DR=75, cold stretching of 35%, followed by hot stretching of 55%. MD ↑ and TD →..... 140

Fig. 6.17 Water vapor transmission rate (WVTR) as a function of cast roll temperature. The inset is a plot of WVTR as a function of air flow rate condition for T_{cast}=120 °C..... 141

Fig. 7.1 Complex viscosity as a function of angular frequency; T=190 °C. The inset is weighted relaxation spectra for the resins (the vertical dash lines represent the range of frequencies covered during the experiments)..... 160

Fig. 7.2 DSC heating thermograms for single layers as well as multilayer films; DR=90 and H-AFR..... 161

Fig. 7.3 2D WAXD patterns and diffraction spectrum with integration through the circles

for PP and HDPE monolayer films; DR=90 and H-AFR..... 163

Fig. 7.4 2D WAXD patterns and pole figures for films obtained under different DR, AFR, and annealing: a) PP monolayer, b) PP in multilayer, and c) HDPE monolayer. Annealing was performed at 120 °C for 30 min..... 166

Fig. 7.5 Orientation characteristics as $\cos^2(\phi)$ of the crystal axes (*a*, *b* and *c*) along MD, TD, and ND for the films obtained under different DR, AFR, and annealing: a) *c*-axis, b) *a*-axis, and c) *b*-axis. Annealing was performed at 120 °C for 30 min..... 167

Fig. 7.6 Lorentz corrected SAXS intensity profiles for precursor and annealed PP and HDPE films. Annealing was performed at 120 °C for 30 min; DR=90 and H-AFR..... 169

Fig. 7.7 SEM micrographs of the surface of the etched precursor films: a) PP and b) HDPE. The right images are high magnification micrographs of the left ones; DR=90 and H-AFR. MD ↑ and TD →..... 170

Fig. 7.8 Interfacial morphology of etched PP/HDPE multilayer films at different magnifications; DR=90 and H-AFR. MD ↑ and ND →..... 172

Fig. 7.9 SEM micrographs of the surface of microporous membranes (20 μm thick): a) PP and b) HDPE; DR=90, H-AFR, cold stretching of 55%, followed by hot stretching of 75%. MD ↑ and TD →..... 174

Fig. 7.10 SEM micrographs of the cross-section of trilayer microporous membranes (20 μm thick) at different magnifications; DR=90, H-AFR, cold stretching of 55%, followed by hot stretching of 75%..... 175

Fig. 7.11 Normalized water vapor permeability for PP and HDPE membranes as a function of extension during cold stretching at 25 °C; DR=90, H-AFR, hot stretching of 75%..... 178

Fig. 7.12 Stress-strain behavior for annealed PP and HDPE during the cold stretching step; Annealing was performed at 120 °C for 30 min; DR=90, H-AFR..... 180

Fig. 7.13 Nitrogen adsorption isotherms (77 K) measured by BET for PP and HDPE membranes. DR=90, H-AFR, cold stretching of 35%, followed by hot stretching of 75%..... 180

Fig. 7.14 SEM micrographs of the cross-section of multilayer microporous membranes; DR=90, H-AFR, cold stretching of 55%, followed by hot stretching of 175% (the arrows indicate the connection of the HDPE interlamellar microfibrils to the lamellae)..... 182

Fig. 8.1 SEM micrographs of the surface of the P-1 precursor film [15]. The right image is a

high magnification micrograph of the section corresponding to the rectangle. MD ↑ and TD →..... 193

Fig. 8.2 DSC heating thermograms for P-1 films obtained under different draw ratios..... 199

Fig. 8.3 Crystalline orientation function as a function of draw ratio..... 200

Fig. 8.4 Crystalline orientation function as a function of draw ratio..... 201

Fig. 8.5 2D WAXD patterns for P-1 (top) and P-2 (bottom) films obtained under different draw ratios..... 203

Fig. 8.6 Pole figures of 110 (top) and 040 (bottom) reflections for P-1 films obtained under different draw ratios..... 205

Fig. 8.7 Orientation characteristics as $\cos^2(\phi)$ of the crystal axes (*a*, *b*, and *c*) along MD, TD, and ND for P-1 (the arrows represent the shift of $\cos^2(\phi)$ with increasing DR)..... 207

Fig. 8.8 2D SAXS patterns for P-1 (top) and P-2 (bottom) films obtained under different draw ratios..... 209

Fig. 8.9 DSC heating thermograms for P-1 and P-2 films obtained under draw ratios of 1.0, 3.2, and 5.2..... 210

Fig. 8.10 Proposed pictograms of the molecular structure for P-1 and P-2 films obtained under low, medium, and high draw ratios..... 213

Fig. 8.11 Tear resistance along MD as a function of draw ratio for P-1 and P-2..... 213

Fig. 8.12 Normalized maximum force for piercing as a function of draw ratio for P-1..... 214

Fig. 8.13 Normalized oxygen transmission rate (OTR) as a function of draw ratio for P-1 and P-2..... 216

Fig. 8.14 Normalized oxygen transmission rate (OTR) as a function of crystalline, F_c, and amorphous, F_a, orientation functions..... 217

Fig. 8.15 DMTA-tan (δ) as a function of temperature for P-1 at different DR..... 218

Fig. 8.16 Normalized oxygen transmission rate as a function of the β relaxation intensity for P-1 and P-2..... 219

Fig. 1 Schematic of the slit die rheometer [9]..... 245

Fig. 2 Normalized storage modulus versus time for the neat PPs and three blends; T= 190 °C and ω=0.628 rad/s..... 247

Fig. 3 Complex viscosity as a function of angular frequency for the neat PPs as well as for two blends; T=190 °C..... 248

Fig. 4 Storage modulus as a function of angular frequency for the neat PPs as well as for two blends; T=190 °C..... 248

Fig. 5 Loss angle versus angular frequency for the neat PPs as well as for three blends; T=190 °C..... 249

Fig. 6 Weighted relaxation spectra for the neat PPs as well as all the blends; T=190 °C (the vertical dash lines represent the range of frequencies covered during the experiments)..... 251

Fig. 7 Cole-Cole plots for the neat PPs as well as all the blends; T=190 °C..... 252

Fig. 8 Complex shear viscosity at different angular frequencies as a function of branched content; T=190 °C (the dash lines show the additivity rule)..... 253

Fig. 9 Shear and complex viscosities as functions of shear rate and frequency for (a) L-PP, (b) 30 wt% LCB-PP, and (c) LCB-PP; T=190 °C..... 257

Fig. 10 Transient elongational viscosities as a function of time at different Hencky strain rates and branched contents: (a) low LCB-PP contents (b) high LCB-PP contents; T=190 °C (the solid lines represent the linear behavior calculated from the relaxation spectrum)..... 259

Fig. 11 Strain-hardening coefficient as a function of Hencky strain rate and branched content; T=190 °C and Hencky strain=2.5..... 261

Fig. 12 Total pressure drop and contributions of the shear and extensional components as a function of flow rate Q for (a) L-PP and (b) LCB-PP; T=190 °C..... 264

Fig. 13 Normalized apparent extensional viscosities calculated using the Cogswell and Binding methods for (a) L-PP and (b) LCB-PP. The complex shear viscosity data are shown for comparison; T=190°C..... 266

Fig. 1 Normalized complex viscosity as a function of frequency for neat PPs; T=190 °C..... 279

Fig. 2 Loss angle versus frequency for neat PPs; T=190 °C..... 280

Fig. 3 Weighted relaxation spectra for neat PPs; T=190 °C (the vertical dash lines represent the range of frequencies covered during the experiments)..... 281

Fig. 4 Complex viscosity as a function of frequency for: (a) PP40/LCB-PP blends and (b) PP04/LCB-PP blends; T=190 °C..... 283

Fig. 5 Complex shear viscosity at different angular frequencies as a function of branched PP content for: (a) PP40/LCB-PP blends and (b) PP04/LCB-PP blends; T=190 °C (the dash lines show the additivity rule)..... 283

Fig. 6 Zero-shear viscosity as a function of LCB-PP content; T=190 °C (the dash lines show the additivity rule)..... 284

Fig. 7 Weighted relaxation spectrum for: (a) PP40/LCB-PP blends and (b) PP04/LCB-PP blends; T=190 °C (the vertical dash lines represent the range of frequencies covered during the experiments)..... 285

Fig. 8 Cole-Cole plots for: (a) PP40/LCB-PP blends and (b) PP04/LCB-PP blends; T=190 °C..... 286

Fig. 9 Storage modulus as a function of frequency for: (a) PP40/LCB-PP blends and (b) PP04/LCB-PP blends; T=190 °C..... 287

Fig. 10 Sensitivity of the Palierne model predictions of G' and G'' to different values of α/R_v for: (a) (80/20) PP40/LCB-PP blend and (b) (80/20) PP04/LCB-PP blend; T=190 °C..... 289

Fig. 11 Time temperature superposition for: (a) (60/40) PP40/LCB-PP blend and (b) (60/40) PP04/LCB-PP blend (the reference temperature is 225 °C)..... 291

Fig. 12 Transient elongational viscosities as a function of time at different Hencky strain rates, $\dot{\varepsilon}$, for: (a) PP40/LCB-PP blends and (b) PP04/LCB-PP blends; T= 190 °C (the solid lines represent the linear behavior calculated from the relaxation time spectrum)..... 293

Fig. 13 DSC cooling thermographs for PP28, LCB-PP, and their blends at 10 °C/min..... 295

Fig. 14 Curves of relative crystallinity versus time for the PP28/LCB-PP blends..... 297

Fig. 15 Plots of log[-ln(1-$X(t)$)] as function of log(t) for PP28, LCB-PP and the 40wt% PP28/LCB-PP blend..... 299

Fig. 16 Optical micrographs at the end of crystallization for samples non isothermally crystallized at 10 °C/min from the melt. a) PP28, b) (98/2) PP28/LCB-PP, c) (80/20)

PP28/LCB-PP, and d) LCB-PP..... 300

Fig. 17 Optical micrographs at the end of crystallization for samples non isothermally crystallized at 10 °C/min from the melt. a) PP28, b) 0.2 wt% nucleated, c) 0.5 wt% nucleated, and d) 1 wt% nucleated..... 301

Fig. 18 Glass transition temperature as a function of LCB-PP content (the solid lines represent the Fox equation)..... 303

LIST OF APPENDIXES

APPENDIX A

Rheological Properties of Blends of Linear and Long Chain Branched Polypropylene 240

1 Introduction 241

2 Experimental 243

2.1 Materials 243

2.2 Rheological measurement 244

3 Results and discussions 247

3.1 Shear measurements 247

3.2 Elongational Measurements 258

4 Conclusions 268

5 Acknowledgements 269

6 References 269

APPENDIX B

Rheological and Thermal Properties of Blends of a Long-Chain Branched Polypropylene and Different Linear Polypropylenes 272

1 Introduction 273

2 Experimental 276

2.1 Materials 276

2.2 Rheological measurements 277

2.3 Thermal analysis 278

2.4 Polarized optical microscopy (POM) 278

2.5 Dynamic mechanical analysis 279

3 Results and discussion 279

3.1 Rheological characterization of the neat PPs 279

3.2 Rheological characterization of the blends 282

3.3 Thermal characterization 294

3.4 Solid state properties 303

4 Conclusions 304

5 Acknowledgement 306

6 References 309

LIST OF SYMBOLS

$A_{\|\|}$	absorption parallel to a reference axis
$A_{\perp}$	absorption perpendicular to a reference axis
D	dichroism ratio
D_{hlk}	average crystal size (Å)
a_T	thermal shift factor
F	orientation function
F_a	amorphous orientation function
F_c	crystalline orientation function
F_{avg}	average orientation function
G'	storage modulus (Pa)
G''	loss modulus (Pa)
G_m^*	matrix complex modulus (Pa)
G_d^*	droplet complex modulus (Pa)
H	relaxation spectrum (Pa)
k	Avrami constant
k_β	Boltzmann constant
M^*	critical molecular weight for orientation
M_n	number average molecular weight (kg/mol)
M_w	weight average molecular weight (kg/mol)
n	Avrami constant
N	nucleation rate in the oriented state
N^o	nucleation rate in the oriented state
P	pressure (Pa)
P^o	saturation pressure (Pa)
R_v	volume average radius (μm)
S	entropy (kJ/Kmol)
t	time (s)
$t_{1/2}$	half time of crystallization (s)
T	temperature (°C)
T_c	crystallization temperature (°C)
T_g	glass transition temperature (°C)
T_m	melting point (°C)
T_o	onset crystallization temperature (°C)
v	volume of the adsorbate (mL) in BET
v_m	monolayer volume of the adsorbate (mL) in BET
w	weight fraction
X	degree of crystallinity
X_c	degree of crystallinity

X_{rel} relative crystallinity

Greek letters

α interfacial tension (mN/m), alpha crystal form
β beta crystal form
θ the diffraction angle in WAXD (degrees)
δ loss angle (degrees)
$\dot{\varepsilon}$ strain rate (s^{-1})
η^* complex viscosity (Pa.s)
η_o zero-shear viscosity (Pa.s)
η' real component of complex viscosity (Pa.s)
η'' imaginary component of complex viscosity (Pa.s)
η_e^+ transient elongational viscosity (Pa.s)
λ relaxation time (s), X-ray wavelength (Å)
μ micron
ϕ_β branched polypropylene content
ϕ azimuthal angle in WAXD
Φ cooling rate (°C/min)
ω frequency (rad/s)
ΔH_f heat of fusion (kJ/mol)
ΔS_f entropy of fusion (kJ/Kmol)
$\Delta(2\theta)$ full width at half maximum

CHAPTER 1

INTRODUCTION

Microporous membranes are commonly used in separation processes such as battery separators and medical applications to control the permeation rate of chemical components. Due to the wide range of chemical structures, optimum physical properties, and low cost of polymers and polymer blends, these materials are known as the best candidates for the fabrication of microporous membranes.

Three commercially available processes are used for making microporous membranes: solution casting (also known as extraction process), particle stretching, and dry-stretching[1]. In the extraction process, the polymeric raw material is mixed with a processing oil or plasticizer, this mixture is extruded and the plasticizer is removed through an extraction process[2]. In the particle stretch process, the polymeric material is mixed with solid particles, this mixture is extruded, and pores are formed during stretching in the interface between the polymer and solid particles[3]. Costly processes and difficulties in dealing with solvent and particle contaminations are main drawbacks of such methods. However, the dry-stretch process, which is the method used in this study, is based on stretching of a polymer film containing a row-nucleated lamellar structure. Three consecutive stages are carried out to obtain porous membranes by this technique: (1) creating a precursor film possessing a row-nucleated lamellar structure through shear

and elongation-induced crystallization of the polymer having proper molecular weight and molecular weight distribution, (2) annealing the precursor film at temperatures near the melting point of the resin to remove imperfections in the crystalline phase and to increase lamellae thickness, and (3) stretching at low and high temperatures to create and enlarge pores, respectively[4,5]. To produce microporous membranes by the stretching technique, obtaining precursor films with an adequate orientation and alignment of the crystal lamellae are needed[4]. The type of resin and applied processing conditions are the key factors for the production of the precursor films with controlled type, thickness, orientation, and connection of the crystals, which in turn control the final membrane structure.

There are two main industrial processes for the production of films: film blowing and cast film extrusion. It is well known that the thickness variation in blown films are considerably greater compared to cast films. For the preparation of porous membranes, obtaining a precursor film with excellent thickness uniformity is strongly recommended since any non uniformity causes irregularities in the stress distribution in the following stretching process. In addition, compared to film blowing, cast film process has more flexibility in the supply of air cooling from both sides, leading to a more uniform lamellar structure in both surfaces.

A few authors have investigated the formation of porous membranes from polypropylene (PP)[4], polyethylene (PE)[5], poly (vinylidene fluoride) (PVDF)[6], polyoxymethylene (POM)[7], and poly (4-methyl-1-pentene) (PMP)[7]. The main applications for

these materials are often for battery separators and blood-oxygenation. In fact, lithium (Li) batteries will generate heat if accidentally overcharged. Separator shutdown is a useful safety feature to restrict thermal reactions in Li-batteries[8,9]. Shutdown occurs close to the melting temperature of the polymer, leading to pores collapse and restricting passage of current through the cell. For instance, PP separators melt around 160 °C whereas PE separators have shutdown temperature between 120 °C and 130 °C.

The main objective of this study is to develop microporous membranes with high performances from monolayer as well as multilayer PP/HDPE films through cast extrusion and stretching of the row-nucleated lamellar structure involving industrial scale capabilities. We believe that by using polymer blends, the pore density, pore size and distribution, porosity, and tortuosity of the porous membranes can be better controlled. In the case of multilayer membranes, the middle layer, which has a lower melt temperature, T_m, is used as a fuse for safety purposes, whereas the side layers, which have higher T_m, provide the mechanical stability at and above T_m of the middle layer. We also investigated the drawing of the polypropylene films with coexisting rows of lamellae and spherulites and only spherulites using a machine direction orientation (MDO) unit to see changes in morphology in relation with the barrier properties as well as tear and puncture properties.

In order to help the readers to follow the results presented in this dissertation, the literature review concerning membrane classification, the most important factors affecting crystalline structure, the previous works carried out on the membrane

fabrication, and the studies on the machine direction orientation (MDO) process for stretching of the semicrystalline films is given in Chapter 2. The materials used and our methodology to achieve the objectives are presented in Chapter 3. Chapter 4 briefly explains the organization of the papers. In Chapter 5, the role of high molecular weight chains on the PP row-nucleated lamellar crystallization and microporous membranes formation was investigated using WAXD, SAXS, FTIR, SEM and mechanical measurements. Chapter 6 discusses in depth the effect of processing parameters such as air cooling conditions, chill roll temperature, and draw ratio on the crystalline orientation, morphology, and mechanical properties of the cast films made at the industrial scale and on the formation of microporous membranes. The results showed that air cooling and cast roll temperature had a crucial role on the orientation and amount of lamellae formation of the cast films. Chapter 7 presents the results on development of microporous membranes from PP/HDPE multilayer films. It will be shown that controlling the processing parameters enables us to control the crystalline structure of the components in the multilayer, leading to the fabrication of microporous trilayer membranes. In Chapter 8, a detailed investigation of the structure evolution of precursors having spherulitic structure and coexisting rows of lamellae and spherulites with uniaxial (MDO) stretching is carried out. In addition, the relationships between morphological transformation, tear, and puncture properties are discussed. In Chapter 9 (general discussion), a full review regarding the most important factors affecting the microporous membranes fabrication and MDO stretching is presented. Finally, Chapter

10 summarizes the most important conclusions of this thesis and outlines some recommendations for the future works in this area.

In addition to the membrane fabrication by stretching, a comprehensive study was conducted on the rheological and thermal properties of blends of linear polypropylenes (L-PP) and a long chain branched polypropylene (LCB-PP). Although the last part of this dissertation deviates from the microporous membrane study, but provides valuable information concerning the resin characteristics particularly the effect of molecular weight and long chain branching on the rheological and thermal properties, which could be helpful for further membrane development. Appendix A elucidates the impact of the addition of a long chain branched polypropylene to a linear polypropylene on the rheological properties, including transient and 'steady' extensional behavior over a wide range of deformation rates. In Appendix B, the role of molecular weight of linear polypropylene on the rheological behavior of blends of linear and long-chain branched polypropylene is considered. In addition, the influence of adding the LCB-PP on the thermal properties, crystallization, and solid state behavior of the blends is explored.

CHAPTER 2

LITERATURE REVIEW

2.1 Membrane classification

A membrane is a semi permeable barrier to separate components of a solution or particles dissolved in a fluid due to their chemical or physical properties when a driving force is applied[10]. Due to the wide range of chemical structures, optimum physical properties, and low cost of polymers and polymer blends, these materials are known as the best candidates for the fabrication of membranes. Polymeric membranes have been developed for various industrial applications such as microfiltration, ultrafiltration, reverse osmosis (RO), gas separation, and wastewater treatment[11]. Membranes are commonly classified based on the size of the separated materials as depicted in Figure 2.1.

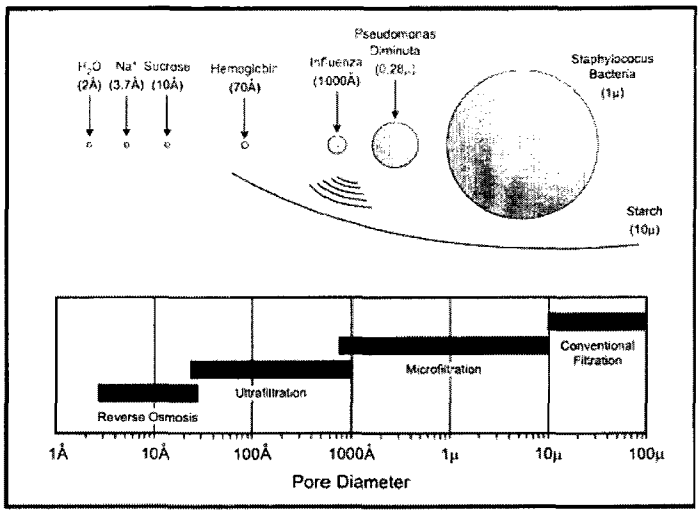

Fig. 2.1 Separation processes differing in the size of the particles to be separated[11].

Depending on the structure, polymeric membranes are divided in two categories: isotropic membranes and anisotropic membranes[11]. Isotropic membranes contain uniform structure while anisotropic membranes have a chemically or a physically heterogeneous structure. Isotropic membranes can also be classified in the three categories as follow[11]:

a) Microporous membranes: this kind of membranes has a highly porous structure with randomly distributed interconnected pores. In microporous membranes, pores size varies from 0.01 to 10 μm in diameter.

b) Nonporous or dense membranes: this is a dense film in which permeates are passed by diffusion under an applied driving force.

c) Electrically charged membranes: in this type of membranes, separation is obtained by exclusion of the particles with same charge.

On the other hand, anisotropic membranes have a skin/core structure. The skin layer is an extremely thin surface layer supported on a much thicker core with porous structure. The skin/core structure can be formed in a single operation or separately. A schematic diagram of isotropic and anisotropic membranes is illustrated in Figure 2.2.

2.2 Techniques for membrane fabrication

Polymeric membranes are made through various techniques such as: phase separation[12,13], track etching[14,15], leaching[16], thermal precipitation[17], and stretching[4,5,7]. In phase inversion, the polymeric raw material is mixed with a solvent as well as a non solvent and during phase separation a first phase rich in polymer forms the matrix and the second phase poor in polymer creates the pores. In track etching the polymeric film is irradiated to create tracks followed by acid etching. Leaching is based on extrusion of the polymeric row material added with the solid particles followed by the extraction of the solid, leading to pores formation. In thermal precipitation cooling of a mixture of a polymer with a solvent is applied to enable phase separation followed by extraction of the solvent. Stretching technique is based on the stretching of a polymer film containing a dispersed phase where upon stretching pores are created due to stress concentration at the interface of these sites[11], or stretching a specific crystalline morphology as detailed below. Table 2.1 summarizes the different techniques for membrane formation.

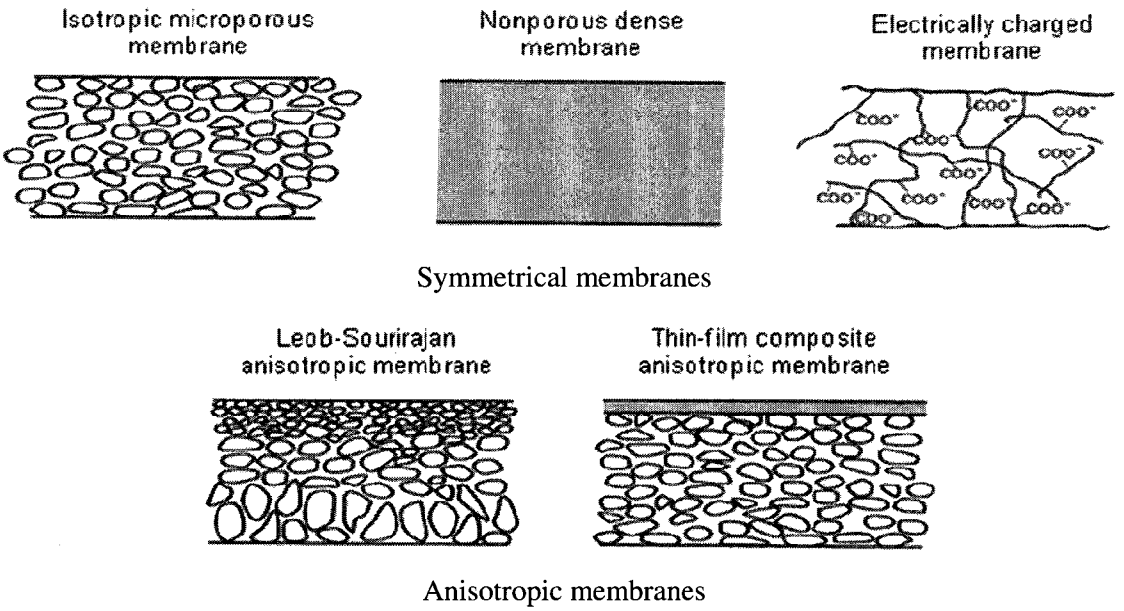

Fig. 2.2 Schematic illustration of various polymeric membranes[11].

Table 2.1 Different major techniques to prepare microporous polymeric membranes[11].

Method	Description
Phase inversion	Phase separation of a ternary mixture of polymer, solvent, and nonsolvent
Stretching	Combined stretching and heat treatments of extruded semicrystalline film or of filled systems
Track etching	Irradiation of polymeric films or foils to create tracks and then followed by acid/caustic etching
Sintering	Pressing a semicrystalline polymer powder of a given size and sintering at elevated temperatures
Leaching	Extraction of solid pore formers
Thermal precipitation	Cooling a mixture of a polymer with a mixed or single solvent to enable phase separation to occur followed by extraction of the solvent phase

2.3 Stretching

This technique is based on the drawing of a polymer film or sheet having one of the followings: filled particles[18-21], droplets of an immiscible polymer component[22,23], a mixed solvent[24], beta or hexagonal unit cell crystals[25-28], or a stacked lamellar structure. Since the aim of this dissertation is making microporous membranes by stretching a stacked lamellar crystalline structure, introducing other stretching techniques will help the reader in understanding the importance of the process used.

In the stretching a filled polymer film, the resin is first mixed with a filler and then melt extruded to make a composite film or sheet. Upon applying stretching, the cracks are initiated and subsequently propagated in the interface of filler particles and polymer matrix. The pore size, pore size distribution, and porosity depend on the type of filler, its interaction with matrix, blending process, amount of filler, and also film thickness. To completely remove the filler from polymer matrix after drawing, the filler should have poor wetting ability with polymer matrix[5]. Nago et al.[20] developed porous membranes by biaxial stretching sheets of a mixed polypropylene with an inorganic filler ($CaCO_3$). As demonstrated in Figure 2.3, by decreasing the mean particle size of the filler the effective porosity increased and also the equivalent pore size decreased.

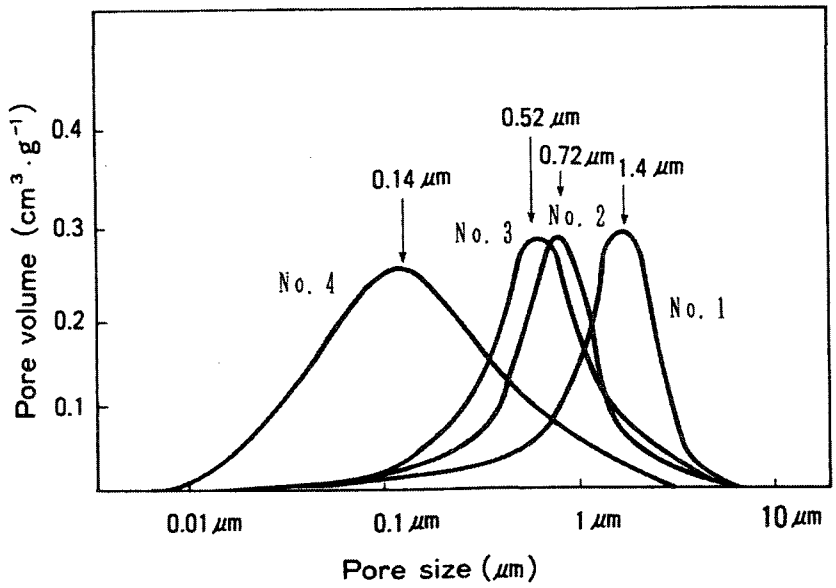

Fig. 2.3 Pore size distributions of the biaxially stretched samples[20].

Nago et al.[21] also developed microporous membranes by adding 56 wt% of an organic filler (polymethylsilsesquioxane) with different sizes into a polypropylene. From Figure 2.4, it is clearly observed that larger pores are formed for the stretched films mixed with particles of a larger size.

Xanthos et al.[22] were probably the first investigators to develop microporous membranes based on the stretching of the immiscible polymer blends. In that study, stretching caused debonding at the interface of incompatible polymer blends of PP and PS and also a small amount of a copolymer as a compatibilizer, resulting in membrane formation. Their findings showed that the dispersion of the minor component with a narrow particle size distribution was the most important factor controlling the pores size.

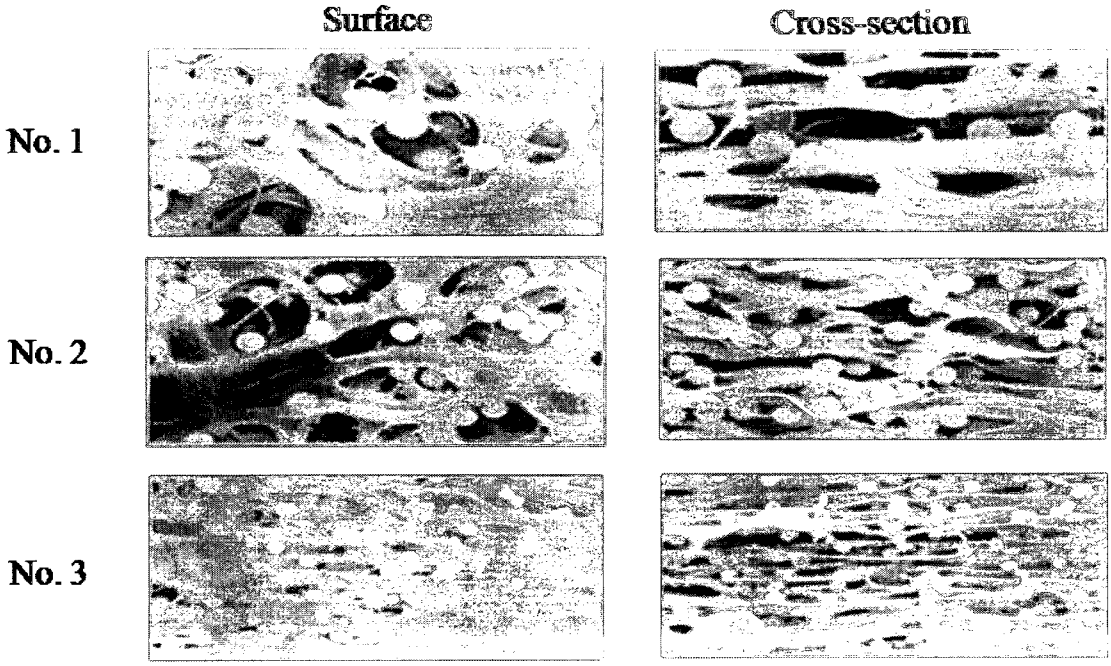

Fig. 2.4 SEM images of biaxially stretched PP microporous sheets. The mean particle size of fillers is: No.1: 2μ, No.2: 1.3 μm, and No.3: 0.8 μm[21].

The solvent stretching technique was first invented by Williams et al.[24] in 1974. In this technique, a polymeric film having at least two components is immersed in the solvent and absorption of the solvent takes place in the component with less volume fraction. Then the film is first stretched in one or two directions while it is in contact with the solvent and then maintained in its stretched form during removal of the solvent.

The β crystalline form is not stable and under certain levels of stress transforms into the more stable α crystalline form. Shi et al.[25] revealed that the β crystals transformed into a smectic state at a drawing temperature below 80 °C, but transformed to the more stable α form at higher temperatures. Since the density of the β crystals is lower than that of the α (0.921 g/cm^3 compared to 0.936 g/cm^3), this transformation caused volume

contraction in the bulk of polymer, resulting in the creation of voids[25-28]. Chu et al.[26] considered the process of void formation in PP during phase transformation. The PP films of different crystalline states were prepared by using 0.1% of a nucleating agent (NU-100 from NJStar Co.) and changing the crystallization temperature ranging from 10 to 110 °C. The results showed that the porosity decreased with an increase in draw temperature and the quantity and dimensions of the micro voids increased with draw ratio up to an optimum value.

Costly processes and difficulties in dealing with solvent and particle contaminations as well as the presence of the nucleating agents are main drawbacks of methods described. However, besides the above stretching methods, uniaxial stretching a stacked lamellar structure has been developed for fabricating microporous membranes. Three consecutive stages are carried out to obtain porous membranes by this technique: (1) creating a precursor film having a row-nucleated lamellar structure by mechanism of shear and elongation-induced crystallization, (2) annealing the precursor film at temperatures near the melting point of the resin to remove imperfections in the crystalline phase and to increase lamellae thickness, and (3) stretching at low and high temperatures to create and enlarge pores, respectively[4,5,7]. For instance, Figure 2.5 illustrates the structure of a PP film before and after stretching. Obviously, a large number of interconnected microvoids are produced upon uniaxial deformation of the annealed film.

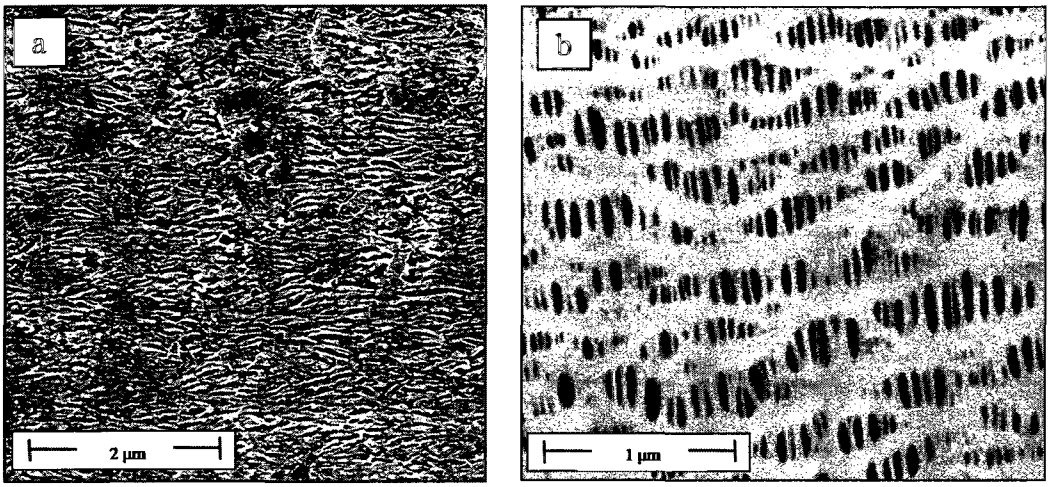

Fig. 2.5 SEM micrographs of surface of a PP film a) before and b) after stretching.

To produce microporous membranes by this technique, precursor films with an adequate orientation and alignment of the crystal lamellae are needed[29]; the higher the crystalline alignment in the precursor, the better is expected the lamellae separation and, as a consequence, the larger the porosity and permeability of the microporous membranes. As will be extensively addressed, in polymer melt, upon applying a large enough shear or extensional stress, the long chains are elongated into the flow direction and serve as nucleating sites for the later lamellae crystallization. As temperature decreases, the shorter chains crystallize on the extended molecules (shish) to form a row-nucleated lamellar structure.

The row-nucleated lamellar structure has been observed for quite a few semi-crystalline polymers such as poly (vinylidene fluoride) (PVDF)[6,30], poly oxymethylene (POM)[7], poly (4methyl-1pentene) (PMP)[7], polypropylene (PP), and polyethylene (PE) (see Figure 2.6).

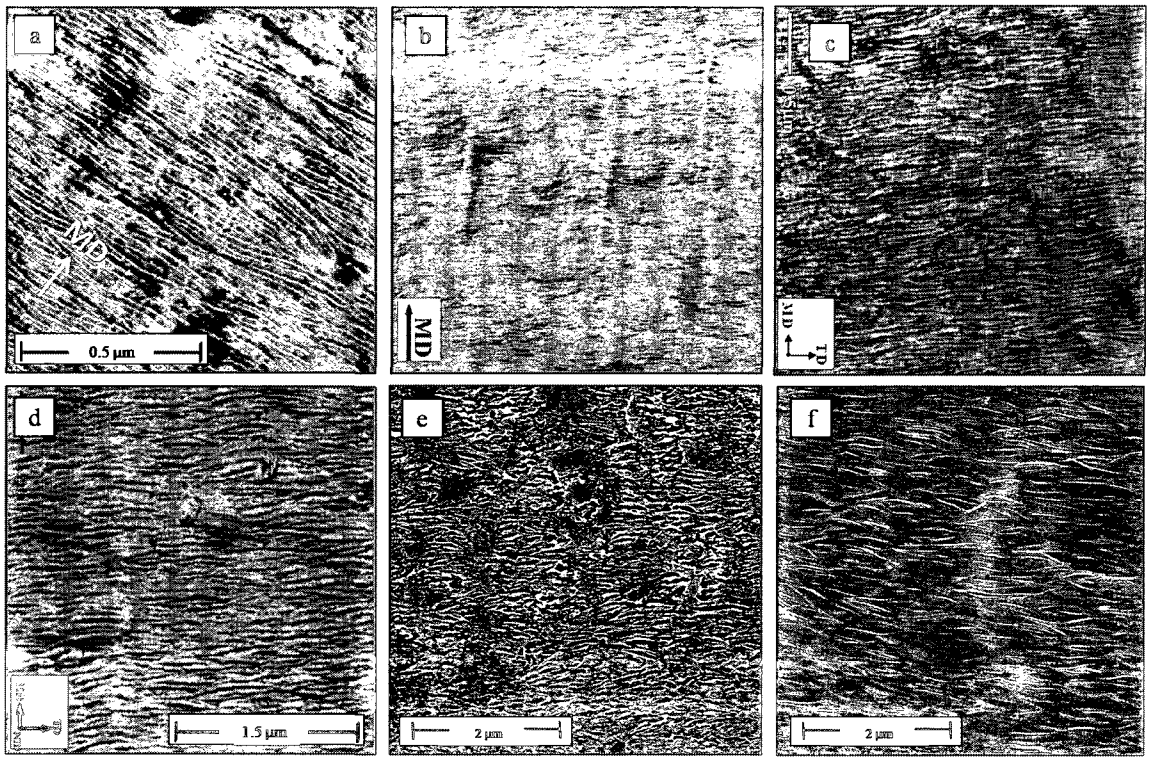

Fig. 2.6 Stacked lamellar crystal structure observed on the surface of a) PVDF (AFM)[30], b) PVDF (SEM)[6], c) POM[7], d) PMP[7], e) PP, and f) PE.

2.4 Polypropylene and polyethylene structure

Polypropylene (PP) is synthesized via Ziegler-Natta and metallocene catalysts with high level of crystallinity and different isotacticity and molecular weight. PP is known as an important industrial polymer due to its versatility and development of new catalysts and polymerization processes[10]. The completely solidified PP is typically about 40-60% crystalline and 60-40% amorphous. At room temperature, the mechanical responses of PP is directly related to the level of crystallinity, since the crystal phase is much stiffer than the amorphous phase at temperatures above the glass transition temperature ($T_{g,pp}$ is about 10 °C)[31].

Three crystalline unit cell structures are possible for PP: α, β, and γ. The α form, which is formed mostly under a slow cooling and high stress, has a monoclinic structure (a=6.65 Å, b=20.96 Å, c=6.5 Å, β=99°20', N=4 (chain per unit cell), and density=0.936 g/cm^3). The alpha crystals melt at about 160 °C for Zeigler-Natta polymerized homopolymers. The β unit cell is hexagonal (a=19.08 Å, c=6.49 Å, N=9, density=0.922 g/cm^3) and is created under large temperature gradient or fast cooling rate and also using certain nucleating agents. In the absence of the nucleating agent, the fraction of the beta crystals is less than 5%, which shows a melting peak that is around 12-14 °C below that of the alpha crystal. The γ crystal structure is tetragonal (a=6.38 Å, c=6.33 Å, N=1, density=0.939 g/cm^3) and appears in low molecular weight PP or when crystallization is performed under high pressure[32].

The crystalline unit cell structure of polyethylene (PE) is well established. The unit cell is orthorhombic (a=7.40 Å, b=4.93 Å, and c=2.534 Å). However, the unit cell dimensions of a linear polyethylene vary with temperature[33,34] and crosslinking[35]. Figure 2.7 shows the arrangement of the polymer chains into the unit cell. The PE polymer chain is arranged in a zigzag conformation with its chain axis along the c-axis[5]. The fact that the molecule of PE is in the range of 5-10 μm and the lamellae thickness is about 10 nm, Keller[36] concluded that the molecules must fold up and down at the surface of the lamellae.

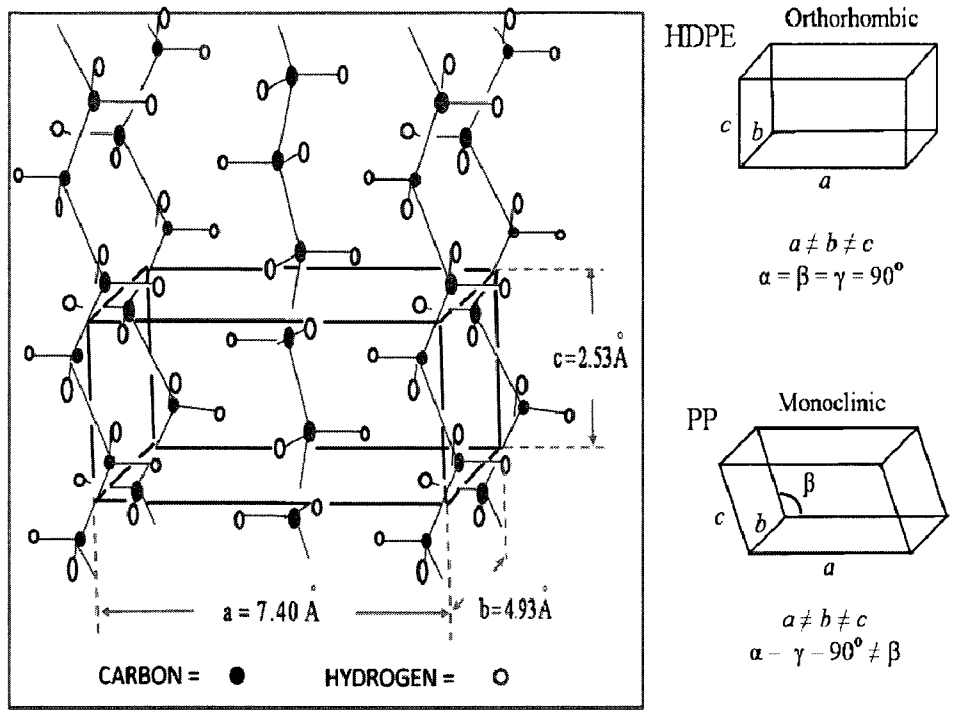

Fig. 2.7 The orthorhombic unit cell structure of polyethylene[5]. The right is also showing the monoclinic unit cell structure of polypropylene.

2.5 Flow induced crystallization (FIC)

The crystallization behavior of semicrystalline polymers is strongly affected by the type (i.e. shear or elongation) and magnitude of flow. To control processing parameters, the shearing protocol, as introduced by Janeschiz-Kriegl et al.[37], is considerably utilized in various experimental set-ups. Differential scanning calorimetry (DSC)[38,39], rheometery[40-42], optical microcopy (OM)[43], birefringence measurements[44,45], small angle X-ray scattering (SAXS)[46-48], and wide angle X-ray diffraction (WAXD)[46-49] are used to investigate the effect of flow on crystallization. Since a row-nucleated lamellar structure

is obtained via the crystallization under flow, in this section, principal influencing parameters on FIC are addressed.

Polypropylene (PP) crystallizes slowly under quiescent conditions and a large amount of the crystals have a spherulitic structure. However, upon applying stress or shear, the amount and rate of crystallization are enhanced drastically. In addition, the crystallization under stress leads to the lamellar structure, which is desirable for producing microporous membranes by stretching. Figure 2.8 illustrates flow induced crystallization (FIC) experiments on an isotactic PP, reported in Ref.[43]. Under quiescent crystallization (Figure 2.8a), spherulites were formed by crystalline lamellae growing in three dimensions initiated from a point-like nuclei. The numbers of spherulites were significantly depended on crystallization temperature[43]. Figure 2.8b displays the influence of shear flow on the orientation of the crystals, where the same thermal history as in Figure 2.8a was applied. In such an experiment, shear flow was applied in a parallel plate geometry by moving the upper plate for a few seconds at 140 °C. Clearly, a huge increase in the number of nuclei could be observed (Figure 2.8b) and highly oriented structures were obtained when the deformation applied was strong (Figure 2.8c). Keller and coworkers[50] showed that a shish-kebab morphology (Figure 3b) could be formed beyond a certain elongation rate, depending on the resin molecular weight. Eder and Janeschitz-Kriegl[51] found that these structures can also be observed in shear flow upon applying high stresses.

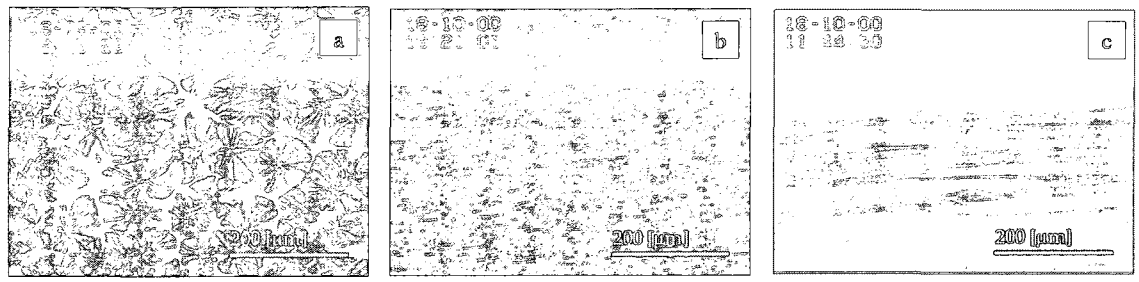

(a) (b) (c)

Fig. 2.8 Crystallization of a PP under different flow conditions: a) quiescent crystallization, b) crystallization under low shear rate, and c) crystallization under high shear rate[43].

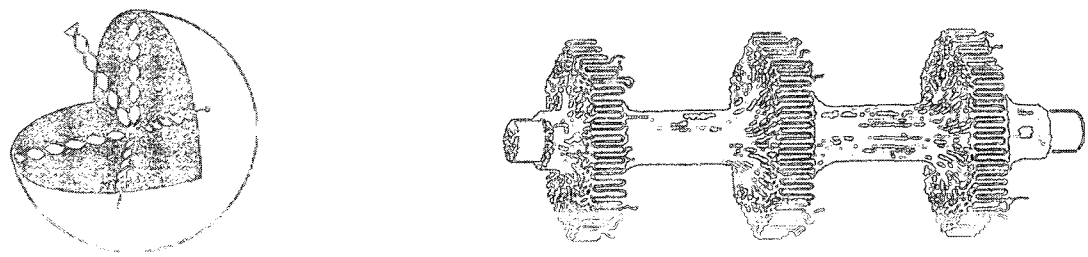

(a) (b)

Fig. 2.9 Schematic of a) a spherulitic and b) a shish-kebab structure[50].

From the literature, two major types of crystallization can occur, depending on the stress in flow[5]: low stress results in twisted kebabs, while high stress produces flat kebabs (planar crystal structure) in which the lamellae grow radially on the shish without twisting[5]. This qualitative description is illustrated in Figure 2.10, which was first proposed by Keller and Machin[52] for films.

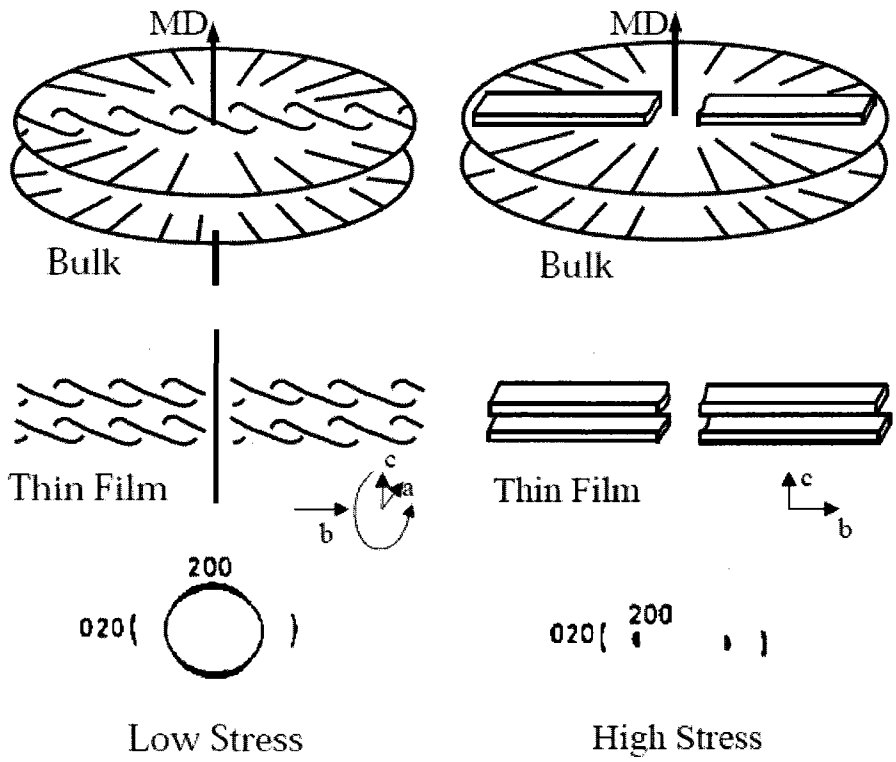

Fig. 2.10 Schematic of the types of row structure with the respective extrusion conditions and the main features of the PE WAXD patterns[5].

The mechanical responses are quite distinct between row-nucleated and spherulitic crystalline structures[53-56]. Films possessing a row-nucleated structure reveal anisotropic tensile properties along MD and TD whereas spherulitic morphologies reveal isotropic (balanced) responses.

The flow induced crystallization can be explained from thermodynamic and kinetic points of view[7]. The nucleation rate at $T > (T_m+T_g)/2$ has been given by Yeh and Hong[57] as follow:

$$\frac{N^\circ}{N} = \exp\left[\frac{\beta\sigma_e\sigma^2}{k_B T}\left(\frac{T_m^{\circ 2}}{\Delta H_f^2 \Delta T^2} - \left(\frac{\Delta H_f \Delta T}{T_m^\circ} + T_m^\circ \Delta S\right)^{-2}\right)\right] \qquad (2.1)$$

where N^o is the nucleation rate in the oriented state, N is the nucleation rate in the quiescent state, k_B is the Boltzmann constant, ΔH_f is the heat of fusion. The impact of orientation on nucleation was suggested to be due the entropy difference between the oriented and unoriented states (i.e. $\Delta S=S_{oriented}-S_{unoriented}$), where oriented entropy is lower than the unoriented one. From the above equation, obviously, faster nucleation under flow is expected. Also from Eq. 2.2, it can be shown that the melting temperature (T_m) increases as entropy due to higher orientation decreases[7]:

$$T_m = \frac{\Delta H_f}{\Delta S_f} \qquad (2.2)$$

where ΔS_f is the difference between the oriented crystal phase and the melt and ΔH_f is the enthalpy difference between the crystalline phase and the melt. The enthalpy change for an oriented melt state compared to an unoriented melt is almost negligible whereas the entropy variation is considerable, hence dominant in T_m.

Using rheometery, in-situ small angle X-ray scattering (SAXS) and/or wide angle X-ray diffraction (WAXD) analyses, the effects of the applied shear rate and shearing time as well as the material parameters on the shear induced crystallization process for PP and PE have extensively been investigated[46-49,58,59]. Housmans et al.[58] used a rheometer with small plate-plate geometry of 8 mm to study the crystallization kinetics. For flow induced crystallization (FIC) experiments, the samples were molten at high temperatures to erase thermomechanical history and cooled to the desired crystallization temperature with a controlled cooling rate. A shear flow for a certain shear time, t_s, was

applied prior to dynamic time sweep tests. The storage modulus evolved by starting crystallization in the melt and reached a plateau at the end of crystallization. Figure 2.11 compares the time of evolution of storage modulus for a PP crystallized at 138 °C under quiescent condition as well as after subjecting it to flow at different shear rates and applying a constant strain. The figure also shows the optical micrographs indicating the characteristic morphologies for the three crystallization experiments. It is obvious that applying shear rate accelerated the crystallization process. They, moreover, showed that a critical shear rate existed, below which no influence of the crystallization kinetic was observed.

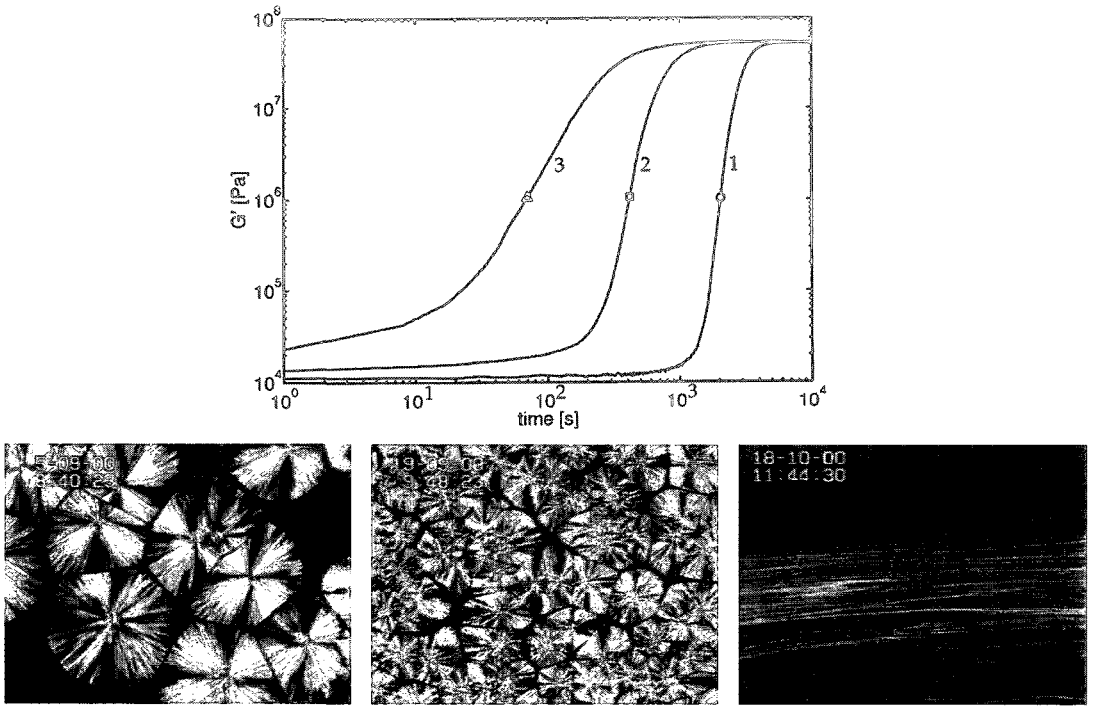

(1) (2) (3)

Fig. 2.11 Evolution of the storage modulus during crystallization of an iPP at T=135 °C, measured under quiescent conditions (o, 1) and after shearing at $\dot{\gamma}$=60 s^{-1} for t_s=1s (□, 2) and t_s=6 s (Δ, 3). Optical micrographs indicate the characteristic morphology for the three crystallization experiments[49].

Somani et al.[49] followed the orientation development upon applying different shear rates. They found that at a certain shear rate only molecules with a chain length (molecular weight) above a critical value (critical orientation molecular weight, M^*) can form stable oriented row-nuclei while the rest create lamellae over these nuclei sites. In addition, it was shown that M^* drops as the imposed shear rate increased, and the following relation between M^* and $\dot{\gamma}$ was introduced:

$$M^* = K\dot{\gamma}^{-\alpha} \qquad (2.3)$$

where M^* is the critical molecular weight for orientation, $\dot{\gamma}$ is the shear rate, K is a proportionality constant, and α is an exponent. Figure 2.12 shows the imposed shear rate dependence of the critical orientation molecular weight. It is clear that compared to the quiescent conditions, the critical molecular weight dropped drastically upon applying shear rate. Additionally, their findings showed that increasing shear rate did not enhance the chain extension, but increased the amount of chains that became oriented. Then a structure with a bimodal population of oriented and non-oriented chains was created.

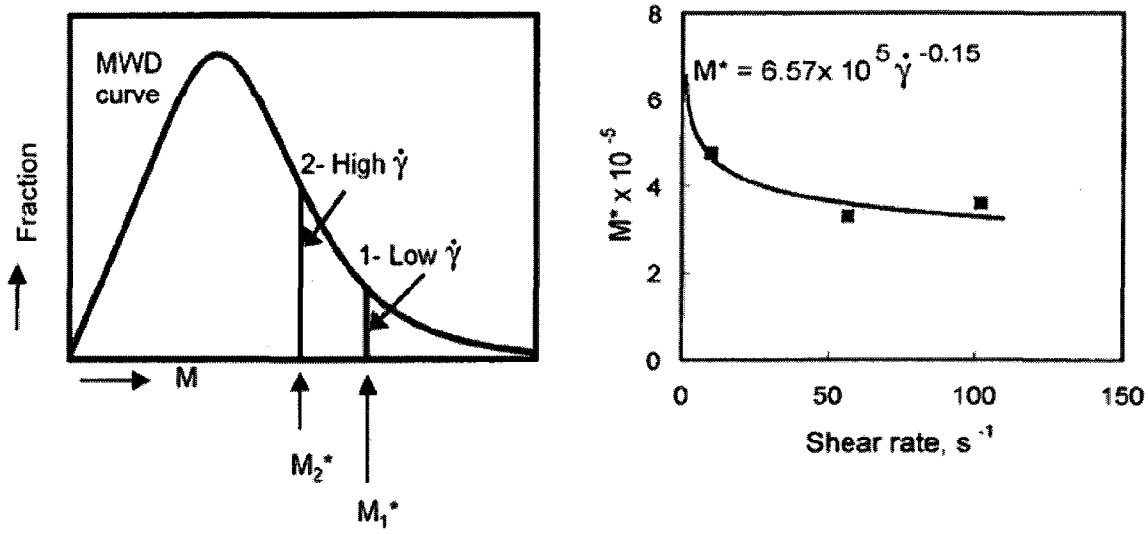

(a) (b)

Fig. 2.12 a) Schematic showing the effect of imposed shear conditions on the shift in the location of the critical molecular weight M^*. b) Critical orientation molecular weight M^* as a function of shear rate at 140 °C[49].

Based on the SAXS and TEM analyses, microstructural pictograms for the nucleation and growth of the crystals were proposed as depicted in Figure 2.13. Figure 2.13a reveals the random distribution of molecules in the melt before applying shear rate. Figure 2.13b presents the shear induced primary nuclei after subjecting to a step shear. As soon as nuclei sites were created, kebabs grew radially perpendicular to the flow direction. In addition, it was shown that the long period distance decreased by growing the lamellae. In another study[59], it was found that upon applying shear, the rate of crystallization enhanced by two orders of magnitudes (see Figure 2.14) due to the orientation-induced primary nuclei. In fact, the presence of extended chain segments initiated primary nuclei, from which, after the cessation of flow, the kebabs formed in perpendicular direction. From Figure 2.14 it is obvious that applying a small amount of

shear rate enhanced the rate of crystallization significantly while further increases in shear rate did not noticeably impact the crystallization kinetics.

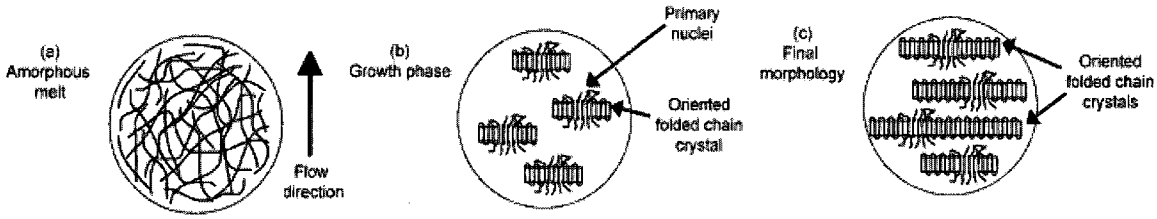

Fig. 2.13 Schematics of the formation of shear-induced primary nuclei and subsequent growth of oriented crystals at the surface undergoing maximum orientation in step-shear experiments[49].

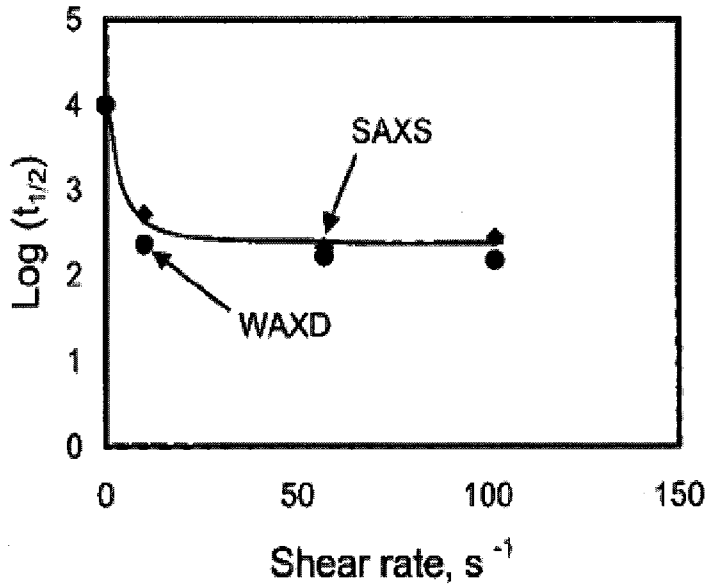

Fig. 2.14 Half time of crystallization of the β-crystals at different shear rates[49].

Seki and coworkers[47] showed that adding a small amount (1 wt%) of high molecular weight component enhanced the formation of the row-nucleated structure due to an increase in nucleating sites. As pointed out previously, when the applied shear stress exceeded its critical value, large molecules started to align in the flow direction followed

by the perpendicular growth of the lamellae on the nuclei sites. Figure 2.15 presents the pictograms of the nature of the shear induced crystallization and the role of the high molecular weight species[47]. Upon applying shear rate, at the initial stages, the large molecules orient in the flow direction, leading to a significant enhancement in the nuclei sites.

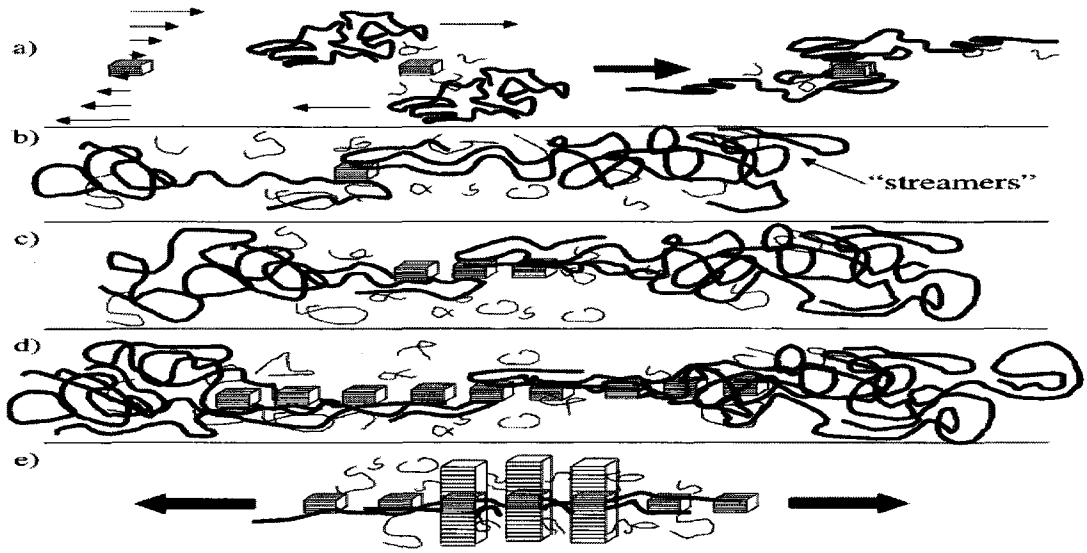

Fig. 2.15 Pictograms of the nature of the shear induced nucleation and subsequent growth of oriented crystalline lamellae[47].

Somani et al.[46] compared the oriented microstructure in isotactic polypropylene melts (PP-A and PP-B) with the same number average molecular weight but different molecular weight distribution (MWD) under shear flow. The amount of the high molecular weight species was larger in PP-B than in PP-A. Both samples were subjected to identical shear conditions (shear rate=60 s^{-1}, duration=5 s, T=155 °C). Their results shown in Figure 2.16 elucidated that the shish structure formed much earlier for PP-B with a more pronounced crystal orientation and a faster crystallization kinetic. They

concluded that even a small increase in the concentration of the high molecular weight chains led to a significant increase in the shish or nuclei sites formation.

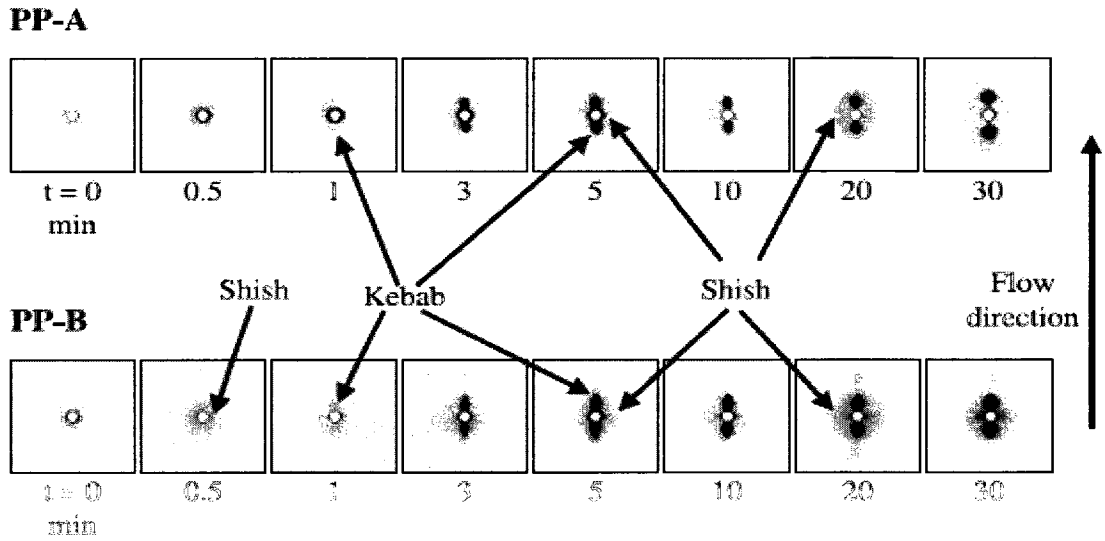

Fig. 2.16 2D SAXS images of PP-A and PP-B at selected times after shear (shear rate=60 s^{-1}, duration=5 s, and T=155 °C)[46].

Agarwal et al.[48] examined the influence of long chain branches on the stress induced crystallization. Long chain branches were introduced via in-situ polymerization of polypropylene and a diene monomer using metallocene catalysts. As reported in Table 2.2, by adding branches, the number average molecular weight remained approximately unchanged while the weight average molecular weight increased significantly. Figure 2.17 exhibits the SAXS patterns obtained after shear for the four selected LCB-iPP samples. The patterns clearly show that due to the oriented structures both SAXS intensities along the equator and the meridian enhanced with the branching level, indicating that oriented structures in the LCB-PP polymers was significantly larger than

in the linear i-PP polymer. They used the Avrami model to obtain quantitative information regarding crystal growth geometry. The Avrami equation is expressed as:

$$1 - X_r = e^{-kt^n} \tag{2.4}$$

$$\ln[-\ln(1 - X_r)] = \ln(k) + n\ln(t) \tag{2.5}$$

where X_r is the relative crystallinity, k and n are the two Avrami parameters, and t is the time. The exponent n depends on the nucleation type and growth geometry[48]. In Figure 2.18, a value of $n \approx 3$ was obtained for the linear iPP polymer (LCB 01) which was indicative of the spherulitic crystal growth in the polymer melt after shear; on the other hand, values of $n \approx 2.8$ and 1.8 were recorded for the branched LCB 05 and LCB 07 polymers, respectively. A lower value indicated a rod/disklike crystal growth geometry[48].

Table 2.2 Composition, thermal properties, and molecular weight of the LCB-PP polymers[48].

sample	diene level (ppm)	mol wt M_n	M_w	M_z	M_{z+1}	T_m (°C)	T_c (°C)
LCB 01	0	51 000	150 000	249 000	356 000	152.2	112.9
LCB 05	170	52 000	203 000	460 000	845 000	153.9	122.2
LCB 07	250	66 000	229 000	527 000	949 000	154.6	124.4
LCB 13	375	112 000	276 000	634 000	1 118 000	154.3	125.2

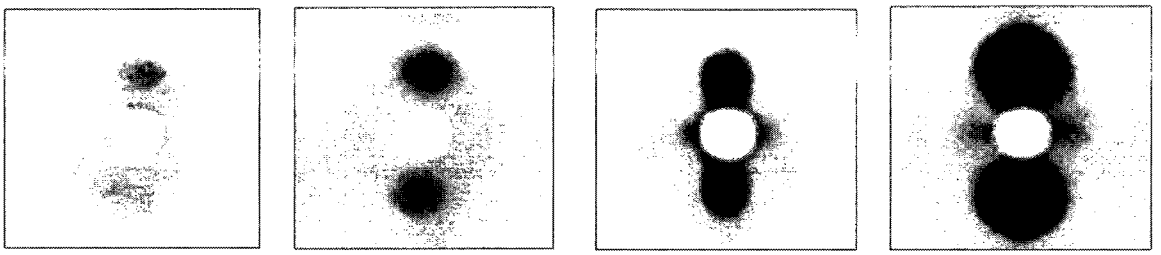

LCB 01 LCB 05 LCB 07 LCB 13

Fig. 2.17 Comparison of 2D SAXS patterns of the four LCB-PP polymers 30 min after shear (shear rate=60 s^{-1}, t_s=0.25 s, T=140 °C)[48].

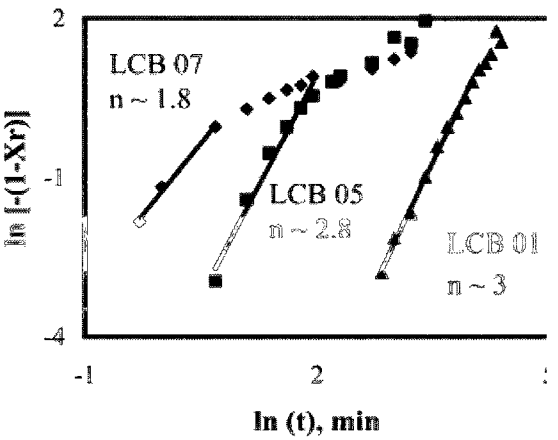

Fig. 2.18 Avrami plot of the crystallization data for LCB 01, 05, 07 polymers at 140 °C after shear (shear rate=60 s^{-1}, t_s=0.25 s)[48].

From the literature, two major types of crystallization can occur in PE depending on the magnitude of stress in flow[60]: low stress produces twisted kebabs, resulting in off-axis 110 and meridian 200 diffractions. In contrast, high stress produces flat kebabs (planar crystal structure), leading to the appearance of equatorial 110 and 200 diffractions. When the magnitude of flow is in-between, an intermediate arrangement is formed, resulting in off-axis 200 and 110 diffractions. Keum et al.[60] used a rheo-XRD technique to investigate the nucleation and growth behavior of twisted lamellae kebabs

from shear induced shish in HDPE melts. Figure 2.19 shows the WAXD patterns collected during crystallization at 134 °C in the sheared HDPE melt (shear rate=70 s^{-1}, t_s=12 s). The initial diffraction showed a pair of highly oriented 110 reflections on the equator, implying that both the *a*-axis and *b*-axis were arranged normal to the flow direction. Such a pattern was consistent with the formation of shish, having *c*-axis parallel to shear direction. As crystallization proceeded, the equatorial 2-arc 110 reflections were broadened (e.g. t=128 s) and then transformed into off-axis 4-arc pattern (e.g. thin arrows at t=263 s in Figure 2.19), and also with the appearance of off-axis 4-arc 200 reflections. The initial azimuthal broadening at the equator and then the off-axis splitting of the 110 reflection was due to the evolution of twisting kebabs[60]. According to Keller and Kolnaar[61,62] the amount of shishs or fibrils in row-nucleated lamellar structure can control the level of lamellar twisting where a larger number of shishs lead to a planar lamellar morphology with a significant orientation of *c*-axis along MD. Recently, Hayashi et al.[63] focused on structure formation of an isotactic polystyrene (iPS) after applying shear rate below and above the melting temperature (T_m=223 °C). An oriented structure named string-like was formed in micro scale even above T_m and was stable for more than 24 hr. This string-like structure acted as nuclei sites for lamellae crystals or kebab, yielding the formation of the shish-kebab structure. Zhang et al.[64] studied the crystalline morphology of poly (phenylene sulphide) (PPS) isothermally crystallized from a melt under shear by polarized optical microscope (POM) equipped with a hot stage. The shish-kebab crystal structure was formed at a certain shear rate or

for a longer shear time, which was attributed to the aggregation of numerous aligned nuclei in the shear direction. In accordance with other researchers, Zhang and coworkers[64] realized that the crystallization time decreased drastically with shear time, indicating that the flow accelerated the formation of crystal nuclei sites. The similar observations for shear-induced crystallization of poly (ethylene terephthalate) (PET)[65,66] and poly amide (PA6)[67] have also been reported. Here, it should be mentioned that besides the molecular weight, molecular weight distribution, and level of long chain branching, which their impacts on crystallization were discussed earlier, it is also known that isotacticity influences the crystallization kinetics. In Choi and White[68], the polypropylene resins with higher isotacticity showed significantly higher rate of crystallization and crystalline chain-axis orientation than the ones with lower isotacticity.

Although numerous studies have been conducted on the effect of shear flow on the crystallization of various resins, very little has been reported on the role of elongational flow. This lack of investigations is due to the difficulties to measure the extensional material functions. For instance, it is still impossible to reach very large strains and deformation rates with the existing elongational rheometers. Due to a stronger flow field in elongational flow compared to shear flow, chain extension can be easily achieved in the former[45]. Elongational flow can be created in many devices and geometries including two roll mill[69,70], four roll mill[71,72], converging flow[73,74] and cross-slot device[45,75]. Swartjes et al.[45] followed stress-induced crystallization in a cross-slit flow cell for an

isotactic polypropylene (iPP). The main advantage of the geometry used was the high attainable strain at the stagnation point. A highly oriented fibrillar-like structure was observed in the flow cell, which survived (did not relax) up to 20 min after the cessation of flow

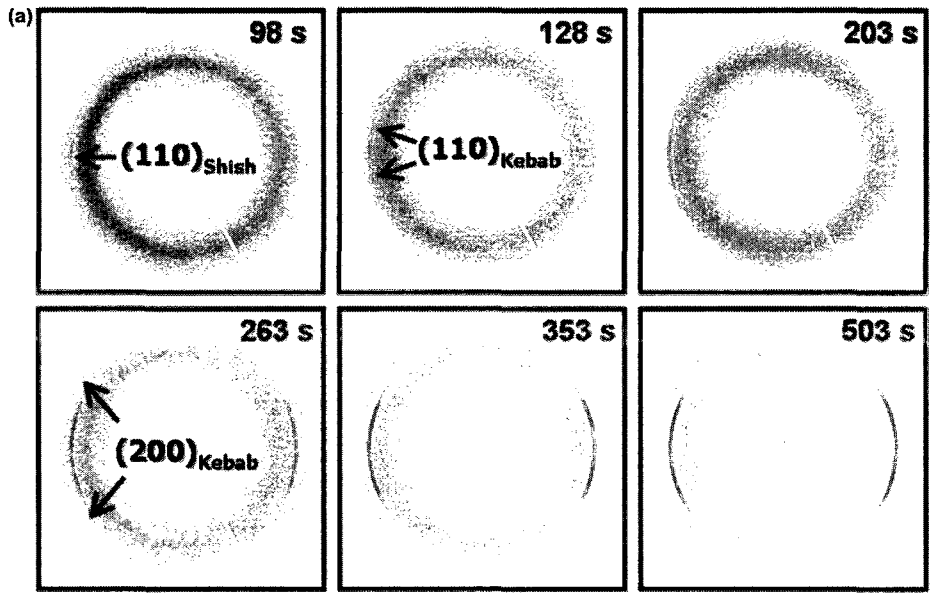

Fig. 2.19 Selected 2D WAXD patterns collected upon crystallization at 134 °C after shear (shear rate=70 s^{-1}, t_s=12 s)[60].

2.6 Microporous membranes by dry-stretching

As stated previously, semicrystalline polymers with a stacked lamellar morphology can be produced as a result of stress induced crystallization. Microporous membranes from stacked lamellae are made after annealing and subsequent stretching in the machine direction (MD). The resin characteristics (e.g. molecular weight, molecular weight distribution, long chain branching) as well as processing parameters (e.g. extrusion

temperature, cooling conditions, line speed, draw ratio) are the key factors for controlling the orientation and morphological features of the extruded precursor films. In precursors, skin-core differences are not desirable and thus a uniform stacked lamellar structure must be present through the cross-section of precursors[7]. During annealing, crystalline perfection and lamellae thickening take place. This requires that chain mobility occurs in the crystalline phase (α relaxation) and that the annealing temperature to be sufficient to active this relaxation[7]. The importance of annealing for the formation of a microporous structure was first elucidated by Sprague et al.[76] and confirmed by other researchers[77,78]. They annealed various semicrystalline films (e.g. PE and PP) possessing stacked lamellar structure prior to their drawing. The lamellae revealed an increase in the long spacing due to an increase in the lamellae thickness. During cold stretching, the pores are nucleated whereas in the subsequent hot stretching they are enlarged. From this brief overview, Johnson[7] introduced a set of criteria to help in the selection of semicrystalline polymers capable of forming microporous membranes via crystal lamellae separation. The proposed criteria are fast crystallization kinetics, a highly planar lamellar morphology for the extruded film, high orientation of the crystalline phase, proper film thickness, and the presence of an α relaxation. For many semicrystalline polymers such as high density polyethylene (HDPE), polypropylene (PP), poly (4methyl-1-pantene) (PMP), and polyoxymethylene (POM) a stacked lamellar morphology and subsequent microporous membranes upon stretching the crystal

lamellae have been reported. Below, we briefly review the works carried out in the literature regarding fabrication of microporous membranes by lamellae separation.

2.6.1 HDPE microporous membranes by stretching

In a dissertation by Yu[5], two high density polyethylene (HDPE) blown films of different M_w but with similar M_n were prepared under the same conditions. Transmission electron microscopy (TEM) images of the film produced from the higher M_w resin showed evident crystal shish (threads) whereas the lower M_w film did not show pronounced threads, which was also confirmed by WAXD. The effects of process conditions such as melt temperature, quench height, air flow rate in air ring, line speed, die gap on the crystalline orientation and crystallinity of the HDPE blown films were investigated. Depending on the process conditions, precursor films having different lamellar crystal structure were formed; low stress (prepared under low air flow rate, low line speed, high melt temperature, and high quench height) led to a twisted lamellar structure whereas high stress (prepared under high air flow rate, high line speed, low melt temperature, and low quench height) resulted in a planar lamellar structure. The produced films were annealed at 120 °C and 105 °C without applying tension and under a slight extension (3%). A significant increase in orientation of the annealed samples was observed, but the annealing time after a certain period had no influence on the orientation. Annealing at 120 °C resulted in a better orientation than 105 °C and annealing under a slight extension was more effective compared to annealing without extension. The annealed samples

were 40% and 80% cold stretched at room temperature and then 120% and 180% hot stretched at 115 °C. At the same hot stretching level, lowering cold stretching percent led to a microporous membrane structure with a larger pore size but lower pore density. Inversely, at the same cold stretch percent, increasing hot stretch level resulted in porous structure with a larger pore size. Their findings showed that the micropores were first developed from the region with a small amount of tie chains. This indicated that the distribution of interlamellar tie chains in the extruded films was not uniform. In addition, it was found that a minimum orientation, which was F_c=0.45 measured by WAXD, must be created in order to produce microporous membranes. However, further increasing the orientation of the precursors had no significant influence on the performance of the membranes. Yu also suggested that the presence of α relaxation, which is associated with the chain mobility in the crystalline phase, is necessary to be able to make microporous membranes with a high permeability. For instance, due to the lack of α relaxation in isotactic poly (1-butene), formation of porous membranes with a high permeability to air was impossible. Kim et al.[79] prepared HDPE hollow fiber membranes by stretching the melt spun hollow fiber precursors. A drastic effect of annealing on the orientation, crystallite size and crystallinity of the precursors were observed. Stretching without annealing failed to make a porous structure whereas high porous microporous membranes with slit-shaped pores were produced from the annealed films (see Figure 2.20). They also found that as take-up speed increased, pore sizes were smaller, but the number of pores per area (pore density) increased due to the better lamellae separation.

Lee et al.[80] studied the influence of hard elastic HDPE precursor films on the microporous membrane formation. The highly oriented lamellar crystalline structure and the larger number of stretched tie chains contributed to the high modulus of elasticity and as a consequence obtaining microporous membranes with a lower Gurley number or larger permeability (the Gurley number is an indication of the permeability of the membrane and is defined as the time required for 10 mL of air to pass through one inch square section of film at a constant pressure of 12.2 inches of H_2O based on the ASTM D726).

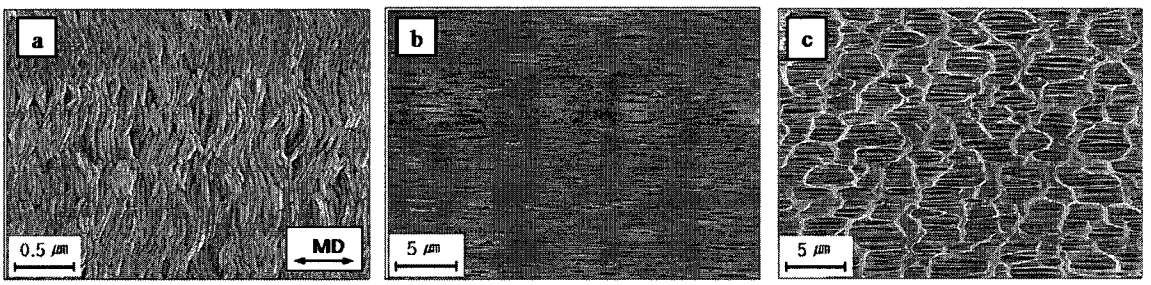

Fig. 2.20 Inner surface images of polyethylene hollow fiber a) precursor after annealing, b) membrane from unannealed precursor, and c) membrane from annealed precursor[79].

2.6.2 PP microporous membranes by stretching

Sadeghi et al.[29,81,82] studied the fabrication of polypropylene (PP) microporous membranes in a lab scale cast process. Their efforts focused on developing a lamellar crystalline morphology appropriate for the microporous membrane formation through the control of processing conditions as well as resin characteristics. For the cast film process, a linear relationship between the PP crystalline orientation and draw ratio was observed. The films produced under a large draw ratio (DR) and a high cooling air rate possessed a large orientation and yielded a better lamellae separation. The analysis of

the orientation measurements and SEM images confirmed that a precursor with an orientation function, F_c, greater than 0.3 was required to make PP microporous membranes by stretching. Moreover, it was shown that molecular weight (M_w) was the main resin factor that controlled the PP crystal structure where the resin with a high M_w formed a planar crystalline morphology. Sadeghi and coworkers[82] also examined the effect of the strain rate in the die on the structure and mechanical properties of the films. The lamellae became thinner and the tensile properties along MD improved by increasing strain rate, which were due to the formation of more shishs at high deformation rates. Their findings showed that the neat branched polypropylene could not form a stacked lamellar structure upon varying the processing conditions. Although it was known that the presence of long chain branches (LCB) increased the number of nuclei site, but these LCB significantly prevented the relaxation of molecules to form a folded lamellae. This issue was studied in details in our recent publications[83,84] presented in appendixes. According to Sadeghi et al.[37] the efficient annealing time for PP was 10 min at 140 °C whereas beyond that the structure remained unchanged. Figure 2.21 shows the SEM micrographs of the two samples of different M_w after cold stretching step. It is clear that the pores size of the cold stretched films obtained from the PP resins with distinct M_w did not vary significantly. However, a difference in the lamellae thickness was observed. The SEM surface images of the hot stretched samples (not shown) revealed more pores with larger size than pores formed after cold stretching.

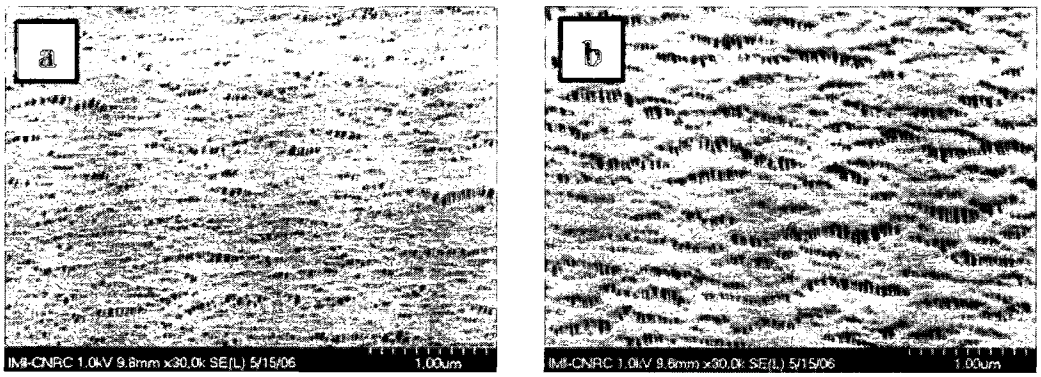

Fig. 2.21 SEM micrograph of the surface of PP (initial draw ratio of 56.5) samples cold stretched to 40% and heated set at 140 °C for 20 min[29].

Sadeghi et al.[85] compared the structure and properties of the microporous membranes obtained from a linear PP and its blend with 2 wt% long chain branched PP (LCB-PP). The addition of a small amount of a branched component drastically affected the row-nucleated crystalline structure in the precursor. Blending improved the orientation of both the crystalline and amorphous phases and led to the formation of much more lamellae than the neat linear resin. In Figure 2.22, the surface image of the membrane obtained from the blend revealed elongated thin fibrils, more pores with somewhat smaller size than the L-PP. The lamellae thickness for the blend was much smaller in comparison with that of the L-PP film. The blend membrane showed a porosity of 53% whereas it was 41% for the L-PP membrane. These resulted in a significant enhancement in water vapor and nitrogen permeabilities for the blend system.

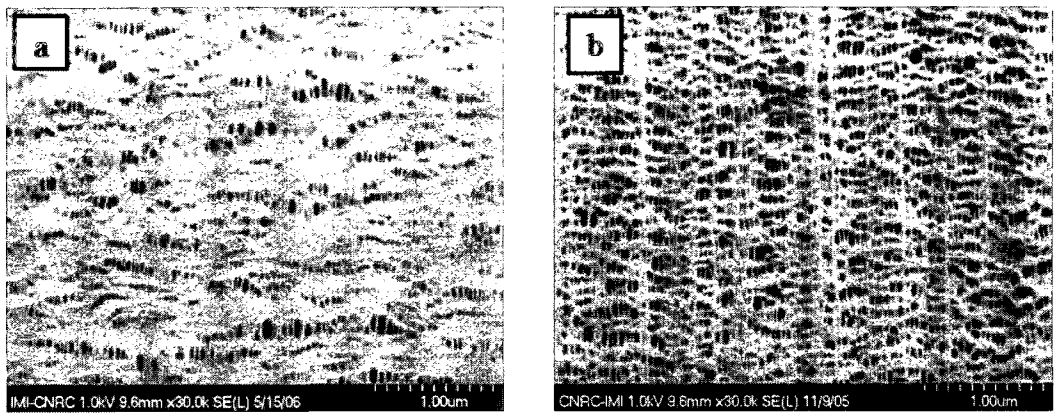

Fig. 2.22 SEM micrographs of the surface of microporous membranes. Left PP28 (linear PP) and right Blend 2 wt% for initial DR=56[85].

Recently, Wei and Haire[1] developed PP microporous membranes with round shaped pores by biaxial stretching of a nonporous precursor film. The total machine direction stretching was in the range of 50-500% whereas the total transverse direction stretching varied in the range of 100-1200%. This technique had the advantage of producing membranes with a porosity of 63% and nearly balanced tensile strength in the machine and transverse directions. The commercially uniaxial stretched PP membranes have slit shaped pores with a porosity of 40% and much higher tensile strength in MD than in TD.

2.6.3 PMP, POM and PVDF microporous membranes by stretching

Johnson[86-89] studied the formation of microporous membranes from poly (4-methyl-1-pentene) (PMP) and polyoxymethylene (POM) by stretching of the blown film precursors. He examined the impact of the resin molecular weight, processing conditions, as well as annealing and stretching variables on the structure and performances of the microporous membranes. A lamellar morphology could be obtained

by controlling the processing conditions, which were a high draw down ratio (DDR) and a rapid quenching of the films at the die exit. The high molecular weight resins showed a larger crystalline orientation. Their findings showed that the precursor crystalline orientation, F_c, had a crucial role on the microporosity and permeability of the final films. A higher F_c resulted in a better lamellae separation and consequently a larger permeability. The annealing variables such as temperature, time as well as the level of applied extension during annealing were investigated. For the POM microporous membranes[88,89], annealing at 145 °C for 20 min without applying extension, and also for the PMP microporous membranes, annealing at 205 °C for 20 min without applying extension were the optimum annealing conditions. As the annealing temperature and time increased, the crystallinity as well as the long period spacing increased, which was explained by the crystalline mobility associated with the α relaxation. The annealed samples were then cold and hot stretched to initiate and enlarge the pores, respectively. For both the PMP and POM microporous membranes, by increasing the total level of extension during cold and hot stretching, the permeability to air increased. The films produced using a larger total stretch revealed a larger micropore structure where the pores shape was approximately the same. Figures 2.23 and 2.24 display the surface morphology of the POM and PMP films, respectively, before and after stretching. It is obvious that the POM microporous membranes had pores shape somewhat different than that of the polyolefin (PP, HDPE, and PMP) membranes. The lamellae individually separated in the POM membranes while the polyolefin membranes tended to possess

many bundles between micropores. In addition, the sizes of the pores in the POM membranes were not as large as those in the polyolefin stretched films.

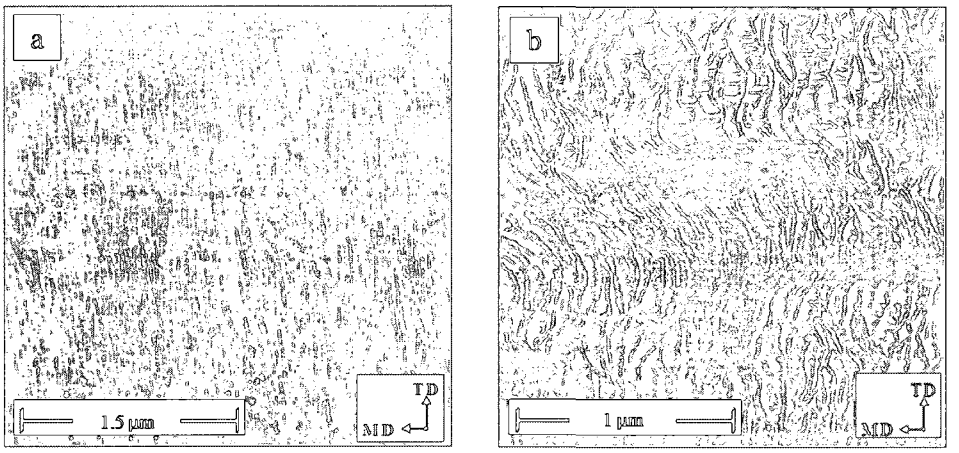

Fig. 2.23 AFM phase images of POM a) annealed at 145 °C for 20 min and b) 50% cold stretched at 70 °C followed by 90% hot stretching at 160 °C[87].

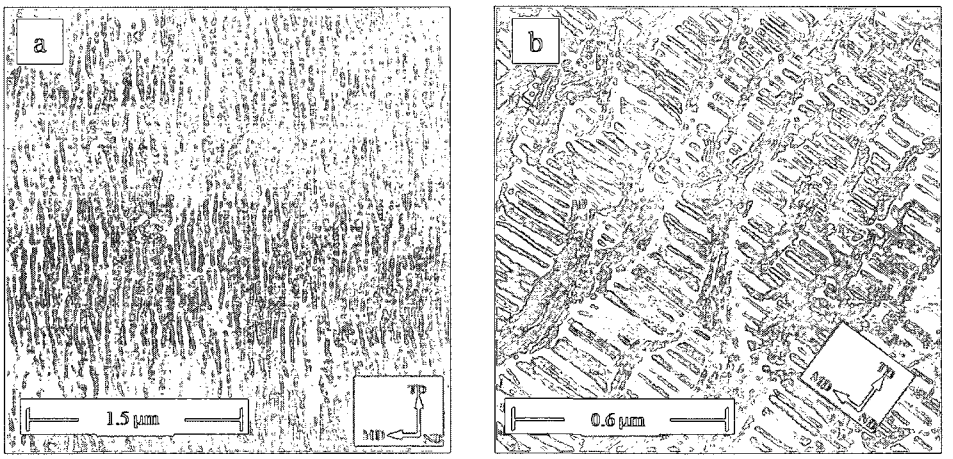

Fig. 2.24 AFM phase images of PMP a) annealed at 205 °C for 20 min and b) 180% total (cold + hot) stretching[89].

Xu et al.[6] studied strain induced morphologies of the blown films of five PVDFs of different molecular weights. It was noted that as the resin molecular weight increased, the structure of the uniaxial films varied from a spherulitic structure to that of an

extremely oriented fibrillar structure. They used the Deborah number, which is defined as the characteristic relaxation time of a resin divided by the melt process time window, as a criterion to explain the various morphologies observed under different conditions. The Deborah number less than unity led to a small crystal orientation whereas in the range of unity, a distinct rise in crystalline alignment occurred, resulting in a shish-kebab lamellar structure. Exceeding a Deborah number of unity yielded a tremendous orientation due to a very high concentration of fibrils. Figure 2.25 illustrates the surface morphology of the PVDF porous membrane obtained from a medium molecular weight resin. Obviously, the pore sizes were much smaller compared to PMP and HDPE membranes, possibly because of the polar nature of PVDF molecules, which resulted in a lower lamellae separation. Recently, Sadeghi et al.[30] studied the role of PVDF melt rheology on the row-nucleated lamellar morphology. A melt strain-hardening behavior was seen for the high molecular weight resins and attributed to the chain interactions. Their results also elucidated that the PVDF molecular weight had a significant impact on obtaining a proper lamellar structure in the precursors.

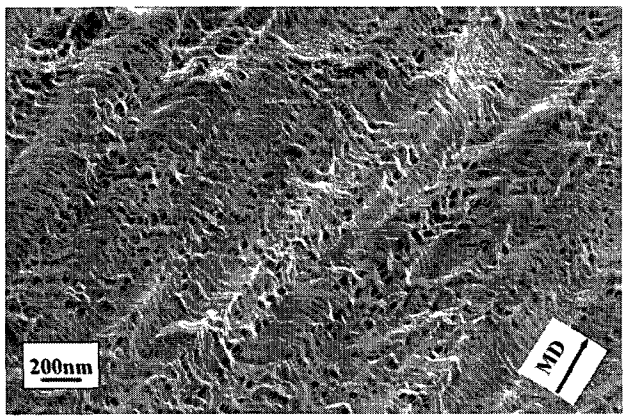

Fig. 2.25 SEM micrograph of PVDF film showing lamellar opening[6].

2.7 Structure and properties of uniaxial and biaxial stretched films

As pointed out previously, the stretching of a well oriented shish-kebab crystal morphology involves the separation of the stacked lamellae, leading to pores formation and subsequent microporous membrane generation. However, the drawing of films possessing spherulitic crystal structure involves a morphological transformation of the spherulites, which will affect their final properties. For the literature, it is well known that uniaxial or biaxial drawing of the polymeric films such as polypropylene, polyester, polyketone, nylon, and ethyl vinyl alcohol can drastically affect their properties, particularly mechanical, impact, barrier, and optical properties[90-96].

The machine direction orientation (MDO) process is widely used for uniaxial stretching of polyethylene and polypropylene films. The MDO unit can be operated either in-line or off-line with extrusion and is controlled via variables such as: the

distance between the draw rollers, draw ratio, drawing speed, drawing times (a film can be stretched many times), drawing temperature, and heat-setting conditions[90]. The stretching is usually performed at a high temperature, below the melt temperature of the polymer, and results in a highly oriented film that causes anisotropy in properties. The drawing process usually improves the strength and barrier properties, but brings some drawbacks such as a reduction of the tear resistance along the machine direction (MD) and a lowering of elongation at break along the transverse direction (TD)[90]. For example, Schut[91] used the MDO process to improve the barrier properties of nylon and ethyl vinyl alcohol, but the films were brittle and had low tear resistance in MD.

The evolution of the crystal structure of biaxial as well as uniaxial drawn films has been investigated in the literature[97-100]. Nie et al.[97] studied the morphological development during biaxial stretching of polypropylene films using atomic force microscopy (AFM). According to their results, the biaxial orientation of polypropylene involved a morphological transformation of the spherulites into a network of microfibrils, which was also confirmed by Diez et al.[98]. Sadeghi et al.[90] studied the morphology development during MDO stretching of PP. Their results showed a fibrillar crystalline structure at a high draw ratio (DR), such as DR=6. Also, a distinctive improvement in the mechanical, clarity, and barrier properties was reported as DR increased. Using in-situ small angle X-ray scattering (SAXS) and wide angle X-ray diffraction (WAXD), Zuo et al.[99] investigated the structure of polypropylene films during uniaxial stretching for various temperatures. The rate of crystal alignment during

deformation at high temperatures was found to be slower than that at low temperature, but the final orientation during deformation at high temperatures was higher due to the larger applied strain. Sakurai et al.[100] investigated the structural deformation behavior of polypropylenes with different molecular weight (M_W), molecular weight distribution (MWD), and isotacticity (IT) during hot drawing process. Significant effects of M_w, MWD, and IT on the mechanical properties, morphology as well as stress distribution in the hot stretched samples were observed.

2.8 Originality of the work

The literature review showed quite a few studies on the preparation of microporous membranes by stretching of precursor films possessing a row-nucleated lamellar structure. In fact, in all the previous studies the precursor films were obtained from film blowing process except in Sadeghi[4] in which a lab scale cast extrusion was utilized. In addition, no study has been conducted on the development of multilayer microporous membranes. We used an industrial scale cast film process instead of film blowing process, because the former has more flexibility in the supply of air cooling from both sides, as well as a better control of the processing parameters and films and/or layers thickness, leading to a better control of film crystalline microstructure. Hence, the main objective of this dissertation is to develop microporous membranes with high performances from monolayer as well as multilayer PP/HDPE cast films by stretching involving industrial scale capabilities. We believe that by using polymer blends as well

as appropriate process conditions, the pore density, pore size and distribution, porosity, and tortuosity of the porous membranes can be better controlled.

In addition, in the literature, very little has been reported on uniaxial drawing of films possessing spherulitic crystal structure. In this study, precursor films with a spherulitic structure and coexisting small rows of lamellae and spherulites were produced and MDO oriented using an industrial scale production line. A detailed investigation of the structure evolution with stretching has been carried out and relationships between morphological transformation and barrier, tear, and puncture properties are discussed.

2.9 Objectives

The main objective of this thesis is to develop microporous membranes with high performances from monolayer as well as multilayer PP/HDPE films through cast film extrusion followed by uniaxial stretching. A secondary objective is to establish relationships between crystalline morphology, processing conditions and barrier and mechanical properties of polypropylene films using a machine direction orientation (MDO) unit.

CHAPTER 3

METHODOLOGY AND MATERIALS

3.1 Methodology

3.1.1 Material characterization

As stated earlier, the resin characteristics such as molecular weight, molecular weight distribution, and level of long chain branching strongly influence the row-nucleated lamellar crystallization. Therefore, the oscillatory shear and transient elongational rheological tests as well as gel permeation chromatography (GPC) measurements were performed to characterize the resins. The linear viscoelastic properties obtained at the low deformation rates described the material structure while the data measured at the high deformation rate predicted the polymer behavior during the processing. The presence and amount of long chain branches were obtained from the extensional viscosity data. The GPC measurements were carried out to measure the molecular weight and molecular weight distribution of the resins.

3.1.2 Extrusion parameters for the fabrication of precursor films

Die temperature, die gap, amount and position of air cooling, chill roll temperature, and draw ratio are the major processing parameters that need to be optimized depending on the resin as well as number of layers in the film (see Figure 3.1). The effects of each

processing variable on orientation, morphology, and mechanical properties of the precursors were examined.

3.1.3 Annealing and stretching conditions

Annealing removes imperfections in the crystalline phase and increases lamellae thickness. The annealing variables investigated included temperature, time, and level of extension applied during annealing. The annealed films were then subjected to the uniaxially drawing stage consisting of a cold and a hot stretching to initiate and enlarge pores, respectively. The amount of extension and stretching speed and temperature were the key drawing factors. The influence of these on the final properties was considered for obtaining microporous membranes with desired performances.

3.1.4 Film and membrane characterization

Thermal analysis: Thermal properties of specimens were analyzed using a TA instrument differential scanning calorimeter (DSC) Q 1000. The thermal behavior of films was obtained by heating from 50 to 220 °C at a heating rate of 10 °C/min. The reported crystallinity results were obtained using a heat of fusion of 209 and 280 J/g for fully crystalline PP and HDPE, respectively[101,102].

Fourier transform infrared spectroscopy (FTIR): For FTIR measurements, a Nicolet Magna 860 FTIR instrument from Thermo Electron Corp. (DTGS detector, resolution 2 cm^{-1}, accumulation of 128 scans) was used. The beam was polarized by means of a Spectra-Tech zinc selenide wire grid polarizer from Thermo Electron Corp. The

measurement is based on the absorption of infrared light at certain frequencies corresponding to the vibration modes of atomic groups present within the molecule. In addition, if a specific vibration is attributed to a specific phase, the orientation within that phase can be determined[81]. If the films are oriented, the absorption of plane-polarized radiation by a vibration in two orthogonal directions, specifically parallel and perpendicular to a reference axis (MD), should be different. The ratio of these two absorption values is defined as the dichroic ratio, D[81]:

$$D = \frac{A_{\parallel}}{A_{\perp}} \qquad (3.1)$$

where $A_{\parallel}$ is the absorption parallel and $A_{\perp}$ is the absorption perpendicular to a specific reference axis. The Herman orientation function of this vibration is obtained according to[81]:

$$F = \frac{D-1}{D+2} \qquad (3.2)$$

For polypropylene, absorption at the wavenumber of 998 cm^{-1} is attributed to the crystalline phase (c-axis) while that at 972 cm^{-1} is due to the contribution of both crystalline and amorphous phases. From the former absorption, the orientation of the crystalline phase, F_c, can be determined while from the latter, the average orientation function, F_{avg}, is obtained. The orientation of the amorphous phase, F_a, can then be calculated according to:

$$F_{avg} = X_c F_c + (1 - X_c) F_a \qquad (3.3)$$

where X_c is the degree of the crystallinity.

For polyethylene, absorption at the wavenumber of 730 cm^{-1} is attributed to the *a*-axis of the unit crystal cell while absorption at the wavenumber of 720 cm^{-1} is due to the *b*-axis. The similarity of the normal (N) and transverse (T) spectra confirmed that the orientation is mostly uniaxial[103]. In such a case, it is not necessary to use the tilted film technique. The orientation function of the *a*- and *b*-axes could be obtained from Eq. 3.2 while that of the *c*-axis orientation is calculated according to the orthogonality equation:

$$F_a + F_b + F_c = 0 \qquad (3.4)$$

X-ray diffraction: XRD measurement was carried out using a Bruker AXS X-ray goniometer equipped with a Hi-STAR two-dimensional area detector. The generator was set up at 40 kV and 40 mA and the copper CuKα radiation (λ = 1.542 A°) was selected using a graphite crystal monochromator. The sample to detector distance was fixed at 9.2 cm for wide angle diffraction and 28.2 cm for small angle X-ray scattering analysis. To get the maximum diffraction intensity several film layers were stacked together to obtain the total thickness of about 2 mm.

Wide angle X-ray diffraction (WAXD) is based on the diffraction of a monochromatic X-ray beam by the crystallographic planes (*hkl*) of the polymer crystalline phase. Using a pole figure accessory, the intensity of the diffracted radiation for a given *hkl* plane is measured as the sample is rotated through all possible spherical angles with respect to the beam. This gives the probability distribution of the orientation of the normal to *hkl* plane with respect to the directions of the sample.

The Herman orientation function F_{ij} of a crystalline axis i with respect to a reference axis j is given by[104]:

$$F_{ij} = \frac{(3\cos^2\phi_{ij} - 1)}{2} \qquad (3.5)$$

where ϕ_{ij} is the angle between the unit cell axes i (a, b, or c) and the reference axis j. The Herman orientation functions were derived from the 110 and 040 pole figures for the PP and the 110 and 200 pole figures for the HDPE. The c-axis of the isotactic polypropylene unit cell is parallel to the helical axis of the PP molecule in that cell while the three crystallographic axes in a monoclinic unit cell are not mutually perpendicular (the angle between a and c axis in isotactic PP is 99° 20′), so a modified coordinate system is utilized for the calculation of orientation parameters. Since the b-axis of unit cells is perpendicular to its 040 plane, its orientation relative to reference (stretch) direction can be measured directly, that is $\cos^2\beta = \cos^2\phi_{040}$, where β is the angle between the stretch direction (machine direction) and the b-axis of the crystal, this value ($\cos^2\phi_{040}$) is measured experimentally and using Herman's equation[104], the orientation for the b-axis will be determined:

$$F_b = F_{040} = \frac{3\cos^2\phi_{040} - 1}{2} \qquad (3.6)$$

On the other hand F_c (orientation of the c-axis) with respect to MD is determined by the combination of data of two planes for the polypropylene which are 040 and 110[104]:

$$\cos^2\phi_c = 1 - 1.099\cos^2\phi_{110} - 0.901\cos^2\phi_{040} \qquad (3.7)$$

Substituting this result in Herman's equation, the orientation factor for the *c*-axis will be also obtained. The other orientation factor, (*a*-axis), can be calculated from the orthogonally relation:

$$\cos^2 \phi_a = 1 - \cos^2 \phi_c - \cos^2 \phi_b \qquad (3.8)$$

As stated earlier, since the unit cell of the polypropylene is not orthogonal, the orientation factor calculated from the above equation is not really the same as that of the *a*-axis of the unit cells, but can be interpreted as an axis that has a small angle with the real *a*-axis and considered as a replacement for *a*-axis[104].

For the HDPE, since the *a*-axis of the unit cells is perpendicular to the 200 plane, its orientation relative to the machine direction can be measured directly as follow:

$$F_a = F_{200} = \frac{3\cos^2 \phi_{200} - 1}{2} \qquad (3.9)$$

On the other hand, F_c (orientation of the *c*-axis) with respect to MD is determined by the combination of data of two planes for the HDPE, which are 110 and 200[104]:

$$\cos^2 \phi_c = 1 - 1.435\cos^2 \phi_{110} - 0.565\cos^2 \phi_{200} \qquad (3.10)$$

The orientation parameter for the *b*-axis can be calculated from the orthogonality relation:

$$\cos^2 \phi_b = 1 - \cos^2 \phi_a - \cos^2 \phi_c \qquad (3.11)$$

The orientation factors from WAXD are mainly due to the crystalline part, therefore no information about the orientation of the amorphous phase can be obtained. Small

angle X-ray scattering (SAXS) was used to compare the level of the lamellae formation for the different samples and to estimate the long period between lamellae.

Mechanical analysis and puncture resistance: Tensile tests were performed using an Instron 5500R machine equipped with an environmental chamber for tests at high temperature. The procedure used was based on the D638-02a ASTM standard. Puncture tests were performed using a 10 N load cell of the Instron machine used for the tensile tests. A needle with 0.5 mm radius was used to pierce the samples. The film was held tight in the camping device with a central hole of 11.3 mm. The displacement of the film was recorded against the force and the maximum force was reported as the puncture strength.

Morphology: To clearly observe the crystal arrangement of the precursor films, an etching method was employed to remove the amorphous part. The films were dissolved in a 0.7% solution of potassium permanganate in a mixture of 35 vol% of orthophosphoric and 65 vol% of sulphuric acid. The potassium permanganate was slowly added to the sulphuric acid under rapid agitation. At the end of the reaction time, the samples were washed as described in Olley and Bassett[105].

A field emission scanning electron microscope (FE-SEM- Hitachi S4700) was employed for the observation of the etched precursor films and microporous membranes surfaces as well as cross-sections. This microscope provides high resolution of 2.5 nm at a low accelerating voltage of 1 kV and high resolution of 1.5 nm at 15 kV with magnification from 20x to 500kx.

Water vapor transmission: The permeability to water vapor was measured via a MOCON PERMATRAN-W Model 101K at room temperature. It is composed of three chambers: an upper chamber containing liquid water and separated from the center chamber by two porous films. Water vapor diffuses from the first film to fill the space between the films to reach 100% relative humidity (*RH*). The center chamber is separated from the lower one by the test film. The diffused vapor is swept away by N_2 gas to a relative humidity (*RH)* sensor.

BET measurement: To obtain the surface area of the membranes, a Micromeritics, BET Tristar 3000 was used. A nitrogen and helium gas mixture was continuously fed through the sample cell, which was kept at liquid nitrogen temperature. At different pressures, the total volume of nitrogen gas adsorbed on the surface was measured. The volume of gas needed to create an adsorbed monomolecular layer was calculated as follows[106]:

$$\frac{P}{P^{\circ}[V(1-\frac{P}{P^{\circ}})]} = \frac{1}{V_m c} + \frac{c-1}{V_m c}\frac{P}{P^{\circ}} \qquad (3.12)$$

where P is the experimental pressure, P^o is the saturation pressure, V is the volume of the adsorbate, V_m is the volume of gas required to form an absorbed monomolecular layer, and c is a constant. The procedure for estimating the surface area from Eq. 3.12 can be found elsewhere[107].

Oxygen transmission: Oxygen transmission rates (OTR) were determined using a modification of the ASTM Standard Method D 3985-81 with an Ox-Tran Model 2/21

apparatus (Mocon Inc., Minneapolis, MN) at 25°C. In this paper, all OTR values presented have been normalized (multiplied) by the films thickness. Two films of each specimen were tested and the average value is reported.

Dynamic mechanical thermal analysis (DMTA): Dynamic thermomechanical properties of different samples were characterized using a dynamic mechanical thermal analyzer (DMTA) 2980 from TA Instruments, inside an environmental test chamber (ETC). Specimens cut parallel to the drawing direction were subjected to a dynamic tensile deformation mode. The temperature ranged from -60 °C to 120 °C at a rate of 2 °C/min and a frequency of 1 Hz was applied to the rectangular samples. To generate low temperatures and to control temperature during heating, liquid nitrogen was used. The β transition was determined from the peak magnitude of the tan δ curves.

3.2 Materials

In this study, four commercial linear polypropylenes (PF6523, PP4712, PP5341, PF6823), a commercial long chain branched polypropylene (PF814), and a commercial high density polyethylene (HDPE 19A) were selected. PP4712 and PP5341 were supplied by ExxonMobil and had melt flow rate (MFR) values of 2.8 and 0.8 g/10min (under ASTM conditions of 230 °C and 2.16 kg), respectively. PF6512, PF6823, and PF814 were provided by Basell and had a MFR of 4.0, 0.8, and 2.5 g/10min, respectively. HDPE 19A was supplied by NOVA Chemical and had a MFR value of 0.8 g/10min (under ASTM conditions of 190 °C and 2.16 kg). The main characteristics of

the resins are shown in Table 1. The molecular weight (M_w) of the L-PPs were evaluated from the relation between the zero-shear viscosity and the molecular weight[108]. The polydispersity index (PDI) of the PPs were measured using a GPC (Viscotek model 350) at 140 °C and 1,2,4-Trichlorobenzene (TCB) as a solvent. M_w and PDI of HDPE 19A were supplied by the company. The zero-shear viscosities were reported from the dynamic rheological measurements at 190 °C. The melting point, T_m, and the crystallization temperature, T_c, of the resins were obtained from differential scanning calorimetry at a rate of 10 °C/min.

Table 3.1 Main characteristics of the neat polymers.

Resin code	Company	MFR (g/10min)	η_o^* (kPa.s)	M_w (kg/mol)	M_w/M_n	T_m (°C)	T_c (°C)
Pro-fax 6523	Basell	4.0	9.8	501	2.8	159.8	119.2
PP4712	ExxonMobil	2.8	12.5	543	8.5	160.0	115.0
PP5341E1	ExxonMobil	0.8	43.6	772	2.7	160.0	117.3
Pro-fax 6823	Basell	0.4	58.3	812	4.3	159.6	116.9
Pro-fax 814	Basell	2.5	18.6	N/A	2.3	158.4	128.4
HDPE 19A	Nova Chemicals	0.8**	30.1	126***	7.8***	129.0	118.0

* Zero-shear viscosity values obtained from the Carreau-Yasuda model, T=190 °C.
** For this resin, MFR was obtained under ASTM conditions of 190 °C and 2.16 kg.
*** Molecular weight and polydispersity index of this resin were supplied by the company.

3.3 Processing

Two cast film processes were used to produce the precursor films. (1) A lab scale cast film extrusion available in IMI (Industrial Material Institute, Boucherville-QC). In this unit, a twin screw extruder with L/D=32 and equipped with a slit die of 1.9 mm opening

and 200 mm width was employed. An air knife was mounted on the die to supply air to the film surface right at the exit of the die. The die temperature was set at 220 °C and the films were produced under draw ratios ranging from 60 to 90. (2) An industrial multilayer cast film unit from Davis Standard Company (Pawcatuck, CT) equipped with a 2.8 mm opening and 122 cm width slit die and two cooling drums was also used. The extrusion was carried out at 220 °C and the distance between the die exit to the nip roll was 15 cm. The die temperature was set at 220 °C and draw ratios of 60, 75, and 90 were applied. An air knife with dimensions of 3 mm opening and 130 cm width was mounted close to the die to provide air to the film surface right at the exit of the die. The variables of interest were chill roll temperature, amount of air flow, and draw ratio. Figure 3.1 illustrates schematically the industrial scale multilayer cast film unit used for the fabrication of the precursor films. An appropriate selection of processing parameters leads to a precursor film with a proper lamellar structure (see the sketches in the red boxes in Figure 3.1).

For membrane fabrication, the precursor films with a thickness, width and length of 35 μm, 46 mm, and 64 mm, respectively, were used. The films were first annealed then cold and hot stretched. Both annealing and stretching were performed in an Instron machine equipped with an environmental chamber. Annealing, cold and hot stretching temperatures varied depending on the resin. The details for the fabrication of the microporous membranes can be found in Chapters 5-7.

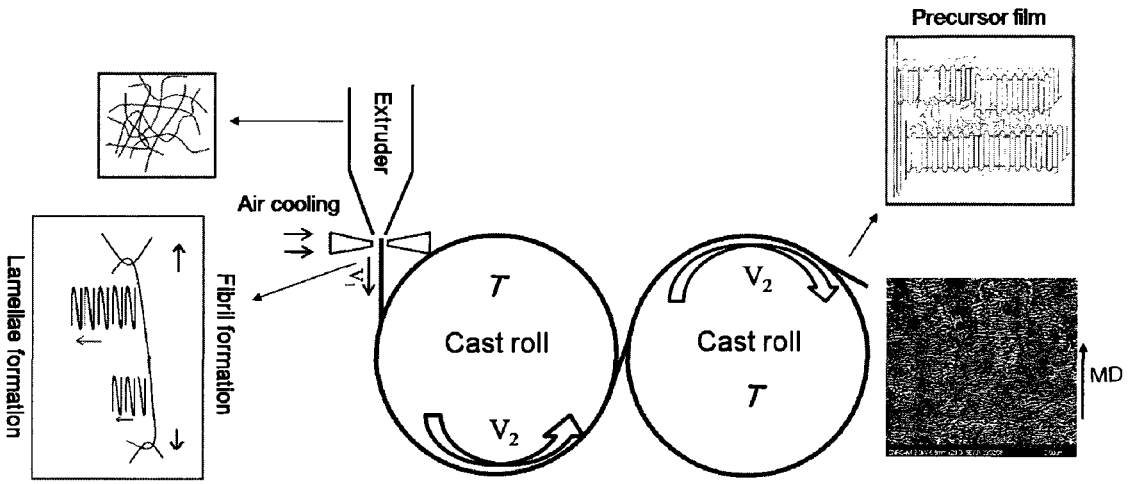

Fig. 3.1 Illustration of the section just after die exit and chill rolls of the industrial scale cast unit for the fabrication of precursor films.

CHAPTER 4

ORGANIZATION OF ARTICLES

In Chapter 5, the influence of high molecular weight chains on the PP row-nucleated lamellar crystallization was investigated using WAXD, SAXS, FTIR, and mechanical measurements. It is shown that by using polymer blends, the pore density, pore size and distribution, porosity, and tortuosity of the porous membranes could be better controlled. Chapter 6 discusses in details the effects of processing parameters such as air cooling conditions, chill roll temperature, and draw ratio on the crystalline orientation, morphology, and mechanical properties of the industrial scale cast films and formation of microporous membranes. Morphological pictograms are proposed to represent the microstructure of the films obtained without and upon applying air cooling for different cast roll temperatures. Also the results on microporous membranes are presented to elucidate the effect of the PP cast film microstructure on the morphology and permeability of membranes. Chapter 7 presents the results on the fabrication of the trilayer PP/HDPE/PP microporous membranes through cast extrusion followed by stretching. The role of processing variables and annealing on the shear and/or elongation-induced crystallization and orientation developed in the single layer as well as the components in the multilayer films are examined and discussed. In Chapter 8, a detailed investigation of the structure evolution of the precursors having spherulitic structure and coexisting rows of lamellae and spherulites with uniaxial (MDO)

stretching are carried out. The relationships between morphological transformation and oxygen transmission, tear, and puncture properties are discussed. In Chapter 9 (general discussion), a full review regarding the most important factors affecting the microporous membranes fabrication and MDO stretching is presented. Chapter 10 summarizes the most important conclusions of this thesis and gives recommendations for the future work.

In addition to the membrane fabrication by stretching, comprehensive investigations were conducted on the rheological and thermal properties of blends of different linear polypropylenes (L-PP) and a long chain branched polypropylene (LCB-PP) and are presented in Appendixes A and B. Although the last part of this thesis deviates from the microporous membrane study, but it provides valuable information concerning the resin characteristics, particularly the effect of molecular weight and long chain branching on the rheological and thermal properties, which could be helpful for further progresses on membrane development. Appendix A elucidates the impact of the addition of a branched PP to a linear PP on the rheological properties of PP, including transient and 'steady' extensional behavior over a wide range of deformation rates. In Appendix B, the role of molecular weight of linear polypropylene on the rheological behavior of blends of a linear polypropylene and a long-chain branched polypropylene is considered. In addition, the influence of adding LCB-PP on the thermal properties, crystallization, and solid state behavior of the blends is explored.

CHAPTER 5

Microporous Membranes Obtained from Polypropylene Blend Films by Stretching[1]

Seyed H. Tabatabaei, Pierre J. Carreau, and Abdellah Ajji

CREPEC, Chemical Engineering Department, Ecole Polytechnique, C.P. 6079, Succ. Centre ville Montreal, QC, H3C 3A7 Canada

Abstract

Blends of two linear polypropylenes (PP, having different molecular weights) were prepared to develop microporous membranes through melt extrusion followed by stretching. The role of high molecular weight chains on the row-nucleated lamellar crystallization was investigated. The orientation of crystalline and amorphous phases was measured by wide angle X-ray diffraction (WAXD) and Fourier transform infrared (FTIR). Long period spacing was obtained using small angle X-ray scattering (SAXS). The effects of annealing temperature and applied elongation during annealing on the crystallinity of the films were studied using differential scanning calorimetry (DSC). It was found that annealing at 140 °C contributed significantly to the perfection of the crystalline phase. Scanning electron microscopy (SEM) images of the membrane surface

---

[1] *Journal of Membrane Science* (2008) **325**, 772-782.

showed more pore density and uniform pore size as the amount of high molecular weight component increased. The addition of the high M_w PP improved the water vapor transmission rate (WVTR) of the membranes, indicating increased interconnectivity of the pores, which was also confirmed from cross-section SEM micrographs of the membranes. The surface area and pore dimensions of the microporous membranes were measured using the BET nitrogen absorption technique and mercury porosimetry, respectively. The influences of temperature and amount of stretching during cold and hot stretching on WVTR were also explored. Tensile properties in the machine and transverse directions (MD and TD, respectively) as well as puncture resistance in the normal direction (ND) were evaluated. As the high M_w PP was added, a slight reduction in the mechanical properties along MD and TD and no changes in ND were observed.

5.1 Introduction

Microporous membranes are commonly used in separation processes such as battery separators and medical applications to control the permeation rate of chemical components. Due to the wide range of chemical structures, optimum physical properties, and low cost of polymers and polymer blends, these materials are known as the best candidates for the fabrication of microporous membranes.

The two main techniques to develop polymeric membranes are: solution casting and extrusion followed by stretching. High cost and solvent contamination are the main drawbacks of the solution technique. Techniques to make porous membranes from

polymers without using any solvent were developed in the seventies of the last century for some applications, but most of the information on these processes remains proprietary to the companies' and are not available to the scientific community. One of the techniques is based on the stretching of a polymer film containing a row-nucleated lamellar structure [1]. Then, three consecutive stages are carried out to obtain porous membranes: (1) creating a precursor film having a row-nucleated lamellar structure by mechanism of shear and elongation-induced crystallization, (2) annealing the precursor film at temperatures near the melting point of the resin to remove imperfections in the crystalline phase and to increase lamellae thickness, and (3) stretching at low and high temperatures to create and enlarge pores, respectively [1, 2]. In fact, in this process the material variables as well as the applied processing conditions are key parameters that control the structure and the final properties of the fabricated microporous membranes [1]. The material variables include molecular weight, molecular weight distribution, and chain structure of the polymer. These factors mainly influence the row-nucleated structure in the precursor films at the first step of the formation of microporous membranes.

Among a wide range of resins, polypropylene (PP) is a well-known semicrystalline polymer and, in comparison with polyethylene, has higher melting point, lower density, higher chemical resistance, and better mechanical properties, which make it useful for many industrial applications.

Using in situ small angle X-ray scattering (SAXS) and/or wide angle X-ray diffraction (WAXD) analyses, the effects of the material parameters on the shear induced crystallization process for PP has been investigated [3-6]. Agarwal et al. [3] examined the influence of long chain branches on the stress-induced crystallization. Adding a certain level of branches improved the orientation of the crystal blocks and the crystallization kinetics, due to the longer relaxation time and molecular structure. Somani et al. [4] followed the orientation development upon applying different shear rates. They found that at a certain shear rate only molecules with a chain length (molecular weight) above a critical value (critical orientation molecular weight, M_c,) can form stable oriented row nuclei while the rest create lamellae over these nuclei sites. In addition, it was shown that M_c drops as the imposed shear rate increased. In another study, Somani et al. [5] compared the oriented microstructure in isotactic polypropylene melts (PP-A and PP-B) with the same number average molecular weight but different molecular weight distribution (MWD) under shear flow. The amount of the high molecular weight species was larger in PP-B than in PP-A. Their results showed that the shish structure evolved much earlier for PP-B with a more pronounced crystal orientation and a faster crystallization kinetic. They concluded that even a small increase in the concentration of the high molecular weight chains led to a significant increase in the shish or nuclei site formation. Seki et al. [6] found that adding a small amount of high molecular weight component enhances the formation of the row-nucleated structure due to an increase in nucleating sites.

A few studies have investigated the fabrication of porous membranes by stretching of lamellar morphology using polypropylene [7-9]. Sadeghi et al. [7, 8] considered the influence of molecular weight on orientation of the row-nucleated lamellar structure. They found that molecular weight was the main material parameter that controlled the orientation of the crystalline phase. It was demonstrated that the resin with high molecular weight developed larger orientation and thicker lamellae than the resin with low molecular weight. Sadeghi et al. [9] realized that an initial orientation was required in order to obtain a lamellar structure. The crystalline orientation in the precursor film depended on the molecular weight of the resin and the type of process (i.e. cast film or film blowing). It was shown that the cast film process was more efficient than film blowing for producing precursor films with the appropriate crystalline orientation.

Although quite a few authors have investigated the formation of porous membranes from various resins, information is still lacking on the control of morphology and performances of membranes. We believe that by using polymer blends, the pore density, pore size and distribution, porosity, and tortuosity of the porous membranes can be better controlled. In Sadeghi et al. [10] a superior permeability was obtained by adding a small amount of a long-chain branched polypropylene (LCB-PP) to a linear polypropylene (L-PP). In this study, following Sadeghi et al. [10] we investigate the role of adding high molecular weight chains of linear PP to a low molecular weight linear PP on the structure and performances of microporous membranes.

Sadeghi et al. [8] examined the role of draw ratio and annealing on the orientation of crystalline and amorphous phases. They also compared the cold and hot stretching behavior of PP films obtained from resins with distinct M_w. However, no work has been published regarding the effects of annealing and stretching on the performance of porous PP membranes. In this work a detailed structural and morphological characterization of the membranes is performed. In addition, the influence of temperature and applied extension during annealing and stretching steps are examined.

5.2 Experimental

5.2.1 Materials

Two commercial linear polypropylenes (PP28, PP08) were selected. Both PPs were supplied by ExxonMobil Company and had MFR values of 2.8 g/10min (under ASTM conditions of 230 °C and 2.16 kg) and 0.8 g/10min, respectively. The main characteristics of the resins are shown in Table 5.1. The molecular weight of the linear PPs was evaluated using the relation between the zero-shear viscosity and the molecular weight [11]. The melting point, T_m, and the crystallization temperature, T_c, of the resins were obtained using differential scanning calorimetry. For the rheological characterization, blends containing 2, 5, 10, 30, 50, and 70 wt% PP08 were prepared using a twin screw extruder (Leistritz Model ZSE 18HP co-rotating twin screw extruder) followed by water cooling and pelletizing. The temperature profile along the barrel was set at 160/180/190/200/200/200/200 °C. The extrusion was carried out at 80 rpm. During

blending, 3000 ppm of a stabilizer, Irganox B225, was added to avoid thermal degradation of the polymers. To make sure that all samples have the same thermal and mechanical history, unblended components were extruded under the same conditions.

Table 5.1. Main characteristics of neat polymers.

Resin code	Company	MFR 230 °C / 2.16 kg	Nomenclature	η_0 (Pa.s)	M_w (kg/mol)	T_m (°C)	T_c (°C)
PP4712	ExxonMobil	2.8	PP28	12500	543	160	115
PP5341	ExxonMobil	0.8	PP08	41600	772	160	117

5.2.2 Rheological characterization

Dynamic rheological measurements were carried out using a Rheometric Scientific SR5000 stress controlled rheometer with a parallel plate geometry of 25 mm diameter and a gap equal to 1.5 mm at the temperature of 190 °C under nitrogen atmosphere. Molded discs of 2 mm thick and 25 mm in diameter were prepared using a hydraulic press at 190 °C. Time sweep test was first performed at a frequency of 0.628 rad/s for two hours. Material functions such as complex viscosity, elastic modulus, and weighted relaxation spectrum in the linear viscoelastic regime were determined in the frequency range from 0.01 to 500 rad/s. In order to obtain more accurate data, the frequency sweep test was carried out in four sequences while the amount of applied stress in each sequence was determined by a stress sweep test.

5.2.3 Film and membrane preparation

The precursor films from PP28 and blends containing 2, 5, 10, and 20 wt% PP08 were prepared by extrusion using a slit die of 1.9 mm thick and 200 mm width. An air knife was mounted on the die to supply air to the film surface right at the exit of the die. The main parameters were die temperature, cooling rate, and draw ratio (ratio of the roll speed to the die exit velocity) [7]. In this study the die temperature was set at 220 °C and the maximum speed of the fan was applied, thus the only variable was the draw ratio. The film samples were prepared under draw ratios of 70, 80, and 90.

For membrane preparation, precursor films having a thickness, width and length of 35 μm, 46 mm and 64 mm, respectively, were used. Both annealing and stretching were performed using an Instron machine equipped with an environmental chamber. A drawing speed of 50 mm/min was applied during the cold and hot stretching steps.

5.2.4 Film and membrane characterization

Fourier transform infrared spectroscopy (FTIR): For FTIR measurements, a Nicolet Magna 860 FTIR instrument from Thermo Electron Corp. (DTGS detector, resolution 4 cm^{-1}, accumulation of 128 scans) was used. The measurement is based on the absorption of infrared light at certain frequencies corresponding to the vibration modes of atomic groups present within the molecule. In addition, if a specific vibration is attributed to a specific phase, the orientation within that phase can be determined [8]. If the films are oriented, the absorption of plane-polarized radiation by a vibration in two orthogonal

directions, specifically parallel and perpendicular to a reference axis (MD), should be unequal. The ratio of these two absorption values is defined as the dichroic ratio, D [12]:

$$D = \frac{A_{\parallel}}{A_{\perp}} \tag{5.1}$$

where $A_{\parallel}$ is the absorption parallel and $A_{\perp}$ is the absorption perpendicular to a specific reference axis. The Herman orientation function of this vibration is obtained according to [12]:

$$f = \frac{D-1}{D+2} \tag{5.2}$$

For polypropylenes, absorption at the wavelength of 998 cm^{-1} is attributed to the crystalline phase (c-axis) while absorption at the wavelength of 972 cm^{-1} is due to the contribution of both crystalline and amorphous phases. From the former absorption, the orientation of the crystalline phase, f_c, can be determined while from the latter, the average orientation function, f_{av}, is obtained. The orientation of the amorphous phase, f_{am}, can be calculated according to:

$$f_{av} = X_c f_c + (1 - X_c) f_{am} \tag{5.3}$$

where X_c is the degree of the crystallinity. Using FTIR, the global, crystalline and amorphous orientations can be determined.

X-ray diffraction: XRD measurement was carried out using a Bruker AXS X-ray goniometer equipped with a Hi-STAR two-dimensional area detector. The generator was set up at 40 kV and 40 mA and the copper Cu Kα radiation (λ=1.542 A°) was selected

using a graphite crystal monochromator. The sample to detector distance was fixed at 9.2 cm for wide angle diffraction and 28.2 cm for small angle x-ray scattering analysis. To get the maximum diffraction intensity several film layers were stacked together to obtain the total thickness of about 2 mm.

Wide angle X-ray diffraction (WAXD) is based on the diffraction of a monochromatic X-ray beam by the crystallographic planes (*hkl*) of the polymer crystalline phase. Using a pole figure accessory, the intensity of the diffracted radiation for a given *hkl* plane is measured as the sample is rotated through all possible spherical angles with respect to the beam. This gives the probability distribution of the orientation of the normal to *hkl* plane with respect to the directions of the sample.

The Herman orientation function is given by [7]:

$$f = \frac{(3\cos^2\phi - 1)}{2} \qquad (5.4)$$

where ϕ is the angle between the unit cell axes (*a*, *b*, and *c*) and reference axes. Details about the calculations can be found elsewhere [7].

The orientation factors from WAXD are mainly due to the crystalline part, therefore no information about the orientation of the amorphous phase can be obtained. Small angle X-ray scattering (SAXS) was utilized to estimate the long period distance between the lamellae.

Thermal analysis: Thermal properties of specimens were analyzed using a TA instrument differential scanning calorimeter (DSC) Q 1000. Samples were heated from 50 to 220 °C at a heating rate of 10 °C/ min.

BET measurement: To obtain the surface area and pore diameter of the membranes, a flowsorb Quantachrome instrument BET ASI-MP-9 was used. A nitrogen and helium gas mixture was continuously fed through the sample cell, which was kept at liquid nitrogen temperature. At different pressures, the total volume of nitrogen gas adsorbed on the surface was measured. The volume of gas needed to create an adsorbed monomolecular layer was calculated as follows [13]:

$$\frac{P}{P^{\circ}[v(1-\frac{P}{P^{\circ}})]} = \frac{1}{v_m c} + \frac{c-1}{v_m c}\frac{P}{P^{\circ}} \qquad (5.5)$$

where P is the experimental pressure, P^o is the saturation pressure, v is the volume of the adsorbate, v_m is the volume of gas required to form an absorbed monomolecular layer, and c is a constant. The procedure for estimating the surface area from Eq. 5.5 can be found elsewhere [14].

Mercury porosimetry: The average pore size, pore size distribution, and porosity of the membranes were also evaluated using a mercury porosimeter (PoreMaster PM33). After evacuation of the cell, it is filled by mercury and then pressure is applied to force mercury into the porous sample. The amount of intruded mercury is related to the pore size and porosity.

Water vapor transmission: The permeability to water vapor was measured via a MOCON PERMATRAN-W Model 101K at room temperature. It is composed of three chambers: an upper chamber containing the liquid water and separated from the center chamber by two porous films. Water vapor diffuses from the first film to fill the space between the films to reach 100% relative humidity (RH). The center chamber is separated from the lower one by the test film. The diffused vapor is swept away by N_2 gas to a RH sensor.

Mechanical analysis: Tensile tests were performed using an Instron 5500R machine equipped with a chamber for running tests at high temperature. The procedure used was based on the D638-02a ASTM standard.

Puncture resistance: Puncture tests were performed using a 10 N load cell of the Instron machine used for the tensile tests. A needle with 0.5 mm radius was used to pierce the samples. The film was held tight in the camping device with a central hole of 11.3 mm. The displacement of the film was recorded against the force (Newton) and the maximum force was reported as the puncture strength.

5.3 Results and discussion

5.3.1 Rheological characterization

The complex shear viscosities as a function of frequency for the neat PPs as well as for the blends are shown in Figure 5.1. The behavior is typical of linear polymer melts and the complex viscosity of the blends follows the log additivity rule as expected for

miscible components. This is shown in Figure 5.2 where the complex shear viscosities at different frequencies are plotted as a function of PP08 content. The logarithmic additivity rule is expressed as [15]:

$$\log \eta^*(\omega) = \phi_\beta \log(\eta^*(\omega))_1 + (1-\phi_\beta)\log(\eta^*(\omega))_2 \qquad (5.6)$$

where ϕ_β is the PP08 content. Adding a high molecular weight component (PP08) causes monotonic increases of the complex shear viscosity, which is due to the presence of the larger molecules of PP08. Good agreement with the logarithmic mixing rule can be observed for all samples, suggesting miscibility of both PP components.

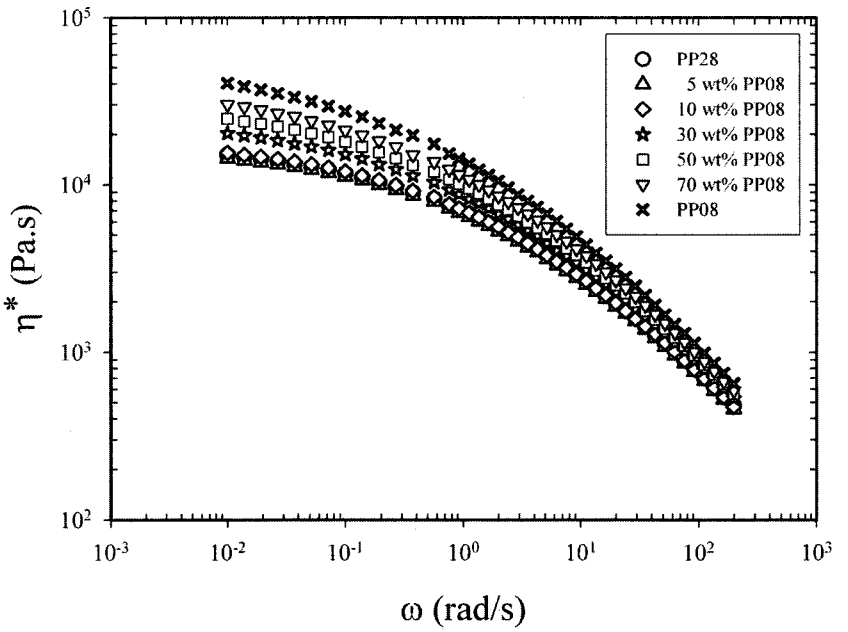

Fig. 5.1 Complex viscosity as a function of angular frequency; T=190 °C.

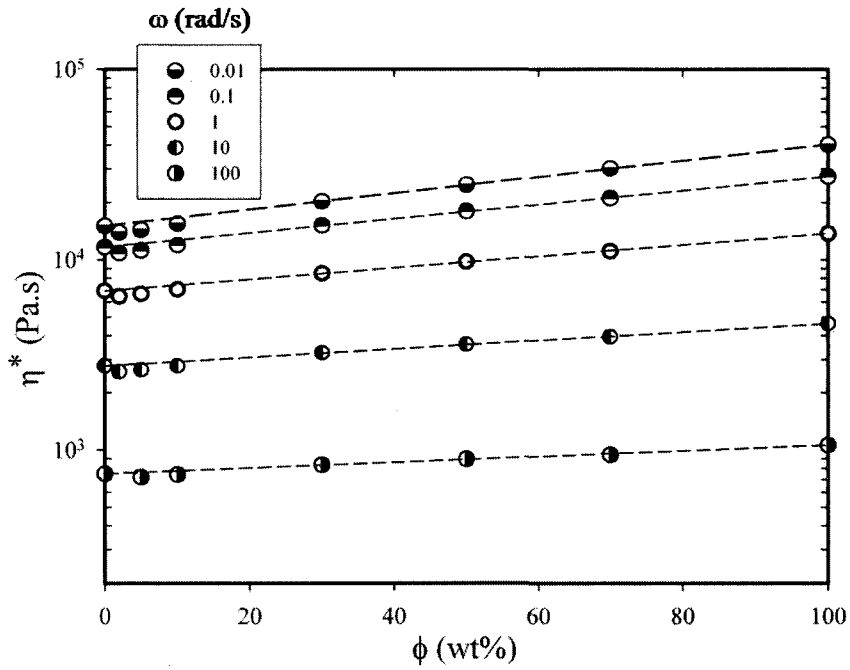

Fig. 5.2 Complex viscosity at different angular frequencies as a function of PP08 content; T=190 °C.

In order to quantitatively analyze the role of adding large chains on the melt relaxation of the blends, the weighted relaxation spectra evaluated from dynamic moduli (G', G'', ω) using the NLREG (non-linear regularization) software [16] are plotted in Figure 5.3 (the vertical dash lines represent the range of frequencies covered during the experiments). The addition of PP08 increases the number of entanglements, which retards the motion of the chains along their backbone, hence, the maximum in the curves is shifted to longer times and the spectrum shape becomes broader. Note that for the blends, the positions of the peaks are intermediate to those for the neat components suggesting again miscibility. The area under the curves is related to the zero shear viscosity and, as expected, increases with molecular weight.

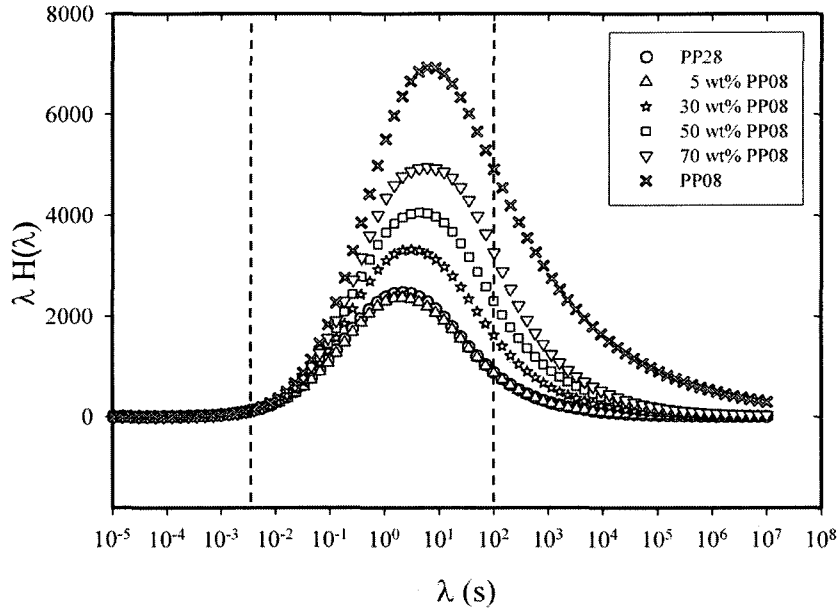

Fig. 5.3 Weighted relaxation spectra for the neat PPs as well as for all the blends; T=190 °C (the vertical dash lines represent the range of frequencies covered during the experiments).

The main mechanism of shear and/or elongation-induced crystallization is the propagation of the lamellae based on the fibrils or nuclei sites [7, 8]. As fibrils are mostly created from the long chains [4-6] and long chains have larger relaxation time (Figure 5.3), therefore, adding a high molecular weight component favors the preparation of precursor films with an adequate level of crystalline lamellae.

The relaxation behavior can also be shown in Cole-Cole plots, which are plot of η'' versus η' as illustrated in Figure 5.4. The semicircular shape of the Cole-Cole for the blends is another evidence of miscibility [17, 18].

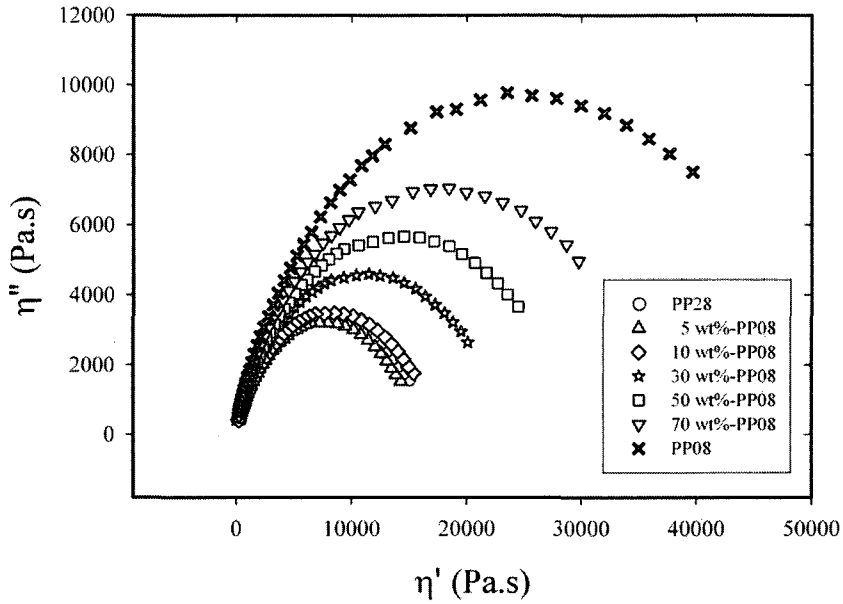

Fig. 5.4 Cole-Cole plots for the neat PPs as well as for all the blends; T=190 °C.

5.3.2 Film and membrane characterization

Draw ratios of 70, 80, and 90 were applied to the extruded films to investigate the role of the extension ratio on the orientation of the precursor films, as illustrated in Figure 5.5. It is obvious that for all the blends, as the draw ratio increases, the orientation function for the crystalline phase obtained from FTIR increases. At the low draw ratios, the lamellae are not well aligned perpendicular to the flow direction, but as draw ratio increases the lamellae align themselves perpendicular to the machine direction. In addition, it should be noted that the blend precursor films exhibit larger crystalline orientation values than the neat PP precursor. These results are in agreement with the findings of Sadeghi et al. [7] for polypropylene (PP) and Johnson and Wilkes [19] for

polyoxymethylene (POM), which showed that the orientation of the crystalline phase of precursor films increases as the molecular weight of the resins increases.

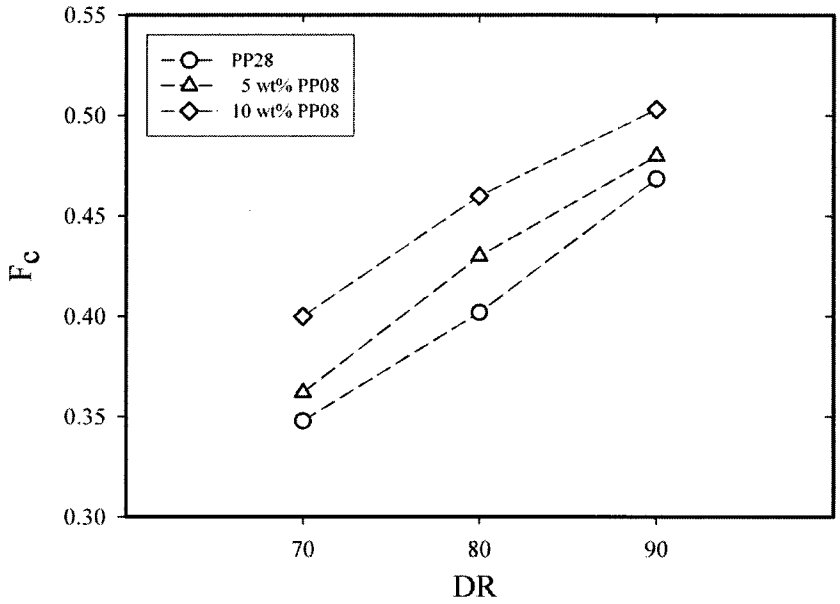

Fig. 5.5 Crystalline orientation function (obtained from FTIR) as a function of draw ratio for precursor films.

To determine the optimum annealing conditions that will lead to the largest amount of crystallinity, annealing at 140 °C without extension, at 140 °C under 5% extension, and at 120 °C without extension was carried out and the measured crystallinity values are plotted in Figure 5.6. It is found that annealing at 140 °C in the absence of strain results into the largest crystallinity content. Large reduction in crystallinity was seen when the samples were annealed under 5% extension with respect to the initial length. This reduction was more pronounced for the blends with a high level of PP08 (i.e. 10 wt% PP08 and 20 wt% PP08). Johnson and Wilkes [20] examined the lamellar structure of polyoxymethylene (POM) annealed films under different levels of extension. Their

experiments showed lamellar deformation for POM films annealed under tension levels larger than 3%. As a consequence, their POM microporous membranes annealed under no tension resulted in highly microporous films upon stretching. As will be shown later, 10 wt% PP08 blend contains more and smaller lamellae than the neat resin and blends of 2 and 5 wt% PP08. Therefore, more lamellae deformation for this blend during annealing under extension is expected, which explains the significant variation of crystallinity compared to the sample annealed without extension. Due to the larger number of nucleating sites for the samples having long chains, the enhancement of the crystallinity is apparent as the amount of PP08 increases.

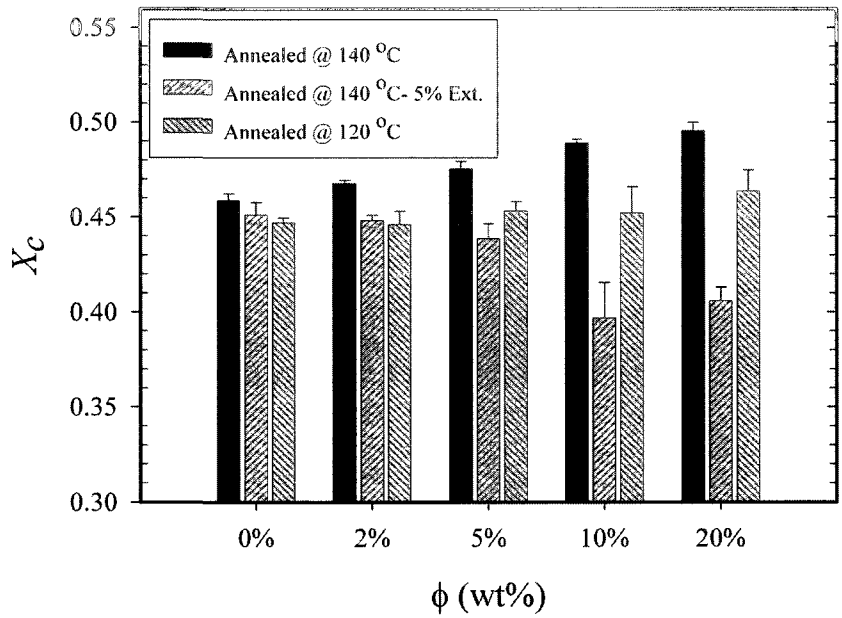

Fig. 5.6 Crystallinity of films at various annealing conditions. (a) annealing at 140 °C, (b) annealing at 140 °C under 5% extension, and (c) annealing at 120 °C. Annealing was performed for 30 min; DR=70, cold stretching of 35% followed by hot stretching of 55%.

Figure 5.7 presents the Herman orientation function of the crystalline phase as well as of the amorphous phase for the precursor and annealed films for all the blends. It is obvious that adding up to 10 wt% PP08 enhances the orientation of the both crystalline and amorphous phases. In addition, in comparison with the non-annealed films, significant improvement of the orientation is observed for the annealed specimens in the entire range of compositions. As annealing is performed at a temperature that is close to the onset of mobility in the crystalline structure (T_α), it is postulated that during annealing, the lamellae twist and orient perpendicular to the machine direction. Also, melting of small lamellae and their recrystallization with better orientation can occur [8]. The improvement of the orientation of the amorphous phase may be due to a slight movement of the molecules in the amorphous phase and formation of some organized regions. It has been reported that a slight tension during annealing enhances orientation [21], but in our case no dramatic improvement was observed.

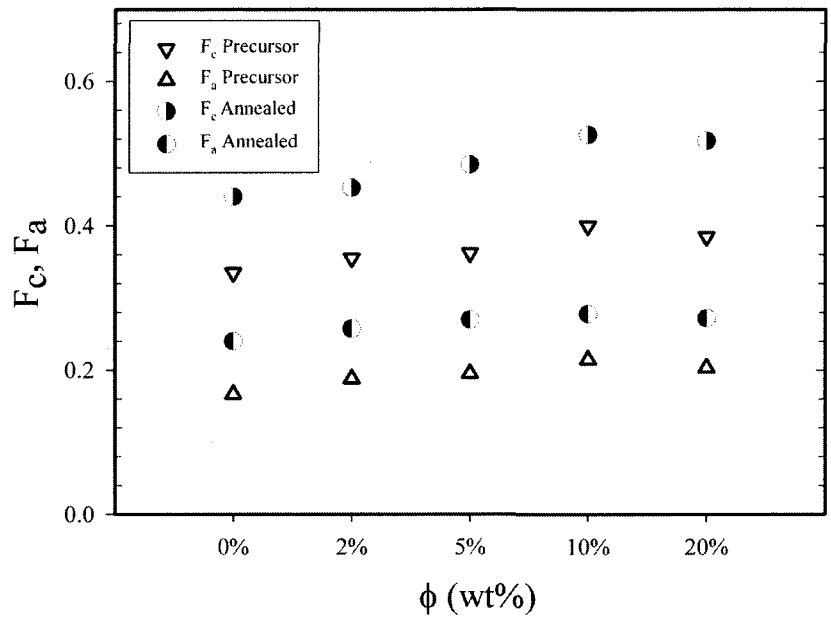

Fig. 5.7 Crystalline and amorphous orientation parameters as a function of PP08 content. Annealing was performed at 140 °C for 30 min; DR=70.

The effects of annealing and stretching on crystallinity were examined using differential scanning calorimetry (DSC) and the results are shown in Figure 5.8. Due to chain rearrangements at temperatures close to the melting point of the samples, annealing improves the crystalline content for all the blends. A slight change in crystallinity was detected after stretching. In the melting curves (not presented here), a small peak close to the annealing temperature was observed for the annealed samples, which is attributed to the bimodal lamellae thickness distribution. This was also observed by other authors [8, 22]. The effect of annealing on crystallization and orientation of the crystalline phase was also considered using WAXD, as shown in Figures 5.9a-c. The arcs are sharper and more concentrated in the center for annealed samples, suggesting more orientation. The orientation features as $\cos^2(\phi)$ of the

crystalline axes (i.e. *a*, *b*, and *c* (see Figure 5.15)) along MD, TD, and ND obtained from the Herman orientation function for the precursor, annealed, and stretched films are plotted in the triangular graph of Figure 5.9d. It is obvious that annealing causes movement of the *c*-axis of the crystals towards MD, while the *a*- and *b*-axes take a position closer to the TD-ND plane. This obviously shows that annealing improves the orientation of the films, in accordance with the FTIR data. Clearly stretching does not dramatically influence the orientation of the unit cell. During the stretching step, only lamellae separation is expected to occur and no changes in the crystalline blocks take place. The 2θ diffraction intensity graph of the samples is shown in Figure 5.9e. After deconvolution of the peaks and from the area under the curves, the crystallinity of the samples was calculated and similarly to the DSC results it was found that annealing improves crystallinity dramatically. However, the crystallinity obtained from WAXD was slightly larger than that obtained using DSC.

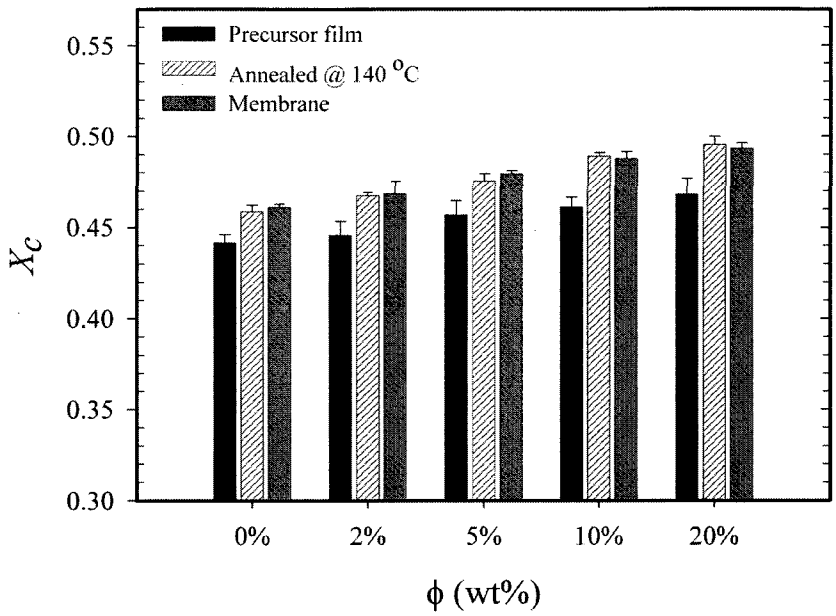

Fig. 5.8 Crystallinity of precursor films, annealed films, and membranes as a function of PP08 content. Annealing was carried out at 140 °C for 30 min; DR=70, cold stretching of 35% followed by hot stretching of 55%.

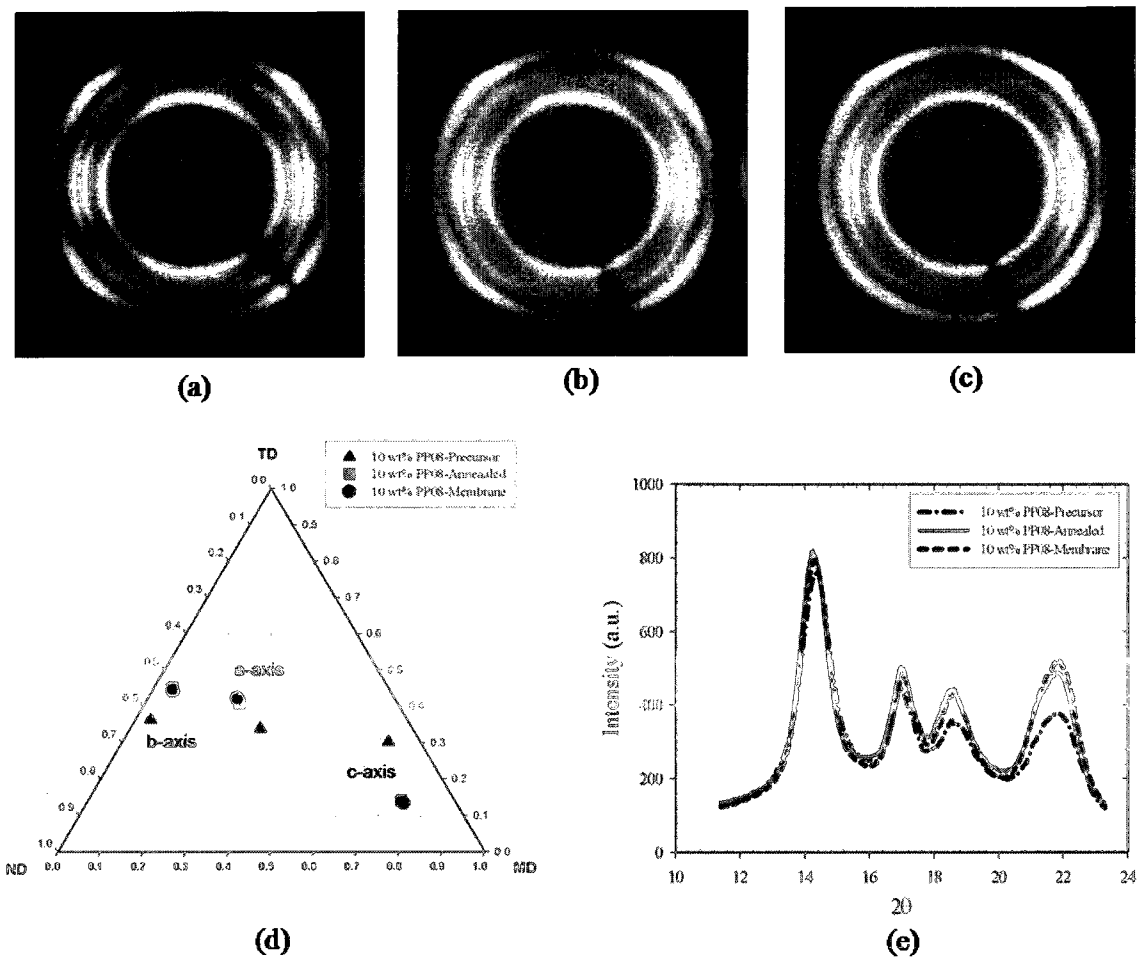

Fig. 5.9 WAXD patterns of 10 wt% PP08 blend for (a) precursor film, (b) annealed sample, (c) membrane, (d) orientation features as $\cos^2(\phi)$ of the crystals along MD, TD, and ND, and (e) diffraction spectrum with integration through the circles. Annealing was performed at 140 °C for 30 min; DR=70, cold stretching of 35% followed by hot stretching of 55%.

SAXS measurements were performed to examine the role of annealing and stretching on the lamellae spacing. The long period distance, L_p, was estimated from the position of the intensity maxima, as demonstrated in Figure 5.10 ($L_p=2/q_{max}$ where q is the intensity vector, $q=4\pi\sin\theta/\lambda$,). Annealing shifts the peaks to lower values, indicating an increase of the long spacing. Long spacing results of the precursor, annealed, and

stretched films for the blend containing 10 wt% PP08 are also reported in Figure 5.10. The value of L_p for the annealed film is much larger than that for the precursor film (L_p= 68 nm compared to 102 nm). As no extension was applied during annealing, this increase is attributed to the increase of lamellae thickness. In contrast to WAXD results, a significant effect of stretching on SAXS intensity profile is observed. As mentioned above, SAXS can detect the distance between the lamellae, and during stretching the lamellae are separated and pores are created, so dramatic influence of stretching is observed in the SAXS patterns.

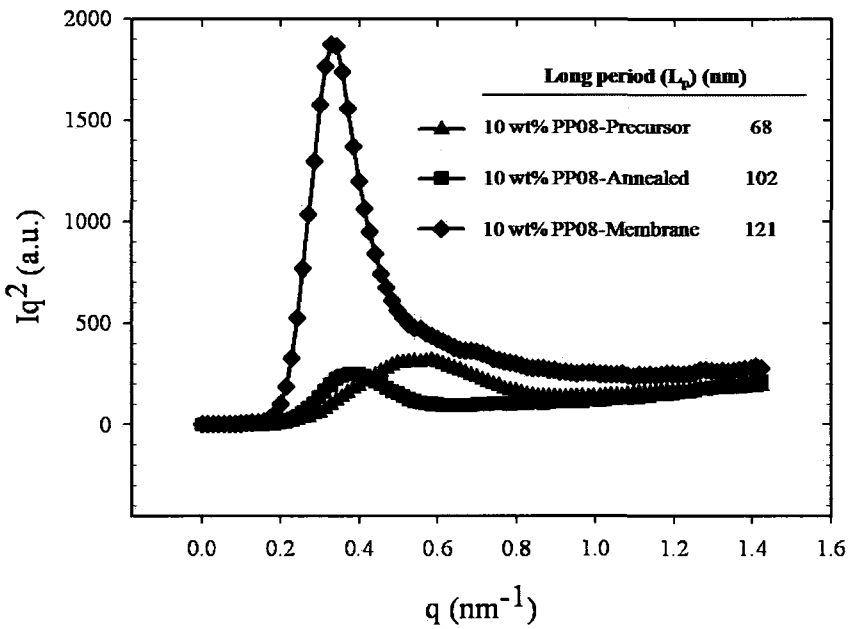

Fig. 5.10 SAXS intensity profiles for precursor, annealed, and stretched 10 wt% PP08 films. Annealing was performed at 140 °C for 30 min; DR=70, cold stretching of 35% followed by hot stretching of 55%.

Figure 5.11 shows the 2D SAXS patterns for the PP28 and 10 wt% PP08 blend films. The equatorial streak in the SAXS patterns is attributed to the formation of the

shish, while meridian maxima are attributed to the lamellae or kebabs [3]. Looking at the meridian intensity, the formation of more lamellae for the blend containing 10 wt% PP08 is evident.

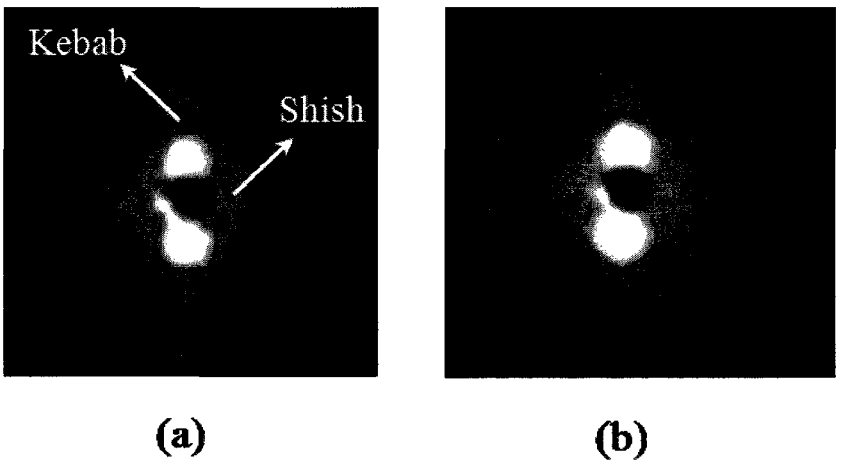

Fig. 5.11 SAXS patterns of precursor films. a) PP28 and b) 10 wt% PP08; DR=7.0.

It has been shown that annealing significantly influences the tensile response of films [7]. According to Sadeghi et al. [7], due to the planar morphology of the annealed sample, the rupture along the MD for the annealed film occurs at much smaller strain than for the non-annealed film. Puncture tests were performed to investigate the effects of annealing on the mechanical properties of the samples along the ND, and the results are presented in Figure 5.12. Each point is an average of over 10 tests. No significant changes were detected when PP08 was added. However, due to the thicker lamellae for the annealed samples, a pronounced increase of the maximum piercing force was observed for the annealed films compared to the precursor ones.

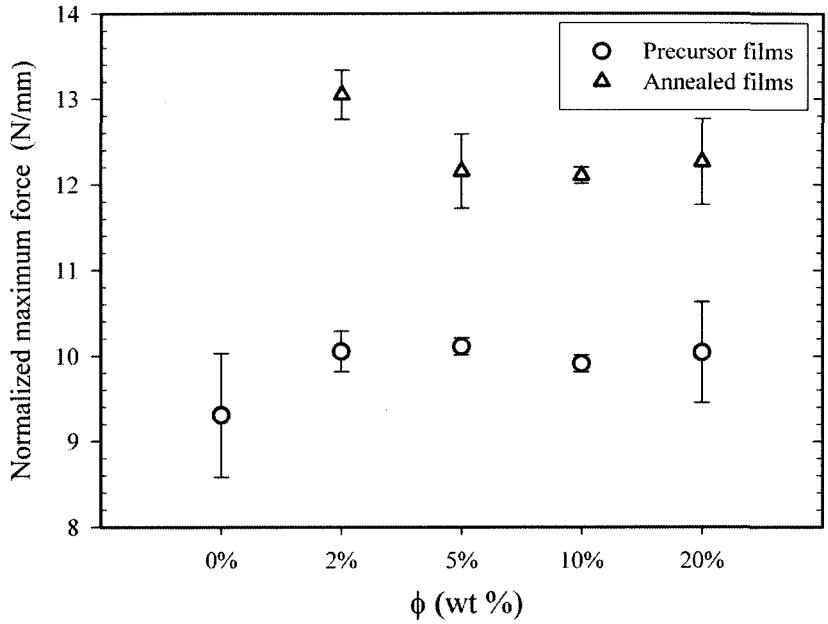

Fig. 5.12 Normalized maximum force for piercing as a function of PP08 content. Annealing was performed at 140 °C for 30 min; DR=70 and strain rate=25 mm/min.

The effect of blending on the mechanical properties of precursor films along MD and TD is illustrated in Figures 5.13 and 5.14, respectively. Figure 5.13 shows that blending reduces the elongation at break for the precursor films along the MD, except for the 5 wt% PP08 sample that shows a peak. The reason for the peak in the elongation at break for the 5 wt% PP08 is unclear at present. The following decrease in the elongation at break for the precursor films containing more PP08 is possibly due to the more orientation of the amorphous and crystalline phases for these samples (see Figure 5.7). The tie chains between lamellae are more oriented and more fibrils are expected as the level of PP08 increases. It is well known that better orientation along MD results in less deformation at break. For the transverse direction, a reduction of the maximum

stress and amount of elongation at break are also observed (Figure 5.14). This can be explained by the larger number of fibrils and smaller lamellae for the blend films.

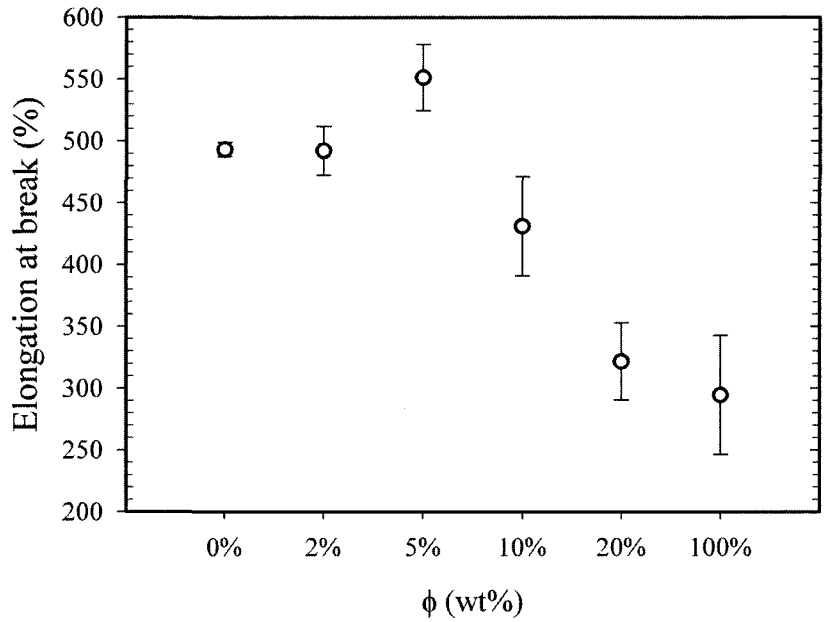

Fig. 5.13 Elongation at break for precursor films along the MD as a function of PP08 content; DR=70 and strain rate=25 mm/min.

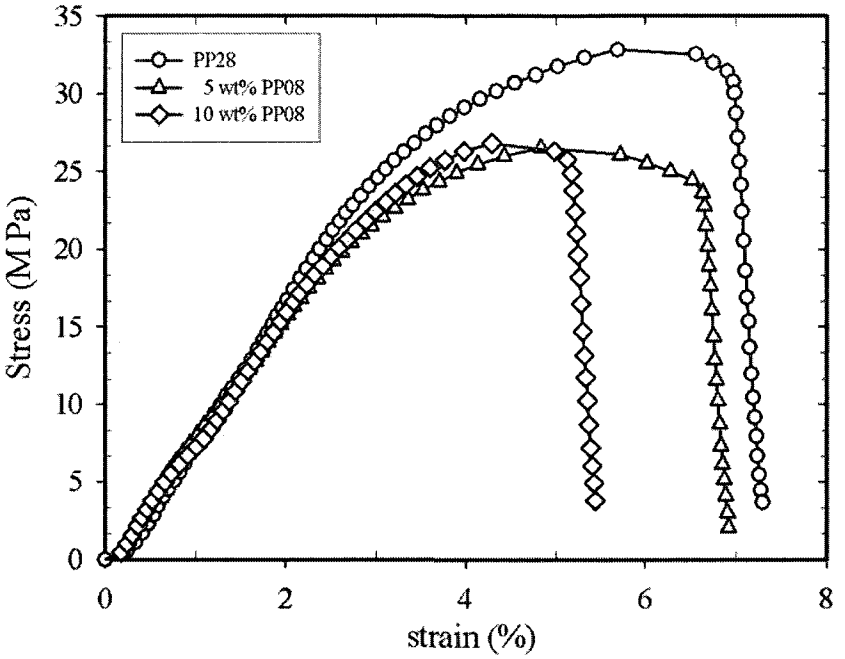

Fig. 5.14 Stress-strain curves along TD for precursor films of PP28 and blends; DR=70 and strain rate=25 mm/min.

To control the final structure of the produced membranes, obtaining a precursor film with the adequate orientation and alignment of the crystal lamellae is needed. The WAXD measurements were performed to consider the influence of blending on the level of orientation, as illustrated in Figure 5.15. The first and second rings of the pole figures show the patterns for the 110 and 040 crystalline planes, respectively [23]. The normal to the 110 plane is the bisector of the *a* and *b* axes and 040 is along the *b*-axis of the unit crystal cells [10]. More intense arcs in the meridian and equatorial zones are apparent for the blend sample, indicating greater orientation for the crystal lamellae [23].

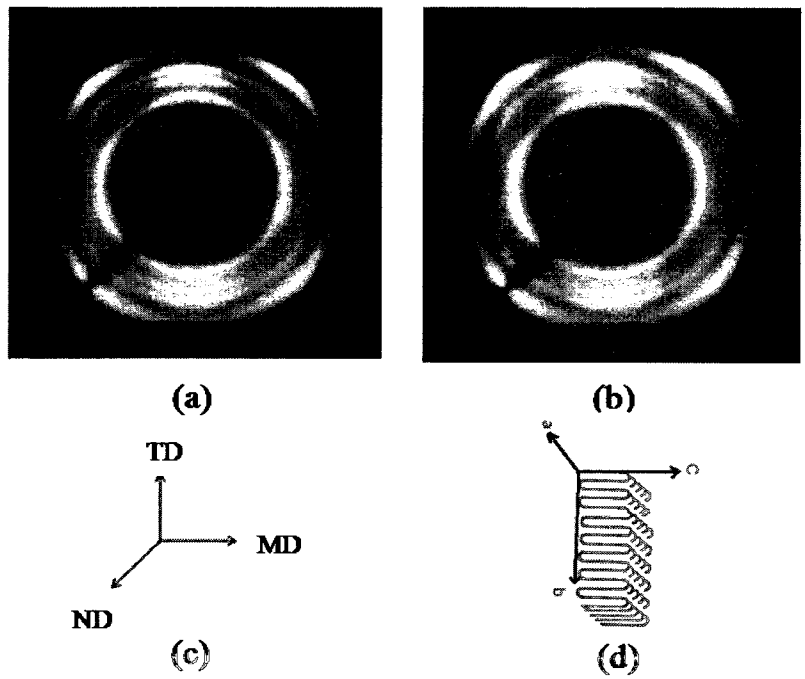

Fig. 5.15 WAXD patterns of the annealed films. a) PP28, b) 10 wt% PP08 blend, (c, d) film production axes and crystal block coordinates, respectively. Annealing was performed at 140 °C for 30 min; DR=70.

Figure 5.16 presents SEM micrographs of the surface and cross-section of the fabricated membranes for PP28 and blends containing 5 wt% PP08 and 10 wt% PP08. Figure 5.16a1 exhibits very thick lamellae and a small amount of pores for PP28 (i.e. low molecular weight component). However, as PP08 (i.e. high molecular weight component) is added, the number of pores increases and more uniform pore size and a better morphology is observed as well (Figures 5.16b1 and 5.16c1). This behavior can be explained as follows. As the content of the high molecular weight component increases, the number of fibrils or nuclei sites increases resulting in smaller lamellae and more pores. In addition, as was shown in Figure 5.3, the long chains have longer relaxation time; this increases the probability for the formation of lamellae by the low

molecular weight chains on the extended fibrils. It should be noted that the surface SEM micrographs of the porous membranes reveal greater lamellae orientation for the blend samples, confirming the WAXD results. Yu [21] investigated the lamellar structure of PE films blown with low and high molecular weight resins. Both polyethylenes exhibited a planar lamellar morphology, but the high M_w PE showed extended-chain nuclei, while the low M_w film possessed no evident extended-chain nuclei. As a result, the lateral lamellae dimensions were greater for the low M_w PE. Their findings are in line with our results shown in Figure 5.16.

The neat PP28 membrane contains thicker lamellae in the precursor films and has lower orientation yielding in a difficult lamellae separation and less interconnectivity (Figure 5.16a2). More pores and thinner lamellae for the 10 wt% PP08 blend membrane lead to a better interconnectivity of the pores (Figure 5.16c2). In addition, the membrane tortuosity, which is defined as the length of the average pore to the membrane thickness [24], seems to be less for the 10 wt% PP08 blend membrane than for the PP28 membrane. When SEM micrographs of the surface of the cold and hot stretched films were compared (SEM micrographs of the cold stretched films are not shown), the number of pores was found to be larger for the hot stretched samples. This confirms the findings of Sadeghi et al. [8] and it was explained by the melting of some lamellae and their recrystallization in the form of interconnected bridges during the hot stretching step.

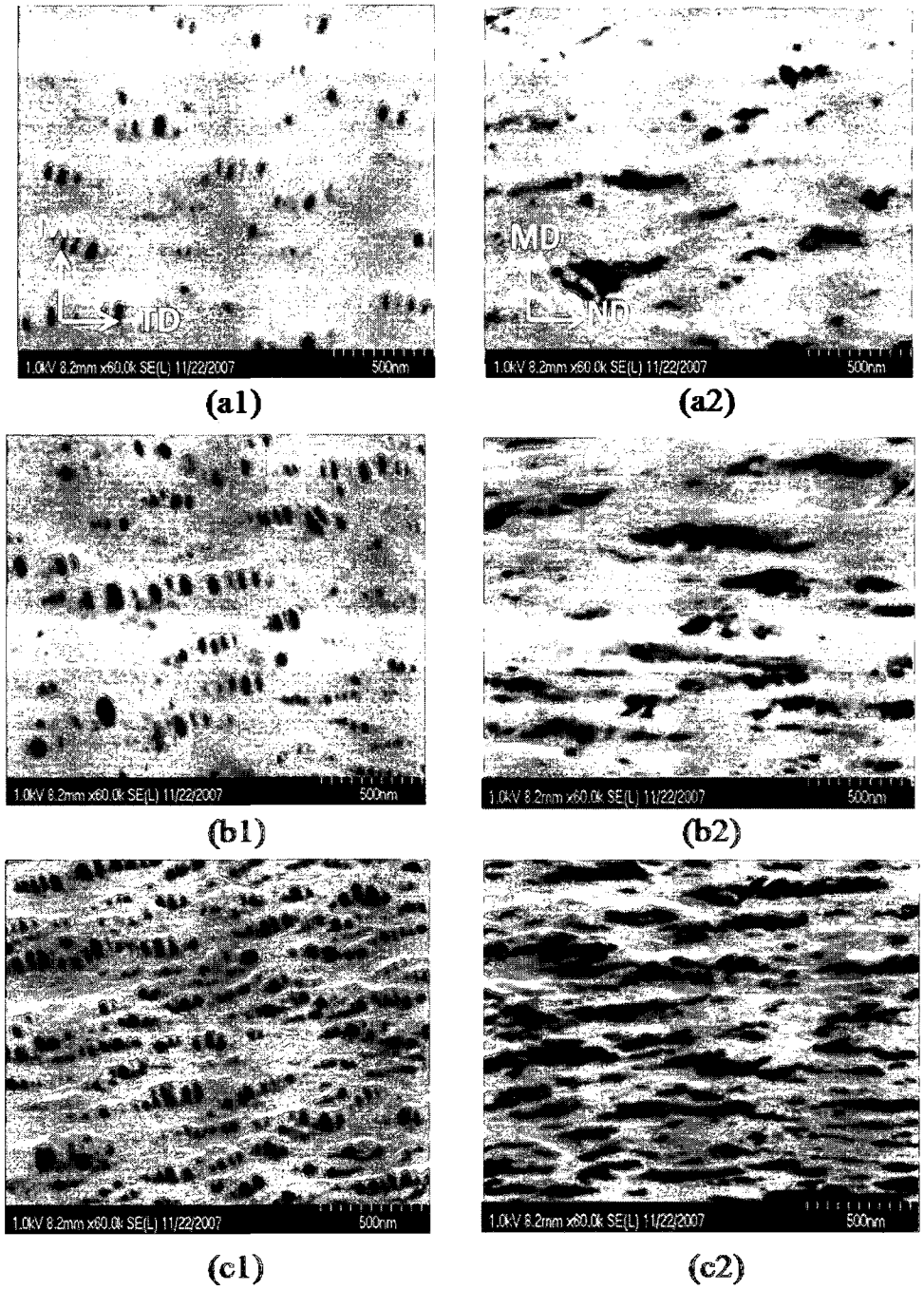

Fig. 5.16 SEM micrographs of the surface (left images) and cross-section (right images) of the microporous membranes. a) PP28, b) 5 wt% PP08 blend, and c) 10 wt% PP08 blend; DR=70, cold stretching of 35%, followed by hot stretching of 55%.

Key properties for membranes made from blends and their neat component are reported in Table 5.2. The membranes containing 5 wt% PP08 and 10 wt% PP08 exhibit pore densities about twice and four times that of the PP28 membrane, respectively. The PP08 microporous membrane shows pore density much lower than the 10 wt% PP08 membrane. The table also compares the results on specific surface area and average pore size of the membranes determined by BET and mercury porosimetry. The pore diameters obtained from BET and mercury porosimetry are almost identical. The specific surface area varies from 5.9 to 26.2 m^2/g depending on the PP08 content. As the 10 wt% PP08 blend microporous membranes has smaller diameter pores the larger value for the specific surface area is due to its larger pore density. An average pore diameter of 0.12 μm was determined for the PP28, 5 wt% PP28 and 10 wt% PP28 membranes. It should be noted that the neat PP08 microporous membrane shows a much lower surface area but larger pores compared to the 10 wt% PP08 microporous membrane and the reason for these is discussed in the following paragraph.

Table 5.2. Properties of microporous membranes (28 μm thick). Annealing was performed at 140 °C for 30 min; DR=70, cold stretching of 35% followed by hot stretching of 55% (values are averaged over 5 tests for each sample).

	Pore density	Specific surface area (m^2/g)	Pore diameter (μm)		Water vapor transmission rate (WVTR)	Young modulus
	(number of pores /square micron)	BET technique	BET technique	Mercury porosimetry	(g/m^2.day) (±10% error)	(GPa)
PP28	19	5.9	0.13	0.11	3200	0.92
5 wt% PP08	37	13.9	0.12	0.11	5300	1.01
10 wt% PP08	77	26.2	0.11	0.12	9800	1.05
PP08	45	14.3	0.21	0.23	16700	1.10

Table 5.2 also presents the water vapor transmission rates for the obtained microporous membranes. The permeability increased by a factor of 3 when 10 wt% PP08 was added to PP28. The addition of a high molecular weight component enhances the permeability, which is attributed to more pores, higher porosity, and better interconnection between the pores for the blend samples containing up to 10 wt% PP08. No significant increase of permeability was observed by further addition of PP08 except for the neat PP08 microporous membrane. In the blends, adding of more than 10 wt% PP08 possibly destroys the lamellar morphology, resulting in no changes or even lower permeability. Microporous membranes made of the neat PP08 showed a fibrillar structure with smaller number of lamellae (not presented here) than the 10 wt% PP08 microporous blend. This was due to the presence of larger number of long chains in PP08. Although the pore density of the PP08 porous membrane is much smaller than for the 10 wt% PP08 membrane, its pores are much larger leading to a better pore interconnection and larger WVTR. Although the permeability of the neat PP08 membrane was larger than that of all blend membranes, the objective of this work as mentioned earlier is to control the performances of microporous membranes using polymer blends.

Also as shown by Table 5.2, the Young modulus of the membranes slightly increases as the amount of the high M_w PP increases (Table 5.2). This can be explained by the better orientation of the lamellae for the blend films compared to the neat PP28.

Figure 5.17 reports the pore size distribution for the microporous neat PP and membranes containing 5 wt% and 10 wt% PP08. It is obvious that blending does not dramatically influence the peak positions in the pore size distribution curves and all the three samples reveal peaks around 0.11 μm. However, adding PP08 significantly enhances the area under curves, indicating porosity increases. Porosity values of 30, 35, and 44 % were evaluated for the PP28, 5 wt% blend, and 10 wt% blend membranes, respectively. The lower porosity of the neat PP membrane is attributed to its thicker lamellae and, consequently, more resistant to lamellae separation. An improvement of porosity for a blend of 2 wt% long-chain branched polypropylene (LCB-PP) and a linear polypropylene (L-PP) was also reported by Sadeghi et al. [10]. This was explained by a better orientation of the crystal blocks for the blend sample.

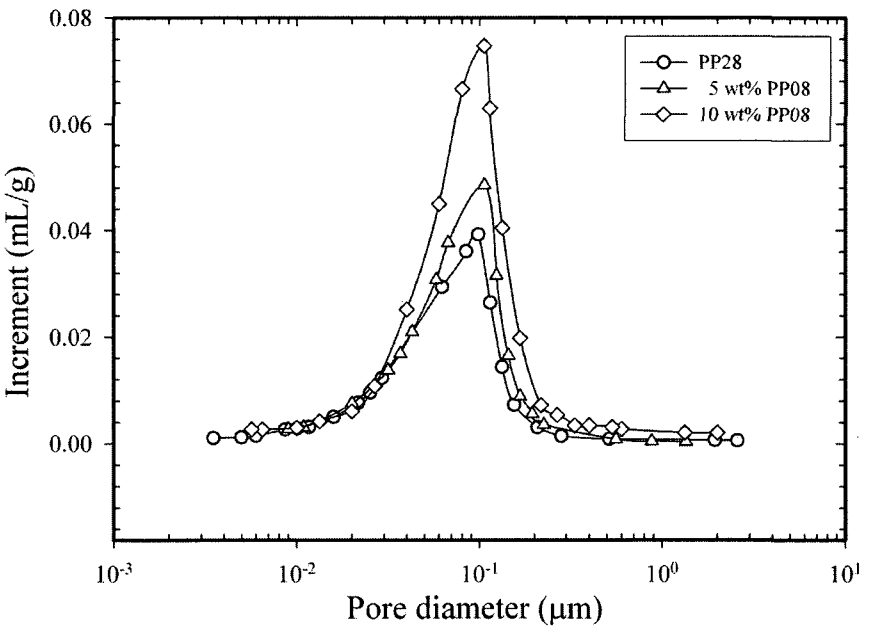

Fig. 5.17 Pore size distribution for microporous PP28, 5 wt% blend, and 10 wt % blend membranes; DR=70, cold stretching of 35% followed by hot stretching of 55%.

In the preparation of porous membranes using the stretching technique, voids are nucleated by cold stretching and enlarged by subsequent hot stretching [1,2]. According to Johnson [2], the micro void morphologies produced via this method are a consequence of inter lamellar separation, which takes place at temperatures above T_g of the specific semi crystalline polymer. This is in contrast to amorphous polymers which reportedly form voids (i.e. crazes, this process is termed crazing) upon deformation at temperatures below their respective T_g. Sadeghi et al. [8] found that the pores size of the cold stretched films obtained from the PP resins with distinct M_w did not significantly vary. However, a difference in the lamellae thickness was observed. To find the optimum cold stretching conditions, cold drawing was carried out at 25 °C and 45 °C and under predetermined amounts of extension while the amount of hot stretching was kept constant. Figure 5.18 reports the water vapor transmission rate (WVTR) normalized (multiplied) by the membrane thickness as a function of the applied extension for 10 wt% PP08 porous membranes. It is obvious that 20% extension during cold stretching was not enough to initiate pores formation. However, a maximum was observed when 30% extension was applied while further stretching reduced the normalized WVTR. It is believed that the high level of extension during cold stretching causes the fibrils to get closer to each other, resulting in the collapse of the pores. Chu and Kimura [25] investigated the effects of stretching on porosity and permeability of microporous polypropylene films prepared by biaxial stretching. In accordance with our results, their findings showed that porosity and permeability of the drawn films increased as the

stretching ratio increased up to an optimum value while further stretching resulted in their reduction. This was explained by pores collapse and closely packed structure due to fibril propagation at large draw ratios. In our case, it was also found that cold stretching at 25 °C yields larger permeability values.

Similar experiments were performed to investigate the influence of hot stretching. In contrast to cold stretching, no maximum was observed when the films were stretched to different levels (Figure 5.19). As mentioned, the pores created in cold stretching are enlarged during the hot stretching step. More flexibility of lamellae at high temperatures can be a reason for the increase of pore size with increasing draw ratio. However, hot stretching at 120 °C yields much larger WVTR values in comparison to stretching at 140 °C.

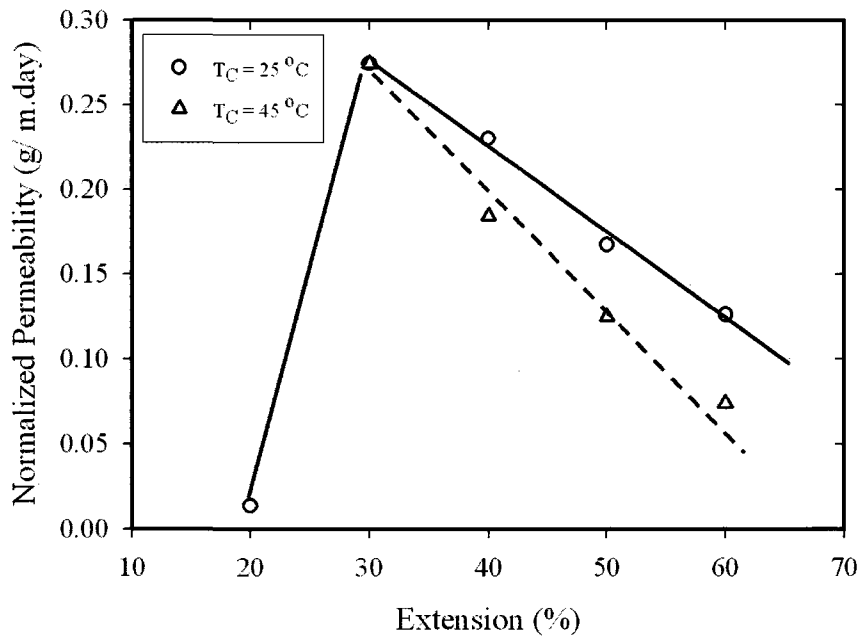

Fig. 5.18 Normalized water vapor permeability for the 10 wt% PP08 blend membrane as a function of extension during cold stretching at temperatures of 25 °C and 45 °C; DR=70, hot stretching of 55%, and draw speed=50 mm/min.

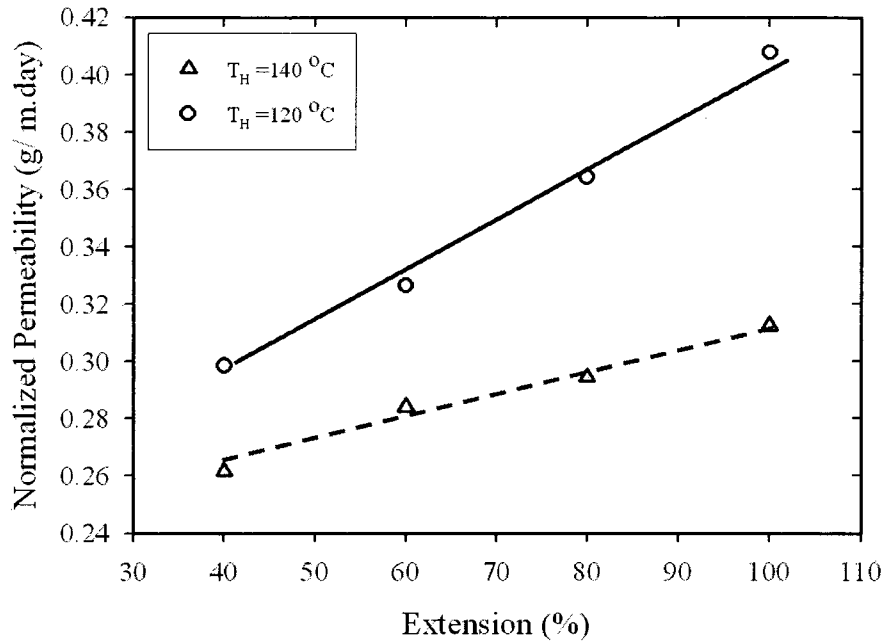

Fig. 5.19 Normalized water vapor permeability for the 10 wt% PP08 blend membrane as a function of extension during hot stretching at temperatures of 140 °C and 120 °C; DR=70, cold stretching of 35%, and draw speed=50 mm/min.

5.4 Conclusions

In this work, we have investigated the structure and performances of microporous membranes made from blends of linear low and high molecular weight PPs. In addition, the influence of annealing conditions on the crystallinity and stretching variables on the water vapor transmission rate (WVTR) were examined. Our findings can be summarized as follows:

- Good agreement with the logarithmic mixing rule of the complex viscosity was observed for all the blends suggesting miscibility of the both PP components.

- Annealing at 140 °C without extension contributed significantly to the crystalline phase perfection. In addition, compared to films annealed without extension, annealing under small amount of extension resulted in a significant reduction of crystallinity.
- SEM micrographs of the surface of membranes showed more uniform pores and a better distribution as the amount of the high molecular weight species increased.
- More interconnectivity of the pores was observed when the level of high M_w PP increased. This was explained by a larger number of pores and thinner lamellae for the blend membranes.
- By increasing the applied extension during hot stretching, water vapor transmission rate rose while for cold stretching the effect was inversed.

Using the puncture test, it was shown that addition of high molecular weight species does not have dramatic influence on the mechanical properties of precursor films along ND. However, tensile tests revealed a slight reduction of the mechanical properties along MD and TD.

5.5 Acknowledgment

Financial support from NSERC (Natural Science and Engineering Research Council of Canada) and from FQRNT (Fonds Québécois de Recherche en Nature et Technologies) is gratefully acknowledged.

5.6 References

[1] F. Sadeghi, Developing of microporous polypropylene by stretching, Ph.D thesis, Ecole Polytechnique, Montreal, 2007.

[2] M.B. Johnson, Investigations of the processing-structure-property relationship of selected semi crystalline polymers, Ph.D thesis, Virginia Polytechnic Institute and State University, 2000.

[3] P.K. Agarwal, R.H. Somani, W. Weng, A. Mehta, L. Yang, S. Ran, L. Liu, B. Hsiao, Shear-induced crystallization in novel long chain branched polypropylenes by in situ rheo-SAXS and –WAXD, Macromolecules 36 (2003) 5226.

[4] R.H. Somani, B.S. Hsiao, A. Nogales, Structure development during shear flow induced crystallization of i-PP: in situ wide-angle X-ray diffraction study, Macromolecules 33 (2000) 9385.

[5] R.H. Somani, L. Yang, B.S. Hsiao, Effects of molecular weight species on shear-induced orientation and crystallization of isotactic polypropylene, Polymer 47 (2006) 5657.

[6] M. Seki, D.W. Thurman, P.J. Oberhauser, J.A. Kornfield, Shear-mediated crystallization of isotactic polypropylene: the role of long chain-long chain overlap, Macromolecules 35 (2002) 2583.

[7] F. Sadeghi, A. Ajji, P.J. Carreau, Orientation analysis of row nucleated lamellar structure of polypropylene obtained from cast film, Polym. Eng. Sci. 47 (2007) 1170.

[8] F. Sadeghi, A. Ajji, P.J. Carreau, Analysis of microporous membranes obtained from polypropylene films by stretching, J. Membr. Sci. 292 (2007) 62.

[9] F. Sadeghi, A. Ajji, P.J. Carreau, Study of polypropylene morphology obtained from blown and cast film processes: initial morphology requirement for making porous membrane by stretching, J. Plastic Film Sheet. 21 (2005) 199.

[10] F. Sadeghi, A. Ajji, P.J. Carreau, Microporous membranes obtained from polypropylene blends with superior permeability properties, J. Polym. Sci., Polym. Phys. 46 (2008) 148.

[11] M. Fujiyama, H. Inata, Rheological properties of metallocene isotactic polypropylenes, J. Appl. Polym. Sci. 84 (2002) 2157.

[12] I.M. Ward, P.D. Coates, M.M. Dumoulin, Solid Phase Processing of Polymers, Hanser, 2000.

[13] S. Brunauer, P.H. Emmett, E. Teller, Adsorption of gases in multimolecular layers, J. Am. Chem. Soc. 60 (1938) 309.

[14] J. Li, B.D. Favis, Characterizing co-continuous high density polyethylene/polystyrene blends, Polymer 42 (2001) 5047.

[15] L.A. Utracki, B. Schlund, Linear low density polyethylene and their blends: Part 4 shear flow of LLDPE blends with LLDPE and LDPE, Polym. Eng. Sci. 27 (1987) 1512.

[16] J. Honerkamp, J. Weese, A non linear regularization method for the calculation of relaxation spectra, Rheol. Acta 32 (1993) 65.

[17] H. Kwang, D. Rana, K. Cho, J. Rhee, T. Woo, B.H. Lee, S. Choe, Binary blends of metallocene polyethylene with conventional polyolefins: rheological and morphological properties, Polym. Eng. Sci. 40 (2000) 1672.

[18] L.A. Utracki, in Two Phase Polymer Systems, Hanser Publisher, New York, 1991.

[19] M.B. Johnson, G.L. Wilkes, Microporous membranes of polyoxymethylene from a melt-extrusion process: (I) Effects of resin variables and extrusion conditions, J. Appl. Polym. Sci. 81 (2000) 2944.

[20] M.B. Johnson, G.L. Wilkes, Microporous membranes of polyoxymethylene from a melt-extrusion process: (II) Effects of thermal annealing and stretching on porosity, J. Appl. Polym. Sci. 84 (2002) 1762.

[21] T.H. Yu, Processing and structure-property behavior of microporous polyethylene: From resin to final film, PhD Thesis, Virginia Polytechnic Institute and State University, 1996.

[22] D. Ferrer-Balas, M.L.L. Maspoch, A.B. Martinez, O.O. Santana, Influence of annealing on the microstructural, tensile and fracture properties of polypropylene films, Polymer 42 (2001) 1697.

[23] L.E. Alexander, X-ray Diffraction Methods in Polymer Science, Wiley Inter science, New York, 1969.

[24] W.B. Baker, Membrane Technology and Applications, 2nd ed., John Wiley & Sons, 2004.

[25] F. Chu, Y. Kimura, Structure and gas permeability of microporous film prepared by biaxial drawing of the beta-form polypropylene, Polymer 37 (1996) 573.

CHAPTER 6

Effect of Processing on the Crystalline Orientation, Morphology, and Mechanical Properties of Polypropylene Cast Films and Microporous Membrane Formation[2]

Seyed H. Tabatabaei, Pierre J. Carreau, and Abdellah Ajji

CREPEC, Chemical Engineering Department, Ecole Polytechnique, C.P. 6079, Succ. Centre ville Montreal, QC, H3C 3A7 Canada

Abstract

Cast films of a high molecular weight linear polypropylene (L-PP) were prepared by extrusion followed by stretching using a chill roll. An air knife was employed to supply air to the film surface right at the exit of the die. The effects of air cooling conditions, chill roll temperature, and draw ratio on the crystalline orientation, morphology, mechanical and tear properties of the PP cast films were investigated. The crystallinity and crystal size distribution of the films were studied using differential scanning calorimetry (DSC). It was found that air blowing on the films contributed significantly to the uniformity of the lamellar structure. The orientation of crystalline and amorphous phases was measured using wide angle X-ray diffraction (WAXD) and Fourier

---

[2] Submitted to *Polymer*.

transform infrared (FTIR). The amount of lamellae formation and long period spacing were obtained via small angle X-ray scattering (SAXS). The results showed that air cooling and the cast roll temperature have a crucial role on the orientation and amount of lamellae formation of the cast films, which was also confirmed from scanning electron microscopy (SEM) images of the films. Tensile properties and tear resistance of the cast films in machine and transverse directions (MD and TD, respectively) were evaluated. Significant increases of the Young modulus, yield stress, tensile strength, and tensile toughness along MD and drastic decreases of elongation at break along TD were observed for films subjected to air blowing. Morphological pictograms are proposed to represent the molecular structure of the films obtained without and upon applying air cooling for different chill roll temperatures. Finally, microporous membranes were prepared from annealed and stretched films to illustrate the effect of the PP cast film microstructure on the morphology and permeability of membranes. The observations of SEM surface images and water vapor transmission rate of the membranes showed higher pore density, uniform pore size, and superior permeability for the ones obtained from the precursor films prepared under controlled air cooling.

6.1 Introduction

Among a wide range of resins, polypropylene (PP) is a well-known semicrystalline polymer and, in comparison with polyethylene (PE), PP has a higher melting point,

lower density, higher chemical resistance, and better mechanical properties, which make it useful for many industrial applications.

The crystalline phase orientation in semicrystalline polymers such as polypropylene enhances many of their properties particularly mechanical, impact, barrier, and optical properties [1]. Obtaining an oriented structure in PP is of great interest to many processes such as film blowing, fiber spinning, film casting, and etc. In these processes the polymer melt is subjected to shear (in the die) and elongational (at the die exit) flow and crystallize during or subsequent to the imposition of the flow.

It is well-known that strain under flow strongly enhances the crystallization kinetics and allows the formation of a lamellar structure instead of the spherulitic one. The effect of flow on crystallization is called flow-induced crystallization (FIC) while the flow can be shear, extensional or both [2]. FIC molecular models show that flow induces orientation of polymer chains, resulting in enhancement of the nucleation rate [2-4]. Under flow, two major types of crystallization can occur, depending on the magnitude of the stress [1]: low stress results in twisted lamellae, while high stress produces a shish-kebab structure in which the lamellae grow radially on the shish without twisting [1].

Similar to shear flow, it has also been reported that extensional flow promotes fibrillar like structure oriented in the flow direction that serves as nucleation for radial growth of chain-folded lamellae perpendicular to the stress direction [5].

The effects of material parameters on shear induced crystallization process for PP have been investigated using in-situ small angle X-ray scattering (SAXS) and/or wide

angle X-ray diffraction (WAXD) analyses [6-8]. Agarwal et al. [6] examined the influence of long chain branches on the stress induced crystallization. Adding a certain level of branches improved the orientation of the crystal blocks and the crystallization kinetics due to the longer relaxation time and the molecular structure. Somani et al. [7] followed the orientation development upon applying different shear rates. They found that, at a certain shear rate, only molecules with a chain length (molecular weight) above a critical value (critical orientation molecular weight, M_c) can form stable oriented row nuclei (shish). The shorter chains create lamellae over these nuclei sites. In another study, Somani et al. [8] compared the oriented microstructure under shear flow of isotactic polypropylene melts (PP-A and PP-B) with the same number average molecular weight but different molecular weight distribution (MWD). The amount of the high molecular weight species was larger in PP-B than in PP-A. Their results showed that the shish structure evolved much earlier for PP-B, which had more pronounced crystal orientation and faster crystallization kinetics. They concluded that even a small increase in the concentration of the high molecular weight chains led to a significant increase in the shish or nuclei site formation. In our recent study [9], addition of up to 10 wt% of a high molecular weight component to a low molecular weight one enhanced the formation of the row-nucleated structure probably due to an increase in the nucleating sites.

The crystallization behavior of semicrystalline polymers is significantly influenced by the process conditions. Under quiescent isothermal crystallization, the size of the

spherulites, the degree of crystallinity, and the kinetics depend on temperature, while in quiescent non-isothermal conditions, both temperature and cooling rate are important factors [2].

Numerous studies have focused on the structure of PE and PP blown films using various materials under different processing conditions. However, as far as we know no experimental study has been conducted on the cast film process with emphasis on the effect of cooling using a chill roll and/or air. Therefore, the main objective of this work is to elucidate the effect of air cooling, in addition to the other process conditions (i.e. chill roll temperature and draw ratio), on the flow-induced crystallization and orientation developed in PP cast films. We also report results on the tear properties and mechanical behavior of the cast films and the properties of the membranes produced from these films. This is the first effort to address this issue from a structural point of view.

6.2 Experimental

6.2.1 Material

A commercial linear polypropylene (PP5341) supplied by ExxonMobil Company was selected. It had a melt flow rate (MFR) value of 0.8 g/10min (under ASTM conditions of 230 ^{o}C and 2.16 kg) Its molecular weight was estimated from the relationship between the zero-shear viscosity and the molecular weight [10] and found to be around 772 kg/mol. The resin showed a polydispersity index (PDI) of 2.7, as measured using a GPC (Viscotek model 350) at 140 ^{o}C and 1,2,4-Trichlorobenzene (TCB) as a solvent. Its

melting point, T_m, and crystallization temperature, T_c, obtained from differential scanning calorimetry at a rate of 10 °C/min, were 161 °C and 118 °C, respectively.

6.2.2 Film and membrane preparation

The cast films were prepared using an industrial multilayer cast film unit from Davis Standard Company (Pawcatuck, CT) equipped with a 2.8 mm thick and 122 cm width slit die and two cooling drums. The extrusion was carried out at 220 °C and the distance between the die exit to the nip roll was 15 cm. The die temperature was set at 220 °C and draw ratios of 60, 75, and 90 were applied. An air knife with dimensions of 3 mm opening and 130 cm width was mounted close to the die to provide air to the film surface right at the exit of the die. The variables of interest were chill roll temperature, amount of air flow, and draw ratio. The films were produced under chill roll temperatures of 120, 110, 100, 80, 50, and 25 °C. For all the cast roll temperatures, the air cooling rates used were 0, 1.2, 7.0, and 12 L/s. These air cooling conditions are noted as: no air flow rate (N-AFR), low air flow rate (L-AFR), medium air flow rate (M-AFR), and high air flow rate (H-AFR), respectively.

For membrane fabrication, the precursor films with a thickness, width and length of 35 μm, 46, and 64 mm, respectively, were used. The films were first annealed at 140 °C for 30 min and then cold and hot stretched at 25 °C and 120 °C, respectively. Both annealing and stretching were performed using an Instron machine equipped with an environmental chamber. A drawing speed of 50 mm/min was applied during cold and

hot stretching steps. The details for the fabrication of the microporous membranes can be found elsewhere [9].

6.2.3 Film and membrane preparation

Fourier transform infrared spectroscopy (FTIR): For FTIR measurements, a Nicolet Magna 860 FTIR instrument from Thermo Electron Corp. (DTGS detector, resolution 2 cm^{-1}, accumulation of 128 scans) was used. The beam was polarized by means of a Spectra-Tech zinc selenide wire grid polarizer from Thermo Electron Corp. The measurement is based on the absorption of infrared light at certain frequencies corresponding to the vibration modes of atomic groups present within the molecule. In addition, if a specific vibration is attributed to a specific phase, the orientation within that phase can be determined [11]. If the films are oriented, the absorption of plane-polarized radiation by a vibration in two orthogonal directions, specifically parallel and perpendicular to a reference axis (MD), should be different. The ratio of these two absorption values is defined as the dichroic ratio, D [11]:

$$D = \frac{A_{\parallel}}{A_{\perp}} \qquad (6.1)$$

where $A_{\parallel}$ is the absorption parallel and $A_{\perp}$ is the absorption perpendicular to a specific reference axis. The Herman orientation function of this vibration is obtained according to [11]:

$$f = \frac{D-1}{D+2} \qquad (6.2)$$

For polypropylene, absorption at the wavenumber of 998 cm^{-1} is attributed to the crystalline phase (*c*-axis) while absorption at the wavenumber of 972 cm^{-1} is due to the contribution of both crystalline and amorphous phases. From the former absorption, the orientation of the crystalline phase, f_c, can be determined while from the latter, the average orientation function, f_{av}, is obtained. The orientation of the amorphous phase, f_{am}, can be calculated according to:

$$f_{av} = X_c f_c + (1 - X_c) f_{am} \qquad (6.3)$$

where X_c is the degree of the crystallinity. Using FTIR, the global, crystalline and amorphous orientations can be determined.

X-ray diffraction: XRD measurement was carried out using a Bruker AXS X-ray goniometer equipped with a Hi-STAR two-dimensional area detector. The generator was set up at 40 kV and 40 mA and the copper CuKα radiation (λ = 1.542 A°) was selected using a graphite crystal monochromator. The sample to detector distance was fixed at 9.2 cm for wide angle diffraction and 28.2 cm for small angle X-ray scattering analysis. To get the maximum diffraction intensity several film layers were stacked together to obtain the total thickness of about 2 mm.

Wide angle X-ray diffraction (WAXD) is based on the diffraction of a monochromatic X-ray beam by the crystallographic planes (*hkl*) of the polymer crystalline phase. Using a pole figure accessory, the intensity of the diffracted radiation for a given *hkl* plane is measured as the sample is rotated through all possible spherical

angles with respect to the beam. This gives the probability distribution of the orientation of the normal to *hkl* plane with respect to the directions of the sample.

The Herman orientation function of a crystalline axis is given by [12]:

$$f = \frac{(3\cos^2 \phi - 1)}{2} \qquad (6.4)$$

where ϕ is the angle between the unit cell axes (*a*, *b*, and *c*) and reference axes. Details about the calculations can be found elsewhere [12].

The orientation factors from WAXD are mainly due to the crystalline part, therefore no information about the orientation of the amorphous phase can be obtained. Small angle X-ray scattering (SAXS) was used to compare the level of the lamellae formation for the different samples and to estimate the long period between lamellae.

Thermal analysis: Thermal properties of specimens were analyzed using a TA instrument differential scanning calorimeter (DSC) Q 1000. The thermal behavior of films was obtained by heating from 50 to 220 °C at a heating rate of 10 °C/min. The reported crystallinity results were obtained using a heat of fusion of 209 J/g for fully crystalline polypropylene (PP) [13].

Mechanical and tear analysis: Tensile tests were performed using an Instron 5500R machine equipped with an environmental chamber for tests at high temperature. The procedure used was based on the D638-02a ASTM standard. A standard test method for the tear resistance of plastic films based on ASTM D1922 was used to obtain the MD and TD tear resistances. According to this standard, the work required in tearing is

measured by the loss of energy of the encoder, which measures the angular position of the pendulum during the tearing operation.

Morphology: To clearly observe the crystal arrangement of the PP cast films, an etching method was employed to remove the amorphous part. The PP films were dissolved in a 0.7% solution of potassium permanganate in a mixture of 35 volume percentage of orthophosphoric and 65 volume percentage of sulfuric acid. The potassium permanganate was slowly added to the sulfuric acid under rapid agitation. At the end of the reaction time, the samples were washed as described in Olley and Bassett [14].

A field emission scanning electron microscope (FESEM- Hitachi S4700) was employed for the observation of the etched films surfaces as well as microporous membranes. This microscope provides high resolution of 2.5 nm at a low accelerating voltage of 1 kV and high resolution of 1.5 nm at 15 kV with magnification from 20x to 500kx.

Water vapor transmission: The permeability to water vapor was measured via a MOCON PERMATRAN-W Model 101K at room temperature. It is composed of three chambers: an upper chamber containing liquid water and separated from the center chamber by two porous films. Water vapor diffuses from the first film to fill the space between the films to reach 100% relative humidity (*RH*). The center chamber is separated from the lower one by the test film. The diffused vapor is swept away by N_2 gas to a relative humidity (*RH*) sensor.

6.2.4 Rheological characterization

Dynamic rheological measurements were carried out using a Rheometric Scientific SR5000 stress controlled rheometer with a parallel plate geometry of 25 mm diameter and a gap equal to 1.5 mm at the temperatures of 180, 195, 210, and 225 °C under nitrogen atmosphere. Molded discs of 2 mm thick and 25 mm in diameter were prepared using a hydraulic press at 190 °C. Prior to frequency sweep tests, time sweep tests at a frequency of 0.628 rad/s and different temperatures were performed for two hours to check the thermal stability of the specimens. No degradation (less than 3% changes) was observed at test temperatures for the duration of the frequency sweep measurements. The dynamic data were obtained in the linear regime and used to evaluate the weighted relaxation spectra of the samples.

6.3 Results and discussion

We first present experimental data that clearly demonstrate the effects of process conditions, particularly air cooling and drum temperature, on crystallization, orientation of the amorphous and crystalline phases, and also tear and mechanical properties. Subsequently, two morphological pictograms are proposed to describe the observed experimental data and the reasons for these observations are discussed. Finally, the structure and properties of the microporous membranes obtained from the PP cast films having different microstructures are presented.

The effects of cast roll temperature (T_{cast}) and air cooling on thermal behavior of the films were examined using differential scanning calorimetry (DSC) and the results are shown in Figure 6.1. The top curves in this figure exhibit the thermograms of the films prepared at the chill roll temperatures of 100, 110, and 120 °C without air cooling. For these films, melting peaks around 163, 162, and 156 °C are observed, respectively. However, for the sample obtained at the drum temperature of 120 °C and no air flow rate condition (N-AFR) an additional peak at 144 °C is observed. Also for the sample obtained at the cast roll temperature of 110 °C a small shoulder at 156 °C is seen. These suggest the presence of a bimodal crystal (either lamellae or spherulite) size distribution (the WAXD measurements for these specimens showed no intensity peaks corresponding to the beta crystal form; therefore, the presence of this type of crystals is excluded). Both the additional peak and shoulder disappeared when T_{cast} was set at 100 °C or less (not shown). The thermograms of the films subjected to a small amount of air flow at different T_{cast} (bottom curves in Figure 6.1) show narrower melting curves without any additional peak or shoulder. These indicate a more uniform crystal size structure for the films prepared at L-AFR condition.

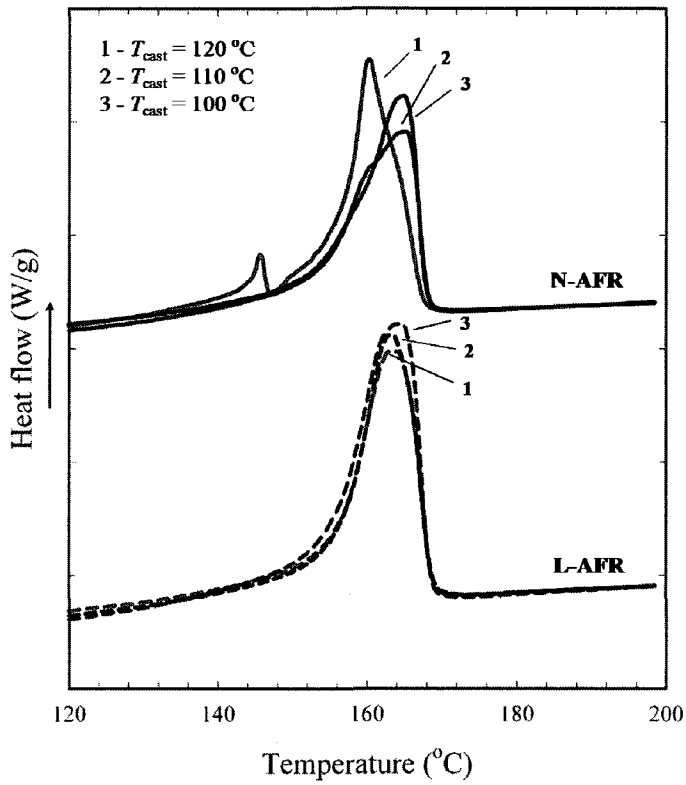

Fig. 6.1 DSC scans of cast films for roll temperatures of 120, 110, and 100 °C. The top curves are the thermograms of cast films produced under N-AFR condition whereas the bottom curves are the thermograms of films fabricated under L-AFR; DR=75.

The orientation and arrangement of the crystal lamellae in the cast films are key factors in controlling the final properties of manufactured films. Figures 6.2 and 6.3 present the Herman orientation functions of the crystalline phase as well as of the amorphous phase obtained from FTIR, respectively. For the N-AFR condition, it is obvious that decreasing T_{cast} reduces the orientation of both the crystalline and amorphous phases (Figures 6.2 and 6.3). For no air flow (N-AFR) and very low T_{cast}, quenching of the polymeric film happens and as a consequence a spherulitic crystal structure is expected, which leads to quite low crystal alignment. However, by

increasing the drum temperature, the film temperature gets close to the crystallization point, T_c, of the resin; thus the molecules have more chance to crystallize in the extended configuration created under high draw ratio. This results in films with higher crystal orientation. Moreover, compared to the no air cooled films, significant improvement in the orientation of the crystalline and amorphous phases is observed when the film surface is exposed to a small amount of air cooling (Figures 6.2 and 6.3). For the samples obtained under air cooling and at a drum temperature of 80 °C and lower, the orientations (not shown) were close to the one at T_{cast} of 100 °C and the reasons for that will be explained later. The insets in Figures 6.2 and 6.3 reveal the Herman orientation functions of the crystalline and amorphous phases of the samples obtained at T_{cast} of 120 °C for different air flow rates, respectively. It is clear that applying a small amount of air flow enhances the orientation of the crystalline and amorphous phases drastically while further increases in air flow do not significantly affect them.

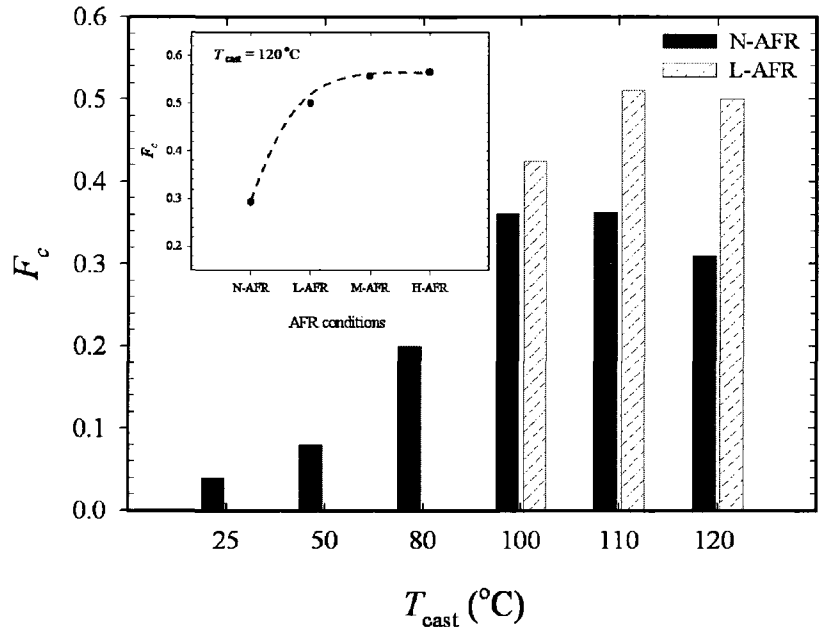

Fig. 6.2 Crystalline orientation functions for different cast roll temperatures. The inset is a plot of the crystalline orientation function versus the air flow rate conditions for T_{cast}=120 °C; DR=75.

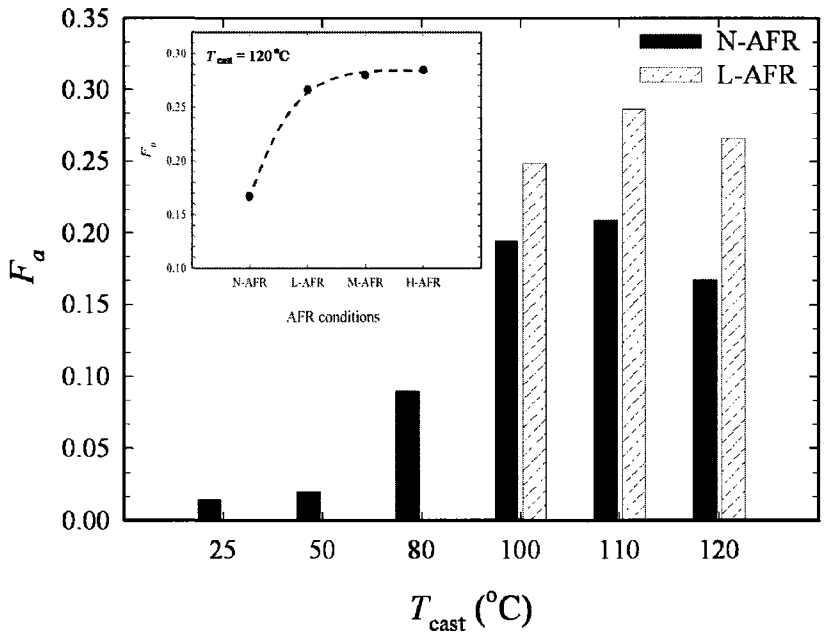

Fig. 6.3 Amorphous orientation functions for different cast roll temperatures. The inset is a plot of the amorphous orientation function versus the air flow rate conditions for T_{cast}=120 °C; DR=75.

The effect of the amount of applied strain, either in shear or elongational flow, on the lamellar structure of the various resins has been investigated recently [7,15-17]. The authors reported that as the level of strain increased, more lamellae accompanied with better orientation were generated. The influence of draw ratio on the orientation of the crystalline and amorphous phases has also been considered [9,17,18]. In the cast film process of PP, an almost linear relationship between the draw ratio and the orientation factor was reported [9,18]. At low draw ratios, the lamellae were not well aligned perpendicular to the flow direction, but at high draw ratios, the lamellae aligned themselves perpendicular to the machine direction, resulting in higher orientation. In this study, the influence of the draw ratio on the orientation function with and without the use of air flow is illustrated in Figure 6.4 for draw ratios of 60, 75, and 90. Obviously, compared to the no air cooled films and for all the draw ratios, a jump in the orientation parameter is seen by the use of low air cooling. In addition, the draw ratio has a stronger effect on the orientation function for the films subjected to air cooling.

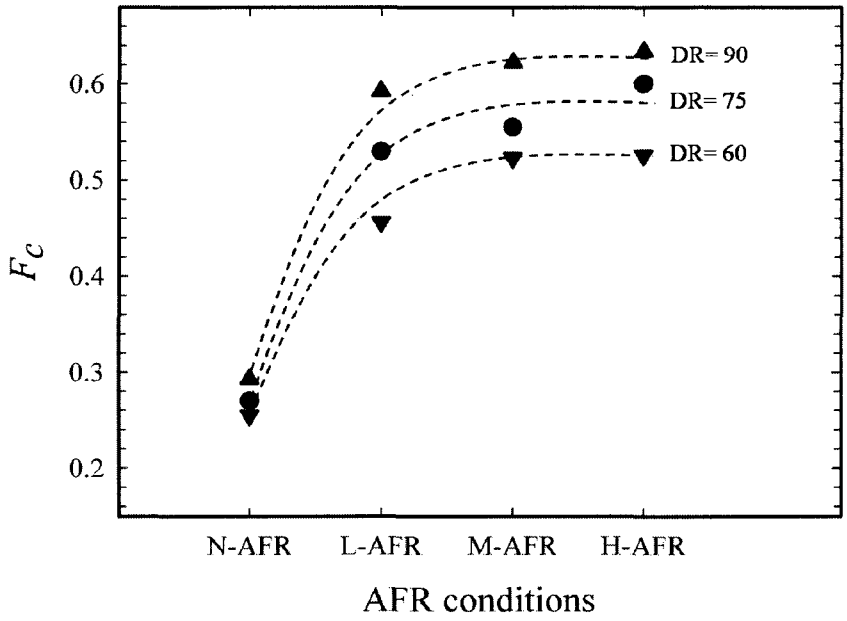

Fig. 6.4 Crystal orientation functions for different air flow rate conditions at draw ratios of 60, 75, and 90; T_{cast}=120 °C.

The effect of air cooling on orientation of the crystalline phase was also considered using WAXD, as shown in Figure 6.5. In the WAXD patterns, the first and second rings represent the patterns for the 110 and 040 crystalline planes, respectively [12]. A diffraction ring is seen for the 110 crystallographic plane for the no air cooled film, indicating a low crystalline phase orientation. However, instead of rings, arcs that are sharper and more concentrated in the center are observed for the air cooled samples, implying more orientation. This behavior can be better shown when the intensity is plotted as a function of the azimuthal angle. The azimuthal angle, ϕ, is 0 or 180° along the equator and 90 or 270° along the meridian. For each ϕ, the average intensity at 2θ (=12.6° ± 0.17°) of the 110 plane was extracted from the 2D WAXD patterns and the results for the samples produced under different air flow rates are plotted in Figure 6.5.

Noticeable jumps at azimuthal angles around 180° as well as about 90° and 270° are observed when a small amount of air blowing is applied while further increases in the air flow rate do not dramatically impact the azimuthal intensity profile. The much sharper peaks for the air cooled films indicate a higher orientation of the crystal lamellae compared to the no air cooled ones.

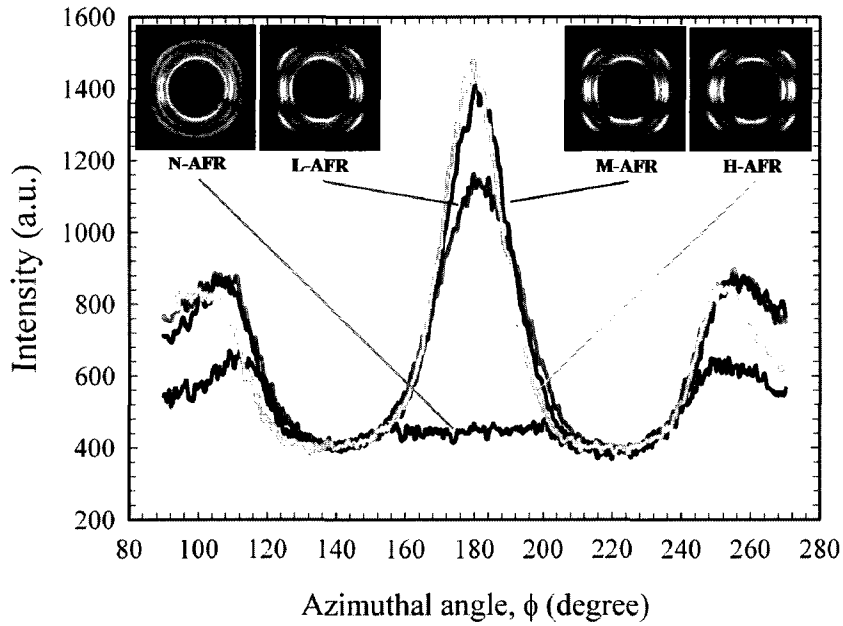

Fig. 6.5 2D WAXD patterns and azimuthal intensity profiles at 2θ of the 110 refection plane of PP at different air cooling conditions; T_{cast}=120 °C and DR=75.

The crystalline orientation can also be analyzed quantitatively from the pole figures of the 110 and 040 planes, as illustrated in Figure 6.6. The normal to the 110 plane is the bisector of the *a* and *b* axes and the 040 plane is along the *b*-axis of unit crystal cells [12]. For the film obtained without air cooling, slight orientations of the 110 and 040 planes are detected in MD and TD, respectively. However, for the film produced at L-AFR a significant orientation of the 110 plane is observed along TD and that of the 040

plane (*b*-axis) is in both TD and ND. The pole figures for the samples obtained at higher air flow rates (i.e. M-AFR and H-AFR) were similar to L-AFR with slightly higher orientation intensities. The schematics in Figure 6.6 represent the crystal alignments based on their pole figures.

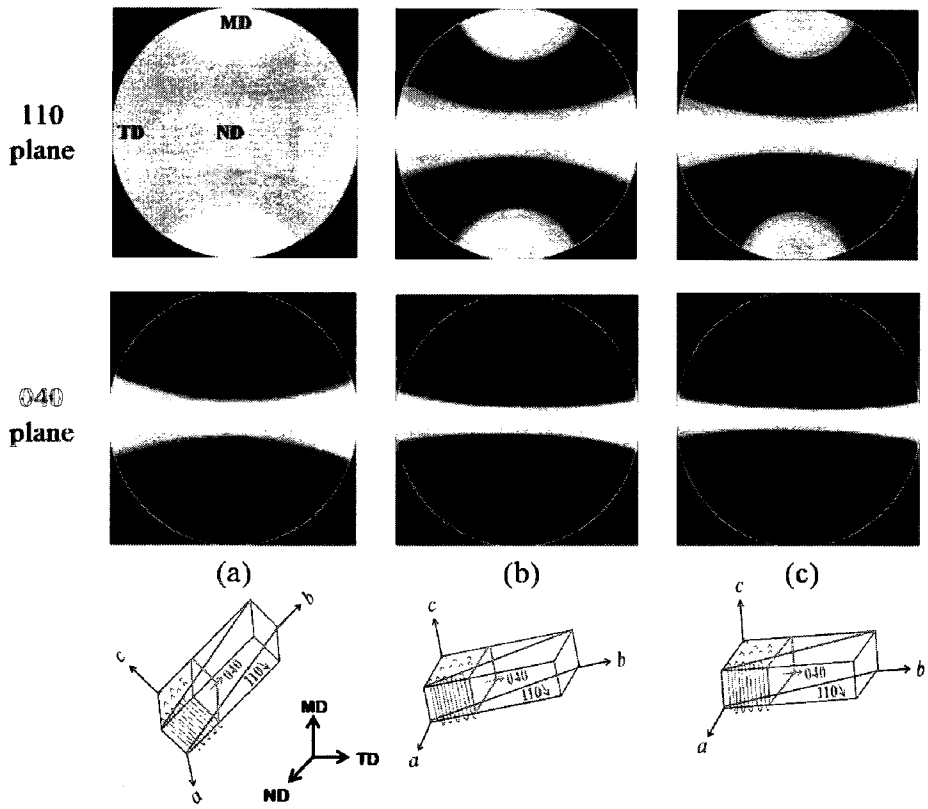

Fig. 6.6 Pole figures for the films obtained under different air cooling conditions. a) N-AFR, b) L-AFR, and c) M-AFR; T_{cast}=120 °C and DR=75. Schematics show the assumed crystal orientation.

The orientation features, in terms of $\cos^2(\phi)$ of the crystalline axes (i.e. *a*, *b*, and *c* (see the sketch in Figure 6.7)) along MD, TD, and ND obtained from the Herman orientation function for the no air cooled as well as the air cooled films casted at the chill

roll temperature of 120 °C are presented in the triangular plot of Figure 6.7. It is obvious that a small amount of cooling causes a large shift of the *c*-axis of the crystals towards the MD, while *a*- and *b*-axes take a position closer to the TD and ND planes. This clearly shows that air cooling enhances the orientation of the films, in accordance with the FTIR data. It should be mentioned that the orientation functions obtained using FTIR were slightly larger than the values from the WAXD pole figure. The discrepancies in the values of the measured *c*-axis orientation may be due to different factors such as peak deconvolution, contribution of the amorphous phase etc., as discussed for PE and PP elsewhere [1,19].

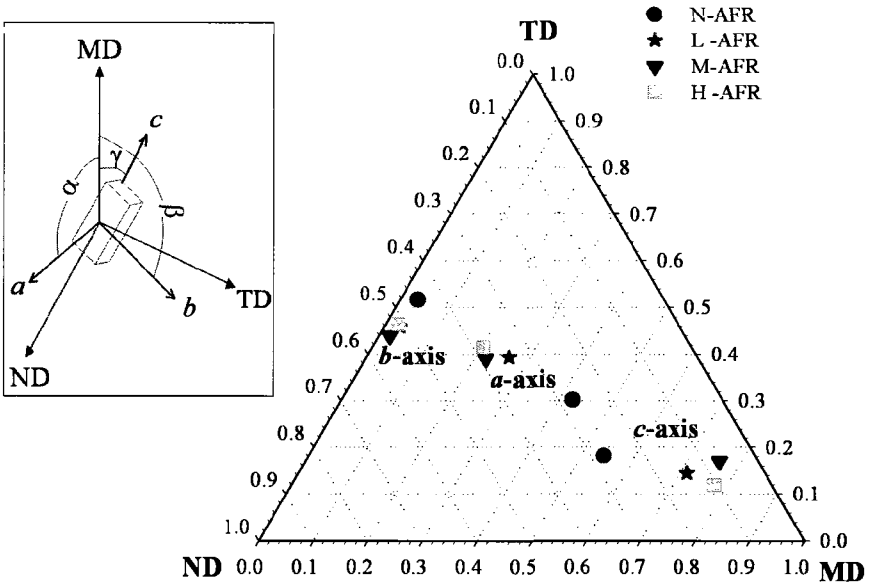

Fig. 6.7 Orientation characteristics as $\cos^2(\phi)$ of the crystal axes (*a*, *b* and *c*) along MD, TD, and ND; T_{cast}=120 °C and DR=75. The schematic represents the film production axes and crystal block coordinates.

The degree of crystallinity (X_c) of the samples determined using WAXD and DSC is presented in Table 6.1. In WAXD, the contributions arising from the crystalline and

amorphous parts were extracted via peak fitting of the 2θ diffraction pattern. Similarly to DSC results, it was observed that cooling improves crystallinity. However, the crystallinity obtained from WAXD was slightly higher than that from DSC. In addition, the average crystal width in the directions of the 110 and 040 crystallographic planes were determined from the full width at half maximum $\Delta(2\theta)$ of the deconvoluted diffraction profiles according to the following equation [20]:

$$D_{hlk} = \frac{K\lambda}{\Delta(2\theta)\cos\theta} \qquad (6.5)$$

where K is a crystallite form coefficient that is taken equal to 1 and λ is the X-ray wavelength. Although it is known that this equation is not accurate because it neglects the broadening due to the lattice distortions, it allows a useful comparison of the crystalline structures for the various films. Table 6.1 also presents the variations of the D_{110} and D_{040} with air cooling for the films casted at 120 °C. Both D_{110} and D_{040} are enhanced by the use of low air cooling and do not vary by further increases of air flow. The D_{040} crystallite size corresponds to an average size of the crystallites that are oriented parallel to the film plane. Therefore, the increase of D_{040} suggests that the crystallite size is increased in a direction parallel to the *b* crystallographic axis. The effect of the cast roll temperature on the D_{040} was also evaluated (not shown here) and no noticeable impacts were found.

Table 6.1 Crystal characteristics of the cast films obtained under different air cooling rates; DR=75.

	FWHM (110)	D_{110} A°	FWHM (040)	D_{040} A°	X_c (XRD)	X_c (DSC)
T_{cast} = 120 °C, N-AFR	1.24	72	1.06	84	42.2	42.2
T_{cast} = 120 °C, L-AFR	1.14	78	0.86	103	44.3	43.2
T_{cast} = 120 °C, M-AFR	1.13	79	0.87	102	45.7	44.4
T_{cast} = 120 °C, H-AFR	1.12	80	0.87	102	46.1	44.6

Figure 6.8 illustrates the SAXS patterns as well as the azimuthal intensity profile for the films obtained under different air cooling rates. The equatorial streak in the SAXS patterns is attributed to the formation of the shish, while the meridian maxima are attributed to the lateral lamellae or kebabs [6]. Looking at the meridian intensity (either pattern or azimuthal profile), the formation of more lamellae for the air cooled samples is obvious. In addition, for all conditions, it is clear that the contribution of the shish to the crystalline phase is much less than that of lamellae, confirming the results of Somani et al. [21] for PE and PP.

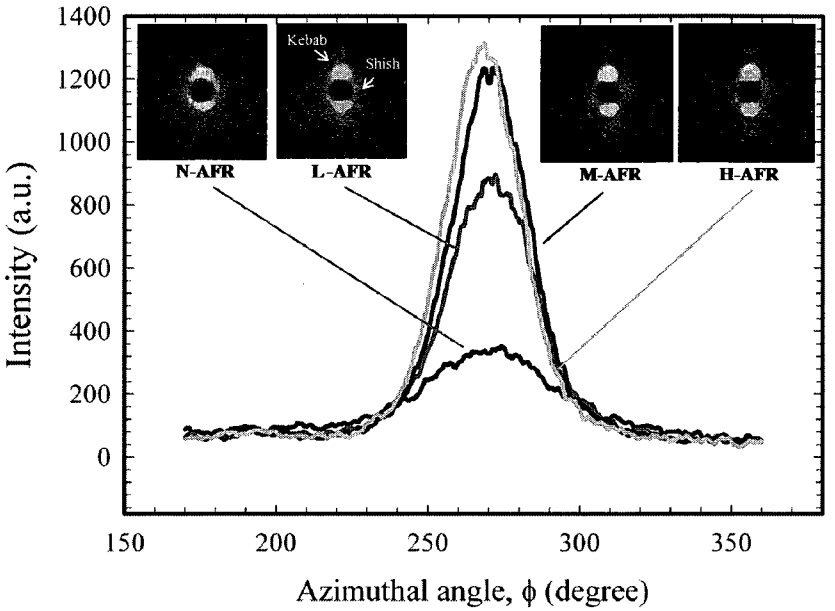

Fig. 6.8 2D SAXS patterns and azimuthal intensity profiles at the meridian of PP films for different air flow cooling conditions; T_{cast}=120 °C and DR=75.

The long period distance, L_p, was estimated from the position of the Lorentz corrected intensity maxima, as demonstrated in Figure 6.9 ($L_p=2\pi/q_{max}$ where q is the intensity vector, $q=4\pi\sin\theta/\lambda$,). We observes a first order peak arising from stacks of parallel lamellae and a second order peak indicating that the periodicity of the lamellae is high [22]. Air cooling slightly shifts the peaks to higher values, indicating a decrease of the long period spacing. Long period spacing results for the no air cooled as well as the air cooled specimens are also reported in Figure 6.9. The value of L_p for the films subjected to air cooling is smaller than that for the films produced without applying air cooling (L_p=14.7 nm compared to 15.7 nm) and decreases with increasing AFR. As all films were produced under the same draw ratio, the decrease of L_p is attributed to the

formation of more lamellae and consequently a more compact structure, which reduces the distance between lamellae.

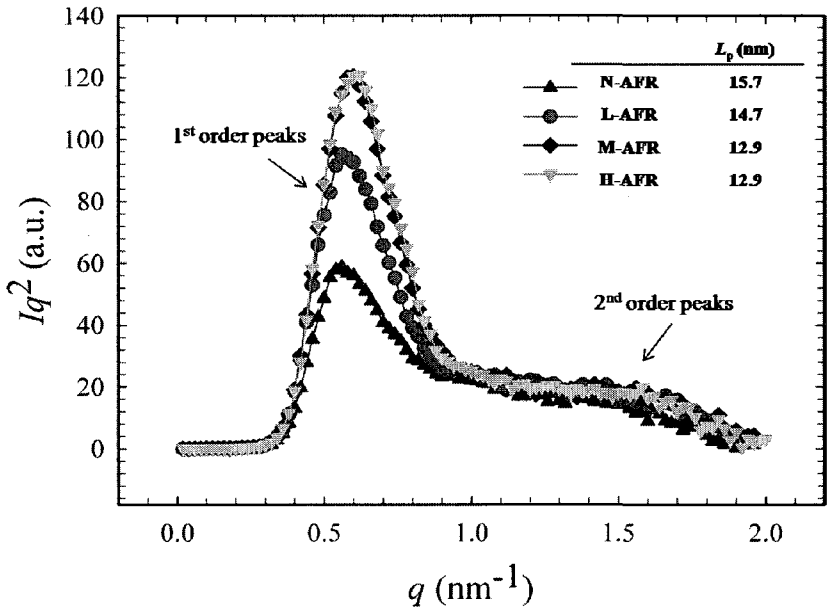

Fig. 6.9 Lorentz corrected SAXS intensity profiles for the films prepared under various air cooling conditions; T_{cast}=120 °C and DR=75.

The previous results imply that an oriented shish-kebab crystal structure is obtained by the use of air cooling in addition to the chill roll, compared to a much less ordered crystal structure for the no air cooled films. These differences can be clearly visualized from SEM surface images of the etched films (etching removes the amorphous region), as demonstrated in Figure 6.10. Figure 6.10a shows the micrograph of the surface of the film obtained without employing air cooling and at T_{cast} of 120 °C. For such conditions, spherulites, small rows of lamellae, and some cross-hatched crystalline structures coexist. The size of the spherulites is much larger than the lamellae, whereas the lamellae have been oriented somehow perpendicular to MD. The rectangle in Figure

6.10a illustrates the interface of a spherulite and rows of lamellae and its higher magnification image is shown on the right. More spherulites and lamellar branching are observed for the films prepared at T_{cast} of 110 °C and without the use of air cooling (Figure 6.10b). The lamellar branching from the primary lamellae is produced by epitaxial growth due to cross-hatched lamellar texture, which is a unique characteristic of PP crystalline structure [1]. The rectangle in Figure 6.10b exhibits the impingement of spherulites, clearly demonstrated by its higher magnification micrograph on the right. For the no air cooling condition, the number of spherulites increased and the cross-hatched morphology became more random (balanced) (not shown) as the cast roll temperature changed from 100 °C to 25 °C. This can be explained by the quenching effect (and hence low crystal orientation) of the cast roll at temperatures much lower than T_c of the resin. In contrast, a more uniform and ordered stacked lamellar structure is observed for the films subjected to a low air cooling (Figure 6.10c), confirming the FTIR and WAXD results (see Figures 6.2 and 6.7). In Figure 6.10c, no spherulites are seen and the sizes of lamellae are much larger than the lamellae shown in Figure 6.10a, which is qualitatively in good agreement with the XRD results (see Table 6.1). The dark spots in Figure 6.10c could be due the presence of very small spherulites or some crystalline parts that have been removed by etching. Applying higher air cooling rate slightly improved the orientation and size of lamellae and for that reason the results are not presented here. Additionally, for the L-AFR condition, it was realized that T_{cast} lower than 100 °C did not noticeably influence the structure of the air cooled films, indicating

that the crystal structure has been established before contacting the nip roll. In other words, by applying air cooling, the frost line has been formed before the extruded film touches the nip roll. Therefore, high T_{cast} (i.e. T_{cast}=120 °C or 110 °C) affects the structure as annealing does (i.e. removes the imperfection in crystalline phase and slightly increases the crystal size and orientation [8,18,23]). This is why the films produced under air cooling and high T_{cast} show slightly higher orientation than the ones obtained at low T_{cast} (i.e. T_{cast}=100 °C or lower).

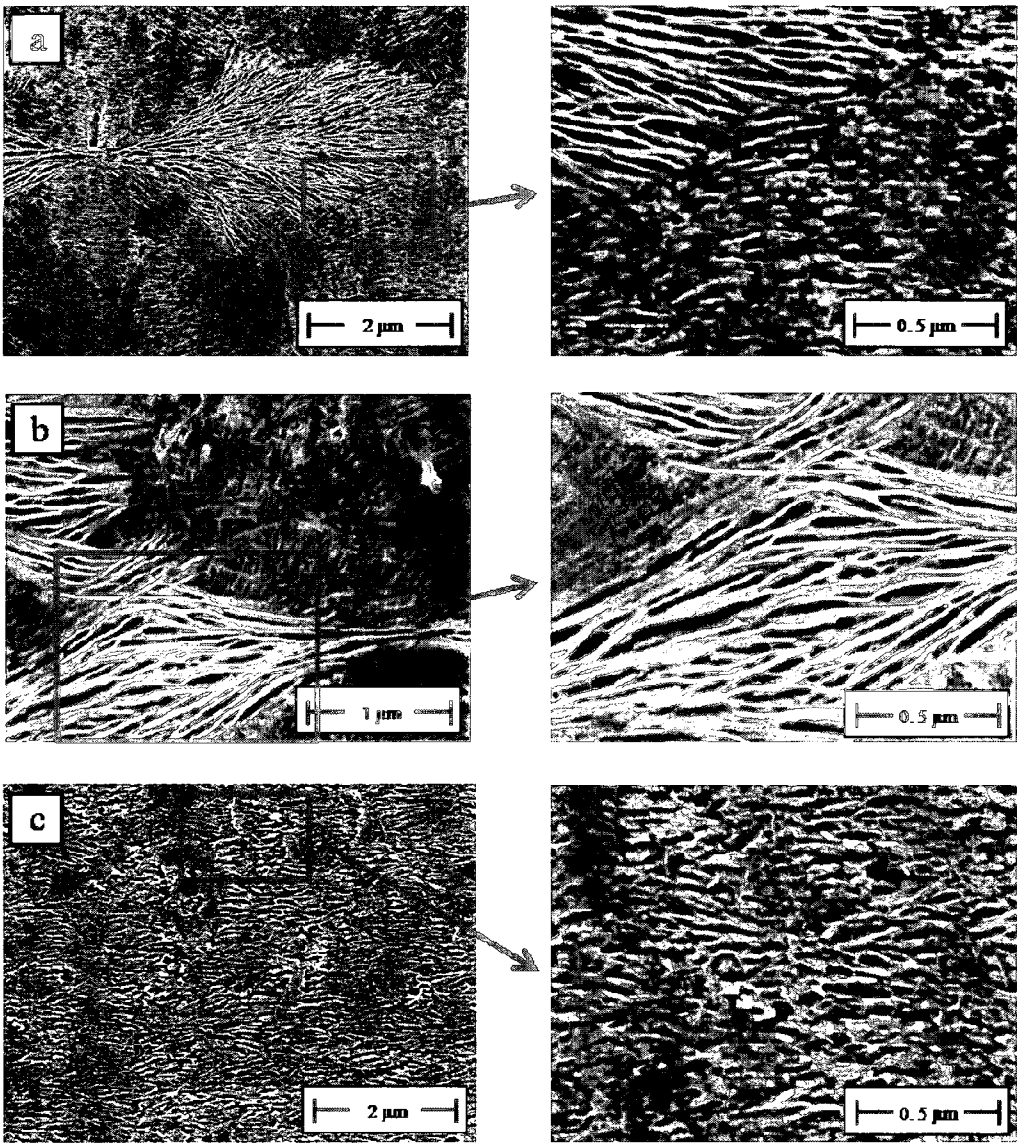

Fig. 6.10 SEM micrographs of the surface of films obtained under: a) N-AFR and T_{cast}=120 °C, b) N-AFR and T_{cast}=110 °C, and c) L-AFR and T_{cast}=120 °C. The right images are high magnification micrographs of the sections corresponding to the rectangles; DR=75. MD ↑ and TD →

It is well established that the structure of the crystalline and amorphous phases strongly influence the mechanical and tear properties of films. In other words, the mechanical and tear behaviors are closely related to structure changes. Zhang et al. [24]

studied the microstructure of LLDPE, LDPE, and HDPE blown films and showed that the type of oriented structure was greatly dependent on the type of polyethylene as well as on the processing conditions. These structure differences were shown to translate into different ratios for MD and TD tear and tensile strengths [24]. Figures 6.11a and b show the typical stress-strain behavior (for samples prepared without and with air cooling) along MD and TD, respectively. The stress-strain response for the no air cooled samples along MD exhibits the typical behavior of films of a spherulitic structure with an elastic response at low deformation, yielding and plastic behavior at medium deformation, and strain hardening at high elongation. In contrast, the stress-strain response of the air cooled specimens along MD reflects the typical behavior of films of a lamellar crystalline morphology with an initial elastic response at low deformation followed by two strain hardening zones. An extensive discussion on this behavior can be found in Samuels [25]. To clearly understand the influences of air cooling on the mechanical properties of the manufactured films, the Young modulus, yield stress, tensile strength, tensile toughness along MD, elongation at break, and yield stress along TD for all the films were determined, as depicted in Figures 6.12 and 6.13, respectively. It is very important to note that all properties along MD (Figure 6.12) improve significantly as the films are subjected to a low level of AFR. This can be easily explained by the much better alignment of the lamellae due to air cooling. Additionally, it should be pointed out that further increases of AFR do not noticeably change the mechanical properties along MD, which is in agreement with their orientation trend (see Figures 6.2 and 6.7).

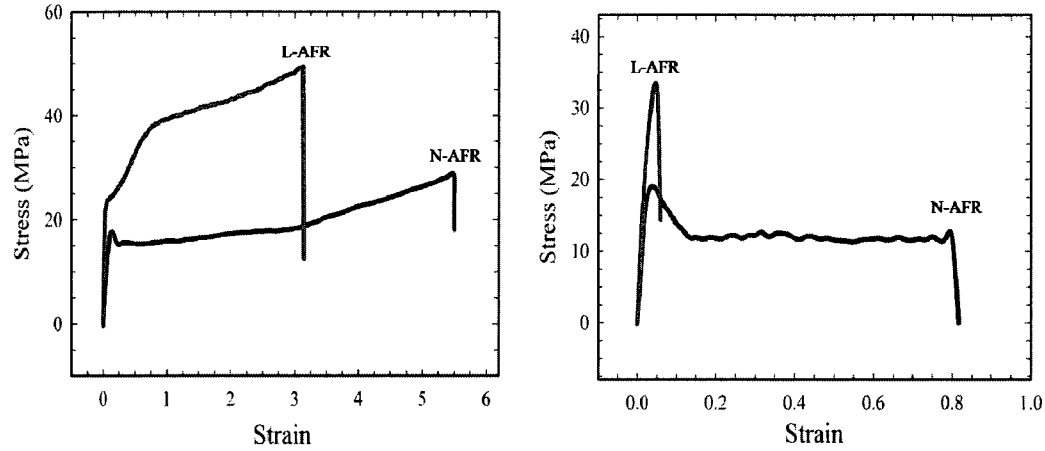

Fig. 6.11 Typical stress-strain behavior for the films prepared under N-AFR and L-AFR conditions along MD (left figure) and TD (right figure); T_{cast}=120 °C and DR=75.

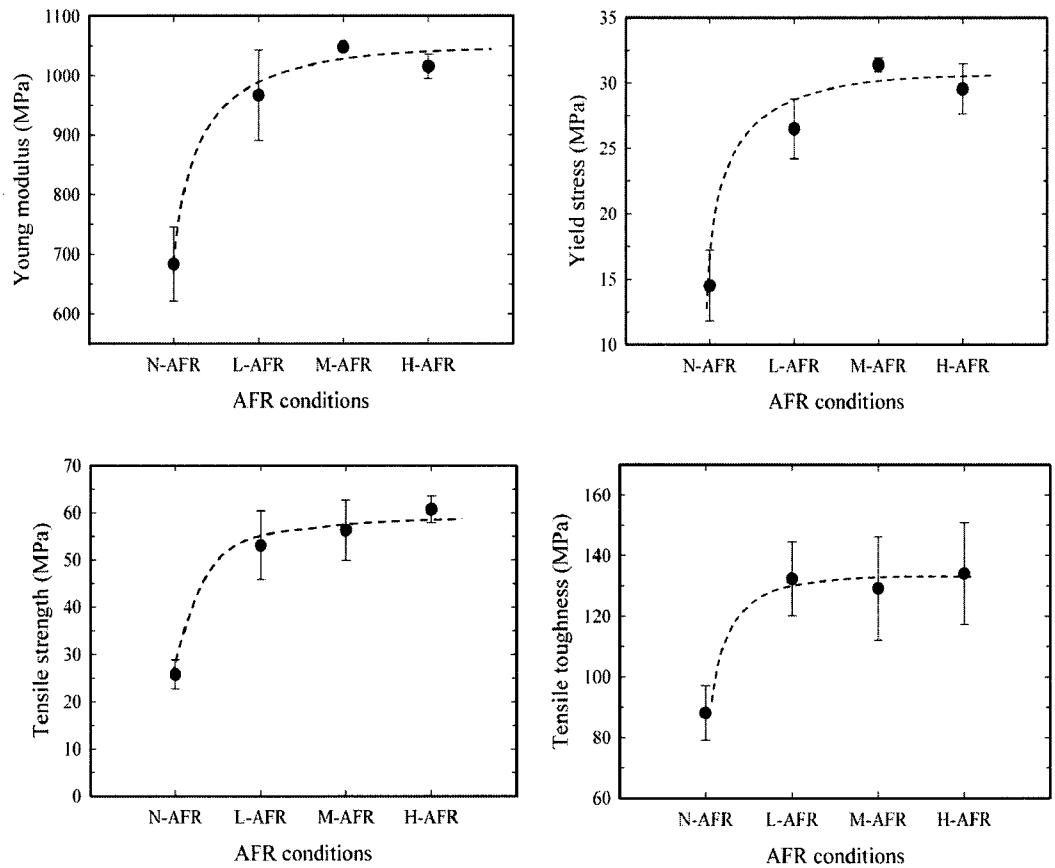

Fig. 6.12 Mechanical properties of the films along MD for various air flow rate conditions; T_{cast}=120 °C and DR=75.

The enhancement of the mechanical response along MD, due to the high orientation of the cooled specimens along MD, was, however, accompanied by significant reductions of the elongation at break along TD (Figure 6.13). This anisotropy of the tensile properties along MD and TD was also reported for different PE resins [24] and it was shown that as the level of orientation increased the anisotropy in the mechanical properties increased. Figure 6.13 also shows that the yield stress along TD is enhanced as the air flow rate is increased. According to Zhou and Wilkes [26], for HDPE having a stacked lamellar structure, stretching perpendicular to MD caused the crystal lamellae to break up or rupture by chain pull-out. In our case, it is postulated that applying air cooling forms more tie chains between the stacked lamellae, which are possibly responsible for the increase of the yield stress with increasing air flow rate.

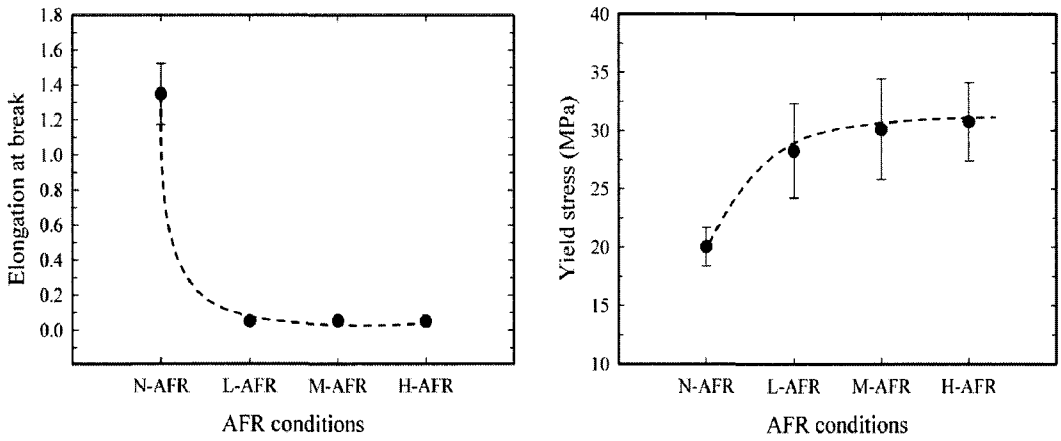

Fig. 6.13 Elongation at break (left figure) and yield stress (right figure) of the films along TD for various air flow rate conditions; T_{cast}=120 °C and DR=75.

Table 6.2 reports the mechanical properties along MD and TD for the films produced at T_{cast} of 120, 110, 100 °C under N-AFR as well as L-AFR conditions.

Compared to the no air cooled films, a significant effect of low air blowing on the mechanical properties, at all drum temperatures, is observed. It is clear that the Young modulus, yield stress, tensile toughness, and tensile strength along MD decrease as T_{cast} decreases. This is due to the formation of more lamellae at higher T_{cast} for the no air subjected films (see Figures 6.10a and b) and annealing effect at high T_{cast} for the air subjected films.

Table 6.2 Mechanical properties of the cast films along MD and TD (the numbers in parenthesis indicate the standard deviation of the measurements); DR=75.

	Mechanical properties along MD					Mechanical properties along TD	
	Young modulus (MPa)	Yield stress (MPa)	Tensile toughness (MPa)	Strain at break	Tensile strength (MPa)	Yield stress (MPa)	Strain at break
T_{cast} = 120 °C, N-AFR	683.5 (61.8)	14.5 (2.7)	93.2 (15.2)	5.5 (0.0)	25.7 (3.1)	20.0 (1.6)	1.2 (0.4)
T_{cast} = 120 °C, L-AFR	967.0 (157.0)	26.1 (4.8)	122.7 (25.3)	2.8 (0.4)	53.0 (7.2)	25.7 (6.1)	0.05 (0.01)
T_{cast} = 110 °C, N-AFR	604.4 (51.2)	12.2 (2.0)	81.3 (13.6)	6.2 (0.4)	21.3 (7.6)	17.5 (1.3)	1.5 (0.1)
T_{cast} = 110 °C, L-AFR	890.2 (98.3)	23.5 (3.3)	106.0 (15.6)	2.7 (0.1)	49.2 (2.4)	25.2 (0.6)	0.05 (0.01)
T_{cast} = 100 °C, N-AFR	562.9 (167.5)	10.8 (3.1)	74.6 (15.4)	6.7 (0.1)	19.7 (4.3)	15.9 (0.8)	1.48 (0.1)
T_{cast} = 100 °C, L-AFR	853.8 (19.8)	22.1 (1.0)	97.8 (1.8)	2.4 (0.0)	46.9 (0.8)	23.5 (4.9)	0.05 (0.01)

It is well understood that tear measurements are very sensitive to the type and alignment of crystalline morphology [24]. Along MD, tear resistance values of 0.178, 0.154, 0.146, and 0.121 g/μm were measured for the films obtained at T_{cast}=120 °C and N-AFR, L-AFR, M-AFR, and H-AFR, respectively: the higher the orientation of the crystalline and amorphous phases, the lower the tear resistance along MD. It was

observed that measurements of the tear resistance along TD for samples subjected to air cooling were impossible, because the tearing direction deviated most of the time to MD. In fact, there is a high resistance in TD when compared to MD, which causes a crack in MD and created non-reproducible data that are not reported here. This implies that for air cooled films, a shish-kebab lamellar crystal structure with shishs aligned in MD is formed.

Based on our observations from thermal analysis, FTIR results, WAXD and SAXS patterns, microscopy, mechanical and tear properties, two microstructural pictograms (one for the no air cooled cast film and another for the cast films produced with the use of air cooling) are proposed as depicted in Figure 6.14.

For the films produced at high chill roll temperatures and without air cooling, FTIR data, WAXD and SAXS patterns suggest the presence of a lamellar crystalline structure (rows of lamellae and/or cross-hatched), which is not preferentially oriented in MD (see Figures 6.2, 6.7, and 6.8). Additionally, the facility of tearing these samples along TD indicates that the shishs are not long. However, for these samples, the stress-strain behavior along MD and TD implies the presence of a spherulitic crystalline structure as well. Therefore, as illustrated in Figure 6.14a, for the films produced without air cooling and at high T_{cast}, it is believed that spherulitic, row nucleated, and cross-hatched lamellar crystalline structures coexist as confirmed by the SEM micrographs of Figures 6.10a and b. In Figure 6.14a, the solid line represents the tear path for the sample torn in MD, whereas the dash line reflects the tear path for the one torn in TD. The cast films having

this mixed structure can be easily torn along both MD and TD. At low cast roll temperatures (i.e. at temperatures far below T_c of the resin), low orientation values for both crystalline and amorphous phases were determined (see Figures 6.2 and 6.3), indicating the formation of more spherulitic and randomly cross-hatched crystal forms.

In contrast, for the films produced under air cooling, FTIR data, SAXS and WAXD patterns suggest the presence of a stacked lamellar crystal structure, which is preferentially oriented into MD (see Figures 6.2 and 6.7). In addition, the impossibility to tear these samples along TD suggests that the size of the shish is much larger in comparison with those for the films casted under N-AFR. Furthermore, a very low elongation at break along TD for the films subjected to air cooling is an indication that the spherulitic crystalline structure does not exist or is present in a very small quantity. This is confirmed by the SEM results shown in Figure 6.10c. Hence, as depicted in Figure 6.14b, a uniform shish-kebab structure for the films produced under air cooling is expected. The cast films having this structure can be easily torn along MD. However, as sketched in Figure 6.14b, because of the presence of the long shishs, tearing along TD is impossible and the tearing direction always deviates to MD. As described before, under air cooling conditions, the variation of T_{cast} does not noticeably affect the shish-kebab structure.

Based on FTIR results for the orientation of the amorphous phase (see Figure 6.3), circles in Figures 6.14a and b also reveal the proposed structure for the amorphous region of films made without and upon air cooling, respectively. By applying air

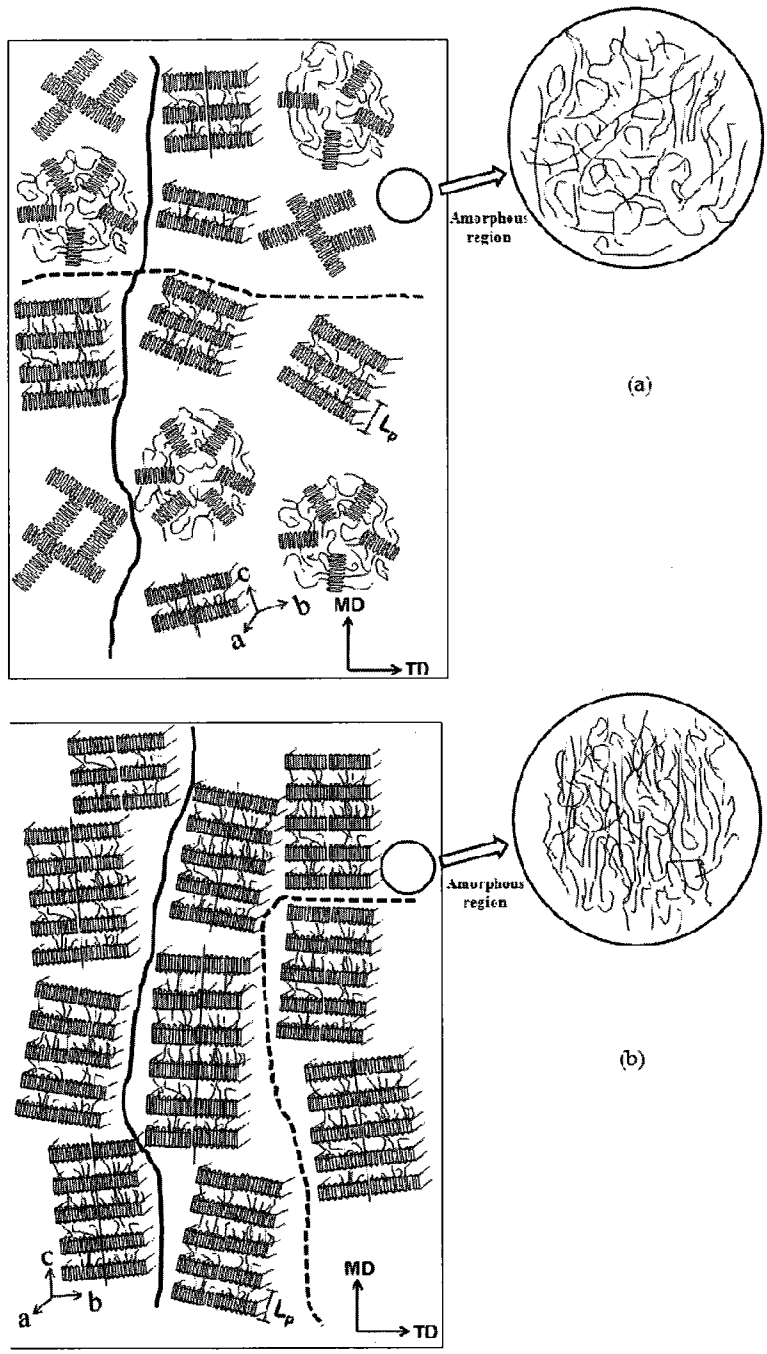

Fig. 6.14 Proposed pictograms of the molecular structure for: a) no air cooled cast films and b) air cooled cast films (the solid lines represent the tear path along MD and the dash lines show the tear path along TD).

cooling, the extruded film temperature at the die exit decreases and, as a consequence, the applied stress on the polymer chains increases. This yields some local organization in the amorphous phase, which is responsible for its higher orientation.

In the following section, justifications regarding the roles of air cooling and drum temperature on the final crystal microstructures are presented. The orientation and morphological differences are believed to originate from the rheological characteristics and crystallization kinetics. It is well known that temperature has a crucial effect on the relaxation time of polymer chains as well as on the crystallization rate. In order to consider the effects of temperature on the applied stress and relaxation time of the molecules, linear dynamic rheological measurements were carried out. Figure 6.15 reports the weighted relaxation spectra for different melt temperatures using the NLREG (non linear regularization) software [27] (the vertical dash lines represent the range of frequencies covered during the experiments). We considered the characteristic relaxation time, λ_c, corresponding to the peak of the curves. From Figure 6.15, as temperature is decreased a longer relaxation time is observed (see the legend in figure). Assuming a linear velocity profile for the melt film between the die exit and cast roll nip and also assuming pure uniaxial flow in this region, the effective deformation rate based on the second invariant of the rate-of-deformation tensor was estimated to be around 65 s^{-1}. The complex shear viscosities at 65 s^{-1} and for different temperatures were taken as estimates of the melt viscosity and their values are reported in the legend of Figure 6.15. Obviously, the lower the temperature the larger the viscosity, and consequently the

higher the applied stress. Hence, as air cooling is used, the melt temperature right at the exit of the die decreases and, as a consequence, the applied stress (or relaxation time) rises drastically. This promotes the number of shishs or nuclei sites, resulting in a noticeable increase of the probability for the formation of lamellae by the low molecular weight chains.

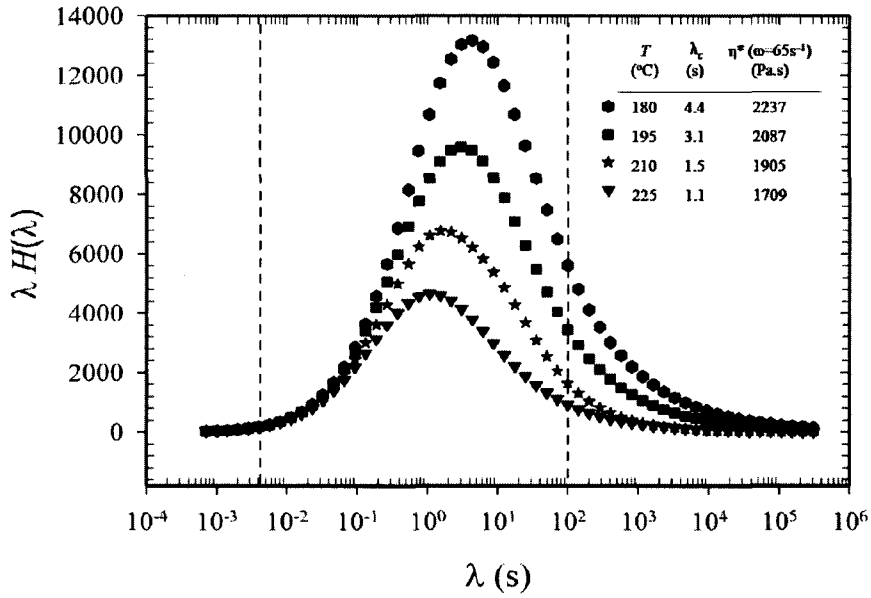

Fig. 6.15 Weighted relaxation spectra for different melt temperatures (the vertical dash lines represent the range of frequencies covered during the experiments).

In general, the rate of crystallization is first controlled by nucleation and then by the growth and packing of the crystals [28]. In our case, the air cooling causes a large decrease in the extruded film temperature such that crystallization temperature of the resin is reached before the frost line is formed. This increases the number of nuclei sites resulting in a much faster crystallization rate. This fact, together with the intrinsic temperature effects on the relaxation time, as discussed above, determines a significant

coupling between temperature and flow, yielding to a novel highly oriented lamellar structure. In other words, the use of air cooling in addition to chill rolls in the cast film process helps flow induced crystallization to occur at lower temperatures. This will noticeably increase the number of shish or nuclei sites, and consequently the crystallization kinetics is promoted resulting in a well oriented shish-kebab structure.

To produce microporous membranes by the stretching technique, precursor films with an adequate orientation and alignment of the crystal lamellae are needed [9,18]. In this study, the effects of microstructure differences of the PP cast films on the microporous membranes morphology and water vapor transmission rate were investigated. Three consecutive stages were carried out to obtain porous membranes: cast or precursor film formation, annealing, and stretching in two steps (cold and hot). During cold stretching, the pores were created whereas in the subsequent hot stretching they were enlarged. WAXD and FTIR measurements clearly showed that cooling drastically enhanced orientation of crystal lamellae in the precursor films; hence, a microporous membrane with more pore density and better tortuosity is expected as air cooling is utilized.

Figure 6.16 presents SEM micrographs of the surface of the fabricated membranes. Very thick lamellae, non uniform pores and a small amount of pores for the porous membrane obtained from the no air cooled film is observed (Figure 6.16a). However, for the membrane prepared from the cast film subjected to a small air cooling rate, the number of pores noticeably increase and more uniform pore sizes and a better

morphology are observed as well (Figure 6.16b). Note more and thinner lamellae appear for the latter compared to the former, supporting the previous results.

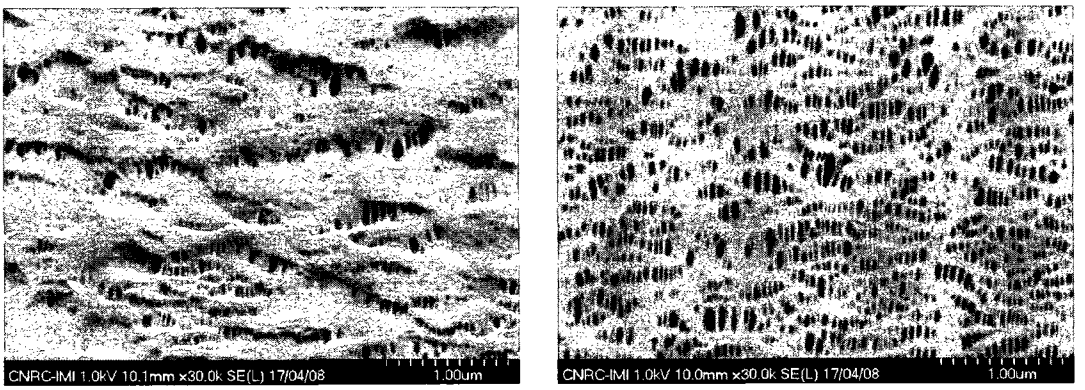

(a) (b)

Fig. 6.16 SEM micrographs of the surface of the films obtained at: a) N-AFR and b) L-AFR; T_{cast}=120 °C and DR=75, cold stretching of 35%, followed by hot stretching of 55%. MD ↑ and TD →

Figure 6.17 presents the water vapor transmission rates (WVTR) of the produced microporous membranes. Small WVTR were recorded for the no air cooled samples produced at different cast roll temperatures. However, interestingly, the WVTR increased by a factor of 20 when the film surface was subjected to a low air flow, which is attributed to the formation of more pores, higher porosity, and better interconnection between the pores. Compared to the sample prepared at L-AFR, further increases of the air cooling rate (i.e. at M-AFR and H-AFR), did not significantly increase the permeability was (see the inset of Figure 6.17), indicating that more air cooling does not dramatically influence the lamellar structure, in accordance with the previous results (see Figures 6.2-6.8).

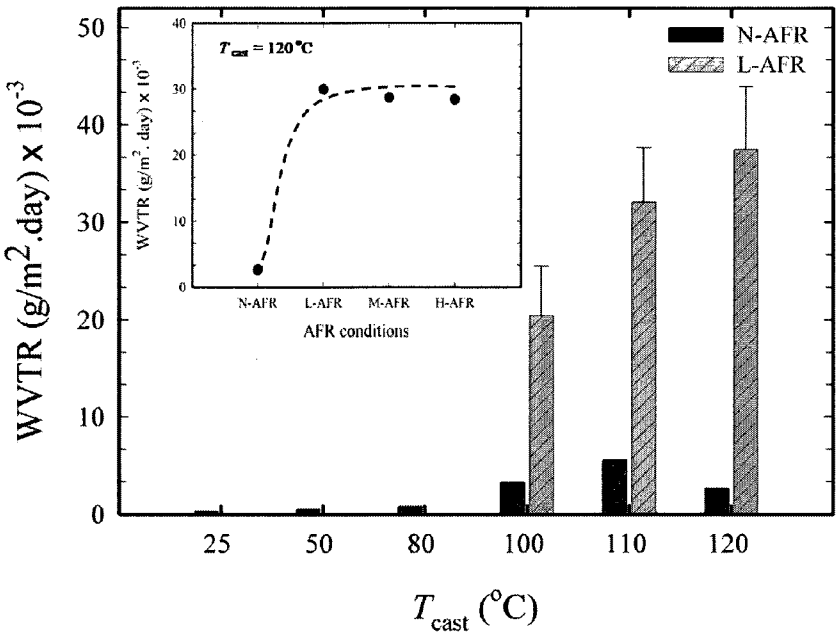

Fig. 6.17 Water vapor transmission rate (WVTR) as a function of cast roll temperature. The inset is a plot of WVTR as a function of air flow rate condition for T_{cast}=120 °C.

6.4 Conclusions

In this work, we have investigated the structure of polypropylene cast films made under different air cooling conditions, chill roll temperatures, and draw ratios. Our findings can be summarized as follows:

- In the cast film process, air cooling and cast roll temperature had a crucial role on the orientation of the crystalline as well as the amorphous phases.
- Increasing the draw ratio increased the crystal orientation (F_c), and a stronger effect of the draw ratio on F_c was observed by applying air cooling.

- The use of a low air cooling rate contributed significantly to the perfection of the crystalline phase, while further increasing of air cooling did not noticeably affect the crystal structure.
- Significant increases of the Young modulus, yield stress, tensile strength, and tensile toughness along MD, and dramatic decreases of elongation at break along TD were observed as air cooling was applied. These were explained by a better molecular and crystal orientation for air cooled cast films.
- For films produced without air cooling and at high roll temperature, coexisting lamellae and spherulites were observed. In contrast, an ordered stacked lamellar structure was seen for the films subjected to a low air cooling.
- Better orientations of the crystalline and amorphous phases for the air cooled films were attributed to the larger relaxation time and faster flow induced crystallization. Applying air cooling in addition to the use of cast rolls helped flow induced crystallization to occur at lower temperatures. This noticeably increased the crystallization kinetics, resulting in a well oriented shish-kebab structure.
- Microporous membranes having high pore density, large porosity, and high water vapor permeability were obtained by lamellae separation for cast films prepared using air cooling.

6.5 Acknowledgement

Financial support from NSERC (Natural Science and Engineering Research Council of Canada) and from FQRNT (Fonds Québécois de Recherche en Nature et Technologies) is gratefully acknowledged. We also acknowledge the large infrastructure grant received from the Canadian Foundation for Innovation (Government of Canada and Province of Quebec), which allowed us to build the unique POLYNOV facility. We are also thankful to Messrs. P. Cigana, L. Parent and P.M. Simard for their technical help. Finally, we are thankful to ExxonMobil who donated the resin used in this work.

6.6 References

[1] Ajji A, Zhang X, Elkoun S. Polymer 2005;46:3838-3846.

[2] Coppola S, Balzano L, Gioffredi E, Maffettone PL, Grizzuti N. Polymer 2004;45:3249-3256.

[3] Doufas AK, Dairanich IS, Mchugh AJ. J Rheol 1999;43:85-109.

[4] Doufas AK, Mchugh AJ. J Non-Newtonian Fluid Mech 2000;92:81-103.

[5] Swartjes FHM. Stress induced crystallization in elongational flow, PhD thesis, Technische Universiteit Eindhoven, 2001.

[6] Agarwal PK, Somani RH, Weng W, Mehta A, Yang L, Ran S, Liu L, Hsiao B. Macromolecules 2003;36:5226-5235.

[7] Somani RH, Hsiao BS, Nogales A, Srinivas S, Tsou AH, Sics I, Balta-Calleja FJ, Ezquerra TA. Macromolecules 2000;33:9385-9394.

[8] Somani RH, Yang L, Hsiao BS. Polymer 2006;47:5657-5668.

[9] Tabatabaei SH, Carreau PJ, Ajji A. J Membr Sci 2008;325:772-782.

[10] Fujiyama M, Inata H. J Appl Polym Sci 2002;84:2157-2170.

[11] Sadeghi F, Ajji A, Carreau PJ. Polym Eng Sci 2007;47:1170-1178.

[12] Alexander LE. X-ray diffraction methods in polymer science, Wiley Inter Science, New York, 1969.

[13] Arroyo M, Lopez-Manchado MA. Polymer 1997;38:5587-5593.

[14] Olley RH, Bassett DC. Polymer 1982;23:1707-1710.

[15] Koerner H, Kelley JJ, Vaia RA. Macromolecules 2008;41:4709-4716.

[16] Kawakami D, Burger C, Ran S, Avila-Orta C, Sics I, Chu B, Chiao S, Hsiao BS, Kikutani T. Macromolecules 2008;41:2859-2867.

[17] Macro Y, Chevalier L, Chaouche M. Polymer 2002;43:6569-6574.

[18] Sadeghi F, Ajji A, Carreau PJ. J Membr Sci 2007;292:62-71.

[19] Ajji A, Zhang X, Elkoun S. Polymer 2005;46:3838-3846.

[20] Klug HP, Alexamder LE. X-ray diffraction procedures, John Wily & Sons, New York, 1954.

[21] Somani RH, Yang L, Zhu L, Hsiao BS. Polymer 2005;46:8587-8623.

[22] Guinier A, Fournet G. Small-angle scattering of X-rays, New York: Wiley, 1955.

[23] Hedesiu C, Demco DE, Kleppinger R, Buda AA, Blumich B, Remerie K, Litvinov VM. Polymer 2007;48:763-777.

[24] Zhang XM, Elkoun S, Ajji A, Huneault MA. Polymer 2004;45:217-229.

[25] Samuels RJ. J Polym Sci Polym Phys Ed 1979;17:535-568.

[26] Zhou H, Wilkes GL. J Mater Sci 1998;33:287-303.

[27] Honerkamp J, Weese J. Rheol Acta 1993;32:65-73.

[28] Tian J, Yu W, Zhou C. J Appl Polym Sci 2007;104:3592-3600.

CHAPTER 7

Microporous Membranes Obtained from PP/HDPE Multilayer Films by Stretching[3]

Seyed H. Tabatabaei, Pierre J. Carreau, and Abdellah Ajji

CREPEC, Chemical Engineering Department, Ecole Polytechnique, C.P. 6079, Succ. Centre ville Montreal, QC, H3C 3A7 Canada

Abstract

Polypropylene/high density polyethylene (PP/HDPE) multilayer as well as monolayer films were prepared to develop microporous membranes using cast film extrusion followed by stretching. The effects of draw ratio (DR), cooling air flow rate (AFR), and annealing on the crystalline structure and orientation of the monolayer and components in the multilayer films were investigated using wide angle X-ray diffraction (WAXD) and Fourier transform infrared (FTIR). Annealing and high DR and AFR enhanced the crystal alignments significantly. However, the orientation of the PP and HDPE in the multilayer film was slightly lower compared to the monolayer films. The amount of lamellae formation, long period spacing (L_p), and lamellae thickness (l_c) were obtained via small angle X-ray scattering (SAXS). A significant influence of annealing on L_p and

---

[3] Submitted to *Polymer*

l_c was observed for the PP. The row-nucleated lamellar crystallization and transcrystallization observed in the surface and cross-section of the films, respectively, are discussed. Scanning electron microscopy (SEM) images of the membrane surface and cross-section obtained for the cold and hot stretch ratios of 55% and 75%, respectively, showed larger pores and higher porosity for the HDPE layer compared to the PP. As the level of the applied extension during cold stretching increased, the water vapor transmission rate (WVTR) of the HDPE monolayer improved while the effect was inversed for the PP single layer. In addition, compared to the monolayer membranes, the multilayer ones showed smaller WVTR. Tensile properties of the precursor films and microporous membranes in the machine and transverse directions (MD and TD, respectively) as well as puncture resistance in the normal direction (ND) were evaluated.

7.1 Introduction

Microporous membranes are commonly used in separation processes such as battery separators and medical applications to control the permeation rate of chemical components. Due to the wide range of chemical structures, optimum physical properties, and low cost of polymers, they are the best candidates for the fabrication of microporous membranes.

Commercially available lithium battery separators are made from polyolefins such as polypropylene (PP) and polyethylene (PE). These materials are compatible with the cell chemistry and can be used for many cycles without significant degradation in

properties [1]. Lithium (Li) batteries will generate heat if accidentally overcharged. Separator shutdown is a useful safety feature for restricting thermal reactions in Li-batteries [1,2]. Shutdown occurs close to the melting temperature of the polymer, leading to pores collapse and restricting passage of current through the cell. PP separators melt around 160 °C whereas PE separators have shutdown temperature between 120 and 130 °C. If in a battery, the heat dissipation is slow, even after shutdown, the cell temperature may continue to increase before starting to cool [1]. Recently, manufacturers have started producing trilayer separators where a porous PE layer is sandwiched between two porous PP layers. In such a case, the PE layer has lower shutdown temperature while PP provides the mechanical stability at and above the shutdown temperature [1].

Three commercially available processes are used for making microporous membranes: solution casting (also known as extraction process), particle stretching, and dry-stretching [3]. In the extraction process, the polymeric raw material is mixed with a processing oil or plasticizer, this mixture is extruded and the plasticizer is removed through an extraction process [4]. In the particle stretch process, the polymeric material is mixed with particles, this mixture is extruded, and pores are formed during stretching at the interface of the polymer and solid particles [5]. Costly processes and difficulties in dealing with solvent and particle contaminations are main drawbacks of such methods. However, the dry-stretch process is based on the stretching of a polymer film containing a row-nucleated lamellar structure [6]. Three consecutive stages are carried out to obtain

porous membranes by this technique: 1) creating a precursor film having a row-nucleated lamellar structure through shear and elongation-induced crystallization of the polymer having proper molecular weight and molecular weight distribution, 2) annealing the precursor film at temperatures near the melting point of the resin to remove imperfections in the crystalline phase and to increase lamellae thickness, and 3) stretching at low and high temperatures to create and enlarge pores, respectively [6,7].

In fact, in this process, the material variables as well as the applied processing conditions are the key parameters that control the structure and the final properties of the fabricated microporous membranes [6]. The material variables include molecular weight, molecular weight distribution, and chain structure of the polymer. These factors mainly influence the row-nucleated structure in the precursor films in the first step of the formation of microporous membranes. According to Sadeghi et al. [8,9], molecular weight was the main material parameter that controlled the orientation of the row-nucleated lamellar structure. The resins with high molecular weight developed larger orientation and thicker lamellae than those with low molecular weight. In our recent study [10], the addition of up to 10 wt% of a high molecular weight component to a low molecular weight resin enhanced the formation of the row-nucleated structure due to an increase in the nucleating sites. In Sadeghi et al. [11], a superior permeability was obtained by adding a small amount of a long-chain branched polypropylene (LCB-PP) to a linear polypropylene (L-PP). Recently [12], we investigated the effects of process conditions such as draw ratio (DR), air flow rate (AFR), and cast roll temperature on the

structure of PP cast films and microporous membranes. A significant enhancement in orientation was observed by applying air cooling and increasing DR. An ordered stacked lamellar structure was seen for the films subjected to low air cooling whereas the films produced without air cooling showed a spherulitic structure.

There are two main industrial processes for the production of films: film blowing and cast film extrusion. It is well known that the thickness variation in blown films are considerably greater compared to cast films. For the preparation of porous membranes, obtaining a precursor film with good thickness uniformity is strongly recommended since any non uniformity causes irregularities in the stress distribution in the following stretching process. In addition, compared to film blowing, cast film process has more flexibility in the supply of air cooling from both sides, leading to a more uniform lamellar structure in both surfaces.

Although a few authors have investigated the formation of porous membranes from polypropylene and high density polyethylene single layer films, no study has been performed on development of multilayer membranes using cast film process. In this study, following our previous studies [10,12] and the ones conducted by Sadeghi et al. [8,9,11] on monolayer PP, we investigate the fabrication of microporous PP/HDPE/PP trilayer membranes using the cast film process. The role of process parameters and annealing on the shear and/or elongation-induced crystallization and orientation developed in the monolayer as well as the components in the multilayer cast films are examined and discussed. A detailed investigation of the structure, particularly in the

cross-section, and performances of the trilayer microporous membranes has been carried out. In addition, the influence of the applied extension during the stretching steps is considered.

7.2 Experimental

7.2.1 Materials

A commercial linear polypropylene (PP) and a commercial high density polyethylene (HDPE) were selected. PP5341E1 was supplied by ExxonMobil and had a melt flow rate (MFR) value of 0.8 g/10min (under ASTM D1238 conditions of 230 °C and 2.16 kg). HDPE 19A was provided by NOVA Chemicals and had an MFR value of 0.72 g/10min (under ASTM D1238 conditions of 190 °C and 2.16 kg). The main characteristics of the resins are shown in Table 7.1. The molecular weight (M_w) and polydispersity index (PDI) of the HDPE was supplied by company and that of the PP was measured using a GPC (Viscotek model 350) with 1,2,4-Trichlorobenzene (TCB) as a solvent at a column temperature of 140 °C. The melting point, T_m, and crystallization temperature, T_c, of the resins obtained from differential scanning calorimetry at a rate of 10 °C/min are also reported in Table 7.1.

Table 7.1 Main characteristics of neat polymers.

Resin code	Company	MFR	M_w (kg/mol)	M_w/M_n	T_m (°C)	T_c (°C)
PP5341E1	ExxonMobil	0.8 230 °C/2.16 kg	361	2.7	162	112
HDPE 19A	NOVA Chemicals	0.72 190 °C/2.16 kg	126	7.8	129	118

7.2.2 Rheological characterization

Dynamic rheological measurements were carried out using a Rheometric Scientific SR5000 stress controlled rheometer with a parallel plate geometry of 25 mm diameter and a gap equal to 1.5 mm at the temperature of 190 °C under nitrogen atmosphere. Molded discs of 2 mm thick and 25 mm in diameter were prepared using a hydraulic press at 190 °C. Prior to frequency sweep tests, time sweep tests at a frequency of 0.628 rad/s and 190 °C were performed for two hours to check the thermal stability of the specimens. No degradation (less than 3% changes) was observed for the duration of the frequency sweep measurements. Complex viscosity and weighted relaxation spectrum in the linear viscoelastic regime were determined in the frequency range from 0.01 to 500 rad/s. In order to obtain more accurate data, the frequency sweep test was carried out in four sequences while the amount of applied stress in each sequence was determined by a stress sweep test.

7.2.3 Film and membrane preparation

The cast films were prepared using an industrial multilayer cast film unit from Davis Standard Company (Pawcatuck, CT) equipped with a 2.8 mm opening and 122 cm width slit die and two cooling drums. The extrusion was carried out at 220 °C and the distance between the die exit to the nip roll was 15 cm. The die temperature was set at 220 °C and draw ratios of 60, 75, and 90 were applied. An air knife with dimensions of 3 mm opening and 130 cm width was mounted close to the die to provide air to the film surface right at the exit of the die. The variables of interest were draw ratio and amount of air flow. The films were produced under chill roll temperature of 50 °C. The air cooling rates used were 1.2 and 12 L/s. These air cooling conditions are noted as: low air flow rate (L-AFR) and high air flow rate (H-AFR), respectively.

For the membrane fabrication, the precursor films with thickness, width, and length of 32 μm, 46 mm, and 64 mm, respectively, were used. The films were first annealed at 120 °C for 30 min and then cold and hot stretched at 25 °C and 120 °C, respectively. Both annealing and stretching were performed in an Instron tensile machine equipped with an environmental chamber. Drawing speeds of 500 mm/min and 25 mm/min were applied during cold and hot stretching steps, respectively.

7.2.4 Film and membrane characterization

Thermal analysis: Thermal properties of specimens were analyzed using a TA instrument differential scanning calorimeter (DSC) Q 1000. The thermal behavior of

films was obtained by heating from 50 to 220 °C at a heating rate of 10 °C/min. The reported crystallinity results were obtained using a heat of fusion of 209 and 280 J/g for fully crystalline PP and HDPE, respectively [13,14].

Fourier transform infrared spectroscopy (FTIR): For FTIR measurements, a Nicolet Magna 860 FTIR instrument from Thermo Electron Corp. (DTGS detector, resolution 2 cm^{-1}, accumulation of 128 scans) was used. The beam was polarized by means of a Spectra-Tech zinc selenide wire grid polarizer from Thermo Electron Corp. The measurement is based on the absorption of infrared light at certain frequencies corresponding to the vibration modes of atomic groups present within the molecule. In addition, if a specific vibration is attributed to a specific phase, the orientation within that phase can be determined [8]. If the films are oriented, the absorption of plane-polarized radiation by a vibration in two orthogonal directions, specifically parallel and perpendicular to a reference axis (MD), should be different. The ratio of these two absorption values is defined as the dichroic ratio, D [8]:

$$D = \frac{A_{\parallel}}{A_{\perp}} \tag{7.1}$$

where $A_{\parallel}$ is the absorption parallel and $A_{\perp}$ is the absorption perpendicular to a specific reference axis. The Herman orientation function of this vibration is obtained according to [8]:

$$F = \frac{D-1}{D+2} \tag{7.2}$$

For polypropylene, absorption at the wavenumber of 998 cm^{-1} is attributed to the crystalline phase (*c*-axis) while that at 972 cm^{-1} is due to the contribution of both crystalline and amorphous phases. From the former absorption, the orientation of the crystalline phase, F_c, can be determined while from the latter, the average orientation function, F_{avg}, is obtained. The orientation of the amorphous phase, F_a, can then be calculated according to:

$$F_{avg} = X_c F_c + (1 - X_c) F_a \qquad (7.3)$$

where X_c is the degree of the crystallinity.

For polyethylene, absorption at the wavenumber of 730 cm^{-1} is attributed to the *a*-axis of the unit crystal cell while absorption at the wavenumber of 720 cm^{-1} is due to the *b*-axis. The similarity of the normal (N) and transverse (T) spectra confirmed that the orientation is mostly uniaxial [15]. In such a case, it is not necessary to use the tilted film technique. The orientation function of the *a*- and *b*-axes could be obtained from Eq. 7.2 while that of the *c*-axis orientation is calculated according to the orthogonality equation:

$$F_a + F_b + F_c = 0 \qquad (7.4)$$

X-ray diffraction: XRD measurement was carried out using a Bruker AXS X-ray goniometer equipped with a Hi-STAR two-dimensional area detector. The generator was set up at 40 kV and 40 mA and the copper CuKα radiation (λ = 1.542 A°) was selected using a graphite crystal monochromator. The sample to detector distance was fixed at 9.2 cm for wide angle diffraction and 28.2 cm for small angle X-ray scattering analysis.

To get the maximum diffraction intensity several film layers were stacked together to obtain the total thickness of about 2 mm.

Wide angle X-ray diffraction (WAXD) is based on the diffraction of a monochromatic X-ray beam by the crystallographic planes (*hkl*) of the polymer crystalline phase. Using a pole figure accessory, the intensity of the diffracted radiation for a given *hkl* plane is measured as the sample is rotated through all possible spherical angles with respect to the beam. This gives the probability distribution of the orientation of the normal to *hkl* plane with respect to the directions of the sample.

The Herman orientation function F_{ij} of a crystalline axis i with respect to a reference axis j is given by [16]:

$$F_{ij} = \frac{(3\cos^2\phi_{ij} - 1)}{2} \qquad (7.5)$$

where ϕ_{ij} is the angle between the unit cell axes i (a, b, or c) and the reference axis j. The Herman orientation functions were derived from the 110 and 040 pole figures for the PP and the 110 and 200 pole figures for the HDPE. Details about the calculations for PP can be found in Sadeghi et al. [8]. For the HDPE, since the a-axis of the unit cells is perpendicular to the 200 plane, its orientation relative to the machine direction can be measured directly as follow:

$$F_a = F_{200} = \frac{3\cos^2\phi_{200} - 1}{2} \qquad (7.6)$$

On the other hand, F_c (orientation of the c-axis) with respect to MD is determined by the combination of data of two planes for the HDPE, which are 110 and 200 [16]:

$$\cos^2 \phi_c = 1 - 1.435 \cos^2 \phi_{110} - 0.565 \cos^2 \phi_{200} \qquad (7.7)$$

The orientation parameter for the *b*-axis can be calculated from the orthogonality relation:

$$\cos^2 \phi_b = 1 - \cos^2 \phi_a - \cos^2 \phi_c \qquad (7.8)$$

The orientation factors from WAXD are mainly due to the crystalline part, therefore no information about the orientation of the amorphous phase can be obtained. Small angle X-ray scattering (SAXS) was used to compare the level of the lamellae formation for the different samples and to estimate the long period between lamellae.

Mechanical analysis and puncture resistance: Tensile tests were performed using an Instron 5500R machine equipped with an environmental chamber for tests at high temperature. The procedure used was based on the D638-02a ASTM standard. Puncture tests were performed using a 10 N load cell of the Instron machine used for the tensile tests. A needle with 0.5 mm radius was used to pierce the samples. The film was held tight in the camping device with a central hole of 11.3 mm. The displacement of the film was recorded against the force and the maximum force was reported as the puncture strength. Strain rates of 50 mm/min and 25 mm/min were utilized during tensile and puncture tests, respectively.

Morphology: To clearly observe the crystal arrangement of the precursor films, an etching method was employed to remove the amorphous part. The films were dissolved in a 0.7% solution of potassium permanganate in a mixture of 35 vol% of

orthophosphoric and 65 vol% of sulphuric acid. The potassium permanganate was slowly added to the sulphuric acid under rapid agitation. At the end of the reaction time, the samples were washed as described in Olley and Bassett [17].

A field emission scanning electron microscope (FE-SEM- Hitachi S4700) was employed for the observation of the etched precursor films and microporous membranes surfaces as well as cross-sections. This microscope provides high resolution of 2.5 nm at a low accelerating voltage of 1 kV and high resolution of 1.5 nm at 15 kV with magnification from 20x to 500kx.

Water vapor transmission: The permeability to water vapor was measured via a MOCON PERMATRAN-W Model 101K at room temperature. It is composed of three chambers: an upper chamber containing liquid water and separated from the center chamber by two porous films. Water vapor diffuses from the first film to fill the space between the films to reach 100% relative humidity (*RH*). The center chamber is separated from the lower one by the test film. The diffused vapor is swept away by N_2 gas to a relative humidity (*RH)* sensor.

BET measurement: To obtain the surface area of the membranes, a Micromeritics, BET Tristar 3000 was used. A nitrogen and helium gas mixture was continuously fed through the sample cell, which was kept at liquid nitrogen temperature. At different pressures, the total volume of nitrogen gas adsorbed on the surface was measured. The volume of gas needed to create an adsorbed monomolecular layer was calculated as follows [18]:

$$\frac{P}{P^{\circ}[V(1-\frac{P}{P^{\circ}})]} = \frac{1}{V_m c} + \frac{c-1}{V_m c}\frac{P}{P^{\circ}} \qquad (7.9)$$

where P is the experimental pressure, P^o is the saturation pressure, V is the volume of the adsorbate, V_m is the volume of gas required to form an absorbed monomolecular layer, and c is a constant. The procedure for estimating the surface area from Eq. 7.9 can be found elsewhere [19].

7.3 Results and discussion

7.3.1 Rheological and film characterization

The complex shear viscosities as a function of frequency for the resins are shown in Figure 7.1. The PP reveals larger viscosity compared to the HDPE in the Newtonian region (low frequencies) while the data cross over in the power-law region (high frequencies). It is well known that for the production of multilayer films the viscosity of the neat polymers should be close to each other in order to prevent instabilities and non uniformities at the interface. In our case, the viscosities of the PP and HDPE are nearly identical at the processing deformation rates (large frequencies). The inset in Figure 7.1 compares the weighted relaxation spectra of the resins evaluated from dynamic moduli (G', G'', ω) using the NLREG (non linear regularization) software [20] (the vertical dash lines represent the range of frequencies covered during the experiments). The area under the spectrum curve represents the zero-shear viscosity of the melt and as expected is

larger for the PP compared to the HDPE. By considering the characteristic relaxation time, λ_c, corresponding to the peak of the curves, it can be seen that the HDPE exhibits slightly larger relaxation time than the PP.

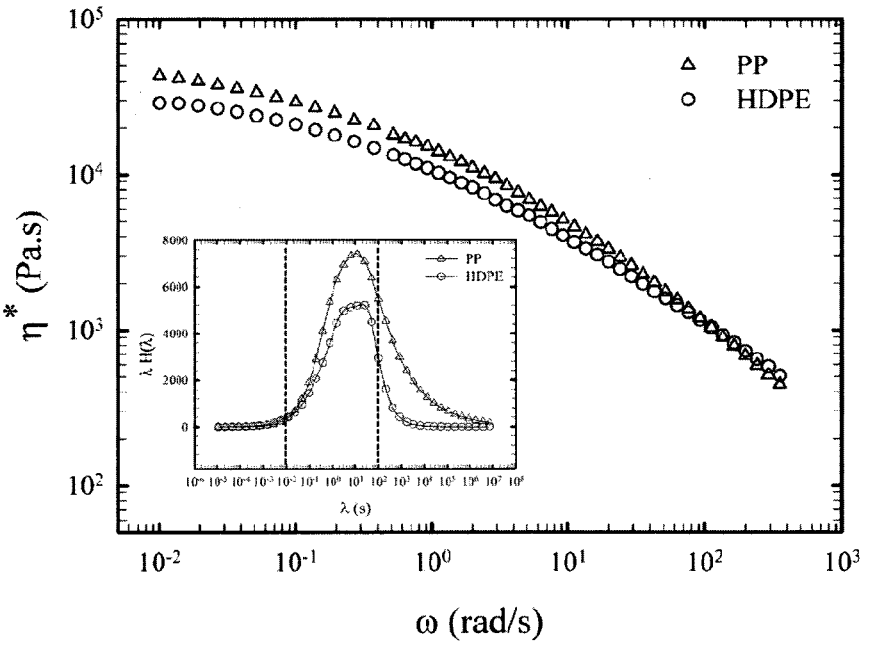

Fig. 7.1 Complex viscosity as a function of angular frequency; T=190 °C. The inset is weighted relaxation spectra for the resins (the vertical dash lines represent the range of frequencies covered during the experiments).

Figure 7.2 presents the DSC heating thermograms for the PP and HDPE monolayer films as well as their multilayer film. The PP and HDPE exhibit melting peaks around 162 °C and 129 °C, respectively, whereas the multilayer film shows two melting peaks at the same temperatures as the single layers. The PP monolayer film prepared under DR=90 and H-AFR showed a crystallinity of 44.2% and the HDPE monolayer film produced under the same conditions had a crystallinity of 74.0%. The crystallinities of

the components in the multilayer film were slightly lower than that measured for the monolayer films.

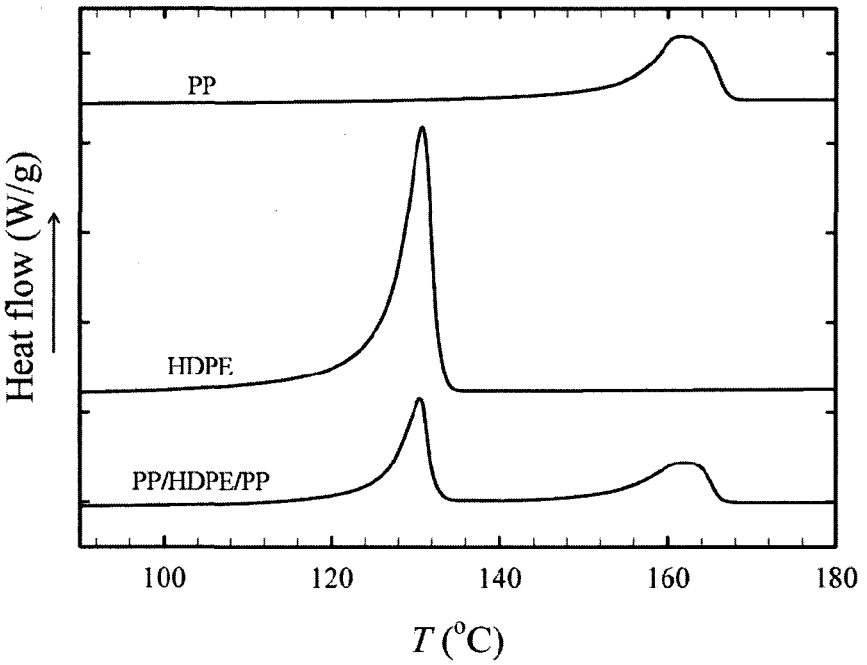

Fig. 7.2 DSC heating thermograms for single layers as well as multilayer films; DR=90 and H-AFR.

To produce microporous membranes by the stretching technique, precursor films with an adequate orientation and alignment of the crystal lamellae are needed [9,10]. The higher the crystalline alignment in the precursor, the better is expected the lamellae separation and, as a consequence, the larger the porosity and permeability of the microporous membranes. In this study, the roles of draw ratio (DR), cooling air flow rate (AFR), and annealing on the crystalline alignments of single layer films as well as the components in a multilayer film are probed using WAXD and FTIR.

From literature, in PE, two major types of crystallization can occur depending on the magnitude of stress in flow [21]: low stress produces kebabs in the form of twisted ribbons resulting in off-axis 110 and meridian 200 diffractions. In contrast, high stress produces flat kebabs (planar crystal structure) leading to the appearance of equatorial 110 and 200 diffractions. When the magnitude of flow is in-between, an intermediate arrangement is formed, resulting in off-axis 200 and 110 diffractions [21]. However, PP under flow usually generates planar lamellar morphology with less dependence on the flow magnitude [12].

The WAXD patterns as well as the diffraction intensity profiles for the PP and HDPE shown in Figure 7.3 reveal four and two diffractions, respectively, corresponding to the indicated crystallographic planes. As described earlier, for the PP, the 110 and 040 crystalline planes and for the HDPE, the 110 and 200 crystalline planes were used to obtain the orientation of the unit crystal cell axes (*a*, *b*, and *c*) with respect to MD, TD, and ND. However, due to overlapping of the 111 crystalline plane of PP and both 110 and 200 crystalline planes of HDPE, WAXD cannot be employed for the orientation measurement of the HDPE phase in the multilayer film. FTIR compensates this disadvantage of WAXD, since the infrared absorption peaks for PP and HDPE are quite distinct.

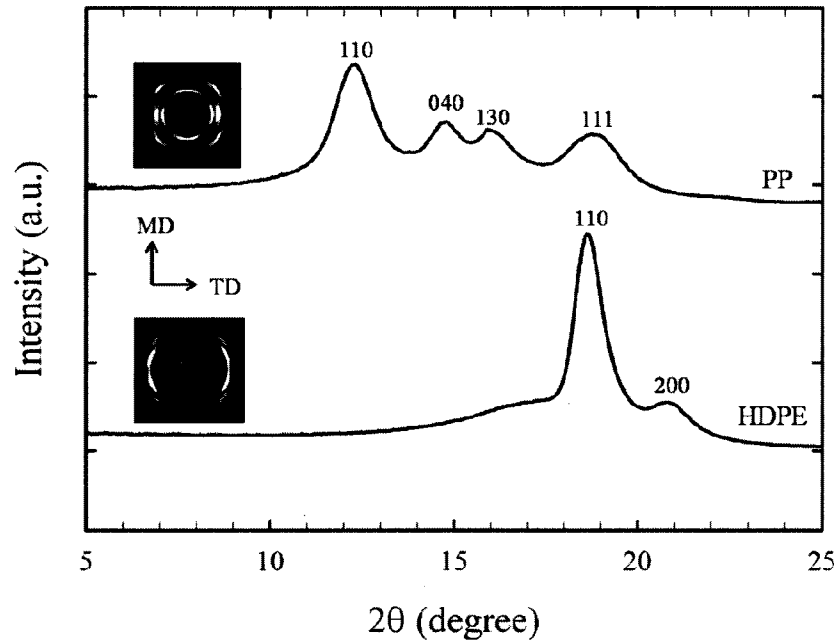

Fig. 7.3 2D WAXD patterns and diffraction spectrum with integration through the circles for PP and HDPE monolayer films; DR=90 and H-AFR.

Figure 7.4 demonstrates the effect of AFR, DR, and annealing on the diffraction patterns as well as on the pole figures of the PP and HDPE monolayer films and the PP in the trilayer film. The normal to the 110 plane is the bisector of the *a* and *b* axes and 040 and 200 are along the *b*-axis and *a*-axis of unit crystal cells, respectively [16]. From the WAXD patterns of the PP monolayer (Figure 7.4a), it is clear that by increasing DR and AFR or annealing, the arcs become sharper and more concentrated in the center, implying more orientation. The pole figures of the PP single layer obtained at DR=60 and L-AFR reveal slight orientations of the 110 and 040 planes in MD and ND, respectively. The PP precursor produced under DR=60 and H-AFR shows significant orientation of the 110 plane along TD. In addition, increasing DR (i.e. DR=90) improves the orientation of the 110 plane along TD and that of the 040 plane (*b*-axis) is aligned in

both TD and ND. Furthermore, annealing causes the 110 plane to be more aligned in TD. Similar trends for the influences of DR, AFR, and annealing on the crystalline alignment of the PP component in the trilayer film are observed (Figure 7.4b). However, the 110 plane of the PP in the multilayer made at DR=60 and H-AFR has not moved into TD, indicating less orientation than the PP monolayer produced under the same conditions. A less alignment of the PP in the multilayer compared to that in single layer is also observed for the films produced under high DR (i.e. DR=90) and for the annealed ones and this will be discussed later. The four off-axes arcs for the 110 plane of the HDPE are observed in Figure 7.4c that is a typical behavior of the twisted lamellar structure of PE where the *a*-axis rotates around the *b*-axis, resulting in the rotation of the reciprocal vector of the 110 plane. The pole figures of the HDPE single layer obtained at DR=60 and L-AFR shows a significant orientation of the 200 plane (*a*-axis) along MD and that of the 110 plane along both TD and ND. Increasing air cooling to the films surface (i.e. H-AFR) improves orientation of the 110 plane along TD and reduces the alignment of the 200 plane along MD drastically. Additionally, increasing DR and annealing slightly enhance the orientation of the crystallographic planes of the HDPE monolayer. As mentioned previously, to determine the orientation of the HDPE phase in the multilayer film, an FTIR technique was used and the results are discussed in the following paragraph. However, before presenting the results, it should be mentioned that the orientation functions for the HDPE single layer obtained using FTIR were slightly

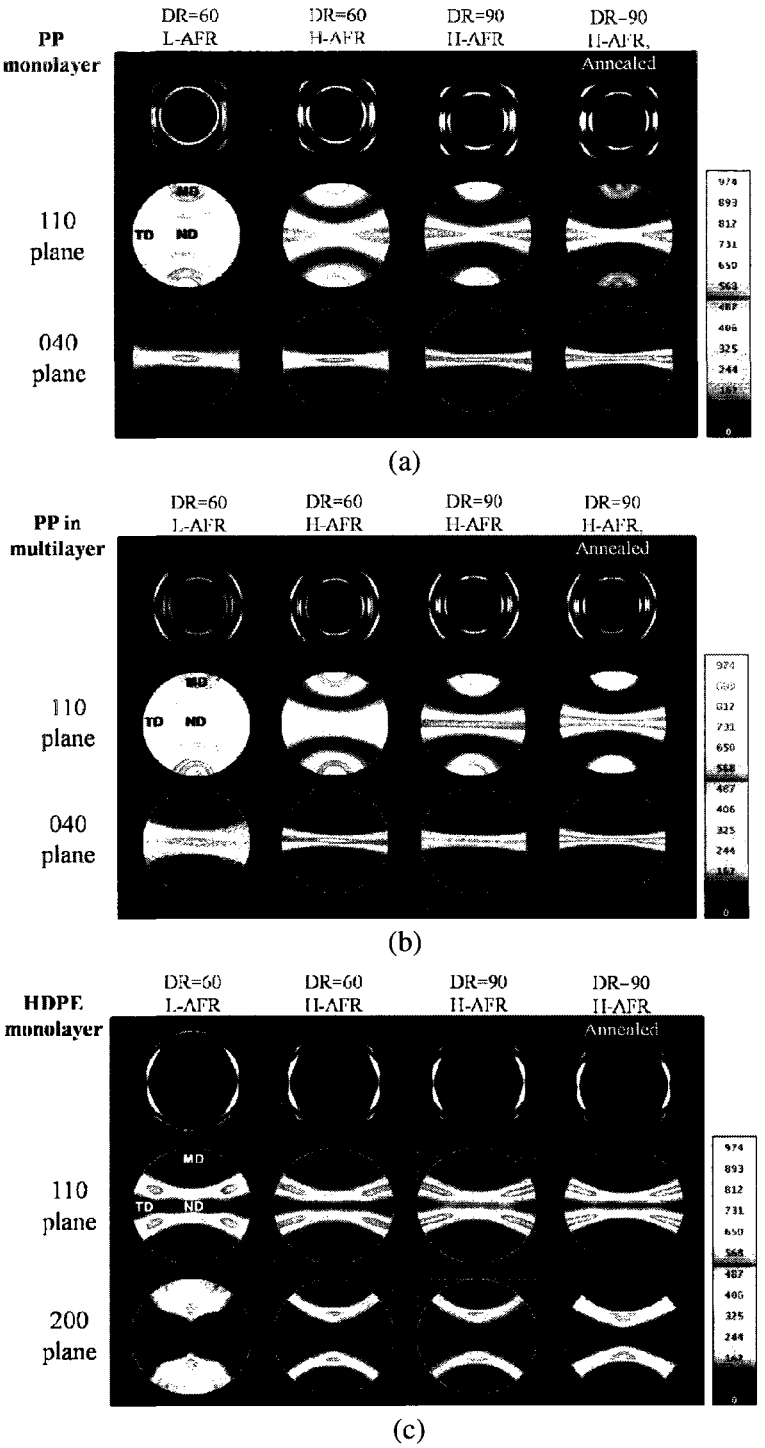

Fig. 7.4 2D WAXD patterns and pole figures for films obtained under different DR, AFR, and annealing: a) PP monolayer, b) PP in multilayer, and c) HDPE monolayer. Annealing was performed at 120 °C for 30 min.

larger than the ones from WAXD pole figures. These discrepancies in the values of measured *c*-axis orientation may be due to different factors such as peak deconvolution, contributions of the amorphous phase, etc. as discussed for PE and PP elsewhere [22,23].

The orientation features, in terms of $\cos^2(\phi)$ of the crystalline axes (i.e. *a*, *b*, and *c*) along MD, TD, and ND obtained from the Herman orientation function for the PP and HDPE single layers as well as the components in the multilayer film are presented in Figure 7.5. As expected, the *c*-axis orientation characteristics along MD (Figure 7.5a) improve by increasing AFR and DR or by annealing. In addition, obviously, the *c*-axis alignment of the HDPE (both in the monolayer and multilayer) is significantly lower than that of the PP and also the *c*-axis orientation along MD of the PP and HDPE in the multilayer is lower than in the monolayer made under the same conditions, in accordance with the results discussed in Figure 7.4. As reported above, the HDPE has much higher crystallinity and larger heat of fusion compared to the PP, resulting in a large heat release during its crystallization. This can explain lower orientation of the PP component in the trilayer than the PP monolayer. Looking at the orientation characteristics of the *a*-axis (Figure 7.5b), significant orientation of this axis along MD is seen for the HDPE whereas the PP shows much lower values, confirming the presence of a different row-nucleated lamellar crystal morphology in the HDPE compared to the PP. As pointed out earlier, the large alignment of the *a*-axis along MD is a typical behavior of the twisted lamellar morphology. However, it should be noted that

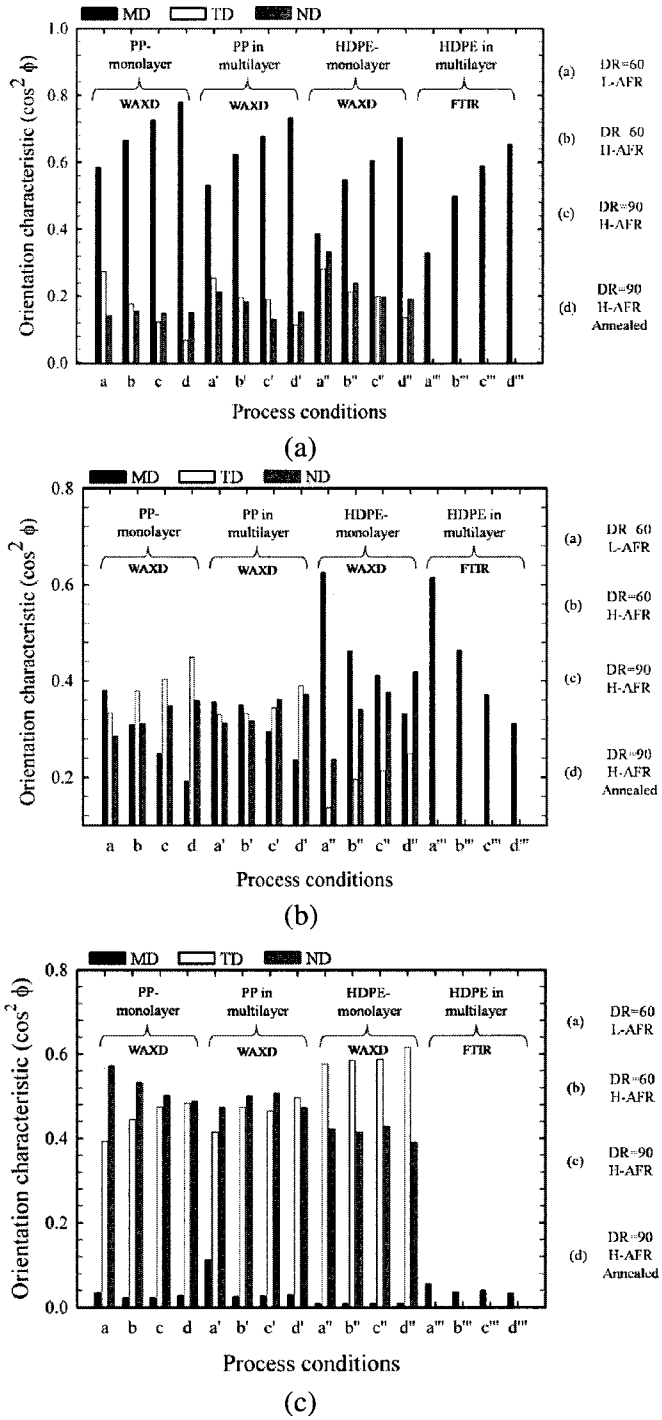

Fig. 7.5 Orientation characteristics as $\cos^2(\phi)$ of the crystal axes (*a*, *b* and *c*) along MD, TD, and ND for the films obtained under different DR, AFR, and annealing: a) *c*-axis, b) *a*-axis, and c) *b*-axis. Annealing was performed at 120 °C for 30 min.

orientation of the *a*-axis along MD decreases drastically by increasing AFR and DR. This implies the presence of an intermediate structure between twisted and flat kebabs for HDPE, which was supported by the appearance of off-axis equatorial 110 and 200 diffractions in their WAXD patterns as well as pole figures (see Figure 7.4c). The orientation characteristics of the *b*-axis along MD are very small for both the PP and HDPE (Figure 7.5c) and do not change drastically with the process conditions.

Figure 7.6 illustrates the SAXS patterns as well as the Lorentz corrected intensity profile for the precursor and annealed single layer films of the PP and HDPE obtained at DR=90 and H-AFR. The equatorial streak in the SAXS patterns is attributed to the formation of the shish, while the meridian maxima are attributed to the lateral lamellae or kebabs [24]. Looking at the meridian intensity, the formation of more lamellae for the HDPE is obvious. In addition, it is clear that the contribution of the shish to the crystalline phase is much less than that of lamellae, confirming the results of Somani et al. [25] for PE and PP. The long period distance, L_p, was estimated from the position of the Lorentz corrected intensity maxima, as demonstrated in Figure 7.6 ($L_p=2\pi/q_{max}$ where q is the intensity vector, $q=4\pi\sin\theta/\lambda$,). Annealing shifts the peak of the PP precursor to lower values, indicating an increase of the long period spacing. However, annealing does not impact the peak position of the HDPE, implying that L_p remains mainly unchanged. The lamellae thickness, l_c, could be calculated by multiplying L_p by the crystalline fraction (see the legend in figure). The values of L_p and l_c for the PP precursor film are much smaller than those for the HDPE and increase with annealing.

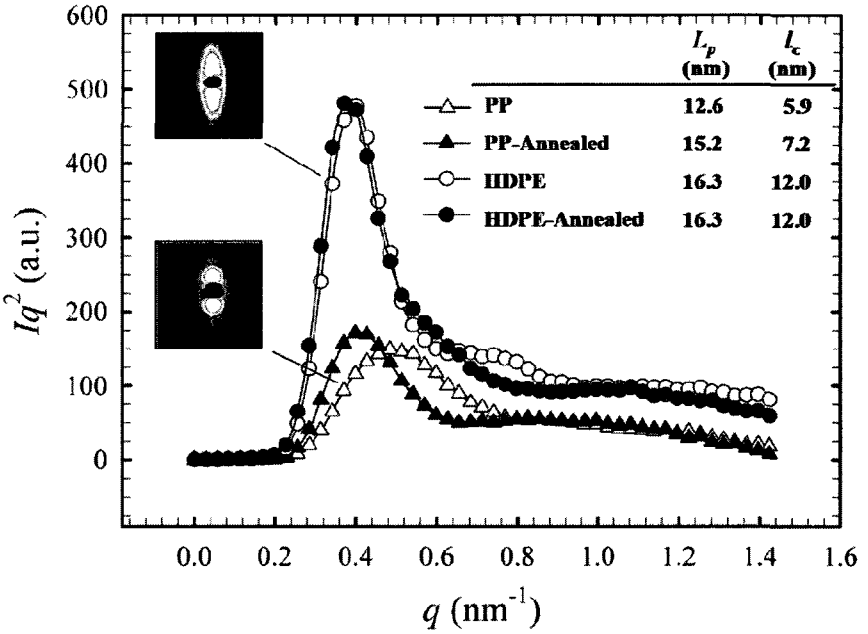

Fig. 7.6 Lorentz corrected SAXS intensity profiles for precursor and annealed PP and HDPE films. Annealing was performed at 120 °C for 30 min; DR=90 and H-AFR.

Differences in the crystal structure and arrangement of the precursor films can be clearly visualized from SEM surface images of the etched films (etching removes the amorphous region), as demonstrated in Figure 7.7. A uniform and ordered stacked lamellar structure and a uniform twisted lamellar morphology are seen for the PP and HDPE films, respectively (higher magnification images are shown on the right), confirming the XRD results of Figures 7.4 and 7.5.

It is well established that the structure of the crystalline phase strongly influences the mechanical properties of films. Zhang et al. [26] studied the microstructure of LLDPE, LDPE, and HDPE blown films and showed that the type of oriented structure was greatly dependent on the type of polyethylene as well as on the processing

conditions. In our previous study [12], significant increases in the Young modulus, yield stress, tensile

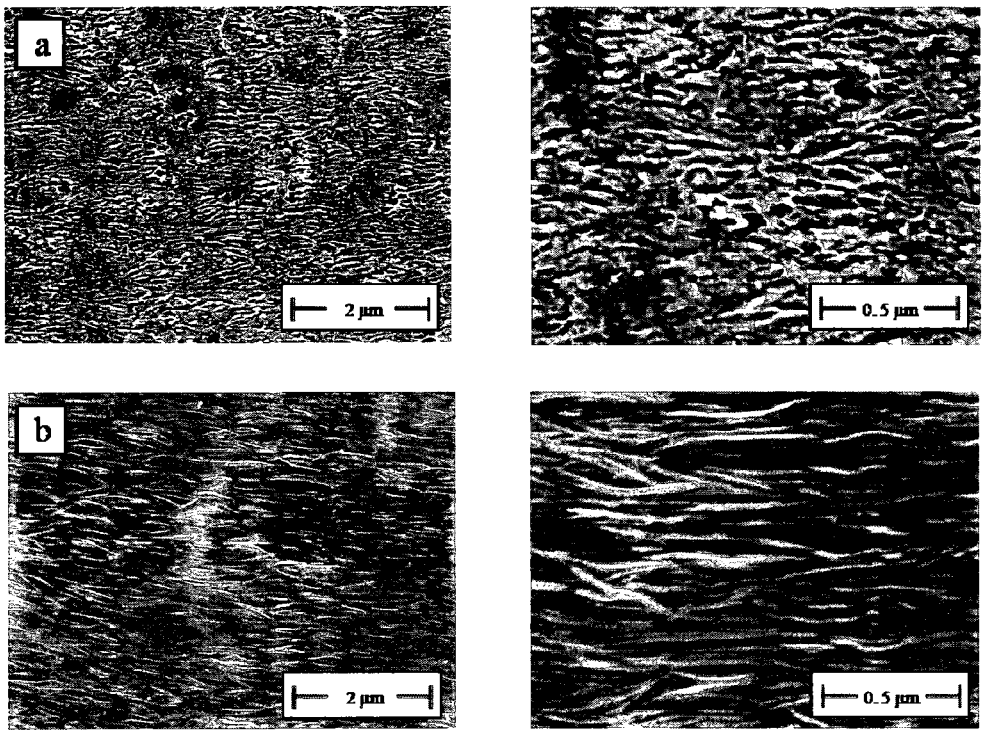

Fig. 7.7 SEM micrographs of the surface of the etched precursor films: a) PP and b) HDPE. The right images are high magnification micrographs of the left ones; DR=90 and H-AFR. MD ↑ and TD →

strength, tensile toughness along MD and a drastic decrease in the elongation at break along TD were observed for polypropylene cast films subjected to air cooling. Table 7.2 reports the results on the mechanical properties of the films along MD and TD for DR=60 and 90. All the properties improve along MD and elongation at break along TD reduces with increasing DR, due to better crystal alignment. Additionally, it should be noticed that the mechanical properties of the trilayer films are between those of the monolayer films.

In general, blends of PP and HDPE are known to be immiscible systems. The interfacial morphology for the etched multilayer film is illustrated in Figure 7.8. Some transcrystallization zone around the interface can be easily distinguished; they are the PE

Table 7.2 Mechanical properties of the cast films along MD and TD (the numbers in parentheses indicate the standard deviation of the measurements); H-AFR.

	Mechanical properties along MD				Mechanical properties along TD	
	Young modulus (MPa)	Tensile strength (MPa)	Tensile toughness (MPa)	Strain at break	Tensile strength (MPa)	Strain at break
PP-DR=60	898.0 (35.5)	46.7 (5.2)	106.7 (3.3)	4.0 (0.1)	16.2 (1.9)	0.456 (0.191)
PP-DR=90	956.5 (34.2)	60.7 (3.3)	154.0 (16.8)	3.7 (0.3)	16.6 (1.4)	0.065 (0.005)
HDPE-DR=60	973.7 (90.0)	51.0 (1.5)	88.6 (4.2)	2.9 (0.1)	16.5 (1.6)	0.014 (0.003)
HDPE-DR=90	1138.8 (69.8)	51.7 (2.3)	96.0 (5.1)	3.2 (0.2)	21.6 (0.4)	0.021 (0.002)
PP/HDPE/PP-DR=60	920.0 (85.2)	55.0 (5.1)	140.4 (20.0)	5.2 (0.4)	15.6 (1.2)	0.024 (0.003)
PP/HDPE/PP-DR=90	1037.3 (126.0)	60.4 (3.4)	164.5 (18.9)	4.0 (0.5)	18.7 (3.0)	0.036 (0.004)

lamellae nucleated on the PP. In other words, crystallization of the PE overgrows at the interface. A transcrystalline layer is formed when a large number of nuclei are formed on an interface such that the crystallites are forced to grow normal to the interface and when a larger difference in crystallization temperature is present [26], which is the case between HDPE and PP (see Table 7.1). It should also be noted that at the interface, the HDPE lamellae penetrate into the PP phase. Some transcrystallization at the interface of

a PP and a LLDPE was moreover observed by Zhang and Ajji [23]. However, in that case, the LLDPE lamellae could not diffuse into the PP. This behavior was explained as due to the much lower crystallization temperature, T_c, of the LLDPE (i.e. 104 °C) than the PP (i.e. 112 °C) [26] that prevented the penetration of the LLDPE lamellae into the initially crystallized PP layer. However, in our case, T_c of the HDPE (i.e. 118 °C) was larger than that of the PP (i.e. 112 °C), hence the HDPE crystallites could diffuse inside the molten PP layer.

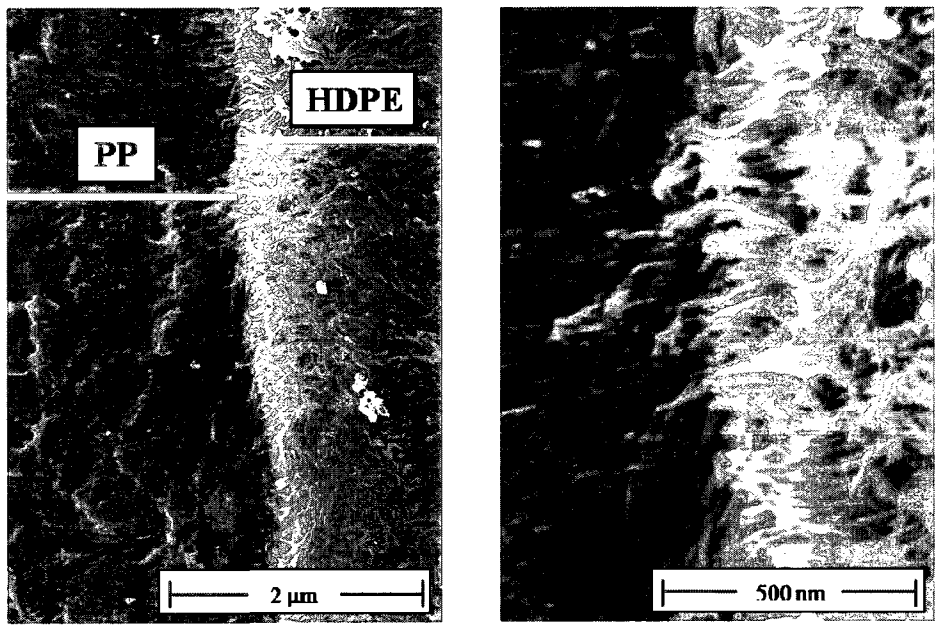

Fig. 7.8 Interfacial morphology of etched PP/HDPE multilayer films at different magnifications; DR=90 and H-AFR. MD ↑ and ND →

The produced precursor films should be annealed at a proper temperature before to be cold and hot stretched. As annealing is performed at a temperature that is above the onset of mobility in the crystalline structure (T_α), it is postulated that during annealing, the lamellae twist and orient perpendicular to the machine direction. Also, melting of

small lamellae and their recrystallization with better orientation can occur [10]. Our previous study [10] showed that annealing at 140 °C without extension was the optimum annealing condition for PP. However, because T_m of the HDPE is around 129 °C, the annealing temperature of the trilayer film should be lower than the HDPE melting point and above the alpha transition temperature, T_α, of the PP ($T_{\alpha,PP}$ =110 °C obtained from the dynamic mechanical thermal analysis). Therefore, we selected 120 °C for annealing of the trilayer film. In order to be able to compare the results, the single layer precursor films were annealed at the same temperature.

7.3.2 Membrane characterization

Figure 7.9 presents SEM micrographs of the surface of the monolayer microporous membranes prepared at the cold and hot stretching extensions of 55% and 75%, respectively. The details about the optimum cold and hot stretching levels will be discussed later. The distribution of interlamellar tie chains in the precursor films may not be uniform [27]. Therefore, it is believed that the micropores are first developed in region with a small amount of tie chains. It is clear that the size of the pores in the HDPE microporous membrane is much greater than in the PP membrane. The longer interlamellar microfibrils (bridges) in the HDPE porous membrane compared to the PP porous membrane are believed to be due to the longer tie chains in the precursor film of the former. It should be mentioned that the surface morphology of the PP/HDPE/PP membrane (not shown) was somewhat similar to the surface structure of the PP monolayer exhibited in Figure 7.9.

Figure 7.10 illustrates SEM micrographs of the cross-section of the multilayer porous membrane. In Figure 7.10a, it is obvious that a porous HDPE layer has been sandwiched between two porous PP layers while the three layers have almost identical thicknesses. Figures 7.10b and 10c present the interface between the layers at different magnifications. Similar to the surface micrographs, it is clearly recognized that the HDPE layer has much larger pores than the PP layer. Additionally, a reasonable adhesion between the

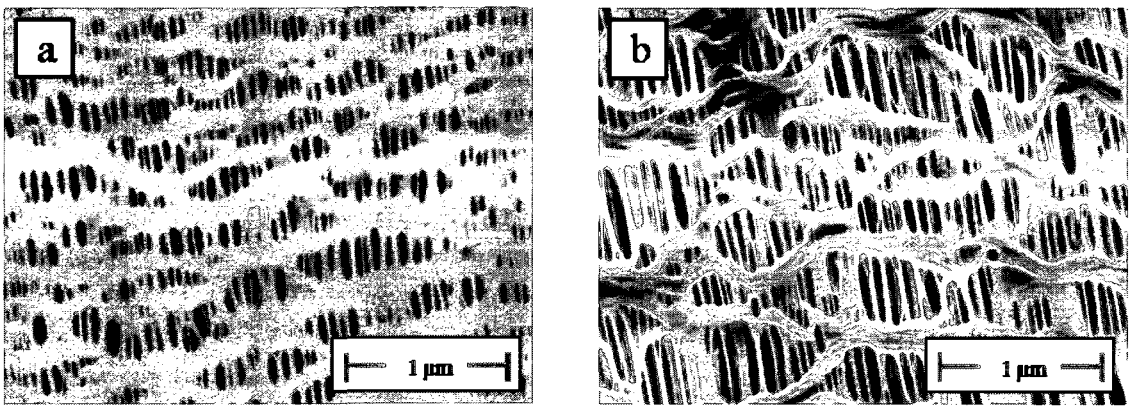

Fig. 7.9 SEM micrographs of the surface of microporous membranes (20 μm thick): a) PP and b) HDPE; DR=90, H-AFR, cold stretching of 55%, followed by hot stretching of 75%. MD ↑ and TD →

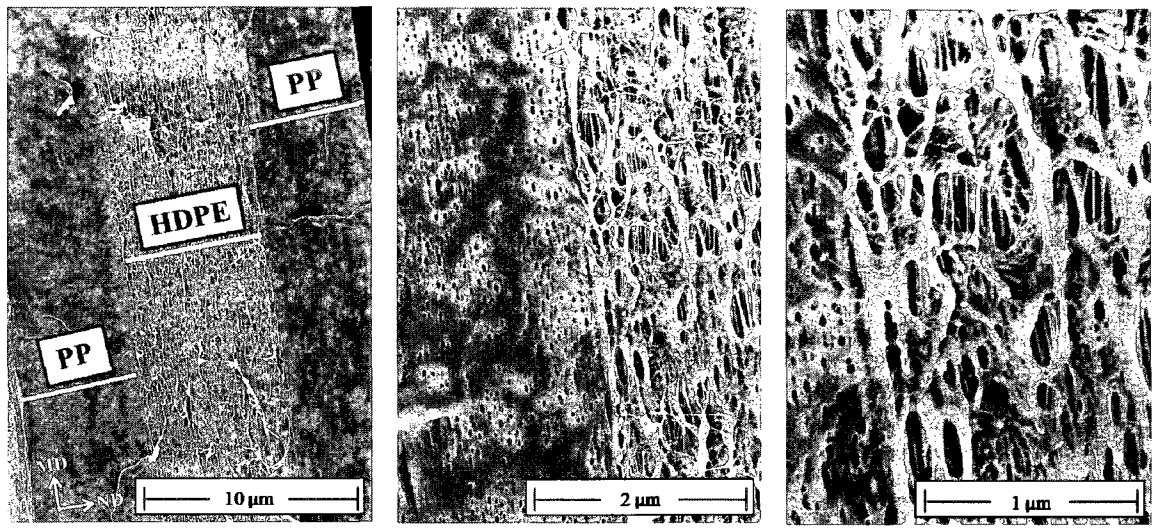

Fig. 7.10 SEM micrographs of the cross-section of trilayer microporous membranes (20 μm thick) at different magnifications; DR=90, H-AFR, cold stretching of 55%, followed by hot stretching of 75%.

layers is seen, which can be explained by the transcrystallization and penetration of the HDPE lamellae into the PP layer observed in the cross-section image of the trilayer precursor film shown in Figure 7.8.

Table 7.3 presents the mechanical properties along MD and TD as well as the puncture resistance along ND for the microporous membranes. Obviously, the porous membranes have nearby similar tensile responses in MD and, as expected, the tensile properties along TD are considerably smaller than in MD. However, the PP microporous membranes show a much lower strain at break along TD than that the HDPE and multilayer membranes. In addition, due to the presence of the elongated interlamellar microfibrils in the microporous membranes, a pronounced increase in the tensile strength and a drastic decrease in elongation at break are observed for the membranes compared to the precursor films (see Tables 7.2 and 7.3). The decrease in the modulus

for the membranes compared to the precursor films is possibly due to the lower interconnection between the lamellae in the membranes as a result of the tie chains pulled out during the pores formation. Also as shown by Table 7.3, the maximum piercing force is considerably larger for the PP membrane than the HDPE membrane, which can be explained by the smaller pores and lower porosity for the former. Therefore, it could be concluded that in the PP/HDPE/PP membranes, the side layers (i.e. PP) improve the puncture resistance drastically.

7.3.3 Effect of cold and hot stretching

In the preparation of porous membranes using the stretching technique, voids are formed by cold stretching and enlarged by subsequent hot stretching [6,7]. According

Table 7.3 Mechanical properties of microporous membranes (20 μm thick). Annealing was performed at 120 °C for 30 min; DR=70, cold stretching of 55% followed by hot stretching of 75% (the numbers in parentheses indicate the standard deviation of the measurements).

	Mechanical properties along MD			Mechanical properties along TD		Normalized maximum force for piercing
	Young modulus (MPa)	Tensile strength (MPa)	Strain at break	Tensile strength (MPa)	Strain at break	(N/μm)
PP	335.0 (69.5)	119.0 (25.1)	0.62 (0.07)	10.9 (1.5)	0.07 (0.01)	0.14 (0.02)
HDPE	315.8 (39.9)	127.3 (11.1)	0.79 (0.14)	7.5 (0.2)	2.70 (0.36)	0.08 (0.01)
PP/HDPE/PP	320.7 (46.0)	121.7 (21.5)	0.82 (0.09)	11.1 (1.0)	1.80 (0.51)	0.12 (0.01)

Johnson [7], the micro void morphologies produced via this method are a consequence of inter lamellar separation, which takes place at temperatures above T_g of the specific

semicrystalline polymers. Sadeghi et al. [9] found that the pores size of the cold stretched films obtained from the PP resins with distinct M_w did not vary significantly. However, a difference in the lamellae thickness was observed. Our previous study [10] showed that the water vapor transmission rate (WVTR) of the cold stretched PP films increased as the stretch ratio increased up to 30% while further stretching resulted in a reduction in WVTR. To find the optimum cold stretching extension for the present PP as well as the HDPE, cold stretching was carried out under predetermined levels of extension while the amount of hot stretching was kept constant. Figure 7.11 reports the WVTR values normalized (multiplied) by the membrane thickness as a function of applied extension for the PP and HDPE monolayer porous membranes. It is obvious that 25% extension during cold stretching is not enough to initiate pores formation for the HDPE and PP. A monotonous increase in WVTR of the HDPE membranes was observed after further extension during cold stretching. In contrast, a significant enhancement in WVTR of the PP membranes was observed when 30% extension was applied while further stretching reduced the normalized WVTR. Additionally, it is clear that both the PP and HDPE have almost identical permeabilities at 55% cold drawing. Therefore, 55% was found to be the optimum cold stretching extension for the fabrication of the multilayer membranes.

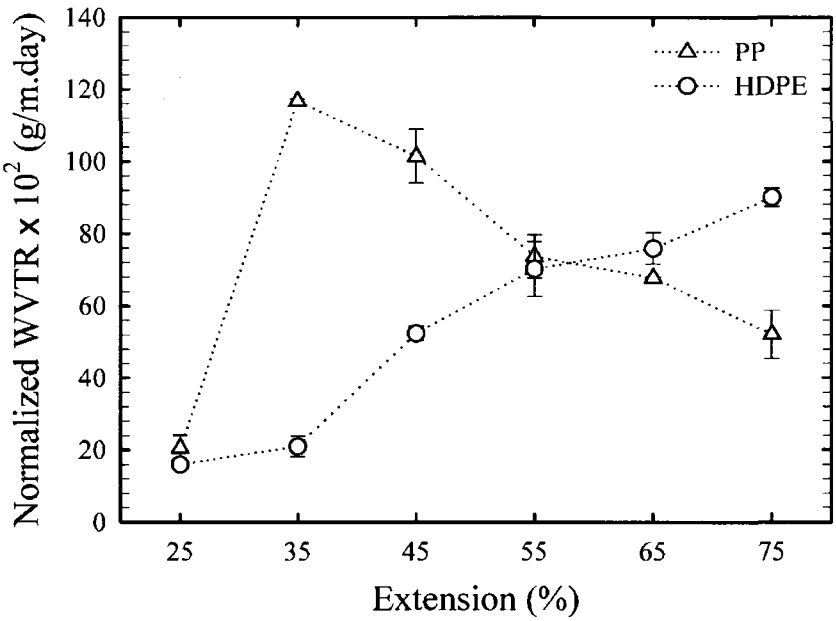

Fig. 7.11 Normalized water vapor permeability for PP and HDPE membranes as a function of extension during cold stretching at 25 °C; DR=90, H-AFR, hot stretching of 75%.

To clearly understand the reasons for the opposite extension dependence of the PP and HDPE in the first stretching step, we show in Figure 7.12 the stress-strain responses along MD during cold stretching as well as sketches illustrating the morphology evolution. The stress-strain response for the PP exhibits an elastic response at low deformations, plastic behavior at medium deformations, and strain hardening at high elongations. Compared to the PP, the HDPE displays a wider plastic deformation zone and a strain-hardening region with much lower slope. In the elastic region, the extension is not enough to initiate pores formation whereas in the plastic zone the lamellae begin to separate and an increased extension enlarges the pores size [14]. According to Zue et al. [28], for PP at low temperatures, as the chain mobility is relatively low, tie chains from entanglements may initiate fragmentation of neighboring crystal lamellae upon

stretching. In fact, in the strain-hardening zone, the load is transferred to the tie chains [29], hence the continuous increase in stress leads to lamellae fragmentation (see the sketches in Figure 7.12). In Figure 7.12, it is obvious that 35% extension is the onset of strain-hardening for the PP. Therefore cold stretching of the PP beyond 35% reduces the crystal alignment, yielding a lower permeability. However, due to the wider plastic region for the HDPE, possibly due to the longer tie chains than for the PP, increasing the level of extension monotonically promotes lamellae separation without breaking lamellae, resulting in an enhancement of WVTR with increasing elongation. To confirm these results, we moreover used BET to determine the pore volume and specific surface area of the membranes obtained for 35% cold stretching followed by 75% hot stretching. The results are presented in Figure 7.13. Obviously, at all the range of experimental pressure, the PP membrane adsorbed more nitrogen, indicating greater porosity for the PP membrane compared to the HDPE membrane. The specific surface area of 43.4 and 19.3 m^2/g were recorded for the PP and HDPE microporous membranes, respectively, supporting the better porosity for the PP membrane made at 35% cold stretching.

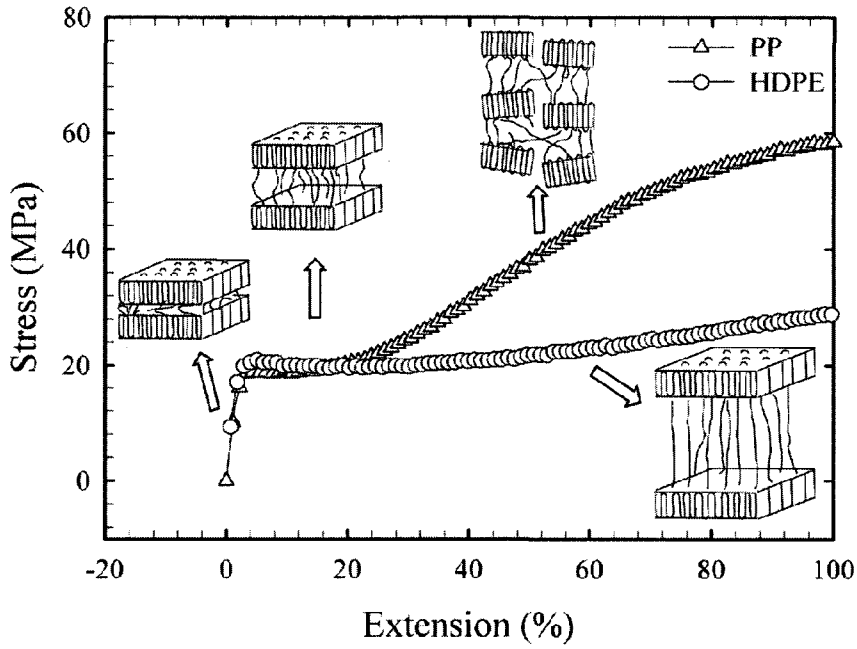

Fig. 7.12 Stress-strain behavior for annealed PP and HDPE during the cold stretching step; Annealing was performed at 120 °C for 30 min; DR=90, H-AFR.

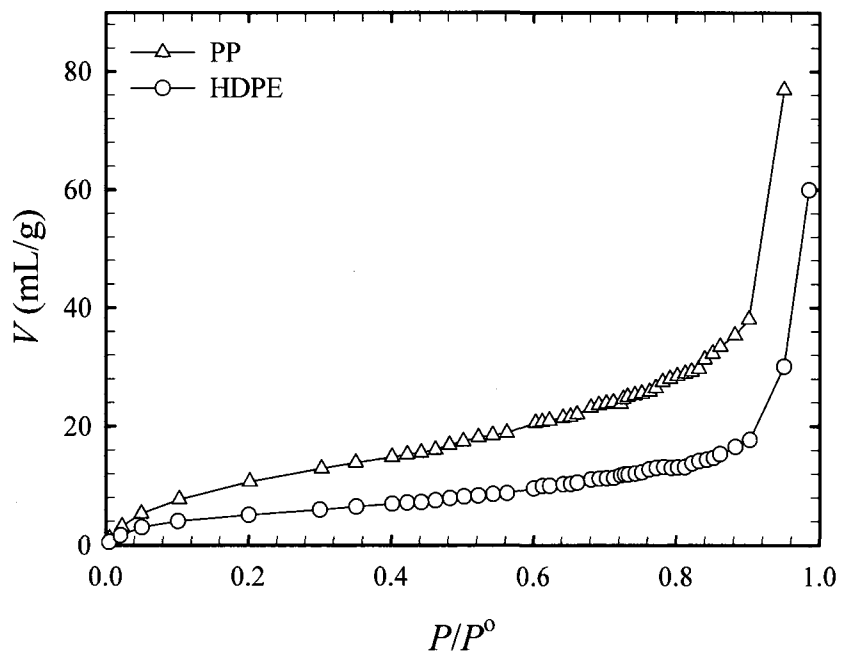

Fig. 7.13 Nitrogen adsorption isotherms (77 K) measured by BET for PP and HDPE membranes. DR=90, H-AFR, cold stretching of 35%, followed by hot stretching of 75%.

Similar experiments (data not shown) were performed to investigate the influence of hot stretching level. In contrast to the cold stretching behavior of the PP, no maximum was observed when the cold drawn films were stretched to different hot stretch levels. The pores created in cold stretching are enlarged during the hot stretching step and consequently enhance WVTR. More flexibility of the lamellae at high temperatures can be a reason for the increase of pore size with increasing extension ratio. Figure 7.14 illustrates the interfacial morphology of the multilayer film membrane prepared with a cold stretching of 55% followed by a hot stretching of 175%. This is 100% more total stretching than for the one shown in Figure 7.10. Very large pores, particularly for the HDPE, are seen and that can explain the improvement in WVTR by increasing hot stretching. The arrows in Figure 7.14 show the connection between interlamellar microfibrils and the lamellae in the HDPE layer. At such a high level of extension, it is clear that the microfibrils have been connected to the surrounded lamellae by bundles of small blocks. According to Yu [27], at high stretch levels, lamellae located at the end of the microfibrils break into small blocks and tilt along the stretching direction.

Finally, the trilayer microporous membranes obtained at 55% cold extension followed by 75% hot extension showed WVTR values about 30% lower than the monolayer PP and HDPE obtained under the same conditions. This could be due to the presence of the interface and lower orientation of the PP and HDPE components in the multilayer film than the monolayer ones (see Figures 7.4 and 7.5).

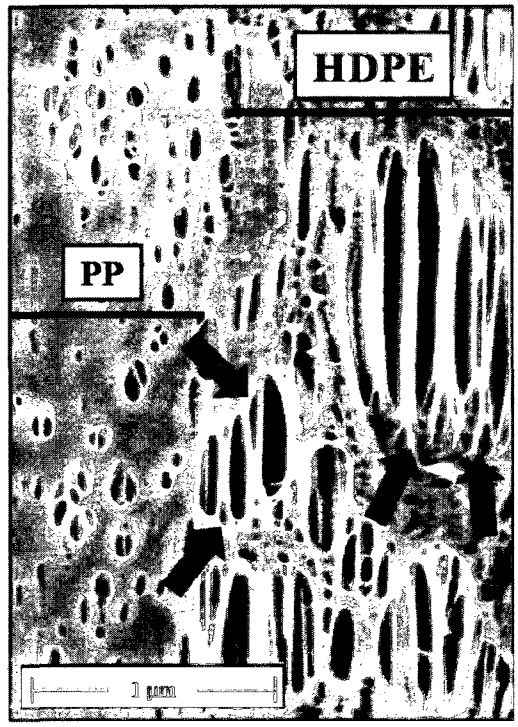

Fig. 7.14 SEM micrographs of the cross-section of multilayer microporous membranes; DR=90, H-AFR, cold stretching of 55%, followed by hot stretching of 175% (the arrows indicate the connection of the HDPE interlamellar microfibrils to the lamellae).

7.4 Conclusions

In this work, we have investigated the structure and performances of microporous membranes made from monolayer and trilayer films of the PP and HDPE. Our findings can be summarized as follows:

- Significant effects of cooling air flow rate (AFR), draw ratio (DR), and annealing on the crystal orientation of the PP and HDPE monolayer films as well as the components in the multilayer one were observed.
- At low AFR, the HDPE showed a twisted lamellar morphology whereas at high AFR an intermediate structure between twisted and flat kebabs was detected.

- A transcrystallization of the HDPE lamellae penetrating into the PP at the interface of the multilayer films was observed and was explained by the difference in the resin crystallization temperature.
- At high cold stretching extensions, the pore size and porosity of the HDPE membranes was much larger compared to those from the PP produced under the same conditions. This was attributed to the longer tie chains in the HDPE membranes compared to the PP.
- Good adhesion at the interface of the porous multilayer membrane was attributed to the transcrystallization observed in the precursor film interface.
- A pronounced increase in the tensile strength and drastic decreases in modulus and elongation at break along MD were observed for the membranes compared to the precursor films.
- By increasing the applied extension during cold stretching, water vapor transmission rate (WVTR) monotonically rose for the HDPE while for the PP, WVTR first increased significantly and then decreased.
- The trilayer microporous membranes showed a lower permeability than the monolayer membranes, possibly due to the presence of the interface as well as the lower orientation of the PP and HDPE components in the multilayer film compared to the monolayer films.

7.5 Acknowledgement

Financial support from NSERC (Natural Science and Engineering Research Council of Canada) and from FQRNT (Fonds Québécois de Recherche en Nature et Technologies) is gratefully acknowledged. We also acknowledge the large infrastructure grant received from the Canadian Foundation for Innovation (Government of Canada and Province of Quebec), which allowed us to build the unique POLYNOV facility. We are also thankful to Messrs. P. Cigana, L. Parent and P.M. Simard for their technical help. Finally, we are thankful to ExxonMobil and NOVA Chemicals who donated the resins used in this work.

7.6 References

[1] Venugopal G, Moore J, Howard J, Pendalwar S. J Power Sourc 1998;77:34-41.

[2] Dahn JR, Fuller EW, Obrovac M, van Sacken U. Solid State Ionics 1994;69:265-270.

[3] Wei X, Haire C. 20070196638A1, 2007 US Patent.

[4] Gozdz AS, Schmtz CN, Tarascon JM, Warren PC. 5607485, 1997 US Patent.

[5] Okazaki MA, kuwana MI, Nagoya ST, Kasugai TI. 4921653, 1990 US Patent.

[6] Sadeghi F. Developing of microporous polypropylene by stretching, Ph.D thesis, Ecole polytechnique de Montreal, 2007.

[7] Johnson MB. Ph.D thesis, Virginia Polytechnic Institute and State University, 2000.

[8] Sadeghi F, Ajji A, Carreau PJ. Polym Eng Sci 2007;47:1170-1178.

[9] Sadeghi F, Ajji A, Carreau PJ. J Membr Sci 2007;292:62-71.

[10] Tabatabaei SH, Carreau PJ, Ajji A. J Membr Sci 2008;325:772-782.

[11] Sadeghi F, Ajji A, Carreau PJ. J Polym Sci Polym Phys 2008;46:148-157.

[12] Tabatabaei SH, Carreau PJ, Ajji A. Submitted to Polymer.

[13] Arroyo M, Lopez-Manchado MA. Polymer 1997;38:5587-5593.

[14] Ajji A, Sammut P, Huneault MA. J Appl Polym Sci 2003;88:3070-3077.

[15] Ward IM, Coates PD, Dumoulin MM. Solid Phase Processing of Polymers 2000 Hanser publisher.

[16] Alexander LE. X-ray diffraction methods in polymer science, Wiley Inter Science, New York, 1969.

[17] Olley RH, Bassett DC. Polymer 1982;23:1707-1710.

[18] Brunauer S, Emmett PH, Teller E. J Am Chem Soc 1938;60:309-319.

[19] Li J, Favis BD. Polymer 2001;42:5047-5053.

[20] Honerkamp J, Weese J. Rheol Acta 1993;32:65-73.

[21] Keum JK, Burger C, Zuo F, Hsiao BS. Polymer 2007;48:4511-4519.

[22] Ajji A, Zhang X, Elkoun S. Polymer 2005;46:3838-3846.

[23] Zhang X, Ajji A. Polymer 2005;46:3885-3393.

[24] Agarwal PK, Somani RH, Weng W, Mehta A, Yang L, Ran S, Liu L, Hsiao B. Macromolecules 2003;36:5226-5235.

[25] Somani RH, Yang L, Zhu L, Hsiao BS. Polymer 2005;46:8587-8623.

[26] Zhang XM, Elkoun S, Ajji A, Huneault MA. Polymer 2004;45:217-229.

[27] Yu TH. Ph.D thesis, Virginia Polytechnic Institute and State University, 1996.

[28] Zuo F, Keum JK, Chen X, Hsiao BS, Chen H, Lai SY, Wevers R, Li J. Polymer;2007:6867-6880.

[29] Samuels RJ. J Polym Sci Polym Phys Ed 2003;17:435-568.

CHAPTER 8

Structure and Properties of MDO Stretched Polypropylene[4]

Seyed H. Tabatabaei, Pierre J. Carreau, and Abdellah Ajji

CREPEC, Chemical Engineering Department, Ecole Polytechnique, C.P. 6079, Succ. Centre ville Montreal, QC, H3C 3A7 Canada

Abstract

Two polypropylene cast films of different crystalline structures (one with coexisting small rows of lamellae and spherulites and the other with only a spherulitic structure) were prepared by extrusion. The produced cast films were uniaxially hot drawn at T = 120 °C using a machine direction orientation (MDO) unit and the changes in structure and morphology were examined and related to barrier as well as tear and puncture properties. Structural changes in terms of the degree of crystallinity and crystal size distribution, orientation of the amorphous and crystalline phases, and the deformation behavior at the crystal lattice and lamellae scales were investigated using differential scanning calorimetry (DSC), Fourier transform infrared spectroscopy (FTIR), wide angle X-ray diffraction (WAXD), and small angle X-ray scattering (SAXS), respectively. A significant effect of the original crystal morphology on the alignment of the amorphous and crystalline phases was observed from FTIR and WAXD. The results

---

[4] Submitted to *Polymer*.

also revealed that the deformation behavior of the crystal structure was dependent on the draw ratio (DR). Our findings showed that by increasing DR the crystal lamellae first broke up and oriented along the drawing direction and then, at large DR, they were deformed and created a fibrillar structure. Morphological pictograms illustrating the effects of original morphology and draw ratio on the stretched film microstructure are proposed. The tear resistance along the machine direction (MD) decreased significantly with increasing DR whereas the puncture resistance increased drastically. Finally, the oxygen transmission rate (OTR) of the MDO stretched films could be correlated with the orientation parameters as well as the β-relaxation peak magnitude of the amorphous tie chains.

8.1 Introduction

Polypropylene is one of the most widely used polymers for the production of plastic films. Applications cover packaging to microporous membranes. There are two main industrial processes for the production of PP films: film blowing and cast film extrusion followed by stretching (above and below the melt temperature). Although the films obtained from both processes could have the same thicknesses, their properties such as mechanical and clarity could be quite different as a result of the differences in the process conditions.

It is well known that uniaxial or biaxial drawing of the polymeric films such as polypropylene, polyester, polyketone, nylon, and ethyl vinyl alcohol can drastically

affect their properties, particularly mechanical, impact, barrier, and optical properties [1-7].

The machine direction orientation (MDO) process is widely used for uniaxial stretching of polyethylene and polypropylene films. The MDO unit can be operated either in-line or off-line with extrusion and is controlled via variables such as: the distance between the draw rollers, draw ratio, drawing speed, drawing times (a film can be stretched many times), drawing temperature, and heat-setting conditions [1]. The stretching is usually performed at a high temperature, below the melt temperature of the polymer, and results in a highly oriented film that causes anisotropy in properties. The drawing process usually improves the strength and barrier properties, but brings some drawbacks such as a reduction of the tear resistance along the machine direction (MD) and a lowering of elongation at break along the transverse direction (TD) [1]. For example, Schut [2] used the MDO process to improve the barrier properties of nylon and ethyl vinyl alcohol, but the films were brittle and had low tear resistance in MD.

The stretching of a well oriented shish-kebab crystal morphology involves the separation of the stacked lamellae, leading to pores formation and subsequent microporous membrane generation [8,9]. However, the drawing of polypropylene films possessing spherulitic crystal structure involves a morphological transformation of the spherulites, which will affect their final properties.

The evolution of the crystal structure of biaxial as well as uniaxial drawn films has been investigated in the literature [10-13]. Nie et al. [10] studied the morphological

development during biaxial stretching of polypropylene films using atomic force microscopy (AFM). According to their results, the biaxial orientation of polypropylene involved a morphological transformation of the spherulites into a network of microfibrils, which was also confirmed by Diez et al. [11]. Sadeghi et al. [1] studied the morphology development during MDO stretching of PP. Their results showed a fibrillar crystalline structure at a high draw ratio (DR), such as DR=6. Also, a distinctive improvement in the mechanical, clarity, and barrier properties was reported as DR increased. Using in-situ small angle X-ray scattering (SAXS) and wide angle X-ray diffraction, Zuo et al. [12] investigated the structure of polypropylene films during uniaxial stretching for various temperatures. The rate of crystal alignment during deformation at high temperatures was found to be slower than that at low temperature, but the final orientation during deformation at high temperatures was higher due to the larger applied strain. Sakurai et al. [13] investigated the structural deformation behavior of polypropylenes with different molecular weight (M_W), molecular weight distribution (MWD), and isotacticity (IT) during hot drawing process. Significant effects of M_w, MWD, and IT on the mechanical properties, morphology as well as stress distribution in the hot stretched samples were observed.

Although few authors have investigated the relationship between biaxial orientation and particularly barrier properties of various resins, very little has been reported on uniaxial drawing involving industrial scale capabilities. In this study, precursor films with a spherulitic structure and coexisting small rows of lamellae and spherulites were

produced and MDO oriented using an industrial scale production line. A detailed investigation of the structure evolution with stretching has been carried out and relationships between morphological transformation and barrier, tear, and puncture properties are discussed.

8.2 Experimental

8.2.1 Material

A commercial linear polypropylene (PP5341) supplied by ExxonMobil and having a melt flow rate (MFR) of 0.8 g/10min (under ASTM D1238 conditions of 230 °C and 2.16 kg) was selected. Its molecular weight was estimated from the relationship between the zero-shear viscosity and molecular weight [14] and found to be around 772 kg/mol. The resin showed a polydispersity index (PDI) of 2.7, as measured using a GPC (Viscotek model 350) with 1,2,4-trichlorobenzene (TCB) as a solvent and column temperature of 140 °C. Its melting point, T_m, and crystallization temperature, T_c, obtained from differential scanning calorimetry at a rate of 10 °C/min, were 161 °C and 118 °C, respectively.

8.2.2 Film preparation

The cast films were prepared using an industrial multilayer cast film from Davis Standard Company (Pawcatuck, CT) equipped with a 122 cm width slit die and two cooling drums. The extrusion was carried out at 220 °C and the distance between the die

exit to the nip roll was 15 cm. Two precursor films of different microstructures were produced. (1) Coexisting rows of lamellae and spherulites: this morphology could be obtained when the cast roll was set at a high temperature (e.g. 120 °C) and the polymer melt at the die exit was subjected to a high draw ratio (e.g. 30). (2) Only spherulitic structure: this structure could be produced when the cast roll was set at a low temperature (e.g. 40 °C) and the film at the die was subjected to a low draw ratio (e.g. 3). Additional details regarding the process conditions could be found elsewhere [15]. In this paper, these precursor films are denoted as P-1 and P-2, respectively. Figure 8.1 represents SEM surface images of the etched P-1 precursor film reported in [15]. We observe that both rows of lamellae and spherulites are present in this precursor film. To get the same final thickness of 150 μm for P-1 and P-2, the die gap was set at 4.5 and 0.45 mm, respectively.

In the MDO unit, the produced films were uniaxially stretched at 120 °C and under draw ratios ranging from 1 to 7.2. Stretching at draw ratios above 7.2 resulted in film breakage.

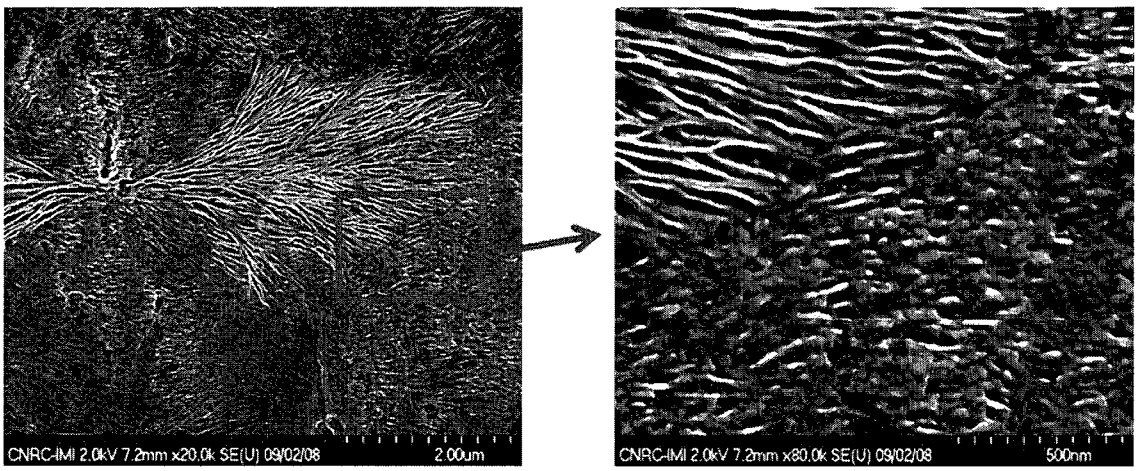

Fig. 8.1 SEM micrographs of the surface of the P-1 precursor film [15]. The right image is a high magnification micrograph of the section corresponding to the rectangle. MD ↑ and TD →

8.2.3 Film characterization

Thermal analysis: The thermal properties of specimens were analyzed using a differential scanning calorimeter (DSC) Q 1000 from TA Instruments. The thermal behavior of the films was obtained by heating from 50 to 220 °C at a rate of 10 °C/min. The reported crystallinity results were calculated using a heat of fusion of 209 J/g for a fully crystalline polypropylene (PP) [16].

Fourier transform infrared spectroscopy (FTIR): For FTIR measurements, a Nicolet Magna 860 FTIR instrument from Thermo Electron Corp. (DTGS detector, resolution 2 cm^{-1}, accumulation of 128 scans) was used. The beam was polarized by means of a Spectra-Tech zinc selenide wire grid polarizer from Thermo Electron Corp. The measurement is based on the absorption of infrared light at certain frequencies corresponding to the vibration modes of atomic groups present within the molecule. In addition, if a specific vibration is attributed to a specific phase, the orientation within

that phase can be determined [17]. If the films are oriented, the absorption of plane-polarized radiation by a vibration in two orthogonal directions, specifically parallel and perpendicular to a reference axis (MD), should be different. The ratio of these two absorption values is defined as the dichroic ratio, D [17]:

$$D = \frac{A_{\parallel}}{A_{\perp}} \tag{8.1}$$

where $A_{\parallel}$ is the absorption parallel and $A_{\perp}$ is the absorption perpendicular to a specific reference axis. The Herman orientation function of this vibration is obtained according to [17]:

$$F = \frac{2}{3\cos^2\alpha - 1} \cdot \frac{D-1}{D+2} \tag{8.2}$$

where α is the angle that the transition moment makes with the polymer chain axis.

For polypropylene, absorption at the wavenumber of 998 cm^{-1} is attributed to the crystalline phase (c-axis) while absorption at the wavenumber of 972 cm^{-1} is due to the contribution of both crystalline and amorphous phases. From the former absorption, the orientation of the crystalline phase, F_c, can be determined while from the latter, the average orientation function, F_{avg}, is obtained. The orientation of the amorphous phase, F_a, can be calculated according to:

$$F_{avg} = X_c F_c + (1 - X_c) F_a \tag{8.3}$$

where X_c is the degree of crystallinity. Using FTIR, the global, crystalline and amorphous orientations can be determined.

X-ray diffraction: XRD measurements were carried out using a Bruker AXS X-ray goniometer equipped with a Hi-STAR two-dimensional area detector. The generator was set up at 40 kV and 40 mA and the copper CuK_α radiation (λ = 1.542 A°) was selected using a graphite crystal monochromator. The sample to detector distance was fixed at 9.2 cm for wide angle diffraction and 28.2 cm for small angle X-ray scattering analysis. To get the maximum diffraction intensity, several film layers were stacked together to obtain a total thickness of about 2 mm.

Wide angle X-ray diffraction (WAXD) is based on the diffraction of a monochromatic X-ray beam by the crystallographic planes (*hkl*) of the polymer crystalline phase. Using a pole figure accessory, the intensity of the diffracted radiation for a given *hkl* plane is measured as the sample is rotated through all possible spherical angles with respect to the beam. This gives the probability distribution of the orientation of the normal to *hkl* plane with respect to the directions of the sample.

The Herman orientation function of a crystalline axis is given by [18]:

$$f = \frac{(3\cos^2\phi - 1)}{2} \qquad (8.4)$$

where ϕ is the angle between the unit cell axes (*a*, *b*, and *c*) and reference axes. Details about the calculations can be found elsewhere [18].

The orientation factors from WAXD are mainly due to the crystalline part, therefore no information about the orientation of the amorphous phase can be obtained.

Small angle X-ray scattering (SAXS) was used to compare the level of lamellae formation for the different samples.

Puncture and tear analysis: Puncture tests were performed using a 10 N load cell of an Instron 5500R machine. A needle with 0.5 mm radius was used to pierce the samples. The film was held tight in the camping device with a central hole of 11.3 mm. The displacement of the film was recorded against the force (Newton) and the maximum force was reported as the puncture strength.

A standard test method for the tear resistance of plastic films based on ASTM D1922 was used to obtain MD and TD tear resistances. According to this standard, the work required in tearing is measured by the loss of energy of an encoder, which records the angular position of the pendulum during the tearing operation.

Oxygen transmission: Oxygen transmission rates (OTR) were determined using a modification of the ASTM Standard Method D 3985-81 with an Ox-Tran Model 2/21 apparatus (Mocon Inc., Minneapolis, MN) at 25°C. In this paper, all OTR values presented have been normalized (multiplied) by the films thickness. Two films of each specimen were tested and the average value is reported.

Dynamic mechanical thermal analysis (DMTA): Dynamic thermomechanical properties of different samples were characterized using a dynamic mechanical thermal analyzer (DMTA) 2980 from TA Instruments, inside an environmental test chamber (ETC). Specimens cut parallel to the drawing direction were subjected to a dynamic tensile deformation mode. The temperature ranged from -60 °C to 120 °C at a rate of 2

°C/min and a frequency of 1 Hz was applied to the rectangular samples. To generate low temperatures and to control temperature during heating, liquid nitrogen was used. The β transition was determined from the peak magnitude of the tan δ curves.

8.3 Results and discussion

We first present experimental data that clearly demonstrate the effect of draw ratio (DR) and initial crystal morphology on the degree of crystallinity and crystal size distribution, orientation of the amorphous and crystalline phases, deformation behavior at the crystal lattice and lamellae scales. Subsequently, morphological pictograms, illustrating the influence of DR and original morphology on the final structure of the drawn films are proposed. Finally, puncture resistance along the normal direction (ND), tear data along the machine direction (MD), and oxygen transmission rate (OTR) results are presented and their correlations with the structural parameters such as orientation function are reported and discussed.

The effect of draw ratio on the thermal behavior of the films for P-1 is shown in Figure 8.2. The thermogram of the film before drawing (DR=1) exhibits a main melting peak at 158 °C and a small peak at 144 °C. The small peak at 144 °C suggests the presence of a bimodal crystal size distribution (the WAXD measurements for this specimen showed no intensity peaks corresponding to the beta crystal form. Therefore, the presence of this type of crystal is excluded). No peak around 144 °C was observed for the unstretched P-2 sample (not shown), indicating the presence of more uniform

crystal sizes. As seen in Figure 8.2, increasing DR shifts the melting peak, $T_{m,max}$, to much higher values and a shoulder at the same temperature as the melting peak of the unstretched film appears, suggesting again the presence of crystals with different sizes. The shoulder is related to the spherulites and/or rows of lamellae that were not or slightly deformed whereas the peak at the higher temperature is due to the formation of fibrils following the deformation, consistent with the SAXS results that will be discussed later. A double melting point for the specific shish-kebab structure of a polypropylene (PP) has also been observed by Somani et al. [19]. According to Somani et al. [19], the shish in PP had a melting temperature of about 5-10 °C higher than that of the kebabs and about 15-20 °C higher than that for spherulites. Elias et al. [20] reported also a double melting peak for a PP drawn by 5.5 times. They attributed their results to a connectivity of the chains in the shish or fibrils that resulted in a large crystal thickness and, as a consequence, a higher melting point than in the case of the spherulites. In our case, it is believed that by increasing DR, a fibrillar structure is formed, leading to a thicker crystal structure and consequently a higher $T_{m,max}$. The DR dependence of the degree of crystallinity (X_c) of the samples was also evaluated using DSC (not shown). The films obtained from P-1 showed crystallinity around 10% larger than those prepared from P-2. In addition, increasing DR up to 7.2 enhanced the crystallinity by about 10% for both P-1 and P-2.

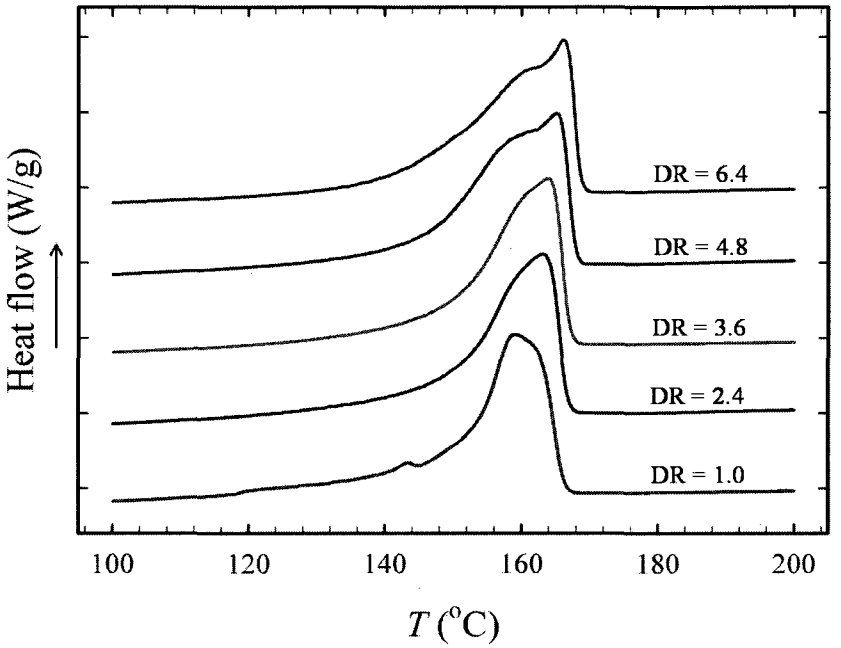

Fig. 8.2 DSC heating thermograms for P-1 films obtained under different draw ratios.

The orientation and arrangement of the phases (either crystalline or amorphous) in polypropylene films are key factors in controlling their final properties. Figures 8.3 and 8.4 present the Herman orientation functions of the crystalline phase, F_c, as well as of the amorphous phase, F_a, obtained from FTIR, respectively. The orientation parameters before stretching (DR=1) are quite low, because of the presence of spherulites. However, as expected increasing DR drastically increases F_c and F_a (Figures 8.3 and 8.4, respectively). Furthermore, the rate of increase of orientation functions for DR between 1 and 3.2 is much larger than beyond DR=3.2, indicating a stronger crystal alignment at the initial stages of deformation. It is postulated that at low DR, break up and tilting of the spherulites and/or rows of lamellae occurs whereas at high deformations the tilted crystals are stretched and form fibrillar structure along the machine direction (MD). Due

to the presence of small rows of lamellae crystals in P-1 films, they show larger crystalline and amorphous orientation functions below DR=1.6 (Figures 8.3 and 8.4, respectively). However, at DR between 1.6 and 3.2, P-2 drawn films show larger alignment compared with those of P-1. This was also confirmed by wide angle X-ray diffraction (WAXD) and our speculation for this behavior will be discussed later. Furthermore, at over DR=3.2, P-1 and P-2 films show almost identical orientation values, indicating somewhat similar microstructures.

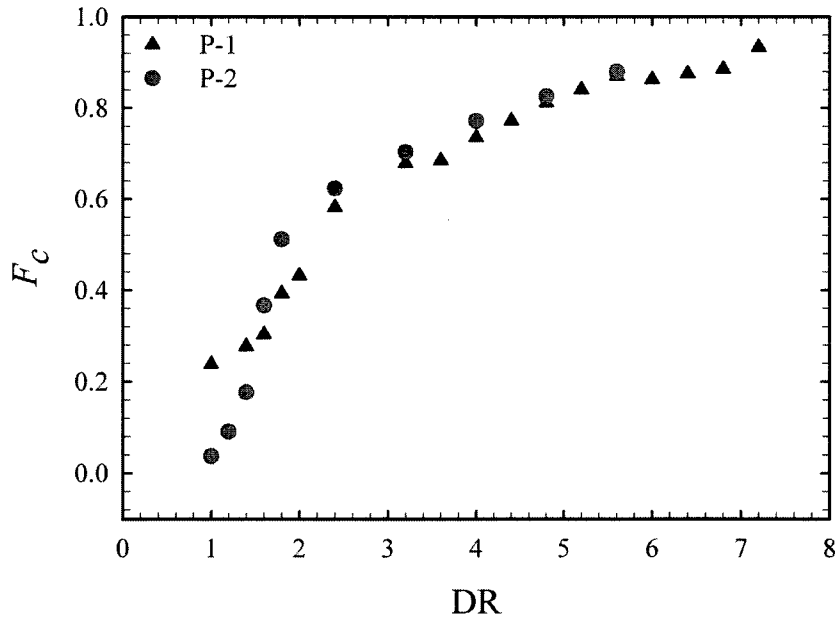

Fig. 8.3 Crystalline orientation function as a function of draw ratio.

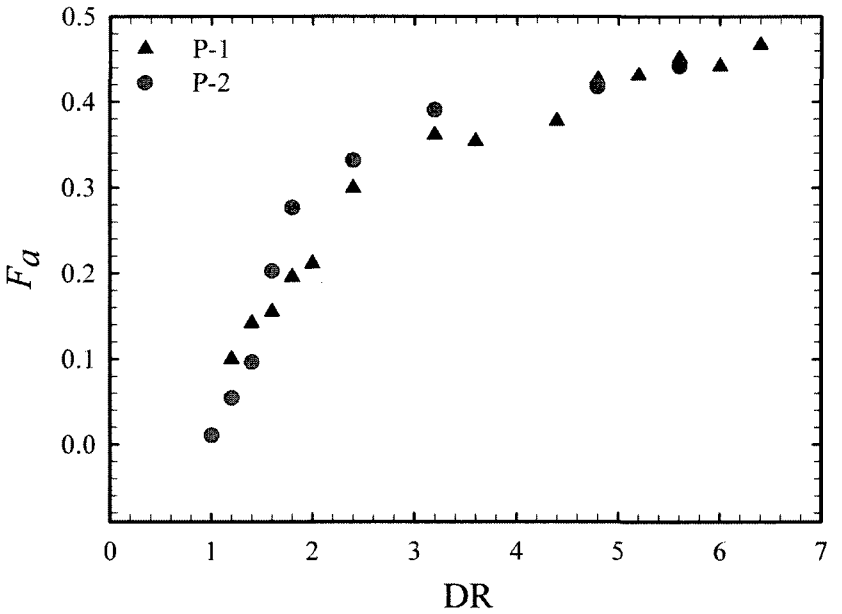

Fig. 8.4 Crystalline orientation function as a function of draw ratio.

The effect of draw ratio on orientation of the crystalline phase was also considered using WAXD, as shown in Figure 8.5. In the WAXD patterns, the first and second rings represent the 110 and 040 crystalline reflections, respectively [18]. At low draw ratios, a diffraction ring is seen for the 110 crystallographic plane for P-1 and P-2, indicating low crystalline phase orientation. However, by increasing DR, the diffraction intensity along the meridian decreases gradually and disappears beyond DR=4.0 and 2.4 for P-1 and P-2, respectively. In contrast, the diffraction intensity in the equator increases drastically when DR increases up to 4, while further increasing DR has slight impacts on the WAXD pattern. As expected, compared with precursor films with coexisting rows of lamellae and spherulites (P-1), the only spherulitic structure (P-2) reveals a ring shape diffraction with less intensities at low DR (e.g. DR=1.2), implying much lower

orientation for P-2. However, at medium draw ratios (e.g. DR=2.8), the diffraction pattern for P-2 demonstrates only arcs that are sharper and more concentrated in the center, indicating more orientation compared to P-1. In PP, due to the larger size of the spherulites than the small rows of lamellae (see Figure 8.1), spherulites are expected to deform more easily than that rows of lamellae. This is possibly why at medium DR, the P-2 samples exhibit a better crystal orientation. In other words, at medium DR, the P-1 films contain some initial rows of lamellae that might not have been completely tilted. At very large DR, no remarkable differences among the WAXD patterns of P-1 and P-2 can be recognized, suggesting that the main structural transformations occur below DR=4.4.

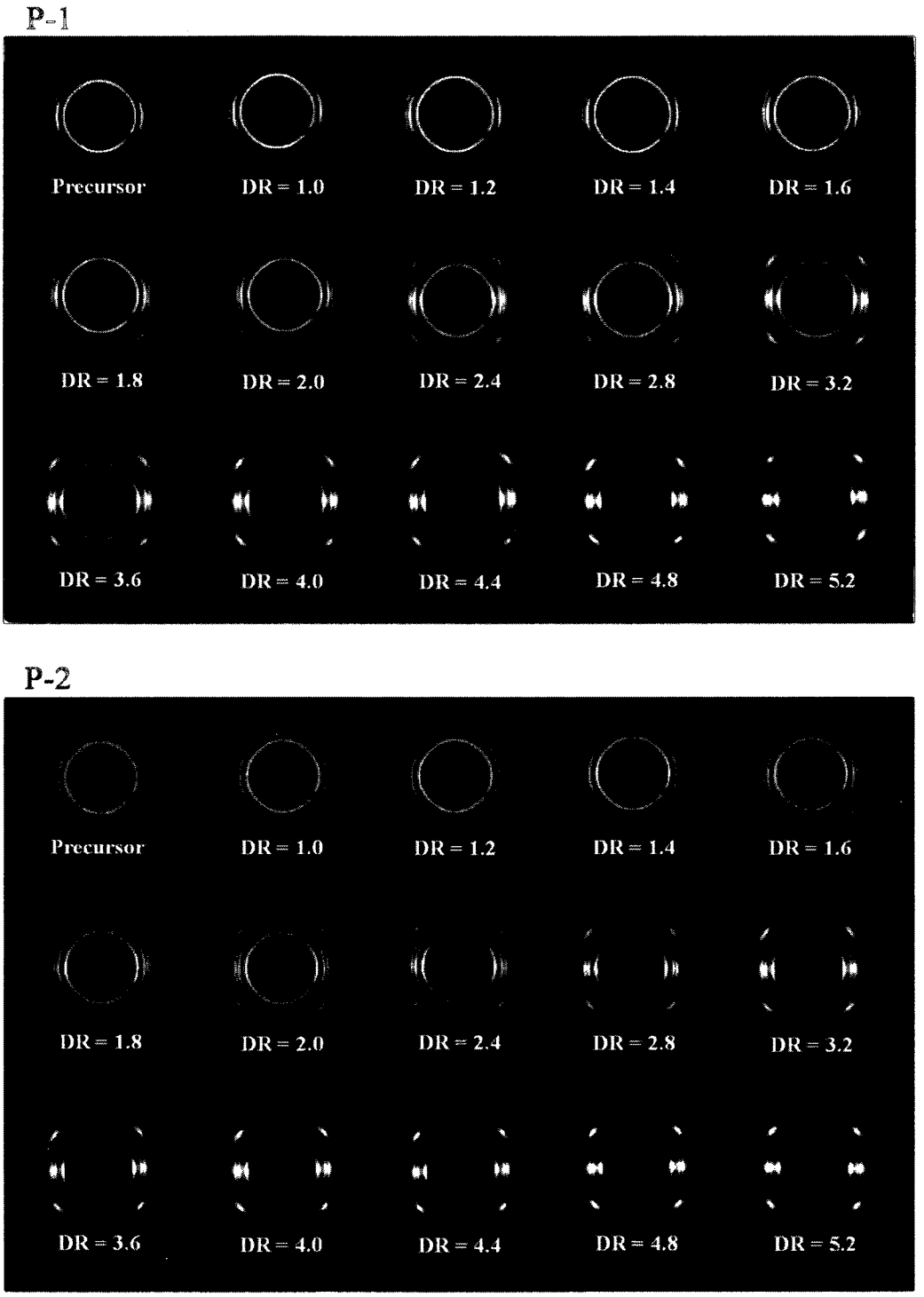

Fig. 8.5 2D WAXD patterns for P-1 (top) and P-2 (bottom) films obtained under different draw ratios.

The crystalline orientation can also be analyzed quantitatively from the pole figures of the 110 and 040 planes and the results for P-1 are illustrated in Figure 8.6. The schematics in the figure represent the crystal alignment based on their pole figures at low, medium, and high stretch ratios. The normal to the 110 plane is the bisector of the *a* and *b* axes and 040 is along the *b*-axis of unit crystal cells [18]. Before drawing (DR=1), slight orientations of the 110 and 040 planes are detected in MD and ND, respectively. Increasing DR causes the orientation of the 110 plane along MD gradually to decrease until it vanishes at large DR. However, this crystallographic plane first moves into TD and then to both TD and ND at large DR. It is clear that the 040 plane (*b*-axis) was initially oriented along ND and upon drawing appreciably moves into TD.

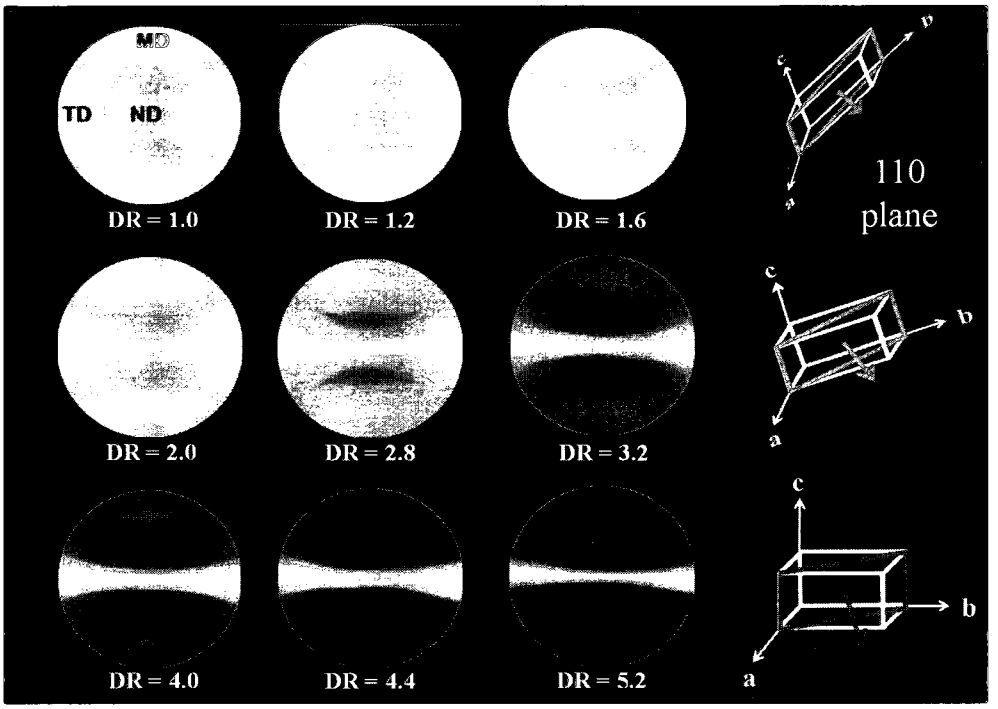

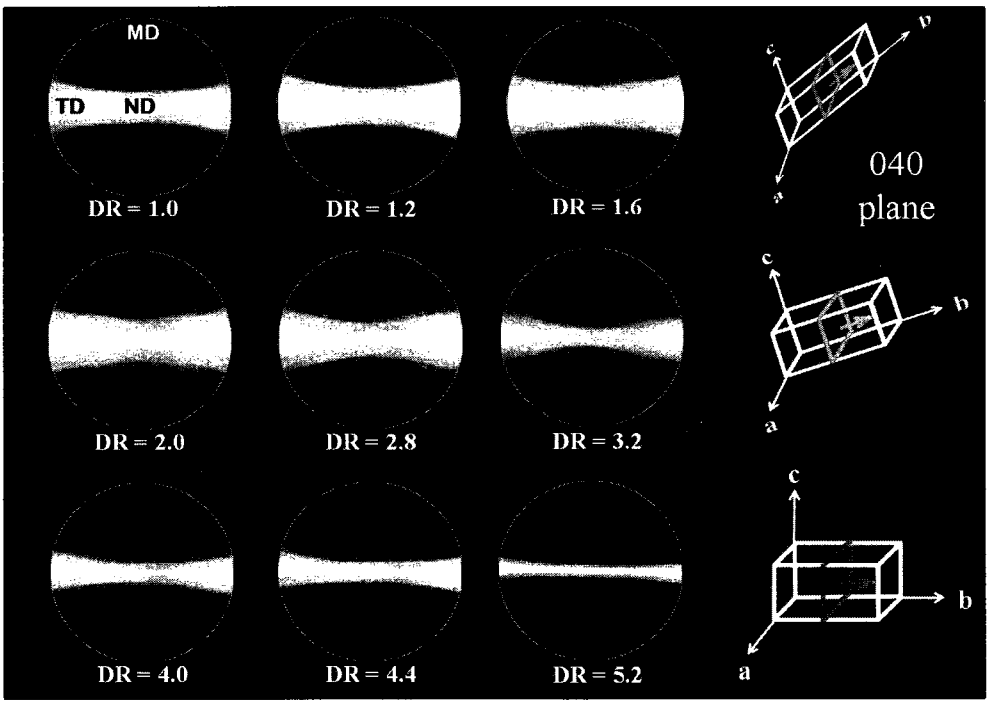

Fig. 8.6 Pole figures of 110 (top) and 040 (bottom) reflections for P-1 films obtained under different draw ratios.

The orientation features, in terms of $\cos^2(\phi)$ of the crystalline axes (i.e. *a*, *b*, and *c* (see the sketch in Figure 8.7)) along MD, TD, and ND obtained from the Herman orientation function for the stretched films of P-1 are plotted in the triangular diagram of Figure 8.7. It is obvious that increasing DR yields a large movement of the *c*-axis of the crystals towards MD (the *c*-axis orientation feature varies from 0.5 to 0.9 as DR changes from 1 to 5.2). Furthermore, increasing DR causes the *a*-axis of the crystals to take a position closer to the TD and ND planes whereas the *b*-axis, for all DR, remains close to the TD and ND planes. These clearly elucidate the significant improvement in orientation by increasing DR, in accordance with the FTIR data presented in Figure 8.3. However, it should be mentioned that the orientation functions obtained using FTIR were slightly larger than the ones from the WAXD pole figures. These discrepancies in the values of the measured *c*-axis orientation may be due to different factors such as peak deconvolution, contribution of the amorphous phase, etc. as discussed for PE and PP elsewhere [21,22].

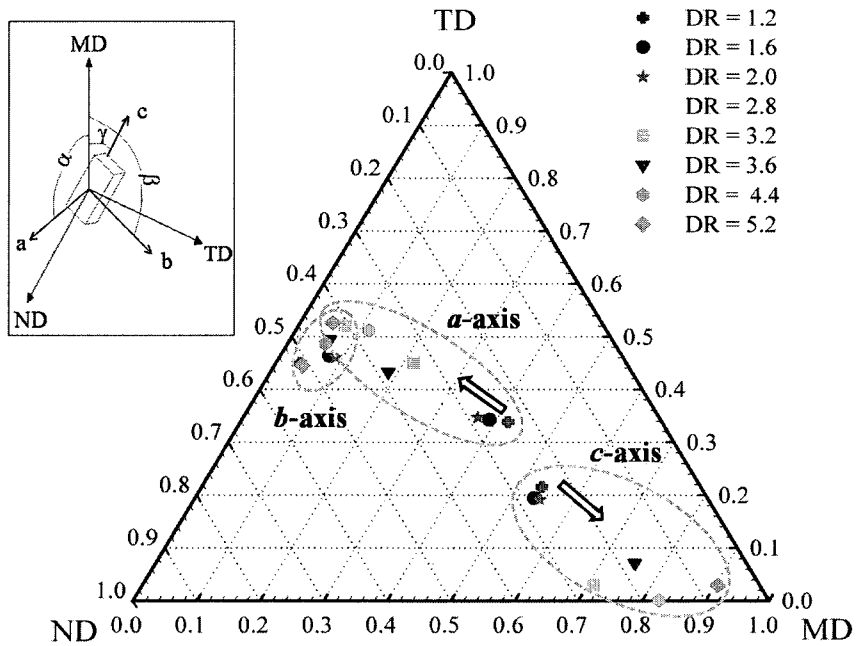

Fig. 8.7 Orientation characteristics as $\cos^2(\phi)$ of the crystal axes (*a*, *b*, and *c*) along MD, TD, and ND for P-1 (the arrows represent the shift of $\cos^2(\phi)$ with increasing DR).

SAXS measurements show in Figure 8.8 the effects of draw ratio as well as initial morphology on lamellae deformation. The meridian streak in the SAXS pattern is attributed to the lamellae perpendicular to the machine direction (MD), while the equatorial maxima are attributed to the lamellae perpendicular to the transverse direction (TD) and/or the fibrils aligned into MD. Before drawing (DR=1), due to the presence of spherulites or random lamellae nearby circular patterns for P-1 as well as P-2 are observed. The more intense streak in the meridian for the precursor (DR=1) of P-1 is related to the presence of rows of lamellae that has been formed somewhat perpendicular to MD. Due to the lamellae deformation, the meridian streak monotonically decreases as DR increases, but does not disappear even at large DR. This suggests the presence of

some lamellae perpendicular to MD even at large DR. However, the equatorial streak decreases as draw ratio increases up to 4.0 and 2.4 for P-1 and P-2, respectively, suggesting again more crystal deformation for P-2 compared to P-1. Further increase of DR causes the equatorial intensity to slightly increase. In fact, drawing of the PP films causes the break up and tilting of the crystal lamellae in the spherulites and the formation of fibrillar structure along MD. On the one hand, the deformation of the lamellae in the spherulites reduces the equatorial intensity, on the other hand fibrils are created leading to an increase in the equatorial intensity. However, it should be mentioned that our SAXS instrument was not very sensitive to the detection of fibrils in the equator. Therefore, in Figure 8.9, we reconsider the DSC data to qualitatively compare the amount of lamellae and/or fibrils in P-1 and P-2 for various DR. Before drawing (DR=1), no significant differences between the melting curve of P-1 and P-2 are observed. However, at DR=3.2, the thermogram of P-1 and P-2 exhibit a peak as well as a small shoulder at temperatures of 163 ^{o}C and 158 ^{o}C, respectively. As mentioned earlier, the peak and shoulder are attributed to the presence of fibrils and lamellae, respectively. Clearly, the contribution of fibrils to the crystals in P-2 is more important than in P-1. At DR=5.2, the shoulder for P-2 becomes very small whereas P-1 shows a large shoulder, which again supports the presence of more fibrils in the stretched film of P-2.

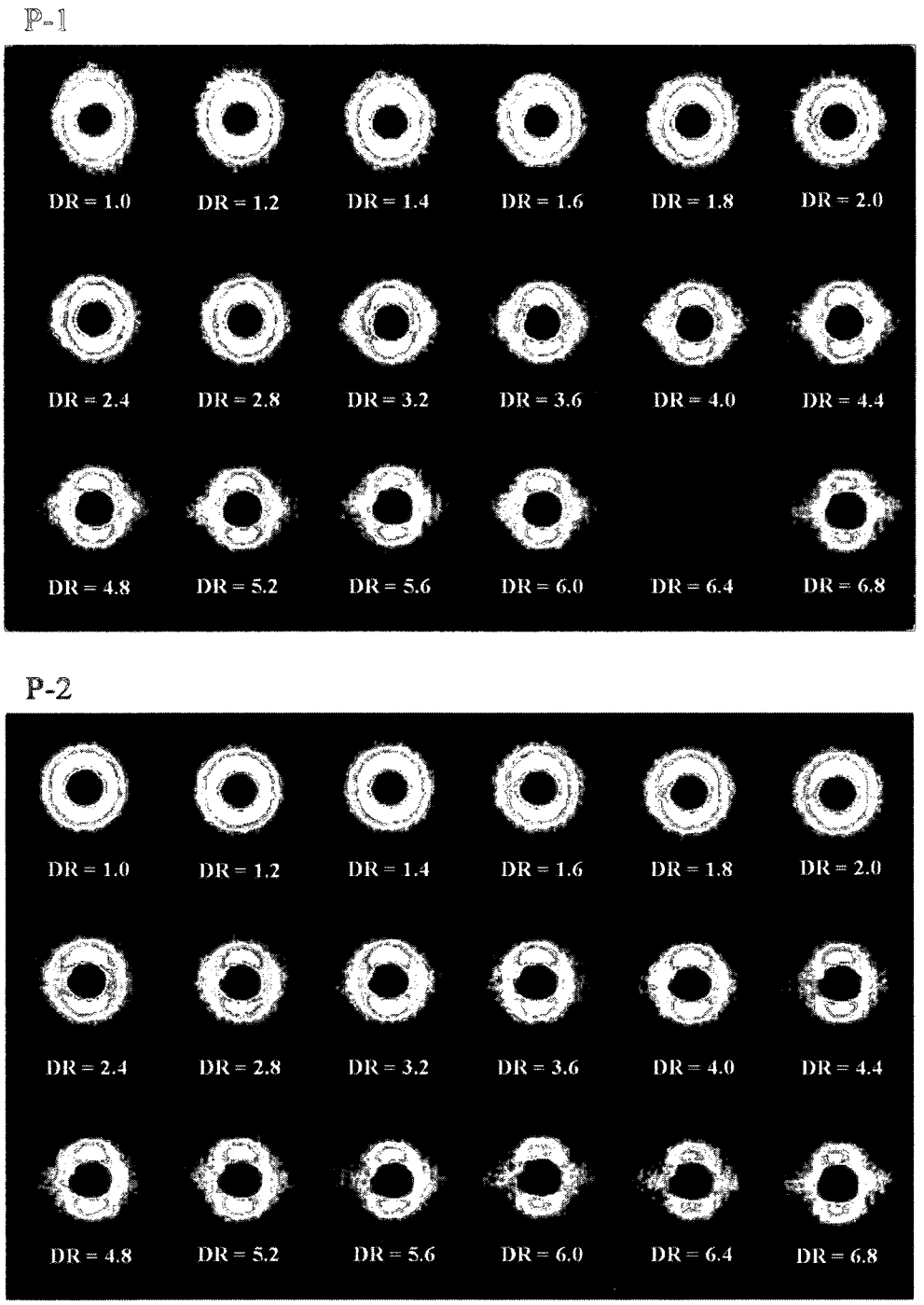

Fig. 8.8 2D SAXS patterns for P-1 (top) and P-2 (bottom) films obtained under different draw ratios.

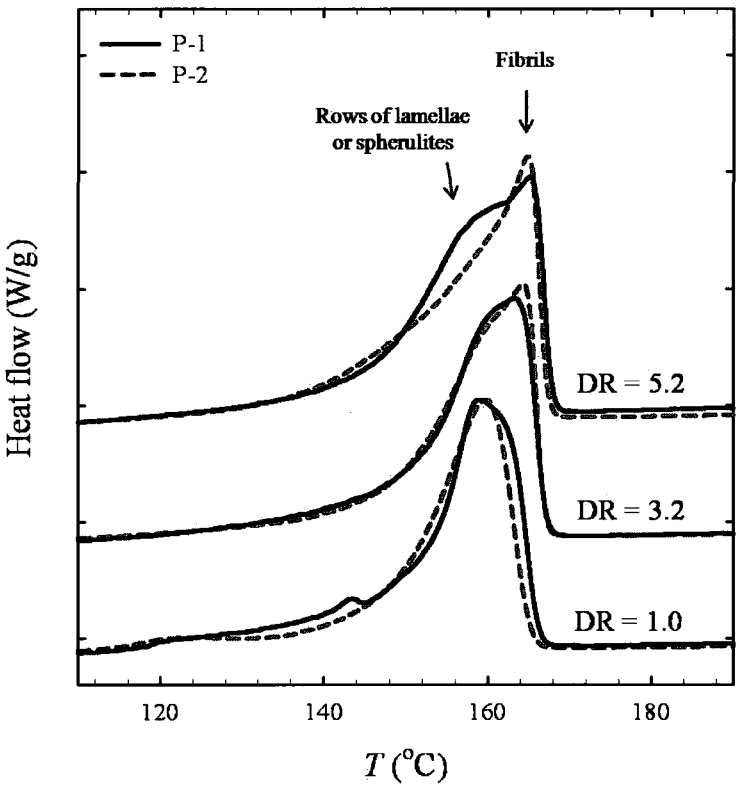

Fig. 8.9 DSC heating thermograms for P-1 and P-2 films obtained under draw ratios of 1.0, 3.2, and 5.2.

Based on our observations from thermal analysis, FTIR results, WAXD and SAXS patterns, microstructural pictograms illustrating the effects of draw ratio and original morphology on the crystallites arrangements are proposed, as depicted in Figure 8.10. At low draw ratios, FTIR data, WAXD and SAXS patterns suggested a crystal structure with coexisting rows of lamellae and spherulites and only spherulites for the films of P-1 and P-2, respectively. At medium DR, the SAXS data revealed that a major part of crystal lamellae are broken up and tilted to form the fibrils. The coexisting lamellae and fibrils for the stretched samples was also confirmed by DSC results (see Figures 8.2 and 8.9). However, WAXD and FTIR analyses indicated that P-2, at medium DR, showed

higher orientation than P-1 and also the SAXS patterns showed a better crystallites deformation and a lower amount of lamellae in P-2. In addition, the DSC data of Figure 8.9 suggested that the amounts of fibrils are greater in P-2 than in P-1. Finally, at large DR, the DSC and SAXS data implied that the most parts of crystals have formed a fibrillar structure, although some lamellae may be still present. In addition, both DSC and SAXS results suggested that the amount of fibrils in P-2 is larger than in P-1 whereas the amount of lamellae is greater in P-1 than in P-2.

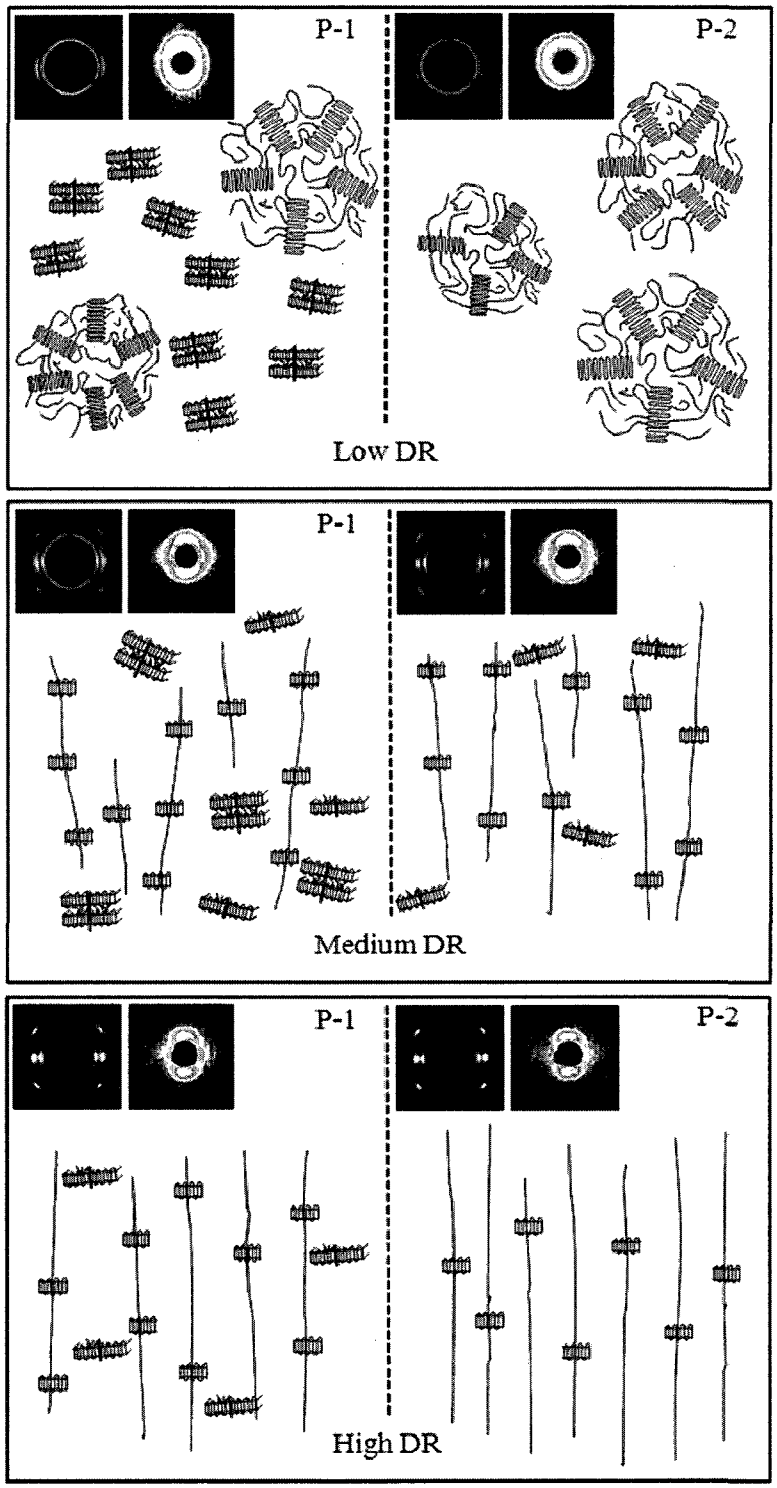

Fig. 8.10 Proposed pictograms of the molecular structure for P-1 and P-2 films obtained under low, medium, and high draw ratios.

The mechanical and tear behaviors are closely related to structure changes [23] as seen in Figure 8.11 that reports the tear resistance of the films along MD. A remarkable reduction in tear occurs when DR varies from 1 to 2.8 while further increasing DR hardly affects the tear resistance: the higher the orientation of the crystalline and amorphous phases, the lower the tear resistance along MD. At low DR, P-1 shows slightly lower tear resistance than P-2, which is due to its better orientation. Measurements of the tear resistance along TD for samples stretched beyond DR=2.4 were not possible, because the tearing direction deviated most of the time to MD. In fact, there was a high resistance in TD when compared to MD, which caused a crack in MD and created errors and non-reproducible data that are not reported here. This implies and confirms that by increasing DR a fibrillar structure with fibrils aligned in MD is formed.

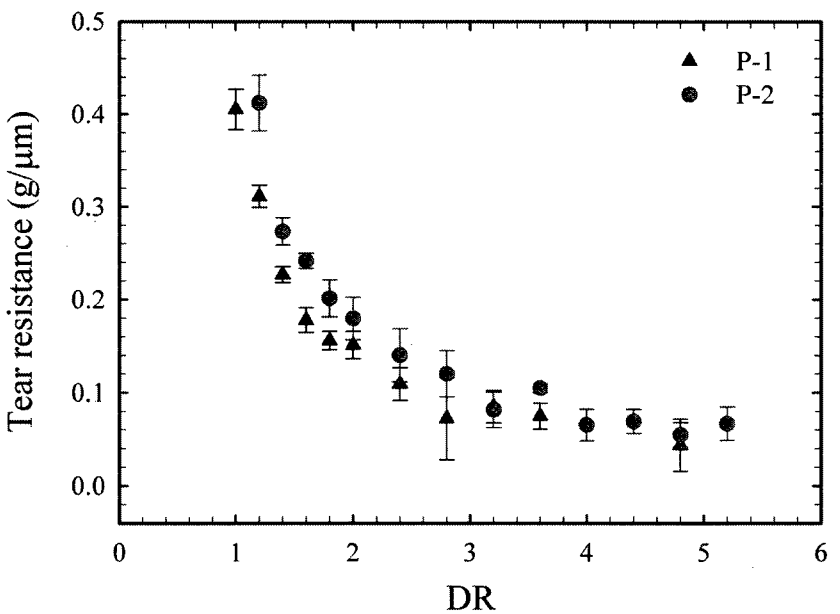

Fig. 8.11 Tear resistance along MD as a function of draw ratio for P-1 and P-2.

Sadeghi et al. [1] reported significant increases of the Young modulus, yield stress, tensile strength along MD and a drastic decrease in elongation at break along TD for uniaxial drawn polypropylene films. In this study, puncture tests were performed to investigate the effects of MDO stretching on the mechanical properties of the samples along ND and the results are presented in Figure 8.12. Each point is an average over 10 samples. A linear dependence of the maximum piercing force as a function of DR is observed. As pointed earlier, increasing DR enhances the crystal thickness as well as the alignment of crystalline and amorphous phases (see Figures 8.2-4). These can explain the improvement of the puncture resistance with increasing DR.

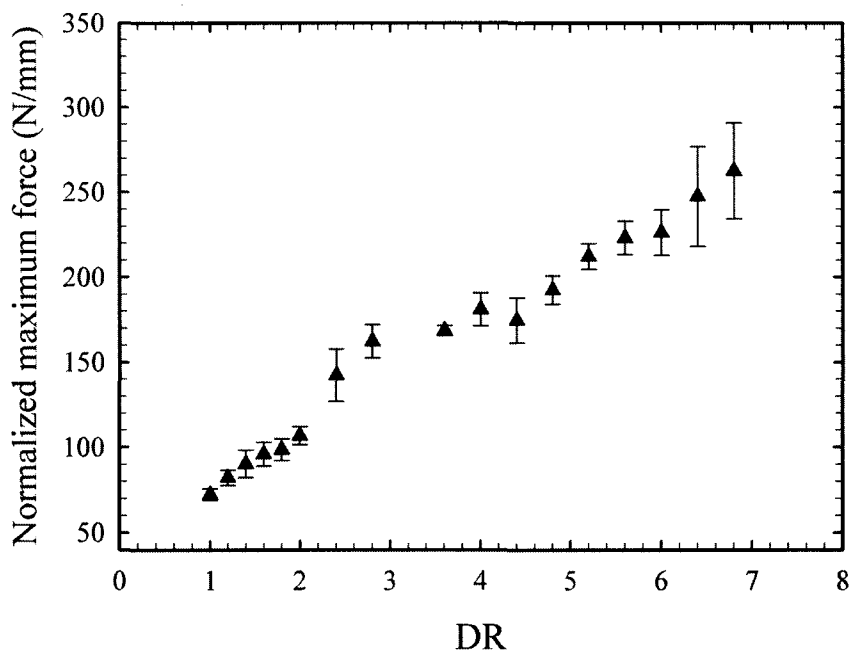

Fig. 8.12 Normalized maximum force for piercing as a function of draw ratio for P-1.

Another application for MDO stretched films is the reduction of gas permeability or improvement of barrier properties. In the literature [24-25], controversies regarding

the interpretations for the relationship between the structural parameters of polymeric films in particular PP and their gas permeability could be found. For example, Hiltner et al. [24] attributed the reduction in oxygen permeability for the drawn PP films to lower free volume, hence, less passage for gas transport. According to Taraiya et al. [25], the key factor that controlled the permeation of gas molecules through the oriented PP films was the orientation of the amorphous phase, although they did not present sufficient data to support this idea. In recent studies [26,27], low gas permeability in biaxially oriented polypropylene (BOPP) films was attributed to the decrease in chain motions in the amorphous phase.

Figure 8.13 reports the oxygen transmission rate (OTR) normalized (multiplied) by the films thickness as a function of DR for P-1 and P-2. OTR is reduced by around 75% when DR increases to 7.2. However, it should be noticed that an appreciable decrease in OTR is seen in the DR range of 1 to 2.4 and the trends for both P-1 and P-2 are somewhat the same. The similarity of the DR dependence of the oxygen transmission rate (Figure 8.13) and orientation functions (Figures 8.3 and 8.4) suggested a correlation between both set of data. Figure 8.14 presents the normalized OTR values as a function of the crystalline, F_c, as well as the amorphous, F_a, orientation functions for P-1. Reasonable linear correlations between the orientation parameters and OTR are observed: the higher the orientation of crystalline and amorphous phases, the lower the oxygen permeability. It is important to note that OTR has a stronger dependence on F_a than on F_c (the slope of the least-squares regression fit is -3.43 for the former and -1.94

for the latter). This suggests that the orientation of the amorphous phase has more impact on the drop in oxygen permeability compared to the orientation of the crystalline phase. A similar behavior for the P-2 films was observed (not shown). In semi-crystalline polymers, it is well understood that the crystalline part is impermeable to gas transport. In other words, the gas diffusion occurs only through the amorphous region. This is in agreement with the interpretations mentioned above about the amorphous phase role in OTR reduction.

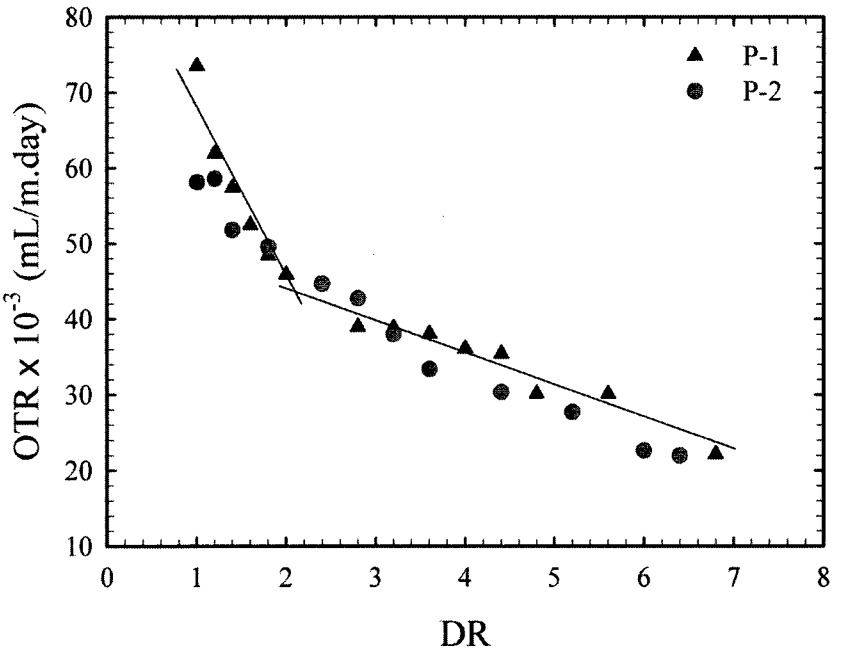

Fig. 8.13 Normalized oxygen transmission rate (OTR) as a function of draw ratio for P-1 and P-2.

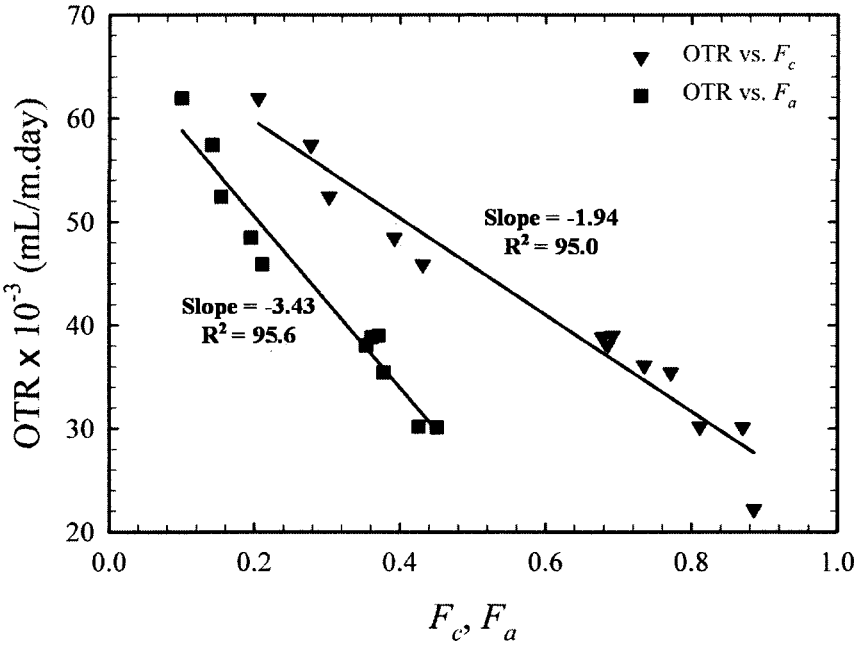

Fig. 8.14 Normalized oxygen transmission rate (OTR) as a function of crystalline, F_c, and amorphous, F_a, orientation functions.

In the MDO process, the crystals are aligned into MD and this not only enhances the orientation of the phases but also increases the tautness of tie chains and hence reduces the amorphous chains mobility [26]. In PP, the main chain motion in the amorphous phase can be characterized through the dynamic mechanical β–relaxation peak [26] as obtained from the dynamic mechanical thermal response of Figure 8.15 (tan δ as a function of temperature, in the range from -60 °C to 115 °C) for P-1 films at four DR values. The first peak at about 10 °C is attributed to the β–relaxation whereas the second peak at about 100 °C to the α–relaxation. Obviously, increasing DR has a major impact on the β–transition peak whereas the α–transition remains almost unchanged. Following Lie et al. [26,27], the OTR data are plotted in Figure 8.16 versus the β–

relaxation intensity, I_β, as determined from the peak magnitude of the DMTA tan δ curves of Figure 8.15. Good linear correlations between the oxygen transmission rate and β–relaxation intensity for P-1 and P-2 are observed, confirming the findings of Lie et al. [27] for biaxially oriented polypropylene (BOPP) films. Limited amorphous tie chains mobility (low I_β) leads to a low oxygen transmission, and inversely, a high amorphous tie chains motion (high I_β) results in a high oxygen permeability. However, it is clear that the data for P-1 and P-2 do not coincide, in contrast to the results of Lie et al. [27] that were independent of the resin type and thermal history. In summary, the improvement of barrier properties with increasing DR could be explained by the enhancement of the crystalline and amorphous phase orientation, but also by the reduction of amorphous tie chains mobility.

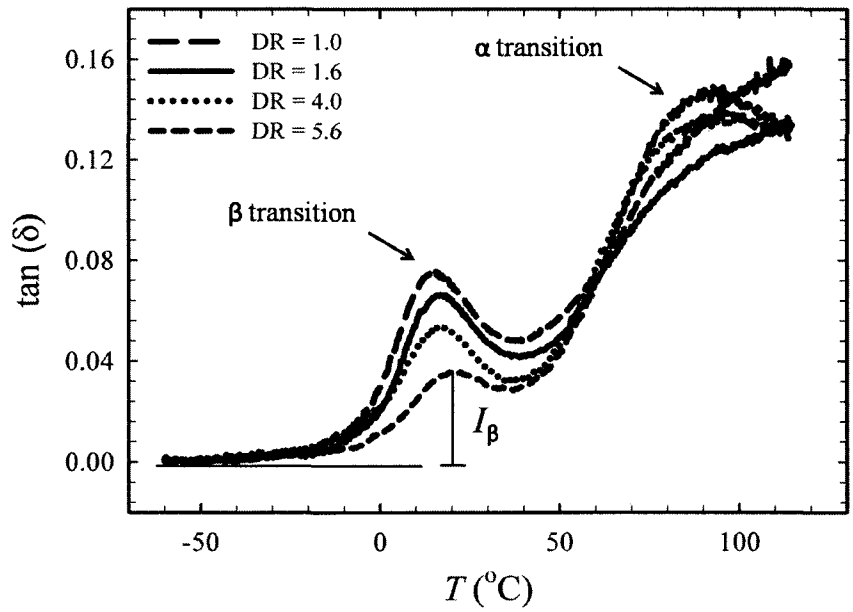

Fig. 8.15 DMTA-tan (δ) as a function of temperature for P-1 at different DR.

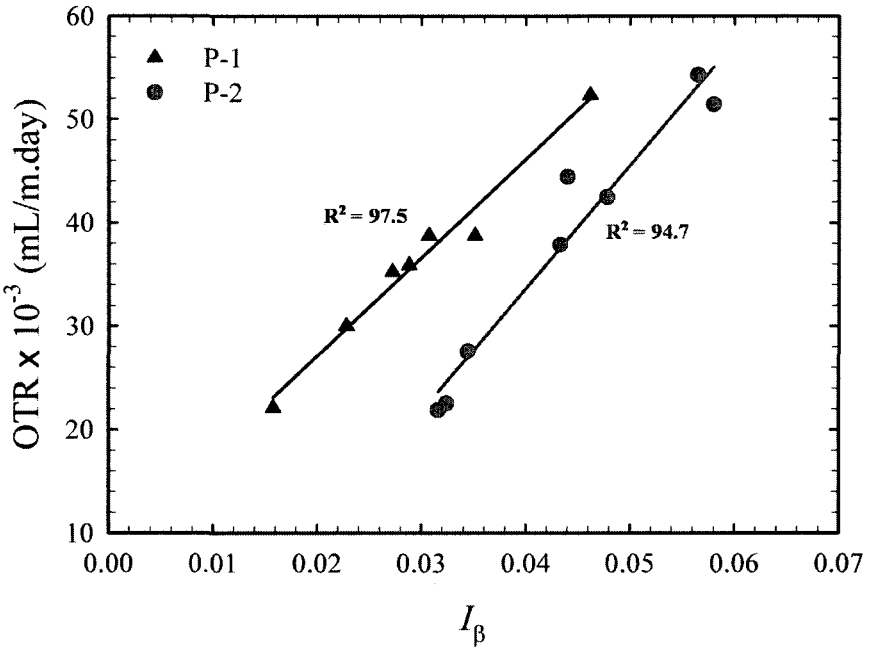

Fig. 8.16 Normalized oxygen transmission rate as a function of the β relaxation intensity for P-1 and P-2

8.4 Conclusions

In this work, precursor films with coexisting rows of lamellae and spherulites and only spherulites were produced and then uniaxially hot stretched using a machine direction orientation (MDO) unit. Changes in morphology in relation with the barrier properties as well as tear and puncture properties were presented. Our findings can be summarized as follows:

- MDO stretching caused a morphological transformation of the spherulites into fibrils at high DR, yielding thicker crystals and, subsequently, a higher melting point.
- Compared to films obtained from precursor films of coexisting rows of lamellae and spherulites (P-1), drawn films made from precursor films of only a spherulitic

structure (P-2) showed a lower crystal orientation at low DR, but a better crystal alignment at high DR. This was explained by the larger size of the PP spherulites compared to the small rows of lamellae, resulting in a better deformation of the spherulites.

- Increasing DR significantly increased the puncture resistance along ND and drastically decreased the tear resistance along MD. These were attributed to the thicker crystal size and higher orientation of the fibrils compared to the random rows of lamellae and/or spherulites.
- Linear correlations between the oxygen transmission rate (OTR) and crystalline as well as amorphous orientation functions (F_c and F_a, respectively) were found.
- OTR was also linearly correlated with the chain mobility in the amorphous part. The higher the amorphous tie chain mobility, the lower the OTR.

8.5 Acknowledgements

Financial support from NSERC (Natural Science and Engineering Research Council of Canada) and from FQRNT (Fonds Québécois de Recherche en Nature et Technologies) is gratefully acknowledged. We also acknowledge the large infrastructure grant received from the Canadian Foundation for Innovation (Governments of Canada and Province of Quebec), which allowed us to build the unique POLYNOV facility. We are also thankful to Messrs. P. Cigana, L. Parent and P.M. Simard for their technical help. Finally, we are thankful to ExxonMobil for donating the resin used in this work.

8.6 References

[1] Sadeghi F, Carreau PJ. Can Chem Eng J 2008;86:1103-1110.

[2] Schut JH. Plastics Techn. 2005;51:48-51.

[3] McGonigle EA, Liggat JJ, Pethrick RA, Jenkins SD, Daly JH, Hayward D. Polymer 2001;42:2413-2426.

[4] Backman A, Lange J, Hedenqvist MS. J Polym Sci Part B Polym Phys 2004;42:947-955.

[5] Dias P, Lin YJ, Hiltner A, Baer E, Chen HY, Chum SP. J Appl Polym Sci 2008;107:1730-1736.

[6] Srinivas S, Brant P, Huang Y, Paul DR. Polym Eng Sci 2003;43:831-849.

[7] Gould RJ. Polym Eng Sci 1988;28:857-861.

[8] Tabatabaei SH, Carreau PJ, Ajji A. J Membr Sci 2008;325:772-782.

[9] Sadeghi F, Ajji A, Carreau PJ. J Membr Sci 2007;292:62-71.

[10] Nie HY, Walzak MJ, McIntyre NS. Polymer 2000;41:2213-2218.

[11] Diez J, Alvarino C, Lopez J, Ramirez C, Abad MJ, Canol J, Garcia-Garabal S, Barral L. J Therm Anal Cal 2005;81:21-25.

[12] Zuo F, Keum JK, Chen X, Hsiao BS, Chen H, Lai SY, Wevers R, Li J. Polymer 2007;48:6867-6880.

[13] Sakurai T, Nozue Y, Kasahara T, Mizunuma K, Tamaguchi N,Tashiro K, Amemiya Y. Polymer 2005;46:8846-8858.

[14] Fujiyama M, Inata H. J Appl Polym Sci 2002;84:2157-2170.

[15] Tabatabaei SH, Carreau PJ, Ajji A. Submitted to Polymer.

[16] Arroyo M, Lopez-Manchado MA. Polymer 1997;38:5587-5593.

[17] Sadeghi F, Ajji A, Carreau PJ. Polym Eng Sci 2007;47:1170-1178.

[18] Alexander LE. X-ray diffraction methods in polymer science, Wiley Inter science, New York, 1969.

[19] Somani RH, Yang L, Zhu L, Hsiao BS. Polymer 2005;46:8587-8623.

[20] Elias MB, Machado R, Canevarolo SV. J Therm Anal Cal 2000;59:143-155.

[21] Ajji A, Zhang X, Elkoun S. Polymer 2005;46:3838-3846.

[22] Zhang X, Ajji A. Polymer 2005;46:3385-3393.

[23] Zhang XM, Elkoun S, Ajji A, Huneault MA. Polymer 2004;45:217-229.

[24] Hiltner A, Liu RYF, HU YS, Baer E. J Polym Sci Part B Polym Phys 2005;43:1047-1063.

[25] Taraiya AK, Orchard GAJ, Ward IM. J Polym Sci Part B Polym Phys 1993;31:641-645.

[26] Lin YJ, Dias P, Chen HY, Chum S, Hiltner A, Baer E. Polym Eng Sci 2008;48:642-648.

[27] Lin YJ, Dias P, Chen HY, Chum S, Hiltner A, Baer E. Polymer 2008;49:2578-2586.

CHAPTER 9

GENERAL DISCUSSION

To produce microporous membranes by the stretching technique, one must obtain precursor films with an adequate orientation and alignment of the crystal lamellae. The higher the crystalline alignment in the precursor, the better is expected the lamellae separation and, as a consequence, the larger the porosity and permeability of the microporous membranes. The type of resin and applied processing conditions are the key factors for the production of the precursor films with appropriate properties, thickness, orientation, and connection of the crystals, which in turn control the final membrane structure. In flow-induced crystallization during film extrusion, shish (fibrils) are created, which act as nuclei sites for lateral lamellae crystallization. As shish are mostly created from the long chains and long chains have larger relaxation time, adding a high molecular weight component favors the preparation of precursor films with an adequate level of crystalline lamellae. Die temperature, die gap, rate and position of the air cooling unit, chill roll temperature, and draw ratio are the major processing parameters that need to be optimized depending on the resin as well as number of layers in the film. The die temperature affects the relaxation of the molecules. Low temperature will slow down the chain relaxation, leading to an increase probability for the formation of lamellae by the low molecular weight chains. However, very low extrusion temperatures prevent the mobility of the molecules, which results in a non appropriate

row-nucleated lamellar structure. Therefore, an optimum temperature needs to be selected for each polymer. In the cast film process, the use of a low air cooling rate contribute significantly to the perfection of the crystalline phase, while further increasing of air cooling does not noticeably affect the crystal structure. In fact, the use of air cooling in addition to chill rolls helps flow induced crystallization to occur at lower temperatures. This will noticeably increase the number of shish or nuclei sites, and consequently the crystallization kinetics are promoted resulting in a well oriented shish-kebab structure. Also, the mechanical properties along MD improve significantly as the films are subjected to a low level of air flow rate. Increasing the draw ratio (DR) increases the crystal orientation (F_c). A linear relationship between F_c and DR was found. At the low draw ratios, the lamellae are not well aligned perpendicular to the flow direction, but as draw ratio increases the lamellae align themselves perpendicular to the machine direction (MD).

The produced precursor films should be annealed at a proper temperature before being cold and hot stretched. As annealing is performed at a temperature that is above the onset of mobility in the crystalline structure (T_α), it is postulated that during annealing, the lamellae twist and orient perpendicular to MD. Also, melting of small lamellae and their recrystallization with better orientation can occur. The annealing variables investigated included temperature, time, and level of extension applied during annealing. It was found that annealing at 140 ^{o}C for 20 min without extension was the optimum annealing condition for PP. However, the annealing temperature of

PP/HDPE/PP trilayer films should be lower than HDPE melting point and above the alpha transition temperature, T_α, of PP ($T_{\alpha,PP}$ is about 110 °C obtained from the dynamic mechanical thermal analysis). Therefore, in our study, 120 °C without extension was selected for annealing of the trilayer films.

In the preparation of porous membranes using the stretching technique, voids are formed by cold stretching and enlarged by subsequent hot stretching. The micro void morphologies produced via this method are a consequence of interlamellar separation, which takes place at temperatures above T_g of the specific semicrystalline polymers. The behavior in cold stretching in comparison to that in hot stretching is different since the temperature is low. In hot stretching the lamellae can move more easily while the crystallization can also take place. However, both processes are very complicated since a combination of events happens simultaneously and it is hard to predict which one exactly is dominating. Our studies showed that by increasing the applied extension during cold stretching, water vapor transmission rate (WVTR) monotonically rose for the HDPE while for the PP, WVTR first increased significantly and then decreased. The pores created in cold stretching are enlarged during the hot stretching step and consequently enhance WVTR. More flexibility of the lamellae at high temperatures can be a reason for the increase of pore size with increasing extension ratio. In hot stretching some surface layers of lamellae are believed to locally melted, detached and rotated to form interconnected bridges. This explains the increase in the number of interconnected bridges after hot stretching.

As stated earlier, the stretching of a well oriented shish-kebab lamellar morphology involves the separation of the stacked lamellae, leading to pores formation and the subsequent microporous membrane generation. However, for films possessing a spherulitic crystal structure a morphological transformation of the spherulites will affect their final properties. The machine direction orientation (MDO) process is widely used for uniaxial stretching of polyethylene and polypropylene films. The MDO unit can be operated either in-line or off-line with extrusion and is controlled via variables such as: the distance between the draw rollers, draw ratio, drawing speed, drawing times (a film can be stretched many times), drawing temperature, and heat-setting conditions. The stretching is usually performed at temperature below the melt temperature of the polymer and results in a highly oriented film that causes anisotropy in properties. The drawing process usually improves the strength and barrier properties, but brings some drawbacks such as a reduction of the tear resistance along the machine direction (MD) and a lowering of elongation at break along the transverse direction (TD). The original crystal morphology as well as draw ratio (DR) influence significantly the alignment of the amorphous and crystalline phases. Our findings showed that by increasing DR, the crystalline lamellae first broke up and oriented along the drawing direction and then, at large DR, they were deformed and transformed into a fibrillar structure.

CHAPTER 10

CONCLUSIONS AND RECOMMENDATIONS

10.1 Conclusions

In this dissertation, the development of microporous membranes with high performances from monolayer as well as multilayer PP/HDPE microporous membranes through cast film extrusion followed by uniaxial stretching has been investigated. We also investigated the drawing of the polypropylene films with coexisting rows of lamellae and spherulites and only spherulites using a machine direction orientation (MDO) unit to see changes in morphology in relation with the barrier properties as well as tear and puncture properties. We have studied using a lab scale cast film extrusion the structure and performances of microporous membranes from blends of linear low and high molecular weight PPs. FTIR, WAXD, and SAXS were employed to measure the orientation and long spacing of crystalline phase. Adding up 10 wt% high M_w PP and increasing draw ratio (DR) enhanced the orientation of both the crystalline and amorphous phases. For all the blends, as the draw ratio increased, the orientation function for the crystalline phase increased. The structural modification promoted by annealing was also explored. Annealing at 140 ^{o}C without extension contributed significantly to the crystalline phase perfection. A larger pore density, greater porosity, and more interconnectivity of the pores were observed when the level of high M_w PP

increased. By increasing the applied extension during hot stretching, the water vapor transmission rate (WVTR) rose while for cold stretching the effect was reversed.

We used an industrial scale cast film process to prepare microporous membranes and investigate in details the effect of the cast processing parameters on the crystalline orientation, morphology, and mechanical properties of cast films and formation of microporous membranes. The use of a low air cooling rate contributed significantly to the perfection of the crystalline phase, while further increasing air cooling rate did not noticeably affect the crystal structure. For the film produced without air cooling and at high roll temperature, coexisting lamellae and spherulites were observed. In contrast, an ordered lamellar structure was seen for the films subjected to a low air cooling. Due to a better molecular and crystal orientation for air cooled cast films, significant increases of the Young modulus, yield stress, tensile strength, and tensile toughness along MD, and dramatic decreases of elongation at break along TD were observed as air cooling was applied. The effects of microstructure differences of the PP cast films on the microporous membranes morphology and water vapor transmission rate were investigated. Microporous membranes possessing high pore density, large porosity, and high water vapor transmission rate were obtained by lamellae separation from cast films prepared using air cooling.

The development of microporous membranes from multilayer and monolayer PP/HDPE films was also studied. The role of the process variables and annealing on the shear and/or elongation-induced crystallization and orientation developed in the

monolayer as well as the components in the multilayer cast films was examined. Increasing cooling air flow rate (AFR), draw ratio (DR) or annealing enhanced noticeably the crystal orientation of the PP and HDPE monolayer films as well as the components in the multilayer film. A transcrystallization of the HDPE lamellae penetrating into the PP at the interface of the multilayer films was observed and was explained by the difference in the resins crystallization temperature. A good adhesion at the interface of the porous multilayer membrane was attributed to the transcrystallization observed in the precursor interface. At high cold stretching extensions, the pore size and porosity of the HDPE membranes was much larger compared to those from the PP produced under the same conditions. The trilayer microporous membranes showed a lower permeability than the single layer membranes, possibly due to the presence of the interface as well as a lower orientation of the PP and HDPE components in the multilayer film compared to the monolayer films.

Microporous membranes from the films possessing a well oriented shish-kebab crystal morphology were produced after annealing and subsequent stretching in the machine direction. However, the drawing of polypropylene films possessing spherulitic structure involves a morphological transformation, which will affect their final properties particularly barrier, tensile, tear, and puncture properties. Therefore, precursor films with coexisting rows of lamellae and spherulites and only spherulites were produced and then uniaxially hot stretched using a machine direction orientation (MDO) unit. Changes in morphology in relation with the barrier properties as well as tear and

puncture properties were presented. MDO stretching caused a morphological transformation of the spherulites into fibrils at high DR, yielding thicker crystals and, subsequently, a higher melting point. Compared to films obtained from precursor films of coexisting rows of lamellae and spherulites (P-1), drawn films made from precursor films of only a spherulitic structure (P-2) showed a lower crystal orientation at low DR, but a better crystal alignment at high DR. This was explained by the larger size of the PP spherulites compared to the small rows of lamellae, resulting in the better deformation of the spherulites. Increasing DR significantly increased the puncture resistance along ND and drastically decreased the tear resistance along MD. These were attributed to the thicker crystal size and higher orientation of the fibrils compared to the random rows of lamellae and/or spherulites. Linear correlations between the oxygen transmission rate (OTR) and crystalline as well as amorphous orientation functions (F_c and F_a, respectively) were found. OTR was also linearly correlated with the chain mobility in the amorphous part.

10.2 Recommendations

In the previous section, we summarized what has been accomplished in this thesis concerning the fabrication of monolayer and multilayer microporous membranes through cast extrusion followed by stretching and MDO drawing of polypropylene films. For the continuation of this work and future research, the following unexplored topics are recommended:

1) The stretching technique should be extended to other semicrystalline polymers with the capability of formation of a planar row-nucleated lamellar structure. Poly (vinylidene fluoride) (PVDF) is considered as a potential resin. Membranes from this polymer is currently being produced via phase inversion for use in water filtration and lithium battery separators[109,110]. The stretching technique provides a less expensive method compared to the phase inversion process. Recently[27], we reported preliminary results on PVDF microporous membranes. The PVDF membranes showed much smaller pores and lower permeabilities than the polyolefin microporous membranes. However, it is believed that the properties can be improved by applying a larger level of total stretching and studying in more depth the role of resin molecular weight, processing parameters as well as annealing variables.

2) Although a few authors have investigated the modeling of crystallization of various resins under different flow magnitudes, no study has been considered the flow-induced crystallization under cooling in the cast film process. Therefore, developing a thermomechanical model that describes polymer crystallization under flow and cooling using air and cast roll is recommended.

3) Developing multilayer microporous membranes with other compositions. In the PP/HDPE/PP microporous membranes developed, due to the lower melting temperature of the middle layer, the HDPE porous layer is utilized as a fuse for safety purposes. However, polyolefin trilayer microporous membranes are hydrophobic and in some cases a hydrophilic film with safety features is desirable. Compared to the PP film, the

polyoxymethylene (POM) film is hydrophilic and possesses approximately identical annealing and melting temperatures. Therefore, a trilayer separator where the PE layer is sandwiched between two porous POM layers can be developed. The problem of weak adhesion between POM and PE at the interface can be solved by using a proper compatibilizer.

4) As pointed out earlier, polypropylene and polyethylene membranes are widely used in microfiltration and ultrafiltration processes because of many desirable properties including very high porosity, good mechanical properties, and chemical inertness. However, the hydrophobicity of polyolefin membranes causes poor wettability and biocompatibility, which limit their applications for aqueous solution separation and biomedical usage[111]. Surface functionalization can improve hydrophilicity and biocompatibility drastically. Therefore, surface modification of the produced PP and HDPE porous membranes is recommended and functionalization can be done by grafting on surface, plasma treatment, etc.

REFERENCES

1. Wei X, Haire C (2007) US patent 0196638.

2. Gozdz AS, Schmtz CN, Tarascon JM, Warren PC (1997) US Patent 5607485.

3. Okazaki MA, kuwana MI, Nagoya ST, Kasugai TI (1990) US Patent 4921653.

4. Sadeghi F (2007) 'Developing of microporous polypropylene by stretching', Ph.D thesis, Ecole Polytechnique de Montreal.

5. Yu TH (1995) 'Processing and structure-property behavior of microporous polyethylene-from resin to final film', Ph.D thesis, Virginia Polytechnic Institute and State University.

6. Xu J, Johnson M, and Wilkes GL (2004) Polymer 45, 5327.

7. Johnson M B (2000) 'Investigations of the processing-structure-property relationship of selected semi crystalline polymers', Ph.D thesis, Virginia Polytechnic Institute and State University.

8. Venugopal G, Moore J, Howard J, Pendalwar S (1998) J Power Sourc 77, 34.

9. Dahn JR, Fuller EW, Obrovac M, van Sacken U (1994) Solid State Ionics 69, 265.

10. Chandavasu C (2001) 'Microporous polymeric membranes via melt processing', Ph.D thesis, New Jersey institute of technology.

11. Baker RW (2004) 'Membrane technology and applications', 2nd edition, Wiley-VCH.

12. Yamashita A, Kawai S, Tanii K, Takakura K (1981) US patent 4269713.

13. Hamilton R, Ford C, Colton C, Cross R, Steinmuller S, Henderson L (1971) Trans Am Soc Artif Intern Organs 17, 259.

14. Takita K, Kono K, Takashima T, Okamota K (1991) US patent 5051183.

15. Rein DH, Baddour RF, Cohen RE (1993) J Polym Eng 12, 353.

16. Strathmann H (1983) "Synthetic Membranes: Science, Engineering, and Applications", Riedel Publishing, New York.

17. Mulder M (1996) "Basic Principles of Membrane Technology", 2nd edition, Springer Publisher.

18. Yu TH (2000) US patent 6080507.

19. Callahan RW, Kim H (1997) US patent 6057061.

20. Nago S, Nakamura S, Mizutani Y (1992) J Appl Polym Sci 45, 1527.

21. Nago S, Mizutani Y (1993) J Appl Polym Sci 50, 1815.

22. Xanthos M, Chandavasu C, Sirkar KK, Gogos CG (2002) Polym Eng Sci 42, 810.

23. Chandavasu C, Xanthos M, Sirkar KK, Gogos CG (2002) Polymer 43, 781.

24. Williams JL, Gunther H, Peterlin A (1974) US patent 3839516.

25. Shi G, Chu F, Zhou G, Han Z (1989) Makromol Chem 190, 907.

26. Chu F, Yamaoka T, Ide H, Kimura Y (1994) Polymer 35, 3442.

27. Chu F, Yamaoka F, Kimura Y (1995) Polymer 36, 2523.

28. Chu F, Kimura Y (1996) Polymer 37, 573.

29. Sadeghi F, Ajji A, Carreau PJ (2007) J Membr Sci 292, 62.

30. Sadeghi F, Tabatabaei SH, Ajji A, Carreau PJ (2009) J Polym Sci Part B Polym Phys, in press.

31. Edward PM (1996) 'Polypropylene Handbook: Polymerization, Characterization, Properties, Processing, Applications', Hanser-Gardner Publications.

32. William D, Callister JR (1997) 'Materials Science and Engineering (An Introduction)', 4th edition, John Wiley & Sons.

33. Swan PR (2003) J Polym Sci Polym Chem 56, 403.

34. Davis GT, Eby RK, Martin GM (1968) J Appl Phys 39, 4973.

35. Rizzo P, Baione F, Guerra G, Martinotto L, Albizzati E (2001) Macromolecules 34, 5175.

36. Keller A (1957) Phil Mag 2, 1171.

37. Liedauer S, Eder G, Janeschitz-Kriegl H, Jerschow P, Geymayer W, Ingolic E (1993) Int Polym Proc 3, 236.

38. Lamberti G (2004) Polymer Bulletin 52, 443.

39. Koscher E, Fulchiron R (2002) Polymer 43, 6931.

40. Vleeshouwers S, Meijer HEH (1996) Rheol Acta 35,391.

41. Khanna YP (1993) Macromolecules 26, 3639.

42. Pogodina NV, Winter HH (1998) Macromolecules 31, 8164.

43. Swartjes FHM (2001) 'Stress induced crystallization in elongational flow', Ph.D thesis, Eindhoven university of technology, The Netherland.

44. Floudas G, Hilliou L, Lellinger D, Alig I (2000) Macromolecules 33, 6466.

45. Swartjes FHM, Peters GWM, Rastogi S, Meijer HEH (2003) Intern Polymer Processing 18, 53.

46. Somani RH, Yang L, Hsiao BS (2006) Polymer 47, 5657.

47. Seki M, Thurman DW, Oberhauser PJ, Kornfield JA (2002) Macromolecules 35, 2583.

48. Agarwal PK, Somani RH, Weng W, Mehta A, Yang L, Ran S, Liu L, Hsiao B (2003) Macromolecules 36, 5226.

49. Somani RH, Hsiao BS, Nogales A (2000) Macromolecules 33, 9385.

50. Bashir Z, Odell JA, Keller A (1986) J Mater Sci 21, 3993.

51. Eder G, Janeschitz-Kriegl, H (1997) "Processing of Polymers" WCH, Weinheim.

52. Machin MJ, Keller A (1967) J Macromol Sci 1, 41.

53. Tabatabaei SH, Carreau PJ, Ajji A (2009) Submitted to Polymer.

54. Zhang XM, Elkoun S, Ajji A, Huneault MA (2004) Polymer 45, 217.

55. Peterlin A (1973) J Macromol Sci-Phys 7, 705.

56. Zhou H, Wilkes GL (1998) J Mater Sci 33, 287.

57. Yeh GSY, Hong HZ (1979) Polym Eng Sci 19, 395.

58. Housmans JW (2008) "Flow Induced Crystallization of Isotactic Polypropylenes", Ph.D thesis, Technische Universiteit Eindhoven.

59. Somani RH, Hsiao BS, Nogales A (2001) Macromolecules 34, 5902.

60. Keum JK, Burger C, Zuo F, Hsiao BS (2007) Polymer 48, 4511.

61. Keller A, Kolnaar JWH (1993) Prog Colloid Polym Sci 92, 81.

62. Keller A, Kolnaar H (1997) "Material Science and Technology a Comprehensive Treatment", John Wiley and Sons.

63. Hayashi Y, Matsuba G, Zhao Y, Nishida K, Kanaya T (2009) Polymer 50, 2095.

64. Zhang RC, Xu Y, Lu A, Cheng K, Huang Y, Li ZM (2008) Polymer 49, 2604.

65. Li ZM, Li L, Shen KZ, Yang MB, Huang R (2005) Polymer 46, 5358.

66. Ahn SH, Cho CB, Lee KY (2002) J Reinforce Plastic and Composite 21, 617.

67. Schultz JM, Hsiao BS, Samon JM (2000) Polymer 41, 8887.

68. Choi D, White J (2004) Polym Eng Sci 44, 210.

69. Frank FC, Mackley MR (1976) J Polym Sci Polym Phys Ed 14, 1121.

70. Geffroy E, Leal LG (1992) J Polym Sci Part B: Polym Phys 30, 1329.

71. Dunlap PN, Leal LG (1987) J Non-Newtonian Fluid Mech 23, 5.

72. McHugh AJ, Guy RK, Tree DA (1993) Colloid Polym Sci 271, 629.

73. Cogswell FN (1972) Polym Eng Sci 12, 64.

74. Binding DM (1989) J Non-Newt Fluid Mech 27, 173.

75. Miles MJ, Keller A (1980) Polymer 21, 1295.

76. Sprague BS (1973) J Macromol Sci-Phys 8, 157.

77. Mansfield M, Boyd R (1978) J Polym Sci Phys Ed 16, 1227.

78. Adams WW, Yang D, Thomas EL (1986) J Mater Sci 21, 2239.

79. Kim J, Kim SS, Park M, Jang M (2008) J Membr Sci 318, 201.

80. Lee SY, Park SY, Song HS (2006) Polymer 47, 3540.

81. Sadeghi F, Ajji A, Carreau PJ (2007) Polym Eng Sci 47, 1170.

82. Sadeghi F, Ajji A, Carreau PJ (2005) J. Plastic Film & Sheeting 21, 199.

83. Tabatabaei SH, Carreau PJ, Ajji A (2009) Chem Eng Sci, in press.

84. Tabatabaei SH, Carreau PJ, Ajji A (2009) Submitted to Polym Eng Sci.

85. Sadeghi F, Ajji A, Carreau PJ (2008) J Polym Sci Part B Polym Phys 46, 148.

86. Johnson MB, Wilkes GL (2001) J Appl Polym Sci 81, 2944.

87. Johnson MB, Wilkes GL (2002) J Appl Polym Sci 84, 1762.

88. Johnson MB, Wilkes GL (2002) J Appl Polym Sci 83, 2095.

89. Johnson MB, Wilkes GL (2002) J Appl Polym Sci 84, 1076.

90. Sadeghi F, Carreau PJ (2008) Can Chem Eng J 86, 1103.

91. Schut JH (2005) Plastics Techn 51, 48.

92. McGonigle EA, Liggat JJ, Pethrick RA, Jenkins SD, Daly JH, Hayward D (2001) Polymer 42, 2413.

93. Backman A, Lange J, Hedenqvist MS (2004) J Polym Sci Part B Polym Phys 42, 947.

94. Dias P, Lin YJ, Hiltner A, Baer E, Chen HY, Chum SP (2008) J Appl Polym Sci 107, 1730.

95. Srinivas S, Brant P, Huang Y, Paul DR (2003) Polym Eng Sci 43, 831.

96. Gould RJ (1988) Polym Eng Sci 28, 857.

97. Nie HY, Walzak MJ, McIntyre NS (2000) Polymer 41, 2213.

98. Diez J, Alvarino C, Lopez J, Ramirez C, Abad MJ, Canol J, Garcia-Garabal S, Barral L (2005) J Therm Anal Cal 81, 21.

99. Zuo F, Keum JK, Chen X, Hsiao BS, Chen H, Lai SY, Wevers R, Li J (2007) Polymer 48, 6867.

100. Sakurai T, Nozue Y, Kasahara T, Mizunuma K, Tamaguchi N,Tashiro K, Amemiya Y (2005) Polymer 46, 8846.

101. Arroyo M, Lopez-Manchado MA (1997) Polymer 38, 5587.

102. Ajji A, Sammut P, Huneault MA (2003) J Appl Polym Sci 88, 3070.

103. Ward IM, Coates PD, Dumoulin MM (2000) Solid Phase Processing of Polymers, Hanser publisher.

104. Alexander LE (1979) X-ray diffraction methods in polymer science, Wiley Inter Science, New York.

105. Olley RH, Bassett DC (1982) Polymer 23, 1707.

106. Brunauer S, Emmett PH, Teller E (1983) J Am Chem Soc 60, 309.

107. Li J, Favis BD (2001) Polymer 42, 5047.

108. Fujiyama M, Inata H (2002) J Appl Polym Sci 84, 2157.

109. Cheng LP, Lin DJ, Shih CH, Dwan AH, Gryte CC (1999) J Polym Sci Part B Polym Phys 37, 2079.

110. Kuo CY, Lin HN, Tsai HA, Wang DM, Lai JY (2008) Desalination 233, 40.

111. Yang Q, Xu ZK, Dai ZW, Wang JL, Ulbricht M (2005) Chem Mater 17, 3050.

APPENDIX A

Rheological Properties of Blends of Linear and Long Chain Branched Polypropylene[5]

Seyed H. Tabatabaei, Pierre J. Carreau, and Abdellah Ajji

CREPEC, Chemical Engineering Department, Ecole Polytechnique, C.P. 6079, Succ. Centre ville Montreal, QC, H3C 3A7 Canada

Abstract

Blends of a long-chain branched polypropylene (LCB-PP) and a linear polypropylene (L-PP) were prepared using a twin screw extruder. Linear viscoelastic properties such as complex viscosity, storage modulus, and weighted relaxation spectrum were determined as functions of LCB-PP content. Shear data obtained from commercial rheometers as well as from a slit die rheometer were used to verify the Cox-Merz relation for the neat components as well as for a blend. Elongational properties were obtained using a SER unit mounted on an ARES rheometer and the converging die. A significant strain-hardening was observed for the neat LCB-PP as well as for all the blends, but the strain-hardening decreased with increasing strain rate. The apparent steady elongational viscosity values evaluated using the converging die were observed to be comparable at

---

[5] *Polymer Engineering and Science,* in press

high deformation rates to those obtained from the SER unit, but the differences increased as the strain rate decreased.

1 Introduction

In comparison with polyethylene, polypropylene (PP) has higher melting point, lower density, higher chemical resistance, and better mechanical properties, which makes it more interesting for many industrial applications. Due to its low melt strength, linear polypropylene cannot be used in processes where elongational properties and melt strength are dominant, such as film blowing, blow molding, and foaming. Enhanced elongational properties can be achieved by blending a branched PP with a linear PP.

The rheological behavior of blends of linear and branched polypropylenes and polyethylenes has been the topic of several investigations [1-4]. Ajji et al. [1] showed that 10-20 wt% of a low density polyethylene (LDPE) was sufficient to obtain a strain-hardening behavior in blends with a linear low density polyethylene (LLDPE). Fang et al. [2] realized that an increase in the length of short branches and, possibly, the presence of a few long branches in metallocene LLDPEs and a comparable molecular weight as that of a LDPE can improve the miscibility of LLDPE/LDPE blends. Stange et al. [3] found that the strain-hardening of PP blends decreased as the strain rate increased while for the neat long-chain branched PP enhancement of strain-hardening was observed. However, due to limitations of their rheometer they were not able to study the elongational behavior at deformation rates larger than 1 s^{-1}. Recently, McCallum et al.

[4] showed that the blending of branched and linear PPs not only promoted the melt strength, but the mechanical properties increased as well.

As extensional flow is dominant in many processes and this type of flow is very sensitive to the molecular structure, there are more and more investigations of the extensional properties [5]. However, it is still impossible to reach very large strains and deformation rates with the existing elongational rheometers. Therefore, indirect methods to determine the extensional viscosity have been proposed, such as that based on the convergent flow analysis. Cogswell [6] was probably the first author to separate the pressure drop in contraction flows into shear and elongational components. The entry pressure drop is:

$$\Delta P = \Delta P_s + \Delta P_e \qquad (1)$$

where ΔP_s and ΔP_e are contributions of the shear and extensional flow components to the total pressure, ΔP. Assuming the extensional viscosity independent of the deformation rate, Cogswell [6] solved the set of momentum balance equations to calculate the two pressure drops separately. In contrast, Binding [7] used an energy balance and allowed the elongational viscosity to vary with the deformation rate.

Although the literature reports some investigations of the rheological behavior of blends of L-PP and LCB-PP, there is still a lack of steady and transient rheological data for a wide range of deformation rates. Therefore, the main objective of this study is to elucidate how the addition of a branched PP to a linear PP affects the rheological properties of PP, including transient and 'steady' extensional behavior over a wide range

of deformation rates. Using various rheological tools, we would like to investigate in more detail than done before the effect of branches on the rheological properties of PP blends.

2 Experimental

2.1 Materials

Two commercial polypropylenes were selected: a linear polypropylene (L-PP) and a long chain branched polypropylene (LCB-PP). The L-PP was supplied by ExxonMobil Company and had a melt flow rate (MFR) of 2.8 g/10min (under ASTM conditions of 230 °C and 2.16 kg). The LCB-PP was obtained from Basell Company and had a MFR of 2.5 g/10min. To separate the effect of branching from molecular weight, resins with close MFRs were selected. The main characteristics of the resins are shown in Table 1. The molecular weight of the linear PP was evaluated using the relation between zero-shear viscosity and the molecular weight [8]. The molecular weight distribution (MWD) was measured using a GPC (Viscotek model 350). The melting point, T_m, and the crystallization temperature, T_c, of the resins were obtained using differential scanning calorimetry. Blends containing 2, 5, 10, 30, 50, and 70 wt% LCB-PP were prepared using a twin screw extruder (Leistritz Model ZSE 18HP co-rotating twin screw extruder) followed by water cooling and pelletizing. The temperature profile along the barrel (from hopper to die) was set at 160/180/190/200/200/200/200 °C. The extrusion was carried out at 80 rpm. During blending, 3000 ppm of a stabilizer, Irganox B225, was

added to avoid thermal degradation of the polymers. To make sure that all samples have the same thermal and mechanical history, unblended components were extruded under the same conditions.

Table 1. Main characteristics of the neat polymers.

Resin code	Company	MFR 230°C/2.16kg	Nomencl.	M_w (kg/mol)	M_w/M_n	T_m (°C)	T_c (°C)
PP4612	ExxonMobil	2.8	L-PP	543	3.9	160	115
Pro-fax 814	Basell	2.5	LCB-PP	N/A	2.3	159	128

2.2 Rheological measurement

2.2.1 Parallel Plate Rheometer

Dynamic data were measured using a Rheometric Scientific SR5000 stress controlled rheometer with a parallel plate geometry of diameter of 25 mm and a gap equal to 1.5 mm. All measurements were carried out at 190 °C under nitrogen atmosphere to avoid thermal degradation. Molded discs of 2 mm thick and 25 mm in diameter were prepared using a hydraulic press at 190 °C. Prior to frequency sweep tests, time sweep tests at a frequency of 0.628 rad/s and different temperatures were performed for two hours to check the thermal stability of the specimens. Changes less than 3% changes were observed for the duration of the time sweep tests. Material functions such as complex viscosity, elastic modulus, and weighted relaxation spectrum in the linear viscoelastic regime were determined in the frequency range from 0.01 to 500 rad/s. In order to obtain

more accurate data, the frequency sweep test was carried out in four sequences while the amount of applied stress in each sequence was determined by a stress sweep test.

2.2.2 Capillary Rheometer

Medium to high shear rate data were recorded using an Instron rheometer with a capillary of aspect ratio (length to diameter) of 80:1 with 1.26 mm diameter and 90° entrance angle. The speed of the piston was varied from 0.05 to 5 cm/s corresponding to shear rates ranging from 3 to 300 s^{-1}. All data were determined at 190 °C. For this aspect ratio, the Bagley correction [9] was found to be negligible, but the Rabinowitch analysis for the parallel plate geometry was applied [10].

2.2.3 In-Situ Rheometer-Slit and Converging Dies

More accurate measurements at high shear rates were made using a slit die mounted in place of the mold in an injection molding machine. The thickness, width and length of the slit die are 1, 25, and 70 mm, respectively. The injection speed of the Sumitomo SE50S electric injection molding machine was varied from 0.5 to 190 mm/s, which can produce viscosity data within shear rates ranging from 30 to 30 000 s^{-1}. The screw diameter was 32 mm and its rotational speed was set at 100 rpm. A schematic of the on-line rheometer, which consists of a converging die, a slit die, and a diverging die, is shown in Figure 1. Five pressure transducers and thermocouples were placed in the rheometer to measure precisely the pressure and temperature along the device. Details about the geometry of our on-line rheometer can be found elsewhere [11].

The converging part of slit die was used for determining the apparent planar extensional viscosity. The inlet thickness, outlet thickness, width, and length of converging die are 4, 1, 12.5, and 12 mm, respectively. All data were determined at 190 °C.

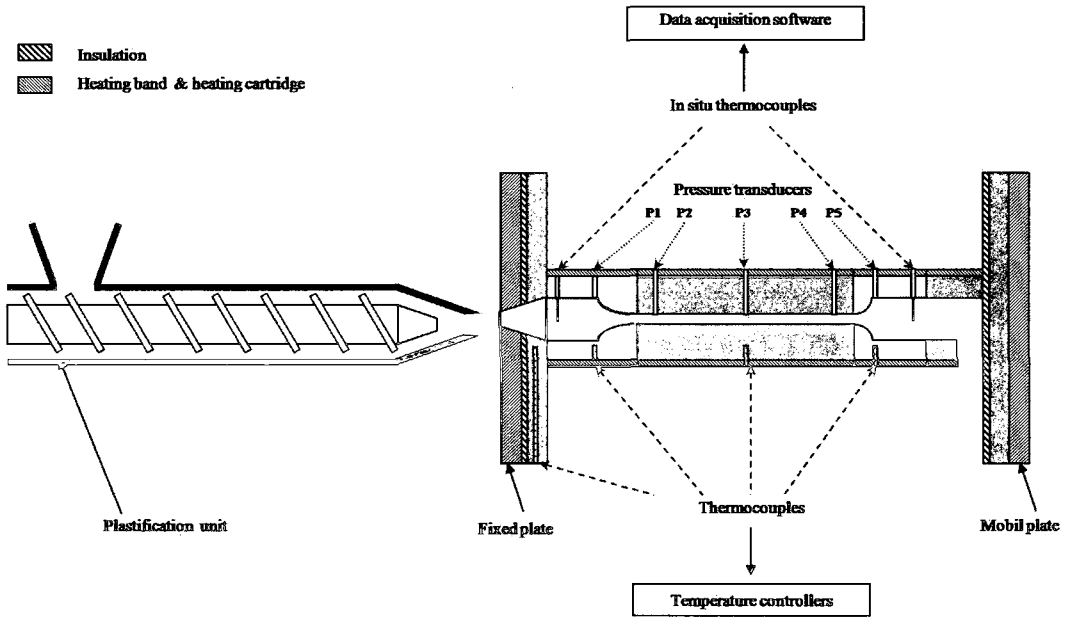

Fig. 1 Schematic of the slit die rheometer [9].

2.2.4 SER Geometry

To measure uniaxial elongational viscosity, an ARES rheometer equipped with a SER universal testing platform [12] from Xpansion Instruments was used. The model used was SER-HV-A01, which is a dual windup extensional rheometer. It is capable of generating elongational rate up to 20 s^{-1}. Measurements were performed at 190 °C under nitrogen atmosphere.

3 Results and discussions

3.1 Shear measurements

Time sweep tests were performed at 0.628 rad/s for 2 h to check the thermal stability of the samples. As done by Stange et al. [3] for a better comparison, $G'(t)$ values were normalized by $G'(t=0)$ and the result is presented in Figure 2. For L-PP a slight decrease of normalized G' with time is visible. This reduction is attributed to the degradation of the L-PP during the long measurements. A significant increase of G' is observed for the LCB-PP, which is attributed to the crosslinking of the sample due to residual catalysts used to create the branches. Stange et al. [3] attributed a similar increase to the reformation of the entanglements between long-chain branched molecules, which were disentangled during the extrusion process. This interpretation does not withstand for our case, as the increase of G' with time was also observed for non extruded LCB-PP samples. As all rheological data were recorded before 80 min, therefore 3% increase of G' for the LCB-PP and 1% reduction for the L-PP, two extreme cases, were found to be negligible.

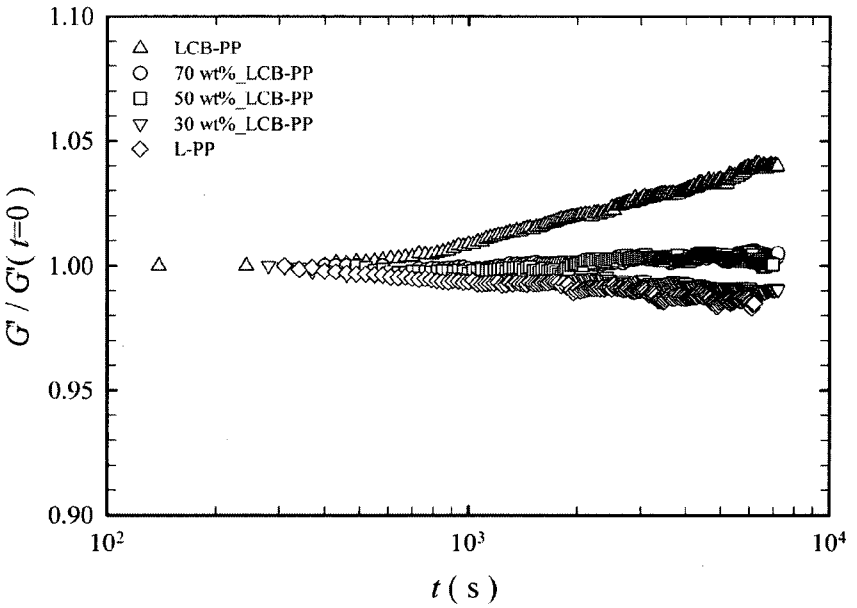

Fig. 2 Normalized storage modulus versus time for the neat PPs and three blends; T= 190 °C and ω=0.628 rad/s.

The complex shear viscosities as a function of frequency for the neat PPs, 30, and 70 wt% LCB-PP blends are shown in Figure 3. Depending on the LCB content, the trends for other blends were intermediate of the curves reported in the figure. Clearly, adding LCB-PP causes pronounced shear-thinning behavior due to the presence of long-chain branches. In addition, it is obvious that the viscosities of the blends are intermediate as expected for miscible components. Figure 4 illustrates the storage modulus of the same blends versus frequency. At low frequencies, the storage modulus of LCB-PP is larger while the effect becomes inversed at high frequencies.

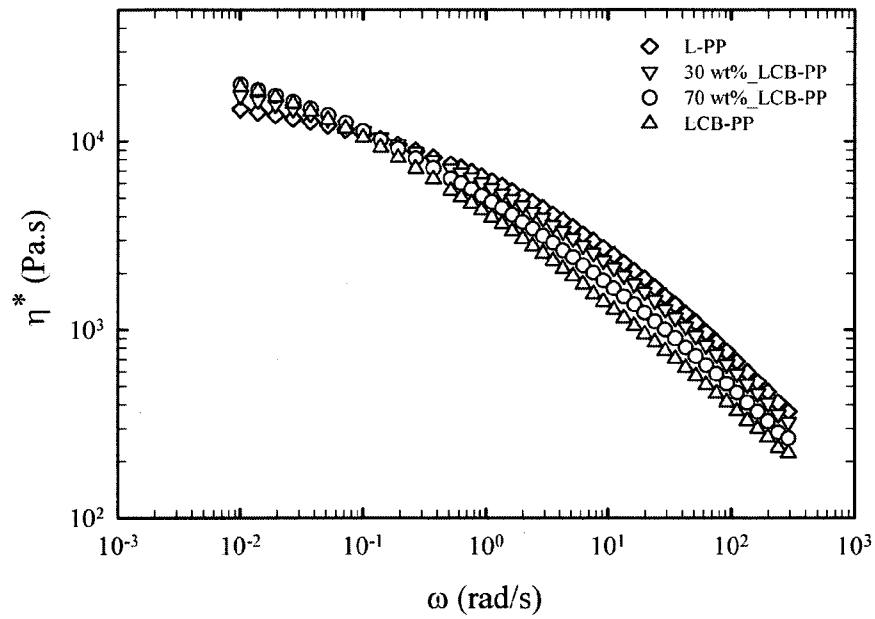

Fig. 3 Complex viscosity as a function of angular frequency for the neat PPs as well as for two blends; T=190 °C.

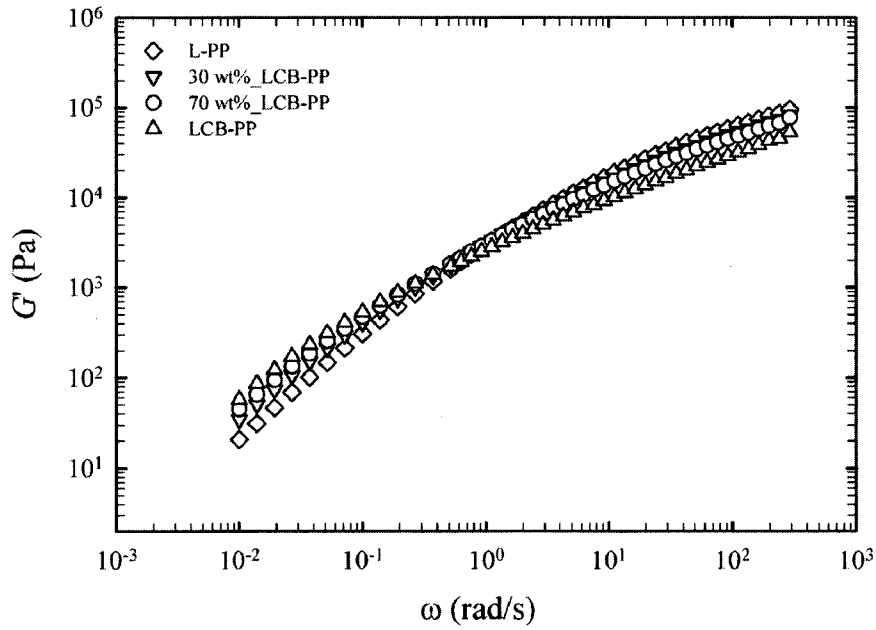

Fig. 4 Storage modulus as a function of angular frequency for the neat PPs as well as for two blends; T=190 °C.

The plot of loss angle, δ (tanδ=G''/G'), as a function of frequency is illustrated in Figure 5. A monotonic decrease of the loss angle is observed for L-PP while samples containing long chain branches demonstrate inflections in the curves with a tendency towards plateaus at high frequencies. Wood-Adams et al. [13] related the magnitude and breath of the plateau of the loss angle to the weight fraction of branched chains. As shown in Figures 4 and 5, the lower G' and δ values of the samples containing LCB-PP compared to L-PP at low frequencies are characteristics of more elastic materials, due to the presence of long-chain branches.

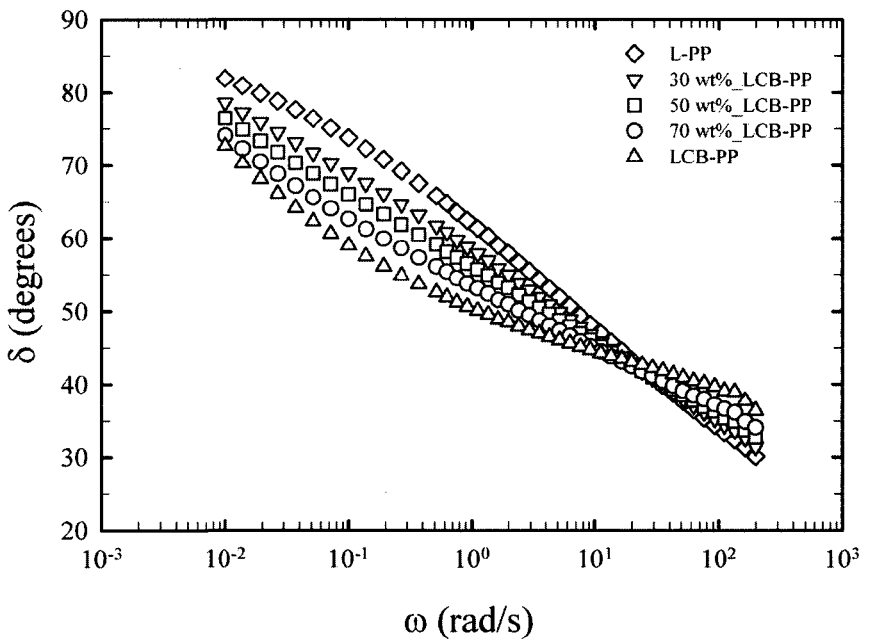

Fig. 5 Loss angle versus angular frequency for the neat PPs as well as for three blends; T=190 °C.

To further analyze the role of adding branched component on the melt relaxation of the blends, the weighted relaxation spectra evaluated from dynamic moduli (G', G'', ω)

using the NLREG (non linear regularization) software [14] are plotted in Figure 6 (the vertical dash lines represent the range of frequencies covered during the experiments). The longer relaxation time for the LCB-PP is attributed to changes in the stress relaxation mechanisms. At low frequencies, the polymer chains are entangled with surrounding macromolecules, and these entanglements create a tube-like region, causing the chains to move slowly [15]. In the linear viscoelastic regime three stress relaxation mechanisms may occur depending on frequency and chains topology: reptation, primitive path fluctuations, and constraint release. The details concerning these mechanisms can be found elsewhere [15]. In linear polymers, reptation is the main relaxation mechanism. However, in branched polymers, the reptation of molecules is inhibited by the presence of branch points; hence, branched polymer chains relax by fluctuations and constraint release [16]. In addition, it is known that chain ends are highly mobile, which accelerate the relaxation of the macromolecules whereas branch points retard relaxation. In the early stages the relaxation of branched polymer chains is faster than that of linear chains, because the presence of additional fast moving branch ends is more important compared to the presence of branch points [15]. Note that in Figure 6 the positions of the peaks for the blends are intermediate with respect to the neat components, suggesting again miscibility. The area under the curves is related to the zero shear viscosity and, as expected, increases with molecular weight. The relaxation behavior can also be shown in the Cole-Cole plot, which is the plot of η''

versus η', as illustrated in Figure 7. The semicircular shape of the blends is an evidence of miscibility [17, 18].

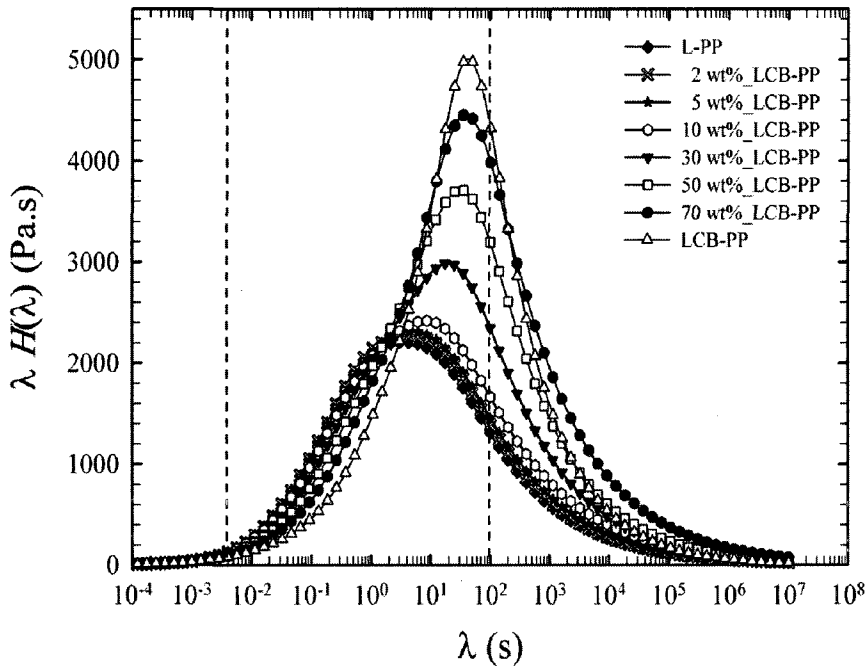

Fig. 6 Weighted relaxation spectra for the neat PPs as well as all the blends; T=190 °C (the vertical dash lines represent the range of frequencies covered during the experiments).

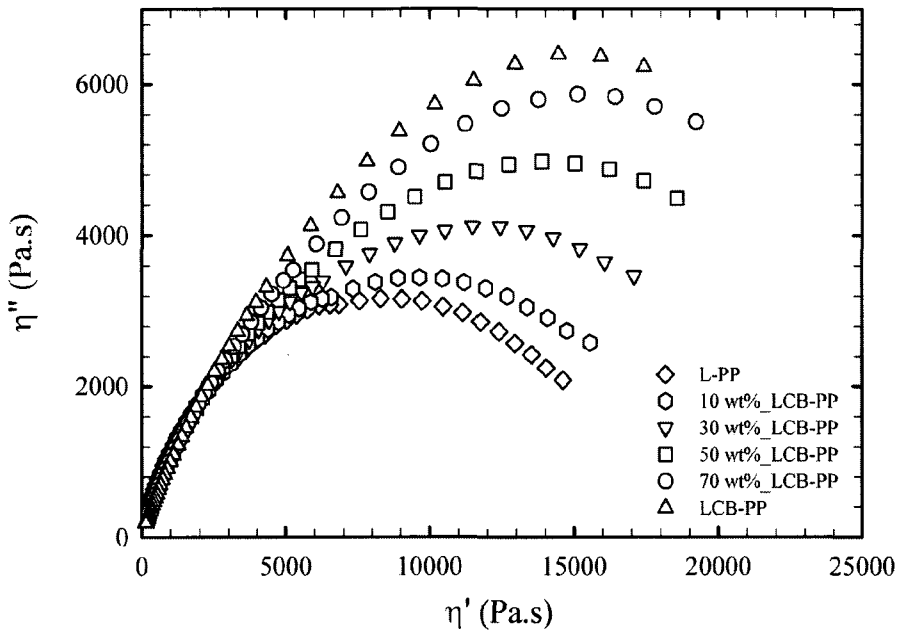

Fig. 7 Cole-Cole plots for the neat PPs as well as all the blends; T=190 °C.

The complex shear viscosities at different frequencies as a function of LCB-PP content are plotted in Figure 8. Good agreement with the logarithmic mixing rule of the complex viscosity can be observed for all samples. It is expressed as [19]:

$$\log \eta^*(\omega) = \phi_\beta \log(\eta^*(\omega))_1 + (1-\phi_\beta)\log(\eta^*(\omega))_2 \qquad (2)$$

where ϕ_β is the branched PP content (vol fraction) and η^* is the complex shear viscosity. The logarithmic additivity rule was verified by Utracki and Schlund for blends of LLDPE and LDPE [19] and more recently by Stange et al. [3] for blends of L-PP and LCB-PP. Fang et al. [5] used the logarithmic mixing rule to probe the miscibility of components in various blends of metallocene-catalyzed linear low-density PEs (m-LLDPE) and LDPE. The respect of the log additivity rule as shown in Figure 8 suggests

miscibility of both PP components. Deviations from the log mixing rule for blends of linear and branched PPs and PEs have been reported in the literature [5, 20-22]. It is believed that the miscibility is not only affected by the amount of the long chain branches, but also by the molecular weight of the polymer components as well as the structure of the branched polymer.

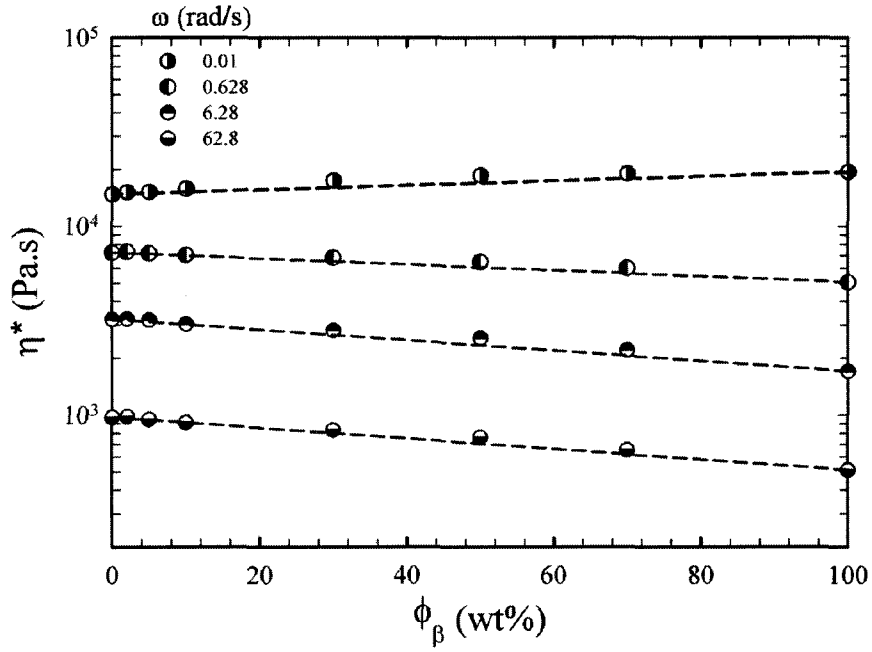

Fig. 8 Complex shear viscosity at different angular frequencies as a function of branched content; T=190 °C (the dash lines show the additivity rule).

To verify the validity of the Cox-Merz [23] analogy, the dynamic and steady shear viscosity data obtained from the various rheometers for the neat polypropylenes and the blend containing 30 wt% LCB-PP are compared in Figure 9. Frequency sweep data in the frequency range from 0.01 to 500 rad/s and steady shear viscosity values for shear rates ranging from 0.001 to 2 s^{-1} were recorded using the parallel plate stress controlled

rheometer (SR5000). The simple shear viscosity data measured using a parallel plate geometry were corrected using the Rabinowitch analysis [10]:

$$\eta(\dot{\gamma}) = \frac{T}{2\pi R^3 \dot{\gamma}_R}(3+n) \qquad (3)$$

where T is the torque exerted on the plate, $\dot{\gamma}$ the shear rate, R is the plate diameter and n the power-law index. Shear viscosities within shear rates ranging from 3 to 600 s^{-1} were obtained using the capillary rheometer. Accurate shear viscosity data at very high shear rates were obtained using the slit die rheometer. The results plotted in Figure 9 show that the Cox-Merz rule was well obeyed by the L-PP. Good agreement of the Cox-Merz relation for another linear neat PP was also reported by Mobuchon et al. [11]. For the 30 wt% LCB-PP blend and neat LCB-PP, the Cox-Merz analogy was verified at high shear rates, but significant discrepancies at frequencies or shear rates lower than 1 s^{-1} were observed, with 7% and 16% differences between the complex and steady shear viscosities for the blend containing 30 wt% LCB-PP and the neat LCB-PP, respectively. Deviations from the Cox-Merz rule have also been reported for filled polymer systems [11, 25]. According to Utracki and Schlund [19], the lack of superposition between dynamic and steady shear viscosities for polymer blends is an indication of immiscibility. However, in the present case the results of different rheological methods discussed above suggest miscibility of the polymer pairs. Furthermore, more deviations of the complex and steady shear data were observed for the neat LCB-PP (Figure 9). Therefore, the non validity of the Cox-Merz rule for the blend is attributed to the

presence of long-chain branches for which the effects are more pronounced at low rates of deformation. At large deformation rates, due to the more shear-thinning behavior of branched polymers, the role of long-chain branches becomes less pronounced. A smaller influence of long-chain branches at large deformation rates in extensional flow was observed and will be discussed in the next section.

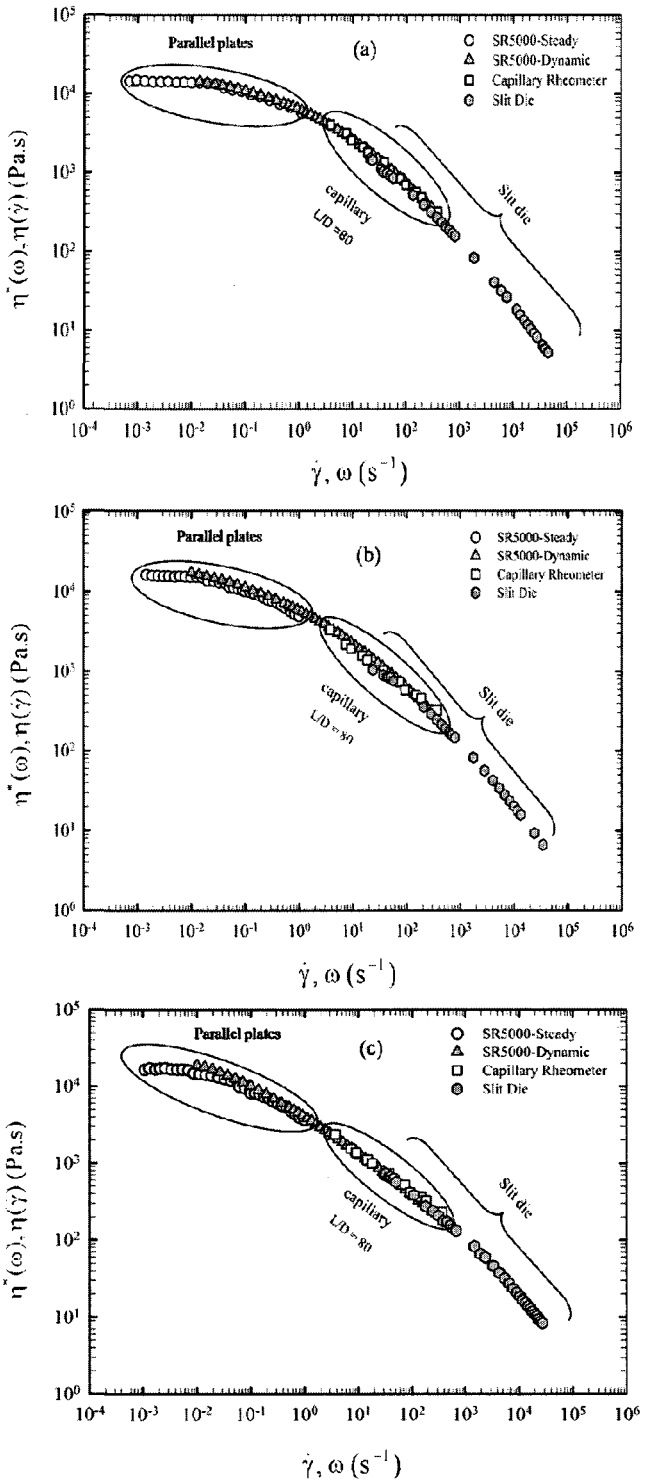

Fig. 9 Shear and complex viscosities as functions of shear rate and frequency for (a) L-PP, (b) 30 wt% LCB-PP, and (c) LCB-PP; T=190 °C.

3.2 Elongational Measurements

The transient elongational viscosities $\eta_e^+(t,\dot{\varepsilon})$ of the resins and blends at different strain rates and 190 °C are illustrated in Figure 10 (to facilitate the comparison between data, the curves of the different data have been multiplied by indicated values). The maximum achievable Hencky strain (ε) was in the range of 2.7 to 3.3 depending on the strain rate and LCB content. As expected, both the linear and branched polypropylenes respect the linear viscoelastic behavior at low strain values (short times) with a transient elongational viscosity equal to three times that in shear determined using the relaxation spectrum according to the following equation:

$$\eta_e^+(t) = 3\sum_{i=1}^{N} \lambda_i H_i (1 - e^{-t/\lambda_i}) \qquad (4)$$

To obtain the transient elongational viscosity from the above equation 100 modes were used. However, the LCB-PP exhibits pronounced strain hardenings with strong departures from the linear regime occurring at shorter times as the elongational rate is increased.

In contrast to oscillatory shear data, uniaxial extension is very sensitive to the macromolecules and microstructure [26, 27]. For blends containing 2 and 5 wt% LCB-PP, small deviations from the linear viscoelastic curve are observed in Figure 10 and indicate some strain-hardening. A similar behavior but at low elongational rates for blends of linear PP and long chain branched PP was also reported by Stange et al. [3]. Our results confirm the findings of Ajji et al. [1] and Wagner et al. [28] who observed a

strain-hardening when 5 wt% LDPE was added to a LLDPE. A more significant strain-hardening is observed for the LCB-PP as well as for blends containing 10 wt% LCB-PP and more. Sharper increases in the extensional curves and clear deviations from the linear viscoelasticity at shorter times are found as the weight fraction of LCB-PP goes from 0.30 to 1.

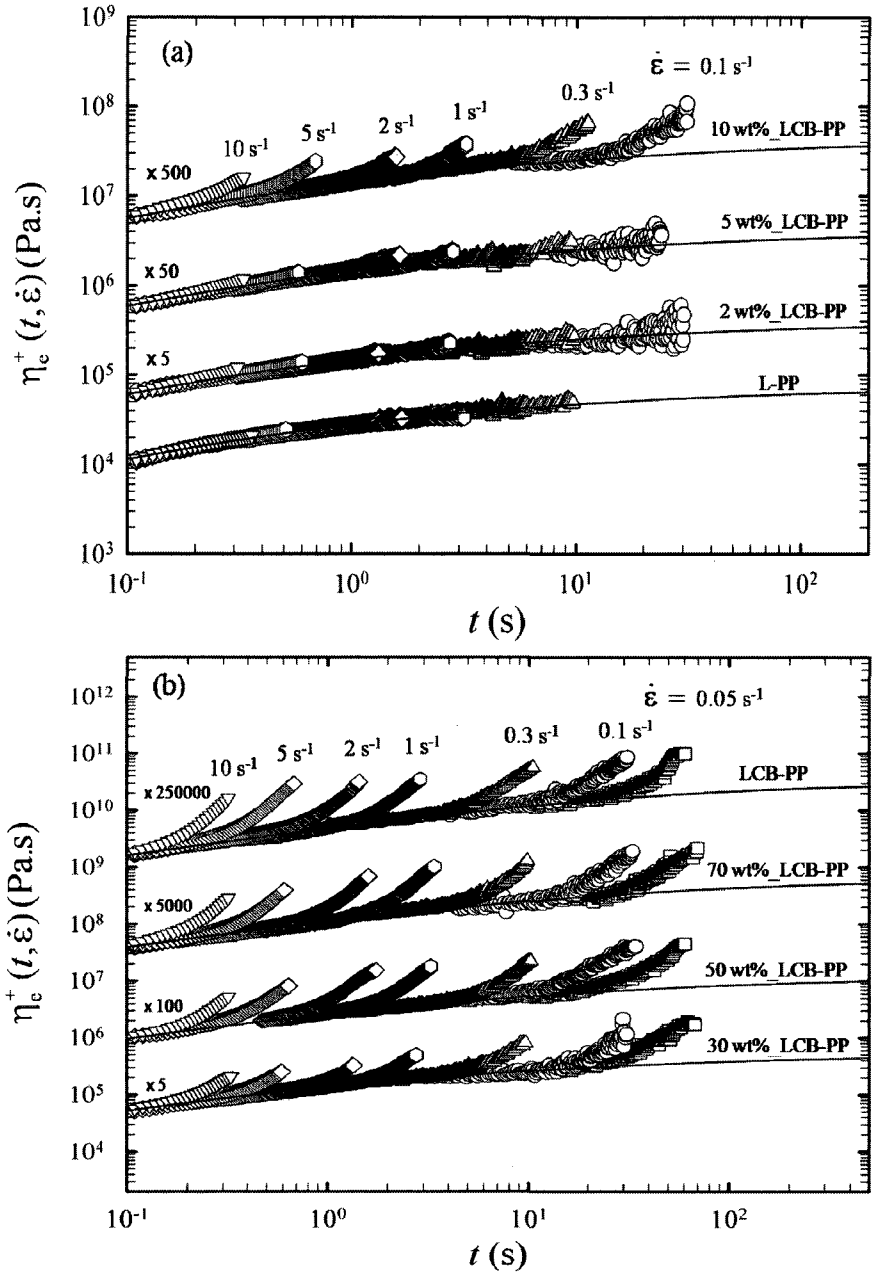

Fig. 10 Transient elongational viscosities as a function of time at different Hencky strain rates and branched contents: (a) low LCB-PP contents (b) high LCB-PP contents; T=190 °C (the solid lines represent the linear behavior calculated from the relaxation spectrum).

The strain-hardening coefficient is determined according as [3]:

$$S = \frac{\eta_e^+(t,\dot{\varepsilon})}{3\eta_o^+(t)} \qquad (5)$$

where $\eta_o^+(t)$ is the transient shear viscosity at low deformation rates, which can also be obtained from the relaxation spectrum using Eq. 4, and $\dot{\varepsilon}$ is the strain rate. The strain-hardening coefficient as a function of the branched PP content at the Hencky strain of 2.5 and for all the blends is plotted in Figure 11. The blends with a low amount of the LCB-PP show small strain-hardening values at low strain rates. The strain-hardening coefficient is considerably larger than 1 for the blends contained 30 wt% LCB-PP and more and increases with the LCB-PP content. However, in all cases we observe significant decreases of S up to a Hencky strain rate of 2 s^{-1}, while further increases of the deformation rate slightly change the strain-hardening coefficient, indicating the smaller effect of branches at high rates. Our results are qualitatively consistent with those of Stange et al. [3] except that they observed an increase of the strain hardening with increasing strain rate for the same neat LCB-PP. From Figure 10, it is obvious that the SER data are far from steady-state values. This can explain the reduction of the strain-hardening coefficient for the LCB-PP with increasing extensional rate. The data obtained from the filament stretching extensional rheometer (Munstedt's rheometer) used by Stange et al. [3] were possibly closer to steady-state values particularly at low strain rates. This is probably why they observed an increase of S for the LCB-PP. It should be mentioned here that, due to the nature of filament elongational rheometers, the

measurements of Stange et al. [3] were limited to Hencky strain rates up to 1 s^{-1}, while those presented here using the SER geometry were up to Hencky strain rates of 10 s^{-1}. The strain rate dependence of the strain-hardening coefficient may also be related to the method used to create the long chain branches. Auhl et al. [29] observed that long chain branched polypropylenes obtained from electron beam irradiation at low irradiation intensities resulted in a reduction of the strain-hardening coefficient with increasing deformation rate while branched PP produced at high irradiation intensities resulted in increases of the strain-hardening coefficient with increasing strain rate.

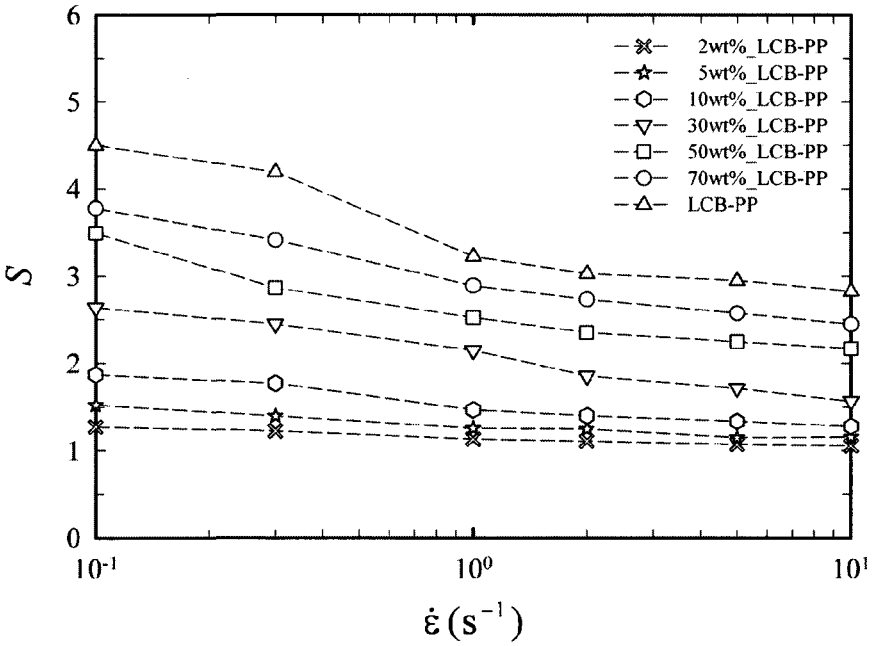

Fig. 11 Strain-hardening coefficient as a function of Hencky strain rate and branched content; T=190 °C and Hencky strain=2.5.

Using Cogswell [6] and Binding [7] analyses, the total pressure drop and its shear and elongational components in the converging part of the slit die were estimated for the L-PP and the LCB-PP. The results are presented in Figure 12. The total pressure drop

was determined experimentally whereas the extensional pressure drop was calculated (details of the procedure can be found in Mobuchon et al. [11]). For the L-PP the extensional flow contribution in the hyperbolic die is around 20 % within the whole range of flow rates. In contrast, the LCB-PP reveals significant extensional pressure drop at low deformation rates in such a way that the shear pressure drop can be neglected. However, as the flow rate increases, the curves tend to cross each other at the flow rate of around 10 mL/s corresponding to a strain rate of 5 s^{-1}. According to these results and those obtained from the uniaxial SER measurements (Figure 11), it can be concluded that the branches have a distinct influence on the extensional properties at low deformation rates, which becomes insignificant at large deformation rates. As pointed out earlier, the polymer chains at low deformations are strongly entangled with surrounding macromolecules.

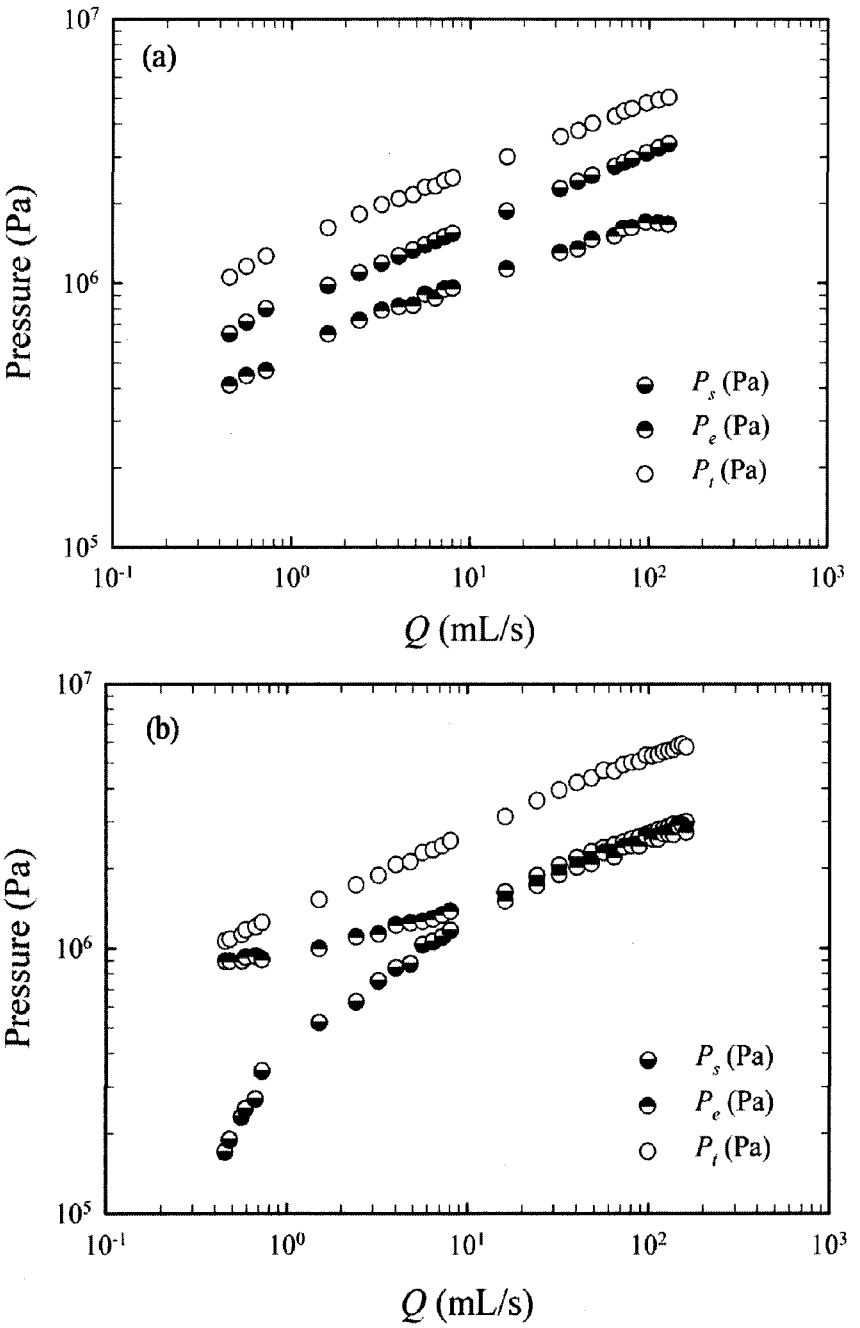

Fig. 12 Total pressure drop and contributions of the shear and extensional components as a function of flow rate Q for (a) L-PP and (b) LCB-PP; T=190 °C.

The apparent extensional viscosity values determined from the slit die for the neat PPs are compared in Figure 13 to the apparently steady uniaxial elongational values obtained using SER geometry. All data were evaluated at the same value of the second invariant of the rate of deformation tensor, which is equal to $2\dot{\varepsilon}$ for planar extensional and $\sqrt{3}\,\dot{\varepsilon}$ for uniaxial elongational flow. We assume that steady conditions were reached for the transient data reported in Figure 10 although there is no evidence in the trends especially for the strain-hardening samples. The values have been normalized by the Trouton ratio, Tr (defined as the ratio of the elongational viscosity to the shear viscosity at low deformation rates and is equal to 3 for the uniaxial elongational and 4 for the planar extensional of a Newtonian behavior). As shown in Figure 13, the Binding analysis predicts smaller values than the Cogswell method within the whole range of the deformation rate. It is believed that the elongational viscosity calculated by the Binding procedure is more meaningful as the assumptions are more realistic [7]. For the linear polypropylene, the uniaxial data obtained from the SER verify the Trouton relation at low strain rates, but large differences between the results of both analyses for the slit die data and the uniaxial extensional viscosities are observed at low deformation rates. Such deviations have been also reported by Ferec et al. [30] for PP and fiber suspensions in PP and tentatively explained by differences in the flow kinematics. Also, our SER data, as mentioned above, are probably far from steady-state values. However, we note that the data tend to coincide at high strain rates. Tremblay [31] has reported a similar behavior for extensional data of a LLDPE. A similar trend is observed for the branched

polypropylene but the values of the elongational viscosities obtained from the different techniques are closer to each other. Due to the pronounced strain-hardening of the LCB-PP as shown in Figure 10, the Trouton relation is not obeyed at the lowest strain rates and clearly the elongational properties of the branched PP are considerably larger that the shear properties in comparison to the linear PP. Finally, it should be mentioned that the entrance flow is quite complex and the above analyses are oversimplifications especially considering the viscoelastic nature of polymer melts.

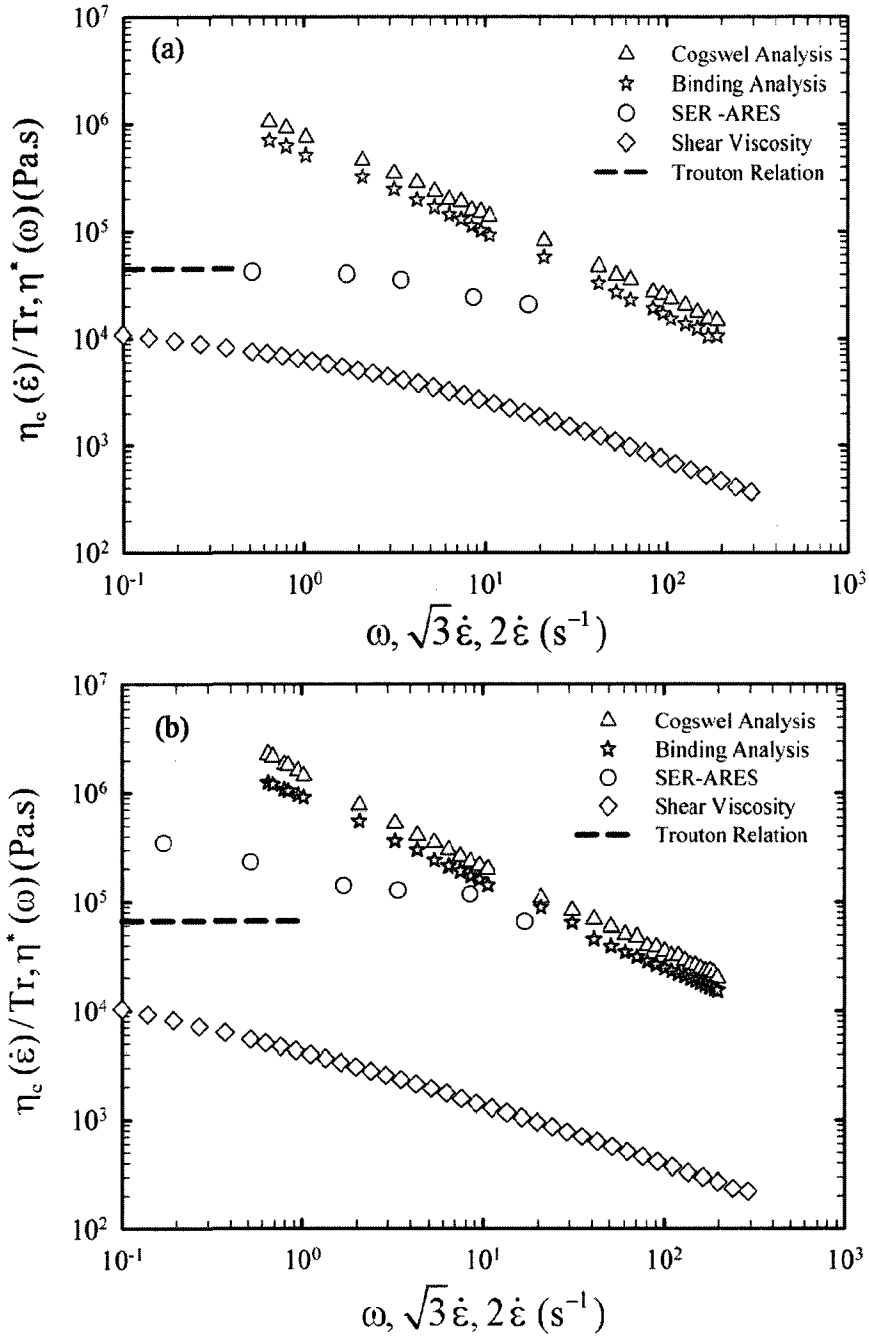

Fig. 13 Normalized apparent extensional viscosities calculated using the Cogswell and Binding methods for (a) L-PP and (b) LCB-PP. The complex shear viscosity data are shown for comparison; T=190°C.

4 Conclusions

In this work shear and elongation properties of blends of a linear and a long-chain branched polypropylene have been studied and the results can be summarized as follows:

- The blends containing more LCB-PP exhibited larger elasticity characteristics at low frequencies. This is believed to be due to more entanglements due to the presence of long chain branches. This effect decreased at high frequencies.
- As the content of LCB-PP increased, the peak of the relaxation spectrum shifted to longer times and the shape of the spectrum became broader indicating a different relaxation mechanism for long chain branched molecules compared to the linear ones.
- The Cox-Merz rule was found to be valid for the neat L-PP, but deviations at low rates were observed for the LCB-PP and the blend containing 30 wt% branched polymer. This was explained by the larger effect of long-chain branches at low deformation rates, which was also confirmed by the extensional measurements.
- Strain-hardening in uniaxial elongational flow was observed at shorter times and was more abrupt for the LCB-PP and the blends. At low extensional rates, the strain-hardening coefficient (S) was observed to considerably decrease as the strain rate increased, whereas at large strain rates, S slightly changed with increasing strain rate, indicating the non significant effect of branches at large deformation rates.

The apparent extensional viscosity values determined using the slit die were found to be much larger than predicted by the Trouton relation. However, the uniaxial elongational data for the linear PP obtained using the SER unit were found to verify the Trouton relation.

5 Acknowledgements

Financial support from NSERC (Natural Science and Engineering Research Council of Canada) and from FQRNT (Fonds Québécois de Recherche en Nature et Technologies) is gratefully acknowledged.

6 References

1. A. Ajji, P. Sammut, and M.A. Huneault, *J. Appl. Polym. Sci.*, **88**, 3070 (2003).

2. Y. Fang, P.J. Carreau, and P.G. Lafleur, *Polym. Eng. Sci.*, **45**, 1254 (2005).

3. J. Stange, C. Uhl, and H. Münstedt, *J. Rheol.*, **49**, 1059 (2005).

4. T.J. McCallum, M. Kontopoulou, C.P. Park, E.B. Muliawan, and S.G. Hatzikiriakos, *Polym. Eng. Sci.*, **47**, 1133 (2007).

5. F.A. Morrison, *Understanding Rheology*, Oxford Univ. Press (2001).

6. F.N. Cogswell, *Polym. Eng. Sci.*, **12**, 64 (1972).

7. D.M. Binding, *J. Non-Newt. Fluid Mech.*, **27**, 173 (1998).

8. M. Fujiyama and H. Inata, *J. Appl. Polym. Sci.*, **84**, 2157 (2002).

9. E.B. Bagley, *J Appl Phys*, **28**, 264 (1957).

10. B.Z. Rabinowitsch, *Physik Chemie*, **A145** (1929).

11. C. Mobuchon, P.J. Carreau, M.C. Heuzey, and M. Sepehr, *Polym. Composites*, **26**, 247 (2005).

12. M.L. Sentmanat, Dual windup extensional rheometer, US patent 6578413 (2003).

13. P.M. Wood-Adams, J.M. Dealy, A.W. Groot, and O.D. Redwine, *Macromolecules*, **33**, 7489 (2000).

14. J. Honerkamp and J. Weese, *Rheol. Acta*, **32**, 65 (1993).

15. J.M. Dealy and R.G. Larson, *Structure and Rheology of Molten Polymers*, Hanser Publisher, Munich (2006).

16. M. Doi and S.F. Edwards, The Theory of Polymer Dynamics, Oxford (1986).

17. H. Kwang, D. Rana, K. Cho, J. Rhee, T. Woo, B.H. Lee, and S. Choe, *Polym. Eng. Sci.*, **40**, 1672 (2000).

18. L.A. Utracki, *in Two Phase Polymer Systems*, Hanser Publisher, New York (1991).

19. L.A. Utracki and B. Schlund, *Polym. Eng. Sci.*, **27**, 1512 (1987).

20. C. Liu, J. Wang, and J. He, *Polymer*, **43**, 3811 (2002).

21. K. Ho, L. Kale, and S. Montgomery, *J. Appl. Polym. Sci.*, **85**, 1408 (2002).

22. Y. Fang, F. Sadeghi, G. Fleuret, and P.J. Carreau, *Can. J. Chem. Eng.*, **86**, 6 (2008).

23. W.P. Cox and E.H. Merz, *J. Polym. Sci.*, **28**, 619 (1958).

24. P.J. Carreau, D.C.R. De Kee, and R.P. Chhabra, *Rheology of Polymeric Systems, Principles and Applications*, Hanser Publisher (1997).

25. J. Thomasset, M. Grmela, and P.J. Carreau, *Non-Newt. Fluid Mech.*, **73**, 195 (1997).

26. H. Münstedt, S. Kurzbeck, and L. Egersdörfer, *Rheol. Acta*, **37**, 21 (1998).

27. M.H. Wagner, H. Bastian, P. Hachmann, J. Meissner, S. Kurzbeck, H. Münstedt, and F. Langouche, *Rheol. Acta*, **39**, 97 (2000).

28. M.H. Wagner, S. Kheirandish, and M. Yamaguchi, *Rheol. Acta*, **44**, 198 (2004).

29. D. Auhl, J. Stange, H. Münstedt, B. Krause, D. Voigt, A. Lederer, U. Lappan, and K. Lunkwitz, *Macromolecules*, **37**, 9465 (2004).

30. J. Férec, M.C. Heuzey, J. Pérez-González, L. de Vargas, G. Ausias, and P.J. Carreau, *Rheol. Acta*, **48**, 59 (2009).

31. B.J. Tremblay, *Non-Newt. Fluid Mech.*, **33**, 137 (1989).

APPENDIX B

Rheological and Thermal Properties of Blends of a Long-Chain Branched Polypropylene and Different Linear Polypropylenes[6]

Seyed H. Tabatabaei, Pierre J. Carreau, and Abdellah Ajji

CREPEC, Chemical Engineering Department, Ecole Polytechnique, C.P. 6079, Succ. Centre ville Montreal, QC, H3C 3A7 Canada

Abstract

Blends of a long-chain branched polypropylene (LCB-PP) and four linear polypropylenes (L-PP) having different molecular weights were prepared using a twin screw extruder. The linear viscoelastic properties suggested the immiscibility of the high molecular weight L-PP based blends, and the miscibility of the low molecular weight L-PP based blends. In addition, the Palierne emulsion model showed good predictions of the linear viscoelastic properties for both miscible and immiscible PP blends. However, as expected, the low-frequency results showed a clear effect of the interfacial tension on the elastic modulus of the blends for the high molecular weight L-PP based blends. A

---

[6] *Chemical Engineering Science*, in press.

successful application of time-temperature superposition (TTS) was found for the blends and neat components. Uniaxial elongational properties were obtained using a SER unit mounted on an ARES rheometer. A significant strain hardening was observed for the neat LCB-PP as well as for all the blends. The influence of adding LCB-PP on the crystallinity, crystallization temperature, melting point, and rate of crystallization were studied using differential scanning calorimetry (DSC). It was found that the melting point and degree of crystallinity of the blends first increased by adding up to 20 wt% of the branched component but decreased by further addition. Adding a small amount of LCB-PP caused significant increase of the crystallization temperature while no dramatic changes were observed for blends containing 10 wt% LCB-PP and more. Furthermore, the crystalline morphology during and after crystallization of the various samples was monitored using polarized optical microscopy (POM). Compared to the neat linear polymers, finer and numerous spherulites were observed for the blends and LCB-PP. Dynamic mechanical (DMA) data of the blends and pure components were also analyzed and positive deviations from the Fox equation for the glass transition temperature, T_g, were observed for the blends.

1 Introduction

Due to the higher melting point, lower density, higher chemical resistance, and better mechanical properties of polypropylene (PP) in comparison to polyethylene (PE), it is widely employed for many industrial applications. However, the linear structure of L-PP

limits its applications for processes where good extensional properties and melt strength are required such as thermoforming, film blowing, foaming and fiber spinning. On the other hand, it is well known that branched polymers have enhanced extensional properties and their blending with linear counterparts can improve their elongational behavior, particularly for PE (Ajji et al., 2003; Lohse et al., 2002; Steffl, 2004). With the recent development of branched PP, it is expected that the elongational properties of L-PP can be effectively enhanced when blended with a long-chain branched polypropylene (LCB-PP).

Long-chain branches are commonly introduced to linear PP via electron beam irradiation and post reactor chemical modification (Auhl et al., 2004; Tian et al., 2006a). Their effects on the processability have been reported in the literature (Gotsis et al., 2004; Stange and Münstedt, 2006). Gotsis et al. (2004) showed that branching up to an optimum level improved the processability in foaming and thermoforming processes, while further branching did not have a dramatic effect. Stange and Münstedt (2006) found that the strain hardening of branched polypropylenes caused not only a high melt strength, but also showed a significant homogeneity of deformation in the elongational experiments, which allowed forming foams with higher expansion ratios than L-PP.

In several cases (Ajji et al., 2003; Stange et al., 2005; McCallum et al., 2007; Fang et al., 2008), the rheological behavior of blends of linear and branched polypropylene and polyethylene has been investigated. It has been reported that branched polymers exhibit higher shear thinning, elasticity, and strain hardening compared to linear ones.

Stange et al. (2005) showed that adding a small amount of LCB-PP significantly influences the rheological properties, especially the elongational behavior of linear PP blends. In addition, they found that the strain hardening of PP blends decreased as the strain rate increased while for the neat LCB-PP, enhancement of strain hardening was observed. McCallum and coworkers (2007) realized that the blending of branched and linear PP not only promoted the melt strength, but the mechanical properties increased as well. Ajji et al. (2003) showed that adding a small amount of low density polyethylene (LDPE) increased the strain hardening of linear low density polyethylene (LLDPE) resins. They also found that 10-20 wt% of LDPE is sufficient for improving the extensional property of LLDPE. Fang et al. (2008) concluded that an increase in the length of short branches and, possibly, the presence of a few long branches in metallocene LLDPEs and comparable molecular weights with LDPE could improve the miscibility of LLDPE/LDPE blends.

To our knowledge no work has been published regarding the effect of molecular weight of linear polypropylene on the rheological behavior of blends of linear and long-chain branched polypropylene. Using different rheological characterization methods, it will be shown that molecular weight has a crucial role on the miscibility of L-PP and LCB-PP. In addition, the influence of adding LCB-PP on the thermal properties, crystallization, and solid state behavior of the blends will be explored.

2 Experimental

2.1 Materials

Four commercial linear polypropylenes (PP40, PP28, PP08, and PP04) and a commercial branched polypropylene (LCB-PP) were selected. The PP28 and PP08 were

Table 1. Main characteristics of the neat polymers.

Resin code	Company	MFR (g/10min)	Nomencl.	η_0^* (kPa.s)	η_0^{**} (kPa.s)	M_w (kg/mol)	M_w/M_n	T_m (°C)	T_c (°C)
Pro-fax 6523	Basell	4.0	PP40	9.8	9.8	501	2.8	159.8	119.2
PP4612	ExxonMobil	2.8	PP28	14.4	16.5	543	3.9	161.0	114.4
PP5341	ExxonMobil	0.8	PP08	43.6	49.5	772	2.7	160.0	117.3
Pro-fax 6823	Basell	0.4	PP04	58.3	67.5	812	4.3	159.6	116.9
Pro-fax 814	Basell	2.5	LCB-PP	18.6	19.5	N/A	2.3	158.4	128.4

* Zero-shear viscosity values obtained from the Carreau-Yasuda model, T=190 °C.

** Zero-shear viscosity values obtained from the area under the weighted relaxation spectrum curves, T=190 °C.

supplied by ExxonMobil Company and had a melt flow rate (MFR) of 2.8 g/10min (under ASTM conditions of 230 °C and 2.16 kg) and 0.8 g/10min, respectively, while the PP40, PP04, and LCB-PP were obtained from Basell Company and had a MFR of 4 g/10min, 0.4 g/10min, and 2.5 g/10min, respectively. The main characteristics of the resins are shown in Table 1. The molecular weights of the L-PPs were evaluated from the relation between the zero-shear viscosity and the molecular weight (Fujiyama and Inata, 2002). The molecular weight distribution (MWD) was measured using a GPC (Viscotek model 350). The melting point, T_m, and the crystallization temperature, T_c, of

the resins were obtained using differential scanning calorimetry. Blends containing 20, 40, and 60 wt% LCB-PP were prepared using a twin screw extruder (Leistritz Model ZSE 18HP co-rotating twin screw extruder) followed by water cooling and pelletizing. The temperature profile along the barrel (from hopper to die) was set at 160/180/190/200/200/200/200 °C. The extrusion was carried out at 80 rpm. During blending, 3000 ppm of a stabilizer, Irganox B225, was added to avoid thermal degradation of the polymers. To make sure that all samples have the same thermal and mechanical history, unblended components were extruded under the same conditions.

2.2 Rheological measurements

Dynamic melt rheological measurements were carried out using a Rheometric Scientific SR5000 stress controlled rheometer with parallel plate geometry (diameter of 25 mm and a gap of 1.5 mm). All measurements were carried out at 190 °C under nitrogen atmosphere to avoid thermal degradation. Molded discs of 2 mm thick and 25 mm in diameter were prepared using a hydraulic press at 190 °C. Time sweep tests were first performed at a frequency of 0.628 rad/s for two hours. Material functions such as complex viscosity, elastic modulus, and weighted relaxation spectrum in the linear viscoelastic regime were determined in the frequency range from 0.01 to 500 rad/s. In order to obtain more accurate data, the frequency sweep test was carried out in four sequences while the amount of applied stress in each sequence was determined by a stress sweep test.

To measure the uniaxial elongational viscosity, an ARES rheometer equipped with a SER universal testing platform from Xpansion Instruments was used. The model used was SER-HV-A01, which is a dual windup extensional rheometer. It is capable of generating elongational rates up to 20 s^{-1}. Measurements were performed at 190 °C under nitrogen atmosphere.

2.3 Thermal analysis

Thermal properties of the various specimens were determined using a TA instrument differential scanning calorimeter (DSC) Q 1000. The samples were heated from 50 °C to 220 °C at a heating rate of 10 °C/min to eliminate initial thermal history, and then cooled to 50 °C at the same rate. The melting point and the degree of crystallinity were determined from the second heating ramp, also performed at a rate of 10 °C/min. Crystallinity values are reported, using a heat of fusion of 209 J/g for fully crystalline polypropylene (PP) (Arroyo and Lopez-Manchado, 1997).

2.4 Polarized optical microscopy (POM)

Crystallization monitoring was performed using polarized optical microscopy (OPTIHOT-2) to follow spherulites growth. For the non isothermal crystallization tests, films with a thickness of 50 μm were prepared using a twin screw extruder equipped with a slit die. The films were first heated on a programmable hot stage (Mettler FP82HT) from room temperature to 200 °C at a heating rate of 10 °C/min and were kept

at that temperature for 1 min to eliminate initial thermomechanical history, and then cooled to room temperature at the same rate.

2.5 Dynamic mechanical analysis

The solid state behavior of different samples was characterized using a TA instrument dynamic mechanical analyzer (DMA) 2980 inside an environmental test chamber (ETC). The temperature ranged from - 40 °C to 100 °C at a rate of 2 °C/min and frequency of 1 Hz was applied to the rectangular shape samples. To generate low temperatures and to control temperature during heating, liquid nitrogen was used. The glass transition temperature was determined from the maximum of the G'' curves.

3 Results and discussion

3.1 Rheological characterization of the neat PPs

The complex shear viscosities normalized by the zero shear viscosities, obtained using the Carreau-Yasuda model (see Table 1), are plotted as a function of frequency for the neat PPs in Figure 1. The LCB-PP exhibits a pronounced shear-thinning behavior due to the presence of long-chain branches. As the molecular weight of the L-PPs increases the behavior becomes more shear-thinning and the transition from the Newtonian plateau to the power-law region occurs at lower frequencies.

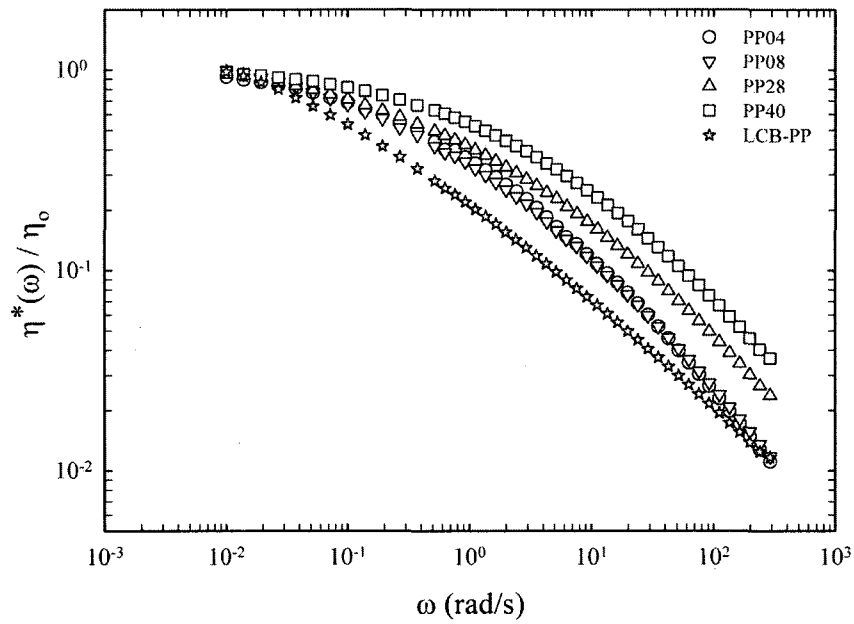

Fig. 1 Normalized complex viscosity as a function of frequency for neat PPs; T=190 °C.

The plot of the loss angle, δ (tanδ = G''/G'), as a function of frequency is shown in Figure 2. A monotonic decrease in the loss angle is observed for the L-PPs while the LCB-PP shows an inflection in the curve with a tendency towards a plateau at high frequencies. Wood-Adams et al. (2000) related the magnitude and breath of the plateau to the weight fraction of branched chains. The larger elasticity of the LCB-PP compared to L-PPs at low frequencies is attributed to more entanglements due to the presence of long-chain branches. However, as the frequency increases, the number of entanglements decreases due to the more shear-thinning character of the branched PP (see Figure 1).

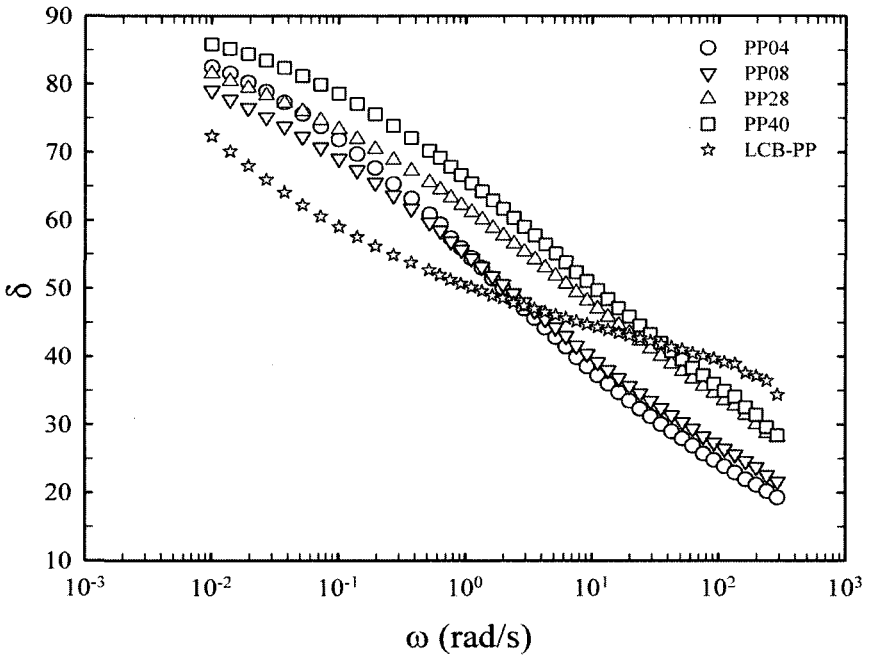

Fig. 2 Loss angle versus frequency for neat PPs; T=190 °C.

To compare the relaxation behavior of the L-PPs and LCB-PP, the weighted relaxation spectra evaluated from dynamic moduli (G', G'', ω) using the NLREG (non linear regularization) software (Honerkamp and Weese, 1993) are plotted in Figure 3 (the vertical dash lines represent the range of frequencies covered during the experiments). The area under the spectrum curve represents the zero-shear viscosity of the melt and it is reported in Table 1. A good agreement between these values and those obtained using the Carreau-Yasuda model is observed, suggesting that the relaxation spectra are accurate. It is obvious that the LCB-PP shows a longer relaxation time than the L-PPs, indicating that long-chain branches affect more the relaxation time than the larger molecules present in PP08 and PP04. The larger relaxation time for LCB-PP is attributed to changes in stress relaxation mechanisms. The simple reptation, as expected

for linear polymers, no longer suffices to relieve stress when there are enough branches present and slower events such as arm retraction must occur.

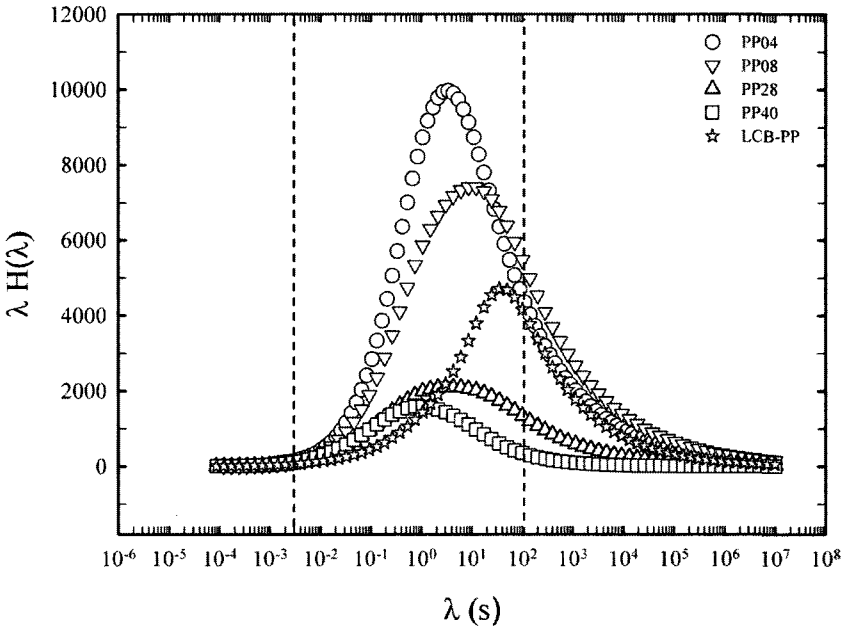

Fig. 3 Weighted relaxation spectra for neat PPs; T=190 °C (the vertical dash lines represent the range of frequencies covered during the experiments).

3.2 Rheological characterization of the blends

The complex shear viscosities as a function of frequency for the PP40/LCB-PP and PP04/LCB-PP blends (two extreme cases) are shown in Figures 4(a) and (b), respectively. It is clear that adding the LCB-PP causes a pronounced shear-thinning behavior due to the presence of long-chain branches. In addition, it is obvious that the viscosities of the PP40 based blends are intermediate between those of the neat components while those of the PP04 based blends are closer to that of the PP04. The behavior is typical of linear polymer melts and the complex viscosity of the blends follows the log additivity rule for low molecular weight based blends. This is shown in

Figures 5(a) and (b), where the complex viscosities at different frequencies are plotted as a function of the LCB-PP content. The logarithmic additivity rule is expressed as (Utracki and Schlund, 1987):

$$\log \eta^*(\omega) = \phi_\beta \log(\eta^*(\omega))_1 + (1-\phi_\beta)\log(\eta^*(\omega))_2 \qquad (1)$$

where ϕ_β is the branched PP content in weight percent and η^* is the complex shear viscosity. The PP40 based blends obey the log additivity rule, as depicted in Figure 5(a), suggesting miscibility of both PP components. However, significant deviations from this empirical relation are observed in Figure 5(b) for the PP04 based blends in the entire composition range, suggesting that these two PP parts are immiscible. Deviations from the log mixing rule for blends of linear and branched PPs and PEs have been reported in the literature (Fang et al., 2008; Ho et al., 2002; Liu et al., 2002). It is believed that not only the amount of LCB-PP influences the miscibility of the blends, but also the molecular weights of both components as well as the branching structure (e.g. star-like or tree-like) of the LCB-PP are important factors affecting the miscibility.

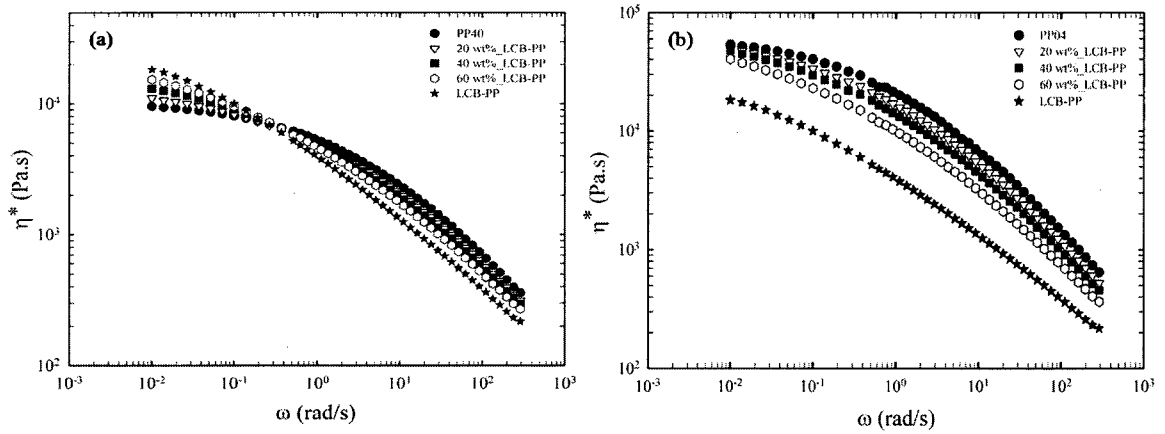

Fig. 4 Complex viscosity as a function of frequency for: (a) PP40/LCB-PP blends and (b) PP04/LCB-PP blends; T=190 °C.

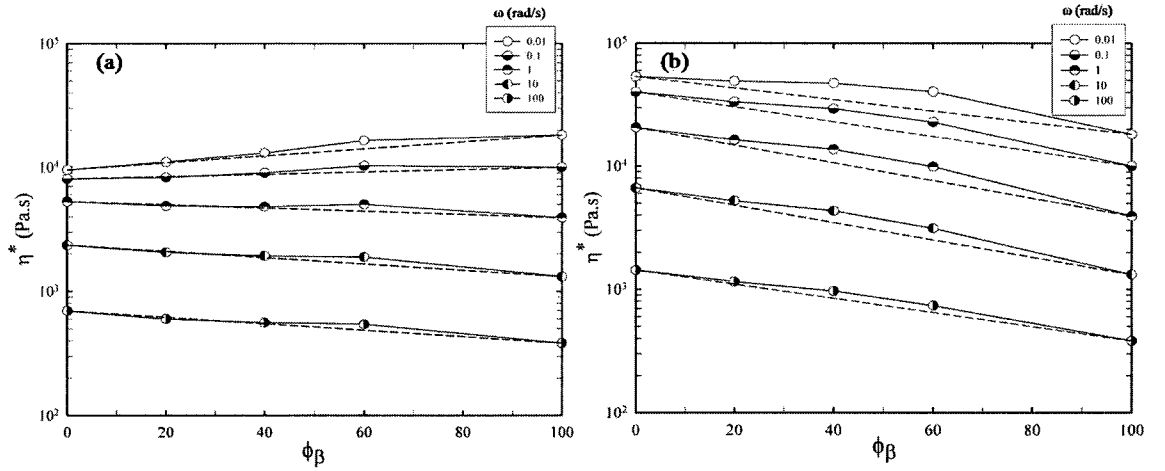

Fig. 5 Complex shear viscosity at different angular frequencies as a function of branched PP content for: (a) PP40/LCB-PP blends and (b) PP04/LCB-PP blends; T=190 °C (the dash lines show the additivity rule).

The zero-shear viscosity obtained from the Carreau-Yasuda model is shown as a function of the LCB-PP content in Figure 6. Good agreement with the log additivity rule for the blends having components with close melt flow indexes (e.i. PP40/LCB-PP and PP28/LCB-PP blends) is found, suggesting miscibility of the PP components. However, large deviations from the empirical rule are observed for the PP04/LCB-PP and

PP08/LCB-PP blends, suggesting that the two components are immiscible. It should be noted that at low frequencies (Newtonian region), a large increase in the number of entanglements due to the LCB-PP addition is expected for all the samples. Therefore, it is unlikely that the deviations from the log mixing rule could be explained for the PP04/LCB-PP and PP08/LCB-PP blends only.

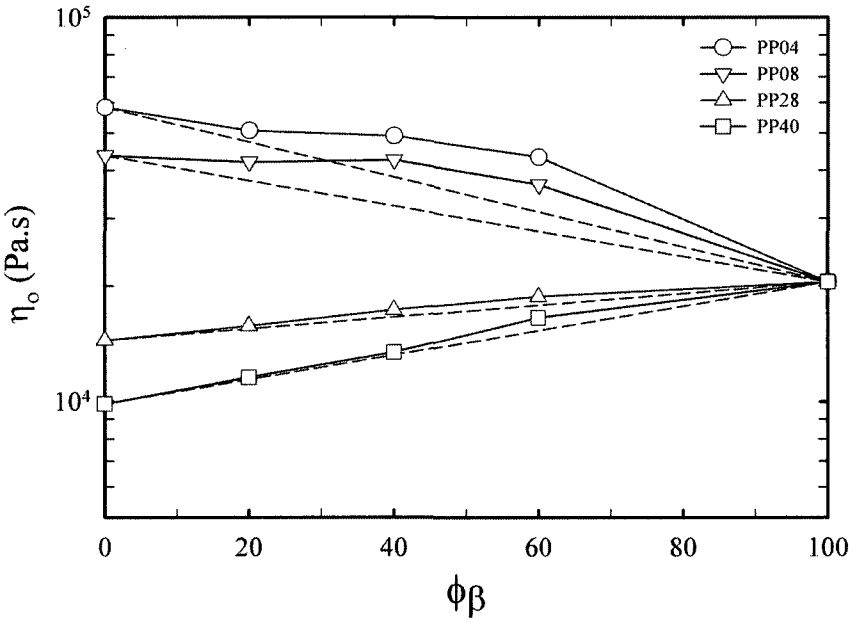

Fig. 6 Zero-shear viscosity as a function of LCB-PP content; T=190 °C (the dash lines show the additivity rule).

To see the effect of molecular weight of L-PP on the relaxation behavior of the blends, the weighted relaxation spectra of the PP40/LCB-PP and PP04/LCB-PP blends are illustrated in Figures 7(a) and (b), respectively. The addition of LCB-PP changes the relaxation mechanism from simple reptation to arm retraction, which retards the movement of chains along their backbone; hence, the maxima in the curves shift to longer times and the spectrum shape becomes broader. Note that for the PP40/LCB-PP

blends, the positions of the peaks are intermediate to those of the neat components, indicating again miscibility, while for the PP04/LCB-PP blends non uniform changes in the peaks are observed.

The behavior can also be analyzed using Cole-Cole plots of η'' versus η', as illustrated in Figure 8. The semicircular shape for the PP40/LCB-PP blends (Figure 8(a)) is another evidence of miscibility (Kwang et al., 2000; Utracki, 1991), while some synergistic effects for the PP04/LCB-PP blends (Figure 8(b)) are observed. It should be noted that the curves of the high M_w based blends are closer to that of the neat L-PP component, which confirms the results demonstrated in Figure 4.

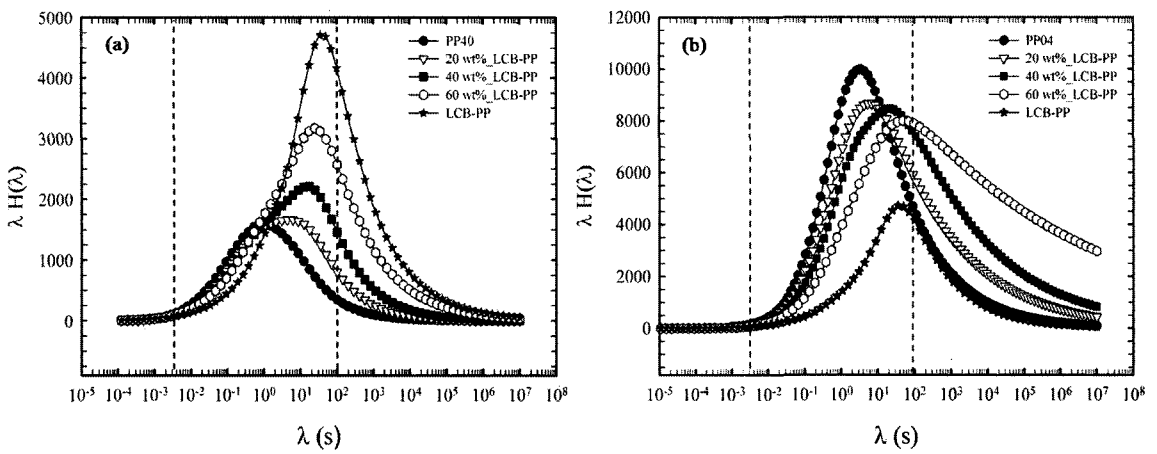

Fig. 7 Weighted relaxation spectrum for: (a) PP40/LCB-PP blends and (b) PP04/LCB-PP blends; T=190 °C (the vertical dash lines represent the range of frequencies covered during the experiments).

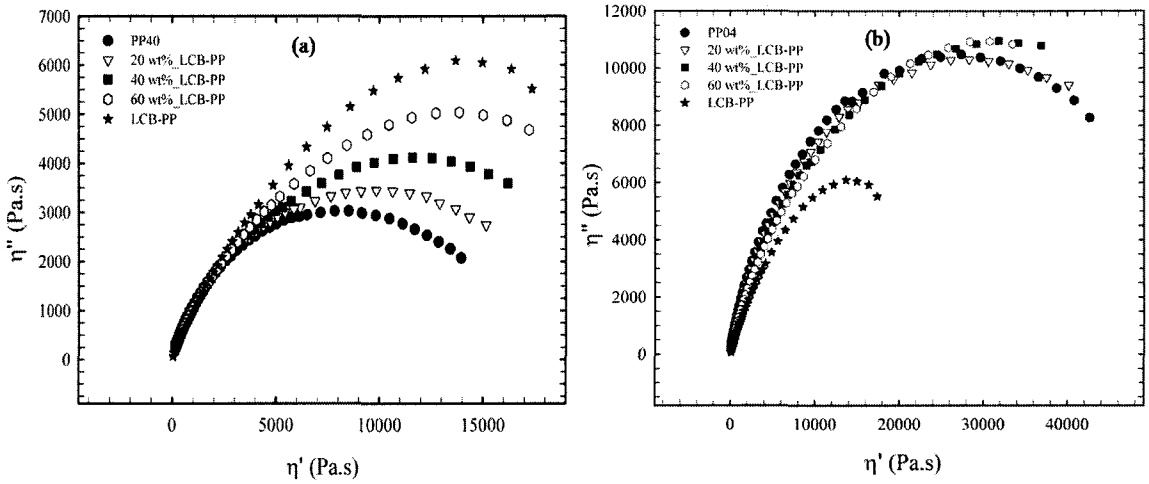

Fig. 8 Cole-Cole plots for: (a) PP40/LCB-PP blends and (b) PP04/LCB-PP blends; T=190 °C.

Figures 9(a) and (b) illustrate the storage modulus of the PP40/LCB-PP and PP04/LCB-PP blends, respectively. For the PP40 based blends, at low frequencies, the storage modulus of the LCB-PP is larger while the effect becomes inversed at high frequencies. For the blends containing a high molecular weight component (Figure 9(b)) some synergistic effects at low frequencies are seen for all compositions, which is possibly due to the immiscibility of these blends. The increase of elasticity at low frequencies is common in immiscible blends and has been interpreted in the context of emulsion models (Chun et al., 2000; Palierne, 1990; Utracki, 1991).

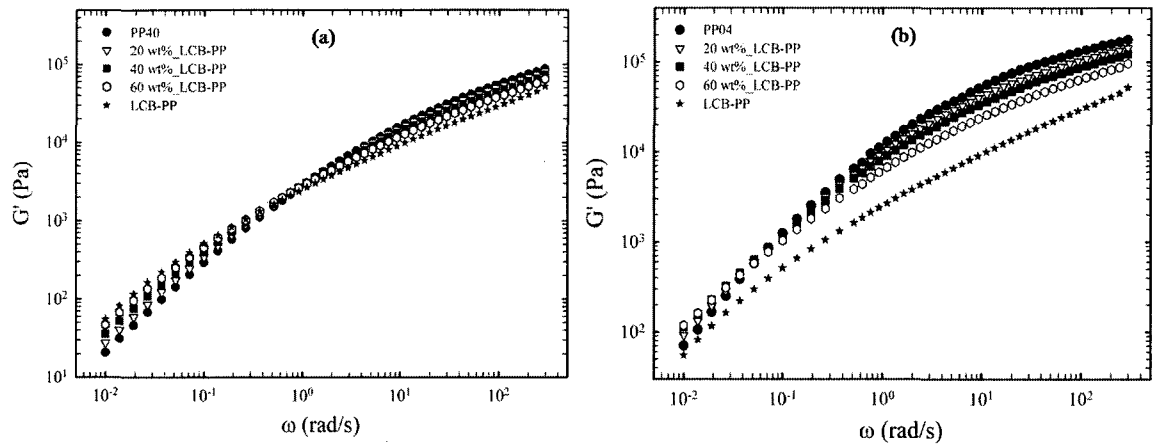

Fig. 9 Storage modulus as a function of frequency for: (a) PP40/LCB-PP blends and (b) PP04/LCB-PP blends; T=190 °C.

Palierne (1990) developed a model to predict the linear viscoelastic properties of immiscible emulsion-type blends. For a narrow distribution of droplet diameters (Bousmina and Muller, 1993) and constant interfacial tension, the complex modulus of the blend is expressed by:

$$G_B^*(\omega) = G_m^*(\omega)\frac{1+3\phi H^*(\omega)}{1-2\phi H^*(\omega)} \tag{2}$$

where H^* is defined as:

$$H^*(\omega) = \frac{\left(\frac{\alpha}{R_v}\right)\left(2G_m^*(\omega)+5G_d^*(\omega)\right)+\left(G_d^*(\omega)-G_m^*(\omega)\right)\left(16G_m^*(\omega)+19G_d^*(\omega)\right)}{10\left(\frac{\alpha}{R_v}\right)\left(G_d^*(\omega)+G_m^*(\omega)\right)+\left(3G_m^*(\omega)+2G_d^*(\omega)\right)\left(16G_m^*(\omega)+19G_d^*(\omega)\right)} \tag{3}$$

where ϕ is the volume fraction of the droplets of volume average radius R_v, α is the interfacial tension, and G_m^* and G_d^* are the complex moduli of the matrix and droplets, respectively.

Due to the low optical contrast between the PP components it was impossible to obtain the dimensions of drops in the PP blends and hence R_v. Following Fang et al. (2005) and Hussein and Williams (2001, 2004), α/R_v was used as a single parameter to find the best fits of the experimental data for the blends containing 20 wt% LCB-PP with low and high molecular weight L-PP components.

Figures 10(a) and (b) demonstrate the influence of α/R_v (0, 100, and 500) on the storage and loss moduli predicted by the Palierne model for the (80/20) PP40/LCB-PP and (80/20) PP04/LCB-PP, respectively. It is obvious that the G'' values predicted by the model are not sensitive to the value of α/R_v and are in good agreement with the experimental data. In contrast, the G' values are dramatically influenced by the value of α/R_v at low frequencies. For the (80/20) PP40/LCB-PP blend the best fit of the model with the experimental data was achieved for α/R_v= 0 while for (80/20) PP04/LCB-PP blend, the best fit was obtained for α/R_v=100. A value of the interfacial tension equal to 0 for the (80/20) PP40/LCB-PP blend is indicative of miscibility. However, the non zero value of α/R_v for the (80/20) PP04/LCB-PP blend is indicative of the presence of a dispersed phase. Assuming an interfacial tension of 0.1 mN/m for the PP pair (PP04/LCB-PP), the corresponding droplet radius is estimated to be around 1 μm. Hence, the hypothesis of immiscibility for these blend components is reasonable.

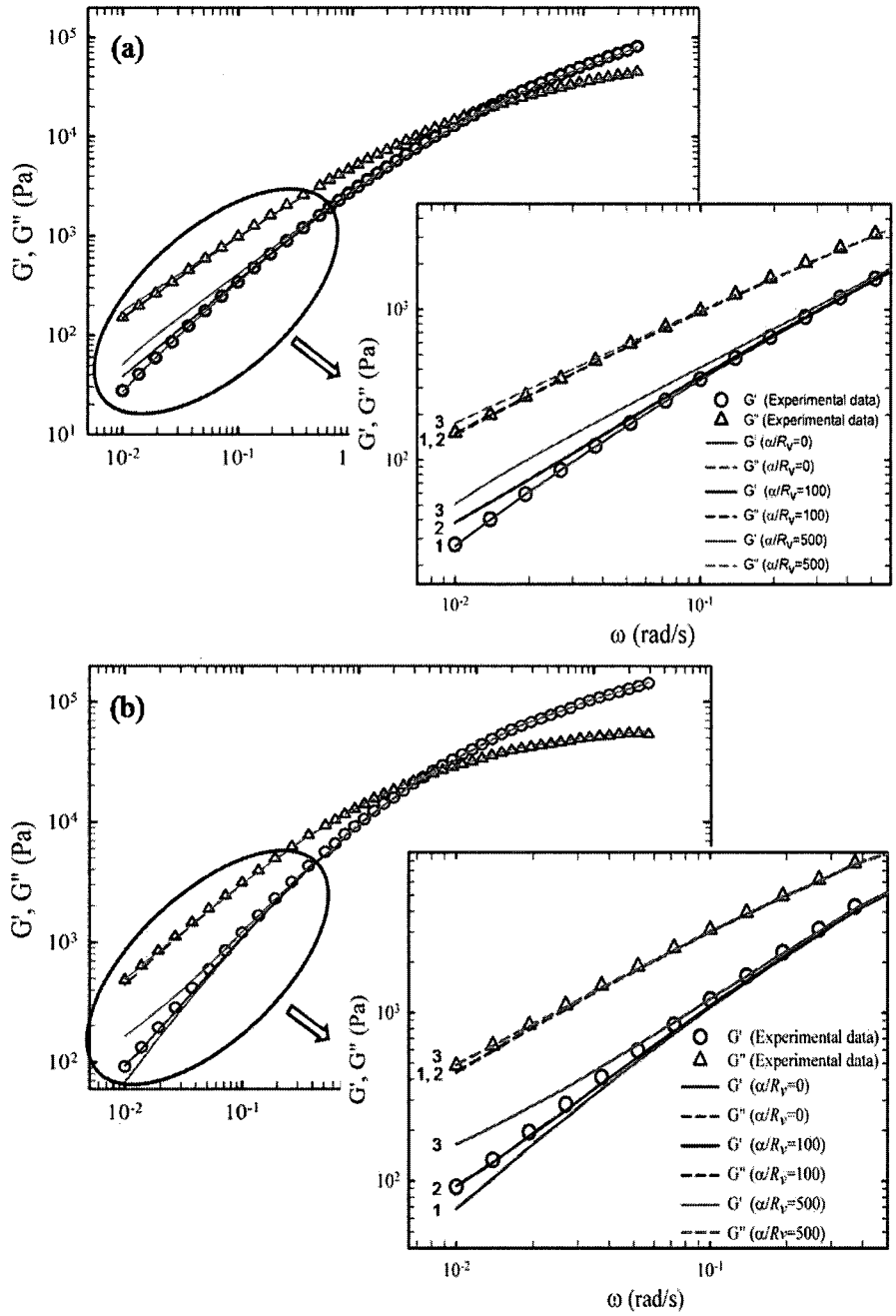

Fig. 10 Sensitivity of the Palierne model predictions of G' and G'' to different values of α/R_v for: (a) (80/20) PP40/LCB-PP blend and (b) (80/20) PP04/LCB-PP blend; T=190 °C.

The role of adding the long-chain branched component on the temperature sensitivity of complex viscosity of the blends is examined via the time-temperature superposition (TTS) principle. The results for the unblended polymers as well as for two blends are depicted in Figures 11(a) and (b), respectively (to facilitate the comparison between data, the curves have been shifted by a multiplication factor as indicated). The shift factor, a_T, was obtained from the temperature dependency of the zero-shear viscosity and was larger for the branched polymer compared to the linear one. From Figure 11, it is clear that TTS holds for all the samples. Van Gurp and Palmen (1998) proposed a refined analysis to check the validity of the TTS principle. The TTS principle is respected when the plot of the loss angle, δ ($\tan\delta=G''/G'$), as a function of complex modulus, $G^*=(G'^2+G''^2)^{1/2}$, superimpose in a single curve for all temperatures. The analysis of van Gurp and Palmen (1998) was examined for (60/40) PP40/LCB-PP and (60/40) PP04/LCB-PP blends as well as their neat components (the results are not shown). A single curve for each sample for various temperatures was observed, indicating that the TTS principle holds for all the samples. Macaubas and Demarquette (2002) investigated the applicability of TTS for a blend containing 10 wt% PP in PS and a blend containing 10 wt% PP in HDPE using the van Gurp-Palmen analysis. The immiscible 10 wt% PP/HDPE blend was observed to respect the principle, but not the immiscible 10 wt% PP/PS blend. This was explained by large differences of the flow activation energy, horizontal shift factor, and of the interfacial tension for PP and PS compared to those of PP and HDPE. In our case, although different rheological

characterization methods suggested immiscibility of the PP04/LCB-PP blend systems, no significant differences for the flow activation energy and the shift factor were found for the blend components. In addition, a small value of interfacial tension between the components is expected. Hence, these observations can explain the validity of TTS for the (60/40) PP04/LCB-PP blend.

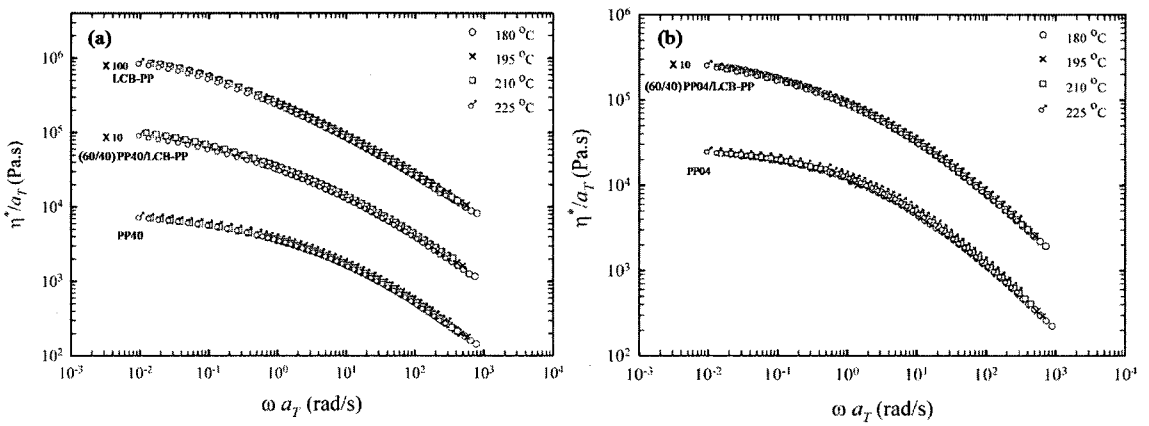

Fig. 11 Time temperature superposition for: (a) (60/40) PP40/LCB-PP blend and (b) (60/40) PP04/LCB-PP blend (the reference temperature is 225 °C).

In contrast to oscillatory shear data, uniaxial extension is very sensitive to molecular and microstructural parameters (Münstedt et al., 1998; Wagner et al., 2000). The transient elongational viscosity $\eta_e^+(t)$ of the resins and blends at different strain rates and 190 °C is illustrated in Figure 12 (as in Figure 11, the curves have been shifted by a multiplication). As expected, the linear polypropylenes respect the linear viscoelastic behavior over a large strain range where the transient elongational viscosity is equal to three times that the transient viscosity in simple shear determined using the relaxation spectrum according to the following equation:

$$\eta_e^+(t) = 3\sum_{i=1}^{N} \lambda_i H_i (1 - e^{-t/\lambda_i}) \tag{4}$$

To obtain the transient elongational viscosity from the above equation 100 modes (N) were used.

A significant strain hardening is observed for the LCB-PP as well as for all the blends. A sharper increase in the extensional viscosity curves and deviations from the linear viscoelasticity at shorter times were found as the weight fraction of the LCB-PP increases from 0.20 to 1. Stange et al. (2005) found that adding a small amount of the same long-chain branched PP to a linear PP (different than those used in this work) caused strain-hardening and the effect was attributed to long-chain branching. Similar results for blends of LDPE and LLDPE were reported by Ajji et al. (2003) and Wagner et al. (2004). Note that for the PP04/LCB-PP blends at all strain rates the shape of the curves are similar to that of the PP04, in accordance with the shear data (see Figures 4 and 8), which is probably due to immiscibility of these blends. As for the shear properties, it is clear that the elongational properties are dominated by the high molecular weight component.

The behavior of the PP28/LCB-PP blends was similar to that of the PP40/LCB-PP blends and that of the PP08/LCB-PP was close to the PP04/LCB-PP. For the sake of simplicity and brevity, the results for the PP28/LCB and PP08/LCB blends are not shown.

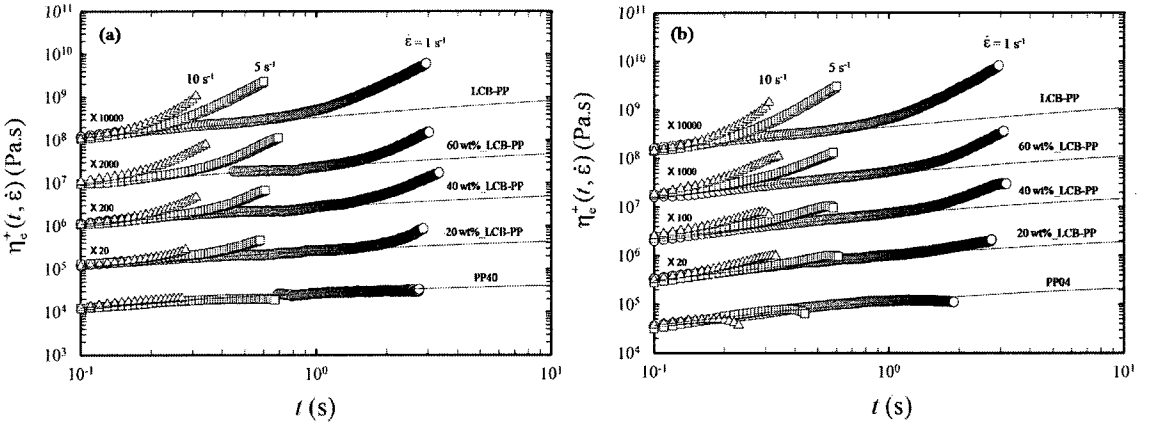

Fig. 12 Transient elongational viscosities as a function of time at different Hencky strain rates, $\dot{\varepsilon}$, for: (a) PP40/LCB-PP blends and (b) PP04/LCB-PP blends; T= 190 °C (the solid lines represent the linear behavior calculated from the relaxation time spectrum).

3.3 Thermal characterization

In the melting curve of the neat L-PPs, a small peak around 148 °C was observed and attributed to the presence of a small amount of beta (β) or hexagonal crystalline form of PP (Jang et al., 2001). The magnitude of the peak was reduced when up to 5 wt% branched PP was added and disappeared by further addition of the LCB-PP. As the peak was not seen for the neat LCB-PP, it could be concluded that the presence of long-chain branches prevented the formation of beta crystals. Tian et al. (2006b) studied the crystalline structures of linear and long chain branched PPs using wide-angle X-ray diffraction (WAXD). In accordance with our DSC results, they found that linear PPs could crystallize in the α and β forms, while branched PPs crystallized only in the α crystalline form.

Melting and crystallization temperatures obtained from the peak positions as well as the degree of crystallinity of the various materials and blends are presented in Table 2.

The melting point of the blends first increases by adding 20 wt% LCB-PP to the linear PPs while further addition reduces it. The reason for this behavior is unclear at present and different trends for the melting point of blends of linear and branched PPs have been reported in the literature (McCallum et al., 2007). Generally, a single melting peak was observed for all the blends. However, as the melting points of the components are very close, this cannot be considered as an indication of miscibility.

Table 2. Melting point (T_m), crystallization temperature (T_c), and degree of crystallinity (X_c) of the neat PPs as well as the blends (the numbers in parenthesis indicate the standard deviation of crystallinity).

Sample	T_m (°C)	T_c (°C)	X_c	Sample	T_m (°C)	T_c (°C)	X_c
PP04	159.6	116.9	36.8±1.1	PP28	161.0	114.4	40.0±0.9
(20/80) PP04/LCB-PP	161.9	125.5	41.6±0.7	(20/80) PP28/LCB-PP	162.1	126.5	42.2±1.4
(40/60) PP04/LCB-PP	161.7	126.4	37.5±0.5	(40/60) PP28/LCB-PP	161.6	127.5	41.3±0.7
(60/40) PP04/LCB-PP	160.5	127.1	36.9±1.2	(60/40) PP28/LCB-PP	160.6	127.7	35.6±1.1
LCB-PP	158.6	128.4	35.0±1.0	LCB-PP	158.6	128.4	35.0±0.9
PP08	160.0	117.3	37.8±1.5	PP40	159.8	119.2	38.8±1.9
(20/80) PP08/LCB-PP	161.5	126.0	40.2±0.8	(20/80) PP40/LCB-PP	161.3	126.9	40.8±1.1
(40/60) PP08/LCB-PP	160.5	127.3	39.6±0.8	(40/60) PP40/LCB-PP	160.9	127.5	40.2±0.7
(60/40) PP08/LCB-PP	160.2	127.6	39.1±0.3	(60/40) PP40/LCB-PP	160.0	127.8	37.3±1.2
LCB-PP	158.6	128.4	35.0±1.0	LCB-PP	158.6	128.4	35.0±0.9

Adding LCB-PP to the linear PPs causes a significant increase in the crystallization temperature, T_c, for all LCB contents, with the maximum change occurring at 20 wt% LCB-PP (see Table 2). Similar observations for blends of other linear and branched PPs were reported by McCallum et al. (2007). To determine at which concentration the transition for the crystallization temperature occurs, additional blends containing 2, 5,

and 10 wt% LCB-PP were prepared and analyzed and the results are shown in Figure 13. It is clear that T_c of PP28 changes from 114.4 to 123.3 °C after adding only 2 wt% LCB-PP while further addition of LCB-PP causes a slight increase of the crystallization temperature. Dramatic increases in the crystallization temperature have also been reported in literature (Zhang et al., 2007) when a nucleating agent was added to a neat polymer. It was interpreted by a lower free energy for the heterogeneous nucleus formation compared to that of the homogeneous nucleus formation. In our case, one possibility for the dramatic rise of T_c can be explained by a large increase of the heterogeneous nuclei sites due to addition of the long-chain branches. However, the residual catalysts used to produce the long-chain branches may also act as nucleating agents, which could be another reason for the increase of T_c.

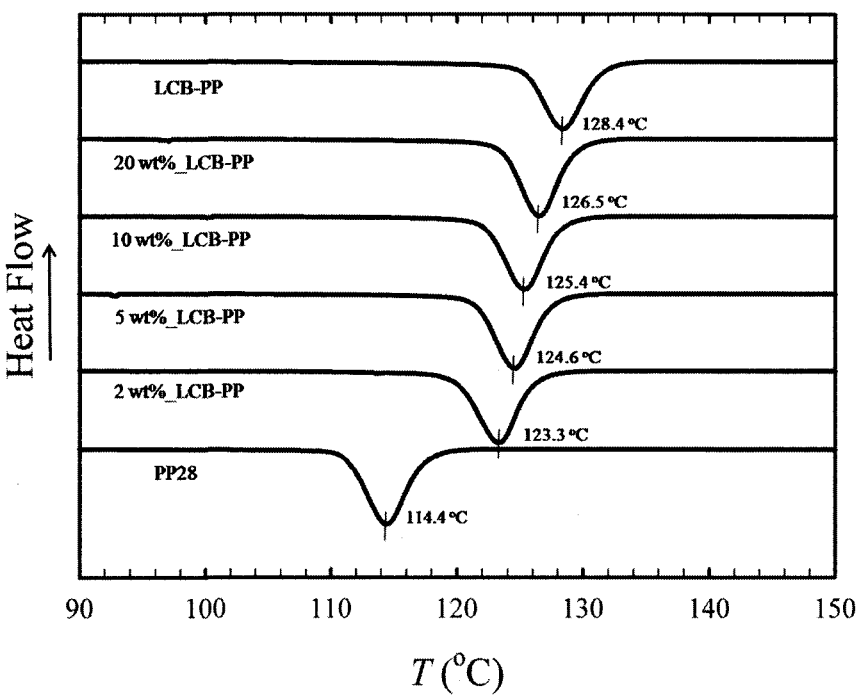

Fig. 13 DSC cooling thermographs for PP28, LCB-PP, and their blends at 10 °C/min.

Table 2 also reports the results of crystallinity measurements for all the blends and for all concentrations. A significant increase of the degree of crystallinity is observed when 20 wt% of LCB-PP is added to the L-PPs, and this for all the blends. It was also found that the transition in this crystallinity increase occurs upon the addition of only 2 wt% LCB-PP (the data are not presented here). It is postulated that a small amount of the LCB-PP increases the number of nuclei sites, resulting in an increase of crystallinity. On the one hand, further addition of the branched polymer increases the number of nuclei sites, on the other hand, the branches prevent chain mobility, leading to a decrease in crystallinity when more than 20 wt% LCB-PP is added.

To examine the effect of adding LCB-PP on the rate of crystallization, the relative crystallinity (obtained from the area under the exotherm peak of the crystallization curve) as a function of time for the PP28/LCB-PP blends was determined and the results are shown in Figure 14. The relation between time, t, temperature, T, and cooling rate, Φ, is expressed as (Tian et al., 2007):

$$t = \frac{T_o - T}{\Phi} \qquad (5)$$

where T_o is the onset crystallization temperature. All the curves show an S shape, similar for all the components and blends, as seen in Figure 14. However, a lower transition appeared at the later crystallization stage for samples containing the LCB-PP. In general, the rate of crystallization is first controlled by nucleation and then by growth of crystals and packing (Tian et al, 2007). As mentioned above, adding a branched polymer to a linear one increases the number of nuclei sites resulting in a larger crystallization rate for

the blends in the early stages of the crystallization. However, due to more impingements of the crystalline parts, crystalline growth is stopped at later stages. Tian et al. (2007) studied the crystallization kinetics of a linear PP and PPs containing different levels of long chain branching (LCB). Similar to our results, their finding showed that the presence of LCB accelerated crystallization at the early stage, and then the reverse effect on crystallization was observed at the later stage. The half-time of crystallization, $t_{1/2}$, can be obtained from Figure 14. It is obvious that the value of $t_{1/2}$ decreases as the level of the LCB-PP increases, indicating that the presence of the LCB-PP accelerates the crystallization behavior of the L-PP. It is speculated that the branches have the role of heterogeneous nucleating sites, which was also mentioned by Tian et al. (2007).

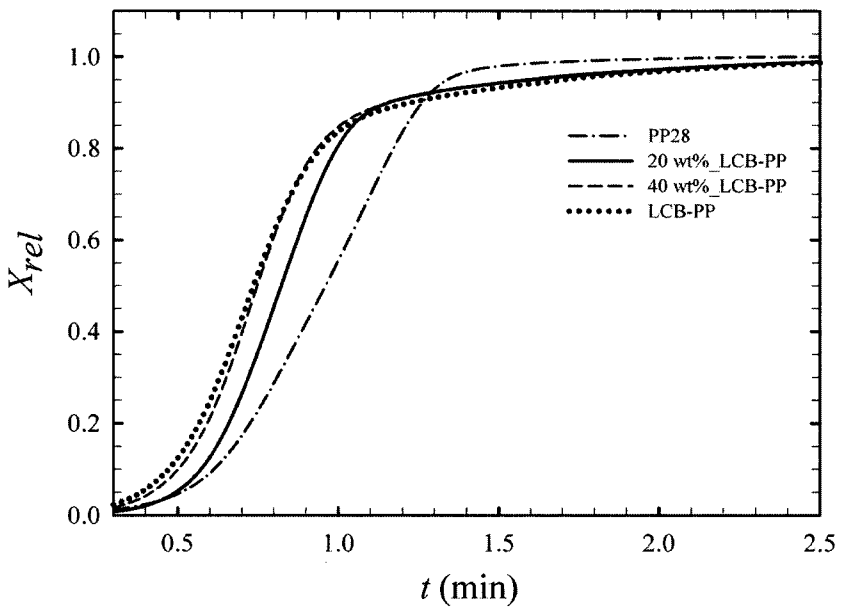

Fig. 14 Curves of relative crystallinity versus time for the PP28/LCB-PP blends.

The Avrami equation can be used to elucidate the differences in the primary nucleation for the blend systems (Agarwal et al., 2003). It is expressed as:

$$1 - X(t) = e^{-kt^n} \quad (6)$$

where $X(t)$ is the amount of crystallinity and n and k are the Avrami constants. The exponent n depends on the nucleation type and growth geometry (Agarwal et al., 2003): n values close to 1, 2, and 3 correspond to a rod, disk, and sphere like growth geometry, respectively (Agarwal et al., 2003). The double logarithm of the above equation leads to:

$$\log[-\ln(1 - X)] = \log(k) + n\log(t) \quad (7)$$

Plots of log [-ln(1-X)] versus log t are illustrated in Figure 15. To facilitate the comparison between data, the non-linear portion of the curves was removed. The value of the Avrami exponent, shown in the figure, is close to 3 indicating sphere like growth of the crystalline phase for all the samples. The value of n changes upon adding LCB-PP to the blends. This suggests different nucleation and growth mechanisms for the samples containing LCB-PP.

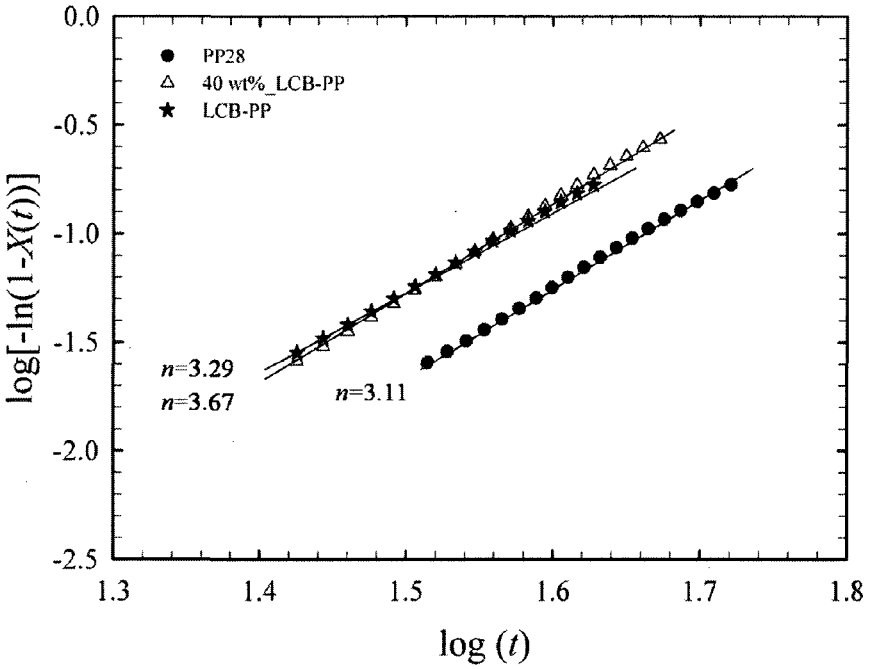

Fig. 15 Plots of log[-ln(1-$X(t)$)] as function of log(t) for PP28, LCB-PP and the 40wt% PP28/LCB-PP blend.

The crystal morphology of the PP28, LCB-PP, and the blends containing 2 and 20 wt % LCB-PP were observed using POM, and presented in Figure 16. Large spherulites, as expected for linear polymers, are observed for PP28 (Figure 16(a)). The number of spherulites increased noticeably and their size decreased by adding only 2 wt% LCB-PP (Figure 16(b)), indicating that more nucleating sites have been created. The crystal structures of the (80/20) PP28/LCB-PP blend was similar to that of (98/2) PP28/LCB-PP and the neat LCB-PP showed slightly smaller spherulites. The optical microscopy revealed that the spherulite growth in PP28 was due to sporadic nucleation, while that of the branched PP containing blends is attributed to an instantaneous nucleation. Sporadic nucleation happens by chain aggregation, which needs a longer time, whereas

heterogeneous nucleation happens as soon as the temperature reaches the crystallization temperature (Guan et al., 2003; Tian et al., 2007). This can explain the results presented in Figure 14.

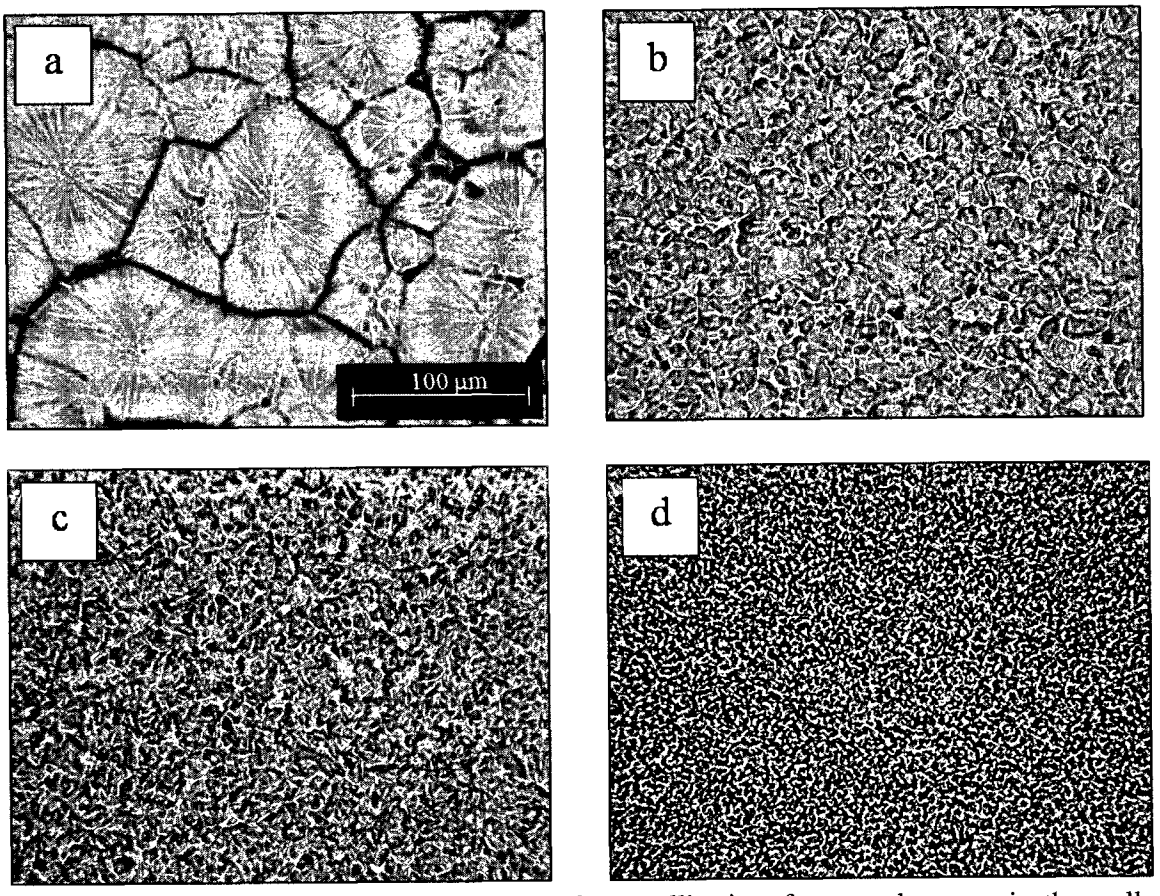

Fig. 16 Optical micrographs at the end of crystallization for samples non isothermally crystallized at 10 °C/min from the melt. a) PP28, b) (98/2) PP28/LCB-PP, c) (80/20) PP28/LCB-PP, and d) LCB-PP.

As mentioned before, it is believed that the residual catalyst in the branched samples act as a nucleating agent. In order to separate the contribution of the residual catalyst from that of long-chain branches on the final morphology, 0.2, 0.5, and 1 wt % sodium benzoate (SB) (supplied by LAB MAT), in the form of powder, were dry

blended with the PP28. From Dong et al., (2008) and Zhu et al., (2006), it is known that SB acts as an α form nucleating agent. Figure 17 illustrates optical micrographs of the PP28 and nucleated samples as well. Obviously, the reduction of the spherulite size is observed when the nucleating agent is added to the linear polymer. These observations accompanied with those presented in Figure 16 suggest a significant coupling effect between residual catalysts and long chain branches, which yields to the presence of large number of very small spherulites for the specimens containing the branched polymer.

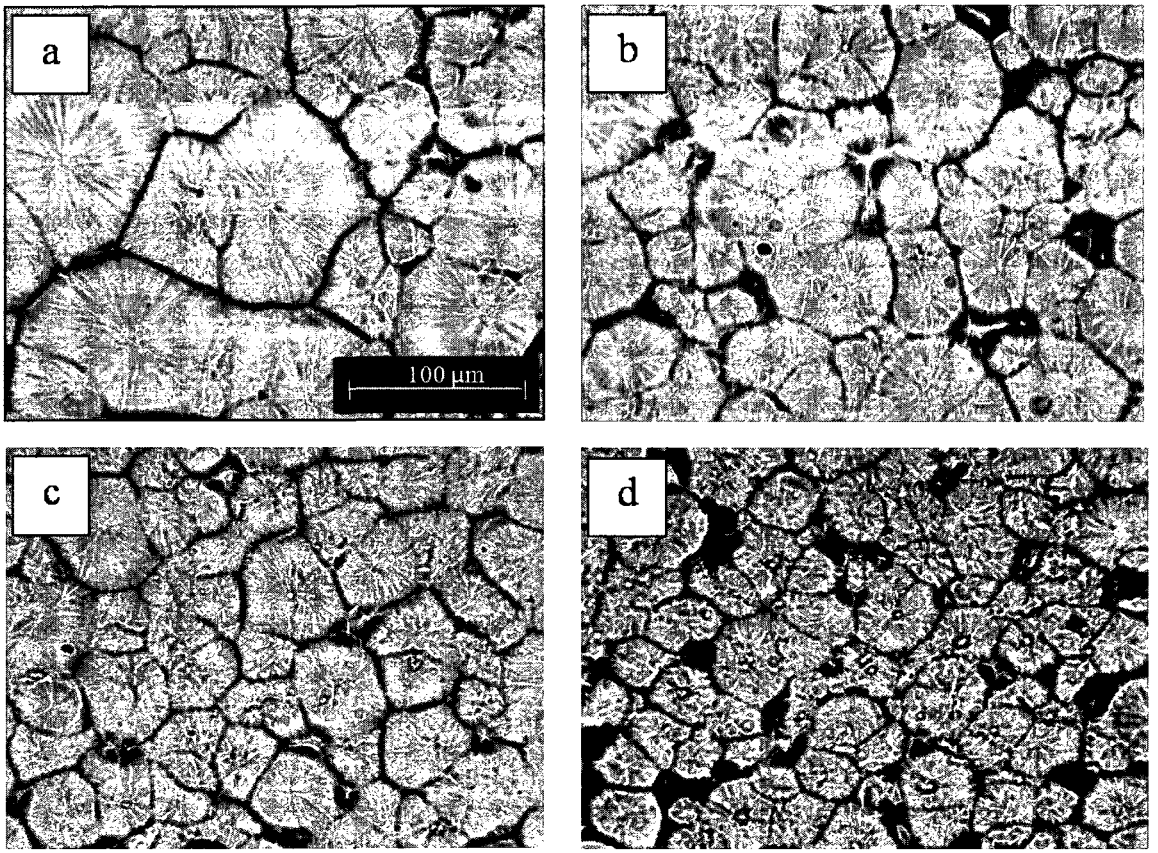

Fig. 17 Optical micrographs at the end of crystallization for samples non isothermally crystallized at 10 °C/min from the melt. a) PP28, b) 0.2 wt% nucleated, c) 0.5 wt% nucleated, and d) 1 wt% nucleated.

3.4 Solid state properties

The glass transition temperature of samples, obtained from the position of the maximum in the G'' curves, is presented in Figure 18. The solid lines were sketched accordance to the Fox equation:

$$\frac{1}{T_g} = \frac{w}{T_{g1}} + \frac{1-w}{T_{g2}} \qquad (8)$$

where T_{g1} and T_{g2} are the glass transition temperature of the unblended samples and w is the weight fraction of the branched component. The Fox equation can describe the T_g of polymer blends when no strong interaction exists between the polymer components (Boileau et al., 2001). In other words, significant deviations from this empirical relation for the polymer systems involving strong forces (e.g. hydrogen bonding) have been reported (Boileau et al., 2001). In our case, a positive deviation, with maximum occurring at 20 wt% of the branched PP, from the Fox equation is observed (Figure 18).

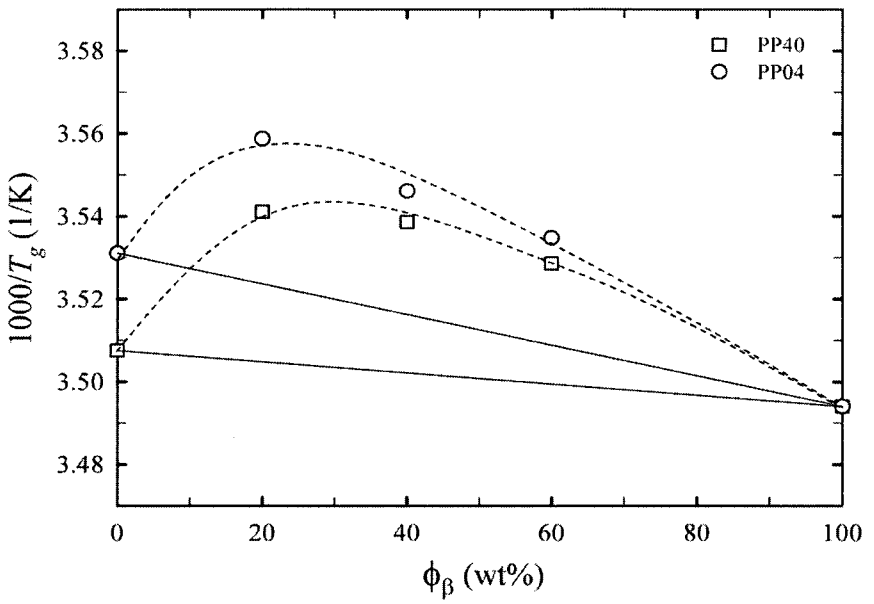

Fig. 18 Glass transition temperature as a function of LCB-PP content (the solid lines represent the Fox equation).

4 Conclusions

In this study, the rheological, crystallization, and thermal properties of blends of different molecular weight linear polypropylenes (L-PP) and a long-chain branched polypropylene (LCB-PP) were investigated. It was found that the shear and extensional properties of the blends were dominated by the L-PP for blends containing high molecular weight component. Based on the log-additivity rule for the zero-shear viscosity, Cole-Cole plots, weighted relaxation spectra, and elongational behavior, the low molecular weight L-PP blends with the branched PP are believed to be miscible, and the high molecular weight L-PP blends to be immiscible. The Palierne model predictions were in good agreement with the experimental data for all of the blends investigated. We

considered α/R_v (e.i. the ratio of interfacial tension α to volume average radius R_v) as a fitting parameter to find the best fit of the model predictions with the experimental data. The low frequency data of a PP40/LCB-PP blend and a PP04/LCB-PP blend was well described by $\alpha/R_v = 0$ and $\alpha/R_v = 100$, respectively, which suggests miscibility of the PP40/LCB-PP blend and immiscibility of the PP04/LCB-PP blend. Our results confirm the finding of Fang et al. (2005) on the miscibility/immiscibility of LLDPE/LDPE blends

The applicability of the time-temperature superposition (TTS) principle was checked for the blends as well as for the neat polymers. A good validity of TTS was found for all the samples and was explained by the close values for the flow activation energy and shift factor of the samples and the small interfacial tension between the PP components.

The results from thermal analysis indicated that, a small amount of long-chain branches increases the number of nuclei sites and alternatively the degree of crystallization and rate of crystallization. By the addition of a branched polymer, a dramatic increase of the crystallization temperature was observed. Finally, it was found that the value of half crystallization time, $t_{1/2}$, decreases as the level of LCB-PP increases, indicating in that the branches behave as heterogeneous nucleating sites.

Polarized optical microscopy of the samples revealed much smaller spherulites for the blends compared to the neat linear PP. This was attributed to the combined effects

between residual catalysts and long-chain branches, indicating that these two act as nucleating agents.

A positive deviation from the Fox equation of glass transition temperature, T_g, was observed for all the blends.

5 Acknowledgement

Financial support from NSERC (Natural Science and Engineering Research Council of Canada) is gratefully acknowledged.

Notation

a_T	thermal shift factor
G'	storage modulus (Pa)
G''	loss modulus (Pa)
G_m^*	matrix complex modulus (Pa)
G_d^*	droplet complex modulus (Pa)
H	relaxation spectrum (Pa)
k	Avrami constant
M_n	number average molecular weight (kg/mol)
M_w	weight average molecular weight (kg/mol)
n	Avrami constant
R_v	volume average radius (μm)
t	time (s)
$t_{1/2}$	half time of crystallization (s)
T	temperature (°C)
T_c	crystallization temperature (°C)
T_g	glass transition temperature (°C)
T_m	melting point (°C)
T_o	onset crystallization temperature (°C)
w	weight fraction
X	degree of crystallinity

X_c degree of crystallinity
X_{rel} relative crystallinity

Greek symbols

α interfacial tension (mN/m), alpha crystal form
β beta crystal form
δ loss angle
$\dot{\varepsilon}$ strain rate (1/s)
η^* complex viscosity (Pa.s)
η_o zero-shear viscosity (Pa.s)
η' real component of complex viscosity (Pa.s)
η'' imaginary component of complex viscosity (Pa.s)
η_e^+ transient elongational viscosity (Pa.s)
λ relaxation time (s)
μ micron
ϕ_β branched polypropylene content
Φ cooling rate (°C/min)
ω frequency (rad/s)

Abbreviations

DMA dynamic mechanical analysis
DSC differential scanning calorimetry
ETC environmental test chamber
GPC gas permeation chromatography
L-PP linear polypropylene
LCB-PP long-chain branched polypropylene
LDPE low density polyethylene
LLDPE linear low density polyethylene
MFR melt flow rate
MWD molecular weight distribution

NLREG non linear regularization
PE polyethylene
POM polarized optical microscopy
PP polypropylene
SB sodium benzoate
TTS time temperature superposition
WAXD wide angle x-ray diffraction

6 References

Agarwal, P.K., Somani, R.H., Weng, W., Mehta, A., Yang, L., Ran, S., Liu, L., Hsiao, B., (2003). Shear-induced crystallization in novel long chain branched polypropylenes by in situ rheo-SAXS and –WAXD. Macromolecules, 36, 5226-5235.

Ajji, A., Sammut, P., Huneault, M.A., (2003). Elongational rheology of LLDPE / LDPE blends. Journal of Applied Polymer & Science, 88, 3070-3077.

Arroyo, M., Lopez-Manchado, M.A., (1997). Crystallization kinetics of polypropylene: II. Effect of the addition of short glass fibres. Polymer, 38, 5587-5593.

Auhl, D., Stange, J., Münstedt, H., (2004). Long-chain branched polypropylenes by electron beam irradiation and their rheological properties. Macromolecules, 37, 9465-9472.

Boileau, S., Bouteiller, L., Foucat, E., Lacoudre, N., (2001). Stable low molecular weight glasses based on mixtures of bisphenol A and bispyridines. Journal of Material Chemistry, 12, 195-199.

Bousmina, M., Muller, R., (1993). Linear viscoelasticity in the melt of impact PMMA. Influence of concentration and aggregation of dispersed rubber particles. Journal of Rheology, 37, 663-679.

Chun, Y.S., Kyung, Y.J., Jung, H.C., Kim, W.N., (2000). Thermal and rheological properties of poly(ε-caprolactone) and polystyrene blends. Polymer, 41, 8729-8733.

Dong, M., Guo, Z., Su, Z., Yu, J., (2008). Study of the crystallization behaviors of isotactic polypropylene with sodium benzoate as a specific versatile nucleating agent. Journal of Polymer Engineering and Science Part B Polymer Physics, 46, 1183-1192.

Fang, Y., Carreau, P.J., Lafleur, P.G., (2005). Thermal and rheological properties of mLLDPE/LDPE blends. Polymer Engineering & Science, 45, 1254-1264.

Fang, Y., Sadeghi, F., Fleuret, G., Carreau, P.J., (2008). Properties of blends of linear and branched polypropylenes in film blowing. Canadian Journal of Chemical Engineering, 86, 6-14.

Fujiyama, M., Inata, H., (2002). Rheological properties of metallocene isotactic polypropylenes. Journal of Applied Polymer & Science, 84, 2157-2170.

Gotsis, A.D., Zeevenhoven, B.L.F., Hogt, A.H., (2004). The effect of long chain branching on the processability of polypropylene in thermoforming. Polymer Enginerring & Science, 44, 973-982.

Guan, Y., Wang, S.Z., Zheng, A.N., Xiao, H.N., (2003). Crystallization behaviors of polypropylene and functional polypropylene. Journal of Applied Polymer & Science, 88, 872-877.

Ho, K., Kale, L., Montgomery, S., (2002). Melt strength of linear low-density polyethylene/low-density polyethylene blend. Journal of Applied Polymer & Science, 85, 1408-1418.

Honerkamp, J., Weese, J., (1993). A non linear regularization method for the calculation of relaxation spectra. Rheologica Acta, 32, 65-73.

Hussein, I.A., Williams, M.C., (2001). Rheological study of the miscibility of LLDPE/LDPE blends and the influence of Tmix. Polymer Engineering & Science, 41, 696-701.

Hussein, I.A., Williams, M.C., (2004). Rheological study of the influence of branch content on the miscibility of octene m-LLDPE and ZN-LLDPE in LDPE. Polymer Engineering & Science, 44, 660-672.

Jang, G.S., Cho, W.J., Ha, C.S., (2001). Crystallization behavior of polypropylene with and without sodium benzoate as a nucleating agent. Journal of Polymer Engineering and Science Part B Polymer Physics, 39, 1001-1016.

Kwang, H., Rana, D., Cho, K., Rhee, J., Woo, T., Lee, B.H., Choe, S., (2000). Binary blends of metallocene polyethylene with conventional polyolefins: Rheological and morphological properties. Polymer Engineering & Science, 40, 1672-1681.

Liu, C., Wang, J., He, J., (2002). Rheological and thermal properties of m-LLDPE blends with m-HDPE and LDPE blends. Polymer, 43, 3811-3818.

Lohse, D.J., Milner, S.T., Fetters, L.J., Xenidou, M., Hadjichristis, N., Mendelson, R.A., Garcia-Franco, C.A., Lyon, M.K., (2002). Well-defined, model long chain branched polyethylenes. 2. Melt rheological behavior. Macromolecules, 35, 3066-3075.

Macaubas, P.H.P., Demarquette, N.R., (2002). Time-temperature superposition principle applicability for blends formed of immiscible polymers. Polymer Engineering & Science, 42, 1509-1519.

McCallum, T.J., Kontopoulou, M., Park, C.P., Muliawan, E.B., Hatzikiriakos, S.G., (2007). The rheological and physical properties of linear and branched polypropylene blends. Polymer Engineering & Science, 47, 1133-1140.

Münstedt, H., Kurzbeck, S., Egersdörfer, L., (1998). Influence of molecular structure on rheological properties of polyethylenes. Part II. Elongational behaviour. Rheologica Acta, 37, 21-29.

Palierne, J.F., (1990). Linear rheology of viscoelastic emulsions with interfacial tension. Rheologica Acta, 29, 204-214.

Stange, J., Uhl, C., Münstedt, H., (2005). Rheological behavior of blends from a linear and a long-chain branched polypropylene. Journal of Rheology, 49, 1059-1079.

Stange, J., Münstedt, H., (2006). Rheological properties and foaming behavior of polypropylenes with different molecular structure. Journal of Rheology, 50, 907-923.

Steffl, T. (2004). Rheological and film blowing properties of various low density polyethylenes and their blends. Dissertation, University Erlangen-Nuremberg.

Tian, J., Yu, W., Zhou, C., (2006a). The preparation and rheology characterization of long chain branching polypropylene. Polymer, 47, 7962-7969.

Tian, J., Yu, W., Zhou, C., (2006b). Crystallization kinetics of linear and long-chain branched polypropylene. Journal of Macromolecular Science Part B Physics, 45, 969-985.

Tian, J., Yu, W., Zhou, C., (2007). Crystallization behavior of linear and long chain branched polypropylene. Journal of Applied Polymer & Science, 104, 3592-3600.

Utracki, L.A., Schlund, B., (1987). Linear low density polyethylene and their blends: Part 4 shear flow of LLDPE blends with LLDPE and LDPE. Polymer Engineering & Science, 27, 1512-1522.

Utracki, L.A. (1991). in Two Phase Polymer Systems. Hanser Publisher, New York.

van Gurp, M., Palmen, J., (1998). Time-temperature superposition for polymeric blends. Rheology Bulletin, 67, 5-8.

Wagner, M.H., Bastian, H., Hachmann, P., Meissner, J., Kurzbeck, S., Münstedt, H., Langouche, F., (2000). The strain hardening behaviour of linear and long-chain-branched polyolefin melts in extensional flows. Rheologica Acta, 39, 97-109.

Wagner, M.H., Kheirandish, S., Yamaguchi, M., (2004). Quantitative analysis of melt elongational behavior of LLDPE/LDPE blends. Rheologica Acta, 44, 198-218.

Wood-Adams, P.M., Dealy, J.M., Groot, A.W., Redwine, O.D., (2000). Effect of molecular structure on the linear viscoelastic behavior of polyethylene. Macromolecules, 33, 7489-7499.

Zhang, R.H., Shi, D., Tjong, S.C., Li, R.K.Y., (2007). Study on the β to α transformation of polypropylene crystals in compatibilized blend of polypropylene/ polyamide-6. Journal of Polymer Engineering and Science Part B Polymer Physics, 45, 2674-2681.

Zhu, P., Tung, J., Phillips, A., Edward, G., (2006). Morphological development of oriented isotactic polypropylene in the presence of a nucleating agent. Macromolecules, 39, 1821-1831.